Mechanical Properties of Septins and Their Role in Establishing Diffusion Barriers

Brieuc Chauvin

Sorbonne Université

Ecole Doctorale Physique en Ile-de-France

Laboratoire Physico Chimie Curie – Insitut Curie

Mechanical Properties of Septins and Their Role in Establishing Diffusion Barriers

Par Brieuc Chauvin

Thèse de doctorat de Physique

Dirigée par Stéphanie Mangenot et Aurélie Bertin

Présentée et soutenue publiquement le 15 novembre 2022

Devant un jury composé de :

Barral	Yves	Professeur	Rapporteur
Bertin	Aurélie	Directrice de Recherche	co-Directrice de thèse
Debregeas	Georges	Directeur de Recherche	Examinateur
Hajj	Bassam	Chargé de Recherche	co-Encadrant
Mangenot	Stéphanie	Professeure	Directrice de Thèse
Masson	Jean-Baptiste	Directeur de Recherche	Examinateur
Piatti	Simonetta	Directrice de Recherche	Examinatrice
Théry	Manuel	Directeur de Recherche	Rapporteur

Acknowledgements

I would like to express my gratitude towards my PhD advisors Stéphanie Mangenot, Aurélie Bertin and Bassam Hajj. You have provided me with the greatest supervision I could have wished for. You have been very supportive, very helpful and always positive !

I would also like to thank Patricia Bassereau, Mathieu Coppey and Daniel Lévy who welcomed me in their team and supported me.

I would like to thank the members of my thesis advisory committee, Stéphanie Descroix and Antoine Jégou. As everything went very smoothly, I did not ask for much help, but I truly appreciated the remote support.

I would like to thank Pierre-Emmanuel Milhiet and Luca Costa for welcoming me at the CBS in Montpellier to perform the AFM indentation experiments. Luca, thank you for all the time you spent with me pressing on vesicles in this dark microscopy room.

I also would like to thank Andreas Janshoff for providing me the Matlab routine to analyse the AFM indentation experiments.

I want to thank Martin Lenz for the insightful discussions and for providing the model to account for the deformations of vesicles.

I would like to thank all the members of my jury, Yves Barral, Georges Degrégeas, Jean-Baptiste Masson, Simonetta Piatti, Jean-Baptiste Masson and Manuel Théry for the time they invested in evaluating my work and for their interest.

I would like to thank the many members of the lab with whom I had the pleasure to interact everyday. They are awesome people making this unit very special. I especially would like to thank all the members of the Bassereau, Coppey and Lévy teams who made this PhD such a pleasant time. I will miss working with you and even more so the time out of the lab ! A special thanks to Koyomi Nakazawa, who is also having fun with septins ! I wish you and Kasumi all the best ! Thank you Alicia Damm for the very nice microscope that you built. Thank you Oleg Mikhajlov for installing the micropipette system on the Nikon Center microscope despite their ill will. Thank you John Manzi for the purification of the aquaporin.

Je voudrais remercier chaleureusement mes amis, qui m'ont soutenu durant ces quatre années de thèse. Je souhaite remercier un groupe d'amis bien particulier, Victor Moinard, Coline Aubert, Marc Oudart, Carole Duchêne, Laure Bernard, Alban Pierre, Lucas Baudin and Quentin Lamy-Besnier. Merci à Alice Williart et Jean Kieffer, et félicitations pour votre récent mariage !

Je souhaiterais également remercier mes amis du meilleur club de badminton qui soit ! Merci à Long Nguyen-Dinh, Max Thelemann, Anouk Chutet, Benjamin Havret, Thomas Rouillard et à toute l'équipe 8, la meilleure bien entendu !

Merci à ma famille, mes frères, César, Émile et Ambroise, ainsi que ma soeur Maëlle. Merci Émile de m'avoir héberger pendant le premier confinement, merci Maëlle d'avoir toujours eu une oreille attentive pour ton petit frère, merci Ambroise d'être un frère aussi cool et merci César d'être notre électron libre préféré. Merci à mes parents qui m'ont toujours soutenu et cru en moi.

Enfin, je tiens à remercier Roxane Ferry, qui a vécu la fin de cette thèse à mes côtés. Merci pour ton soutien quotidien, ta patience et ton amour. Je te souhaite tout le meilleur pour ta thèse à venir et j'espère être à la hauteur !

Résumé

Les septines sont des protéines filamenteuses ubiquitaires considérées comme le quatrième élément du cytosquelette. Elles jouent un rôle dans la stabilisation mécanique de la membrane plasmique et sont impliquées dans l'établissement de barrières de diffusion *in vivo*, permettant la compartimentation des membranes. Bien que les barrières de diffusion soient essentielles à de nombreux processus cellulaires, les principes biophysiques qui régissent leurs fonctions sont encore mal compris. Les systèmes reconstitués *in vitro* sont de bons modèles pour comprendre le rôle des septines dans la formation de ces barrières car ils permettent le contrôle de l'ensemble des paramètres biophysiques. J'ai utilisé un système de membranes biomimétiques (liposomes et bicouche supportée) pour étudier comment la diffusion des lipides et des protéines ancrées aux membranes est modifiée en présence d'un réseau de septine.

J'ai utilisé une combinaison de méthodes (Recouvrement de Fluorescence Après Photoblanchiment et Suivi de Particules Uniques) pour analyser la dynamique des lipides et des protéines membranaires en présence de filaments de septines de levure liés à des membranes biomimétiques. J'ai modélisé l'encombrement stérique des protéines connues pour être séquestrées en présence de septines grâce à trois protéines modèles dont les domaines extra-membranaires (cytosoliques) varient en taille : l'aquaporine (canal aqueux sans domaine cytosolique), la streptavidine (environ 6 nm) liée à des lipides possédant une biotine, et les points quantiques (environ 20 nm), liés à la membrane par un lien streptavidine-biotine. La diffusion des lipides n'est pratiquement pas affectée par la présence de filaments de septine. En revanche, la diffusion des protéines modèles est modifiée en fonction de leur dimension. Les expériences de Suivi de Particules Uniques montrent une diffusion libre de l'aquaporine, proche du mouvement Brownien, tandis que les points quantiques sont piégés dans des régions linéaires contraintes par des filaments parallèles de septine. Enfin, la streptavidine présente deux populations distinctes de particules : immobiles et sous-diffusive. Selon la taille du domaine cytosolique du modèle, les septines affectent donc différemment son comportement diffusif, agissant de manière similaire à un « filtre » des composants liés à la membrane. En outre, j'ai comparé l'impact de l'organisation des filaments de septines sur la restriction de la diffusion des composants liés à la membrane. L'utilisation de septines humaines ou l'ajout de protéines de réticulation aux septines de levure induit l'auto-assemblage de réseaux orthogonaux de filaments sur les membranes. En présence de ces réseaux, la diffusion des points quantiques est totalement entravée. Mes observations pointent vers un effet stérique créé par la présence du réseau de septines et sont en bon accord avec les observations *in vivo*.

Enfin, dans la continuité de travaux antérieurs, j'ai étudié les propriétés mécaniques de filaments de septine liés à des membranes lipidiques. Il a été démontré que les septines affectent les propriétés mécaniques des membranes plasmiques et les observations faites lors des études précédentes restaient énigmatiques. J'ai observé, en réalisant des expériences d'aspiration par micropipette, que les septines étaient capables d'empêchant la déformation de la vésicule. J'ai déterminé, en utilisant la technique d'indentation par Microscopie à Force Atomique sur des GUVs, que les filaments de septine peuvent réduire le module de compressibilité surfacique apparent des vésicules, ce qui était inattendu. Un modèle qui tient compte d'une déformation initiale de la membrane dépendant de la septine permet d'estimer le module de flexion d'un réseau de septine. Ce module de flexion est en accord avec les valeurs connues de la longueur de persistance des filaments de septine et explique l'observation expérimentale contre-intuitive.

Abstract

Septins are ubiquitous filamentous proteins considered as the fourth element of the cytoskeleton. Septins play a role in the mechanical stabilization of the plasma membrane and are involved in the establishment of diffusion barriers *in vivo*, allowing the compartmentalization of membranes. Even though diffusion barriers are essential to many cellular processes, the biophysical principles regulating their functions are still poorly understood. Bottom up *in vitro* reconstituted systems offer powerful tools to understand the role of septins in forming those barriers by controlling independently all the biophysical parameters. During my PhD, I used a system of biomimetic membranes (liposomes and supported bilayer) to study how the diffusion of lipids and proteins anchored to membranes is impacted by the presence of a septin mesh.

I have used a combination of methods – namely Fluorescence Recovery After Photobleaching (FRAP) and Single Particle Tracking (SPT) – to assay the dynamics of lipids and membrane bound proteins in the presence of yeast septin filaments bound to biomimetic membranes. I analysed the diffusion of different model proteins, with varying sizes of the extra-membrane (cytosolic) domains: aquaporin (a transmembrane water channel with no cytosolic domain), streptavidin (about 6 nm) bound to biotin lipids, and quantum dots (about 20 nm), bound to the membrane through a streptavidin-biotin linker. Hence, I have modelled the steric hindrance of membrane bound proteins that are known to be sequestrated in the presence of septins. The diffusion of lipids is barely impacted by the presence of septin filaments. However, the diffusion of model systems mimicking membrane proteins can be altered depending on their dimension. SPT diffusion analysis shows a freely diffusive behaviour of aquaporin, close to Brownian motion, while quantum dots, are trapped in linear regions constrained by sets of parallel septin filaments. Finally, streptavidin displays two distinct populations of immobile and sub-diffusing particles. Depending on the size of the cytosolic domain, septins thereby affect differently their diffusive behavior, acting similarly to a "filter" of membrane bound components. Besides, I have compared the impact of different structural organization of septins on the diffusion restriction of membrane bound components. Using human septins or adding cross-linking proteins to yeast septins induce the self-assembly of orthogonal networks of filaments on membranes. In the presence of those networks, the diffusion of quantum dots is fully impaired. My observations point towards a steric effect created by the presence of the septin network and are in good agreement with the *in vivo* observations.

Finally, following up previous work, I studied the mechanical properties of lipid membranes with septin filaments bound. Indeed, septins have been shown to affect the mechanical properties of plasma membranes and former observations remained puzzling. I observed, performing micropipette aspiration experiments, that septins were able to rigidify the membrane, preventing its deformation. I determined, using Atomic Force Microscopy indentation on GUVs, that septin filaments can reduce the apparent area compressibility modulus of vesicles, which was unexpected. A model that accounts for a septin dependent initial deformation of the vesicles can estimate the bending modulus of a septin mesh. This bending modulus is in good agreement with the known values of persistence length of single septin filaments and accounts for the counter-intuitive experimental observation.

Contents

Abreviations

AFM Atomic Force Microscopy
AOTF Acousto Optic Tunable Filter
BFP Back Focal Plane
CDC Cell Division Cycle
DOPE 1,2-Dioleoyl-sn-glycero-3-phosphoethanolamine
DOPS 1,2-dioleoyl-sn-glycero-3-phospho-L-serine
EggPC L-α-phosphatidylcholine from egg yolk
EM Electron Microscopy
ER Endoplasmic Reticulum
FCS Fluorescence Correlation Microscopy
FLIP Fluorescence Loss In Photobleaching
FRAP Fluorescence Recovery After Photobleaching
GDP Guanosine diphosphate
GFP Green Fluorescent Protein
GTP Guanosine triphosphate
GUV Giant Unilamellar Vesicle
LUV Large Unilamellar Vesicle
MSD Mean-Squared Displacement
NOA Nordland Optics Adhesive
PDMS Polydimethylsiloxane
PEG Polyethylene Glycol
PI(4,5)P_2 Phosphatidylinositol 4,5-bisphosphate (PIP_2)
PSF Point Spread Function
ROI Region Of Interest
SEM Scanning Electron Microscopy
SEPT Human septins
SLB Supported Lipid Bilayer
SPT Single Particle Tracking
STED Stimulated Emission Depletion
SUV Small Unilamellar Vesicle
TIRF Total Internal Reflection Fluorescence
ts Temperature Sensitive

Chapter 1

Introduction

1.1 Roles of septins

1.1.1 The history of septins

In 1967 Hartwell conducted a study on temperature sensitive mutants in yeast Saccharomyces Cerevisiae (Hartwell, 1967). He identified temperature sensitive mutants for which a switch from 23°C to 36 °C induced a loss in viability. He classified such mutants and identified the ones that affected most notably the cell division. Among those mutants, two -ts310 and ts471- induced very peculiar elongated polynucleic phenotypes due to their inability to achieve cell division as is shown in Figure1.1. Later studies identified other genes involved in cell division which were denominated CDC for Cell Division Cycle (Hartwell, 1971). Two new mutants resulting in elongated polynucleic cells were identified.

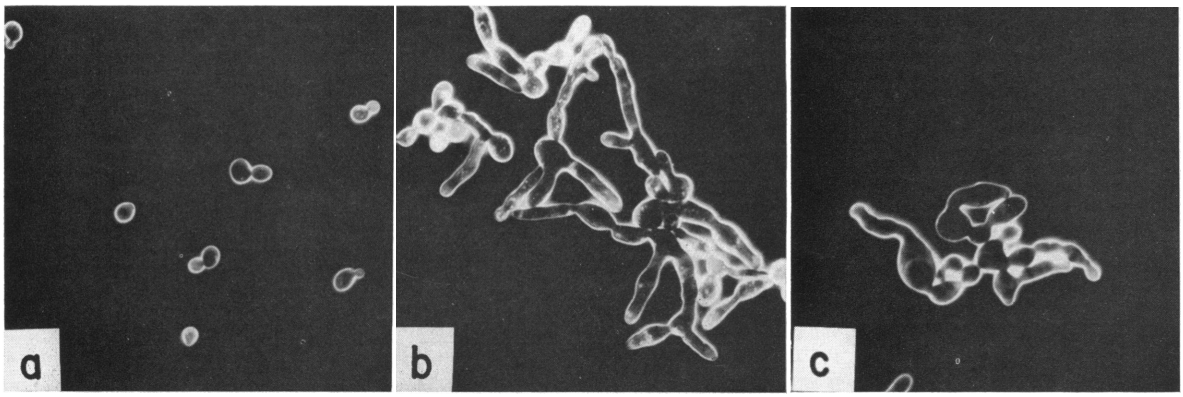

Figure 1.1 – Dark field, phase contrast micrographs of (a) wild type yeast cells, (b) ts471 and (c) ts310 after 12 hours incubation at 36°C. From Hartwell (1967)

Electron microscopy observations showed that filaments were present at the bud neck during cell division in the wild type cells (Byers and Goetsch, 1976). They run orthogonal to the mother bud axis in close proximity with the plasma membrane as can be seen in Figure1.2. The observed filaments were absent from any of the cdc3, cdc10c, cdc11 and cdc12 mutants. A later immunofluorescence study showed that the cdc proteins were present at the bud neck in the wild type cells but absent in the mutant strains (Ford and Pringle, 1991). An immuno electron microscopy study showed the localisation of the cdc proteins and their close proximity to the plasma membrane

(Longtime et al., 1996). Finally, a study followed the localisation of cdc3 in wild type and mutant cells. It then became clear that this family of proteins were assembling into complexes that polymerised into filaments at the bud neck. This family of proteins was named the 'septin' family because they are present throughout the septation of the plasma membrane during the cell division.

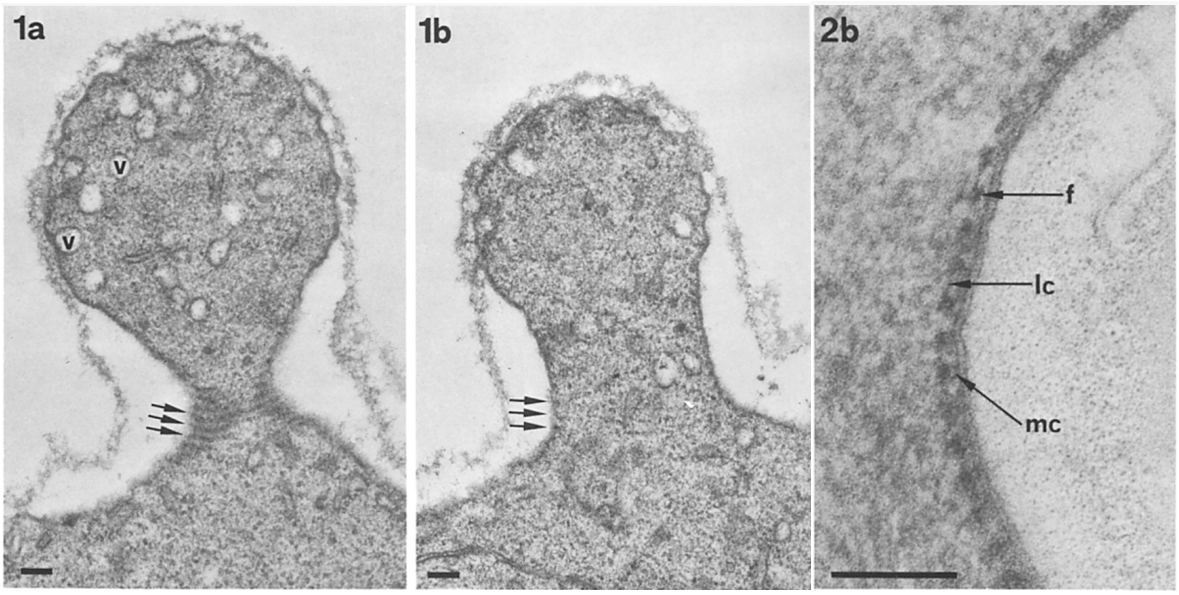

Figure 1.2 – EM sections of an early bud in dividing yeast cells. (1a) Grazing section showing the filaments in longitudinal view. (1b) Medial section showing the filaments in transverse view (arrows). (2b) Higher magnification showing connections between filaments and plasma membrane. Scale bars are 0.1 μm. From Byers and Goetsch (1976)

Following these studies, homologous proteins were found in almost all eukaryotes, including in mammals -the SEPT 1-12, 14 family (Cao et al., 2007; Pan et al., 2007; Nishihama et al., 2011) -, in drosophila -the Pnut/Dsep1-4 family (Neufeld, 1994; Field et al., 1996) - and in C.Elegans -unc59 and unc61 (Nguyen et al., 2000; Maddox et al., 2007). While the number of septins differ for each species, they share a common primary structure, supramolecular organisation and similar functions in vivo. More specifically, a direct comparison can be drawn between the yeast septins -cdc11, cdc10, cdc12 and cdc3- with the human subgroups of septins -SEPT2, SEPT3, SEPT6 and SEPT7 respectively.

1.1.2 Cellular functions

Since their discovery, septins have been shown to be key elements in many cell processes. They play major roles in processes as diverse as cell division, cilia morphogenesis etc. Even though these roles seem very diverse, some common features can be highlighted.

Cell division

Septins play a key role in cell division. This function has been very well documented in Saccharomyces Cerevisiae. During the early stages of cell division (G1)

septins accumulate at the bud site and form a ring (Oh and Bi, 2011; Bi and Park, 2012). They localise at the bud neck during the cell division process while undergoing rearrangements. The ring first elongates along the mother bud axis and later splits in two separate rings around the onset of telophase, one on the mother side of the bud, the other on the daughter side of the bud as seen in Figure 1.3. Since their discovery, septins have been shown to play an essential role in cell division as septin deficient yeast cells cannot undergo scission and end up elongated and polynucleated. Several essential proteins for the selection of the budding site and its morphogenesis, such as Bud4, are recruited in a septin dependent manner (Sanders and Herskowitz, 1996; Chant and Pringle, 1995). Very importantly, the acto myosin ring -responsible for the contraction of the membrane at the bud neck prior to scission- is also recruited in a septin dependent manner (Lippincott and Li, 1998; Bi et al., 1998). This acto myosin ring is located in between the septin rings after the bud emergence and growth as seen in Figure1.4. Septins are also involved in the emergence of a diffusion barrier allowing asymmetry between the mother and daughter cell. This role will be further discussed in section 1.4.1.

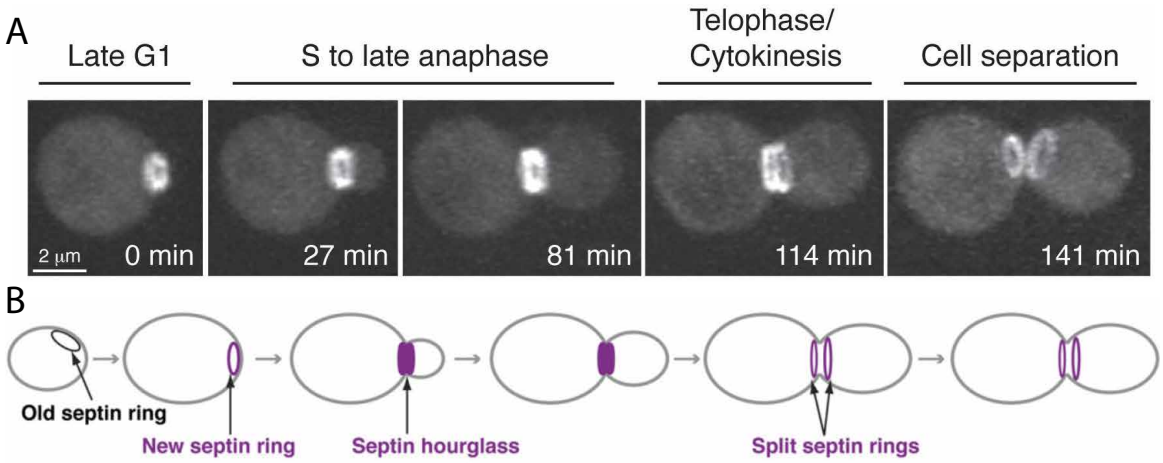

Figure 1.3 – (A) 3D reconstruction of yeast cells containing GFP-tagged cdc3 at selected time points during cytokinesis, from Oh and Bi (2011). (B) Schematic representation of the organisation of septins during cytokinesis from Bi and Park (2012)

Septins also play an important role in cell division in other organisms. In drosophila, three septins have been detected at the cleavage furrow during cytokinesis, Pnut, Dsep1 and 2 (Neufeld, 1994) (Fares et al., 1995). Combined with anilin, they appear downstream from the assembly of the cytokinetic components, and their presence is not necessary for the recruitment of other key proteins for cytokinesis (Maddox et al., 2007; Field et al., 2005). Their role is most likely related to a mechanical function. Together with anilin they form a structure adjacent to the actomyosin ring and can help its closure by extruding membrane domains from the actomyosin ring. This idea is supported by the observation that in Pnut mutants, the epithelial cell-cell junctions fail to disengage due to insufficient contractile force. Genome wide screens have shown that knockdowns of either Pnup or Dsep2 lead to cytokinetic defects, but not as dramatically as for other genes. Interestingly, in both cases, the asymmetry of the embryo division is lost (Maddox et al., 2007).

Finally, in human cells, septins seem to play similar roles as in Drosophila. The overexpression or depletion of SEPT9 can lead to cytokinetic defects (Estey et al., 2010).

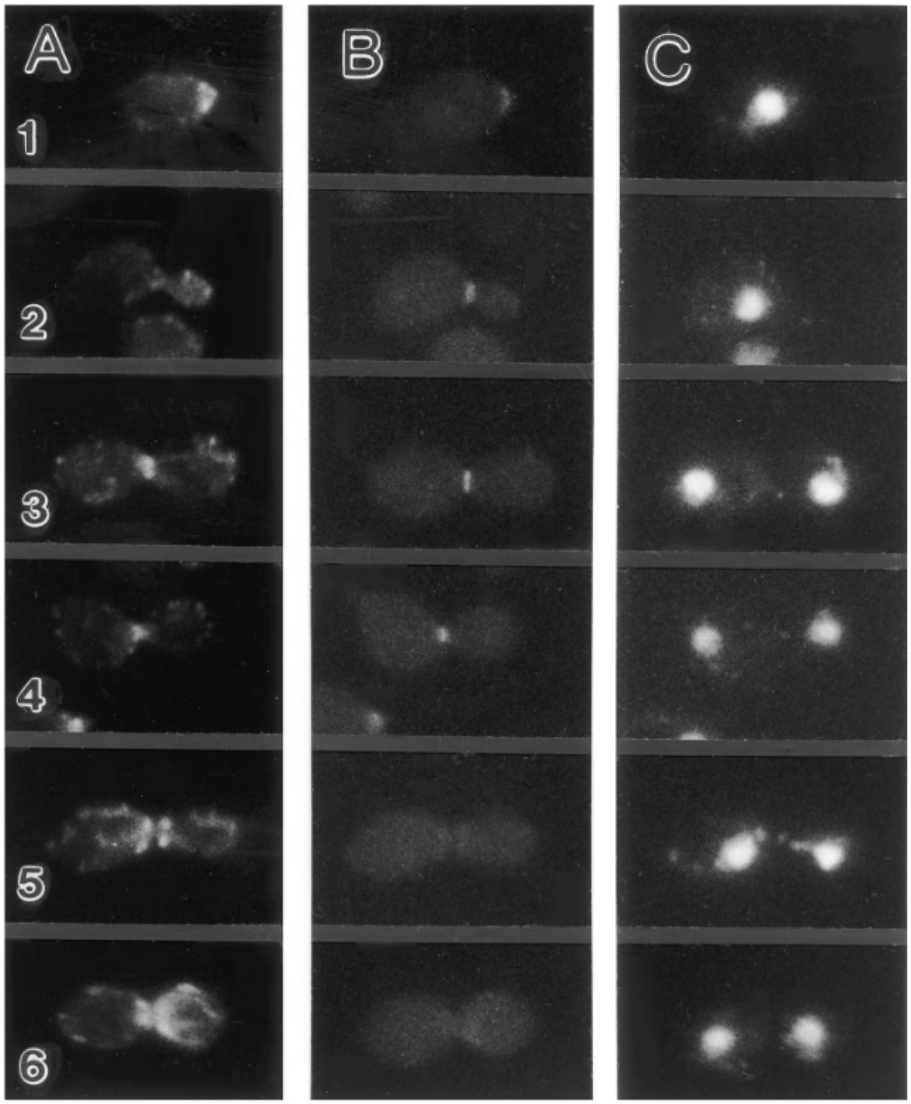

Figure 1.4 – Timelapse of dividing yeast cells (A) F-actin staining, (B) GFP-tagged Myo1p and (C) DNA staining. Recruitment of Myo1p is anterior to the formatin of the actin ring. Upon onset of telophase, the actin colocalises with Myo1p, and the ring will contract. Finally, after scission, both actin and Myo1p are relocated. From Bi et al. (1998)

Septins are located close to the actomyosin structure and recruit essential proteins for the activation of the actomyosin ring contraction (Joo et al., 2007). During the elongation of the Inter Cellular Bridge, septins and anilin form a collar-like structure that elongates through gradual assembly of circular or helical filaments parallel to the division plane (Renshaw et al., 2014). Anilin later translocates to the mid body while septins are excluded from it and stay in the flanking rings as was observed in Karasmanis et al. (2019) and can be seen in Figure 1.5 by fluorescence imaging. Septins are then involved in the recruitment of the ESCRT-III machinery, promoter of the abscission, through the indirect interaction with both anilin and TSG101.

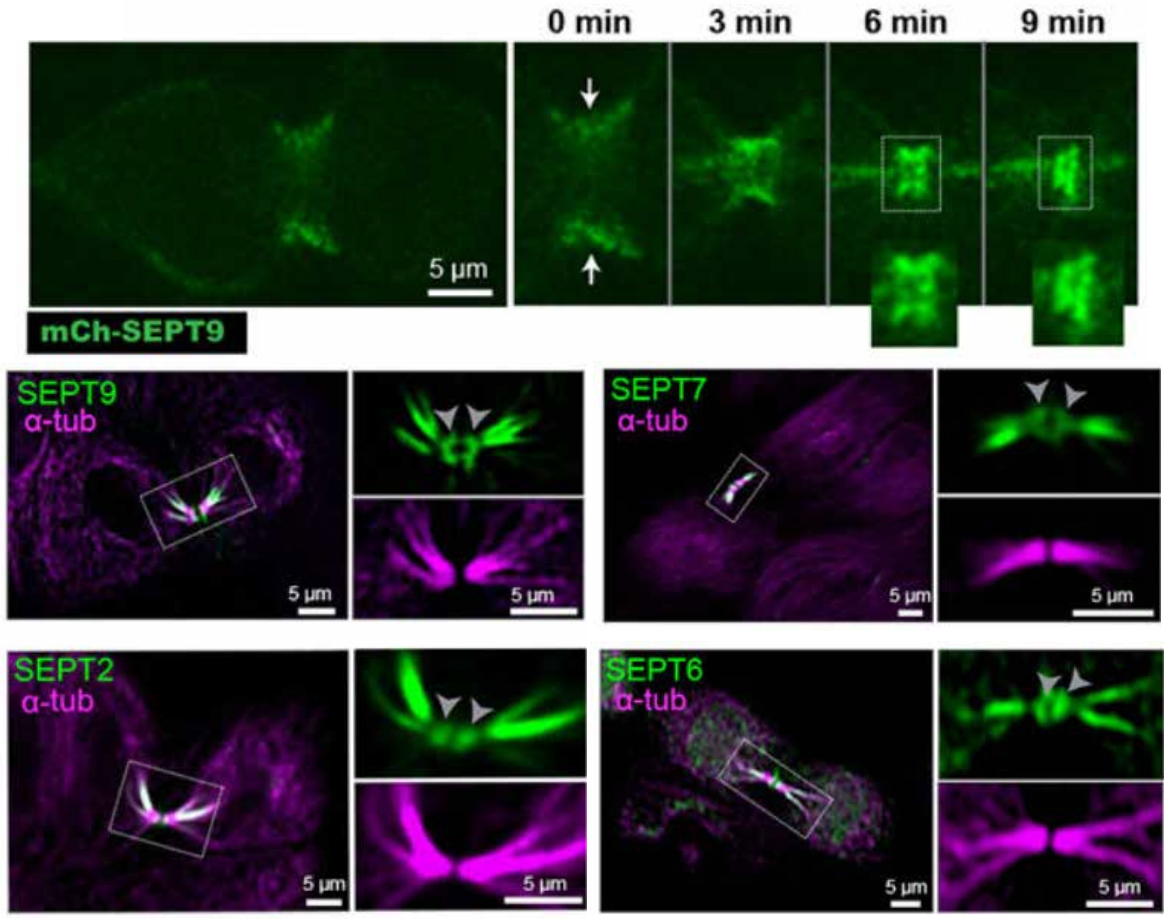

Figure 1.5 – Fluorescence image showing the localisation of septins in the Intercellular Bridge, from Karasmanis et al. (2019)

Bacterial infection

Studies have shown the importance of septins for the cell autonomous immunity. Using different models, it has been observed that septins can promote host defence upon the presence of some pathogens. Their role has been well established in the *Shigella flexneri* bacteria infection and the vaccinia virus.

Shigella flexneri is a bacteria responsible for bacillary dysentery. Upon entry in epithelial cells, it replicates in the cytoplasm and polymerises actin tails at their membrane. These tails promote their motion inside the cytoplasm, the bacteria can thus escape cell autonomous immune system and later infect neighbouring cells (Welch and Way, 2013). Cells use multiple strategies to defend against S.flexneri infection. One of them is caging, which involves both septins and actin (Mostowy et al., 2010; Sirianni et al., 2016). The proteins will entrap the bacteria with multiple rings arranged periodically as displayed in Figure 1.6. The bacteria trapped in the septin-actin cages lose their ability to travel in the cytoplasm and are targeted for autophagy. Some studies suggest that the mechanism for septins' recognition of bacteria relies on the specific curvature displayed during its division (Krokowski et al., 2018). Indeed, initial septin binding happens most of the times at the division site or cell poles. Most of the bacteria (≈93%) are unable to further divide, showing the importance of septin cages to limit their proliferation.

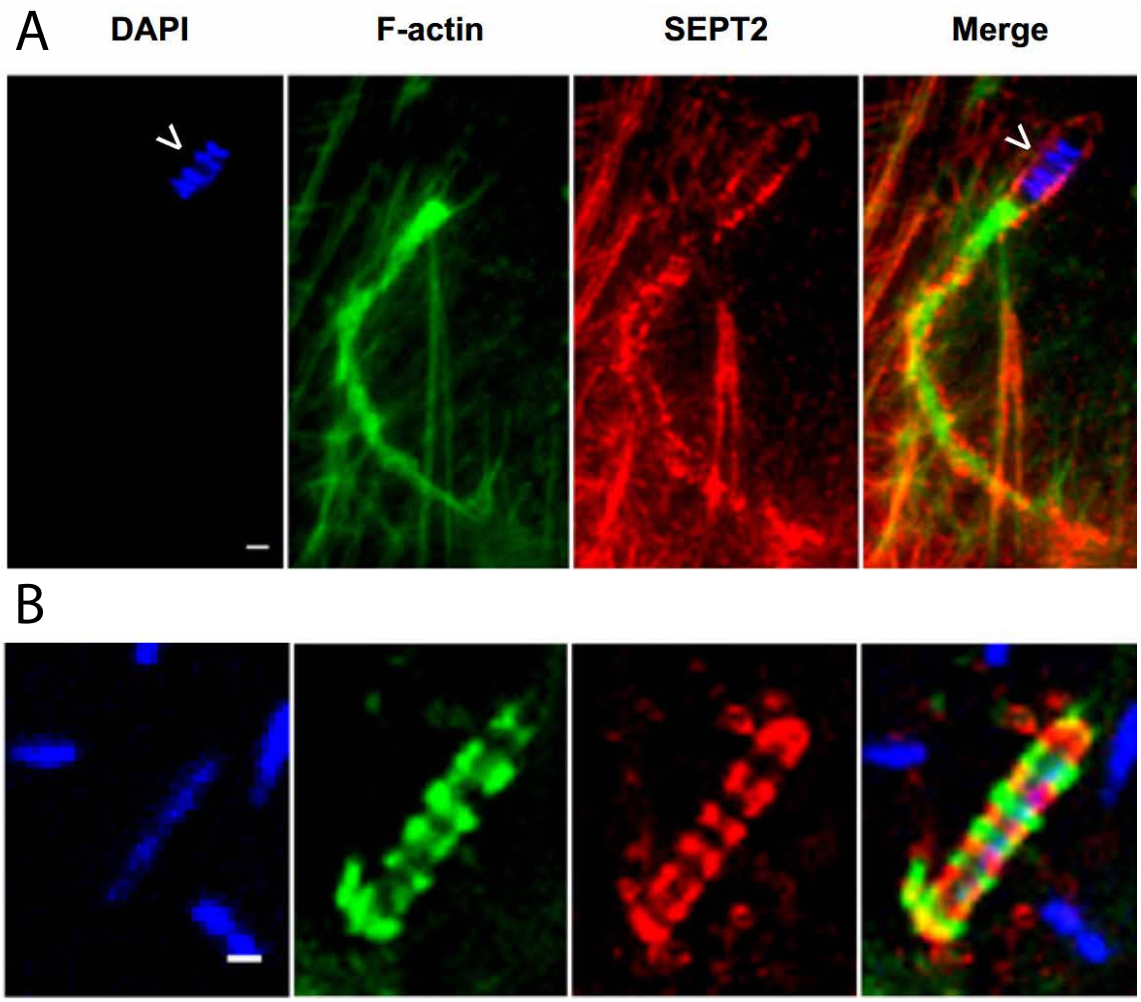

Figure 1.6 – Fluorescence images showing (A) *S.flexneri* bacteria with a motile actin tail and (B) trapped *S.flexneri* bacteria in an actin septin cage. From Mostowy et al. (2010)

Vaccinia virus is well known for having been used as a vaccine that helped eradicating smallpox (Walsh and Dolin, 2011). It is a common model to study the rearrangement of the cytoskeleton during the infection of cells (Leite and Way, 2015). Upon cell infection, vaccinia replicates in the cytoplasm and wraps up in two distinct membranes which will allow its release later on. They are then transported to the cell periphery where the outer membrane fuses with the plasma membrane, creating cell-associated enveloped virus. To enable its final release and allow its spreading, the vaccinia uses actin tails polymerisation as a driving motor (Leite and Way, 2015). Screens performed using siRNA suggested that septins play a role in preventing the release of the vaccinia (Beard et al., 2014). It appeared that indeed, after the fusion of the outer membrane with the plasma membrane, septins are recruited to the plasma membrane and prevent the release of the vaccinia (Pfanzelter et al., 2018). The role of septins in other virus infections has yet to be studied.

Cilia morphogenesis

Cilia are ubiquitous protusions that appear in all cell types. They are 1 to 10 µm long and 1 µm wide. They contain nine pairs of microtubules with extra 2 central microtubules for motile cilia (Webber and Lee, 1975). In humans, cilia cells can be found in many tissues, including the ears, the intestine and the lungs. Different septin complexes can locate at different places in cilia. For instance, in humans, two complexes were characterized, SEPT2/4/6/7 and SEPT2/7/9/11. The first one is localised at the basis of the cilia, while the other one is located in the axoneme (Hu et al., 2010) (Ghossoub et al., 2013) (Fliegauf et al., 2014). Knockdown assays of the SEPT7 gene in the zebra fish embryo lead to ciliopathies due to the reduction of cilia activity (Dash et al., 2014). Cilias were found to be shorter and wider with disorganised basal bodies. Similar effect was reported in the Xenopus embryo, in which knockout of either SEPT2 or SEPT7 led to the loss of planar cell polarity during ciliogenesis and causing a dramatic decrease in the amount of cilia per cell (Collier et al., 2005).

Neuro morphogenesis

In *C.Elegans*, the two septin subunits unc-59 and unc-61 are present in embryonic and larval neurons but absent in mature organisms, showing their importance for neuro morphogenesis (Finger et al., 2003). Mutations of both genes lead to misplacement of axons and occasional discontinuities in the ventral cord. Similarly, studies performed in mammalian cells have shown that septins play an important role in neuro morphogenesis (Xie et al., 2007; Tada et al., 2007; Ageta-Ishihara et al., 2013). Indeed, it was observed by fluorescence immunostaining assays that SEPT7 is located at the base of dendritic protrusion and branching points in hippocampal neurons as can be seen in Figure 1.7. SEPT7 overexpression leads to an increase in the density of dendritic protrusions and an enhanced dendritic branching. Conversely, the knockdown of SEPT7 leads to reduced branching and a decrease in the density of protrusions (Tada et al., 2007). At the branching points, SEPT7 colocalises with SEPT5 and SEPT11, suggesting the existence of a SEPT5/7/11 complex at the base of dendritic spines (Ageta-Ishihara et al., 2013).

Another study, focusing on SEPT6, showed results similar to the assays focused on SEPT7 (Cho et al., 2011). SEPT6 assembles into rings with a diameter of about 0.5 µm at the branching point of developing dendrites where they colocalise with microtubules. Upon the introduction of a RNAi vector targetting SEPT6, the number of branches as well as the dendritic length were significantly reduced. Finally, similar results were also obtained with SEPT11 (Li et al., 2009). Taken together, these results suggest that septin complexes at the base of developing dendrites are necessary for their normal development.

Septins have also been observed in myelinating cells. Myelin is essential for fast nerve conduction which allows normal cognitive, motor and sensory abilities (Lasiene et al., 2009). It is an extension of the plasma membrane produced by glial cells that wraps around axons, serving as insulator. With aging myelin sheath can become abnormal leading to pathologies. It has been observed that SEPT2/4/7/8 form a filamentous scaffold at the inner layer of myelin (Patzig et al., 2016). This scaffold appears at late stages of the myelin maturation. The knockdown of SEPT8 leads to myelin outfolding causing a decrease in the velocity of signal transmission in the axon.

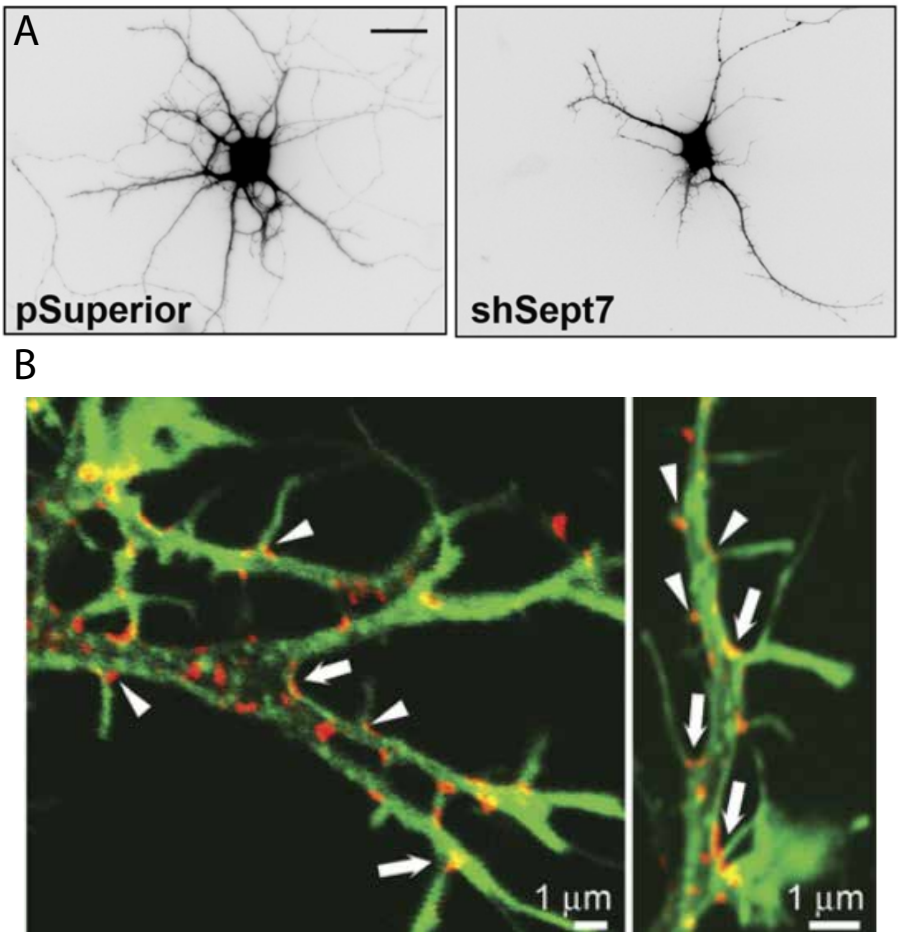

Figure 1.7 – (A) Images from neurons transfected either with control vector (left) or silencing SEPT7 vector (right) from Xie et al. (2007). (B) Fluorescence images of neurons labelled for F-actin with phalloidin (green) and immunostainned for SEPT7 (red) from Tada et al. (2007).

Spermatogenesis

Sperm cells are composed of three distinct regions, the head where the nucleus is located, the mid-piece enclosing the mitochondria and the tail, a large motile cilia called flagellum. Different septins have been identified by immuno-staining (Figure 1.8) at both connections between the three regions, underlying the presence of different septin heteromers at each connection (Ihara et al., 2005; Steels et al., 2007; Kuo et al., 2015). SEPT2, 6 and 12 are present at the connection between the mid-piece and the head, while SEPT2, 4, 6, 7, 12 are present at the connection between the mid piece and the tail. Studies have shown that in mouse sperm cell, the mutation of SEPT4 resulted in the loss of the septin ring at the connection between the mid piece and the tail. This caused flagella to display a sharp bend at their connection to the mid piece and an abnormal rigidity (Ihara et al., 2005; Kissel et al., 2005). The sperm cells were therefore unable to swim. However, if those sperm cell were assisted in the fertilisation process, the oocytes could develop normally indicating that the loss of fertility is only due to the loss of motility. As for SEPT12 mutation, the motility was also lost and after assisted fertilisation, the oocytes would still not develop, indicating that other damages (supposedly DNA damage) must have occurred in the sperm cell (Lin et al.,

2011). Finally, SEPT14 might also play a role because it is expressed exclusively in the testis (Peterson et al., 2007).

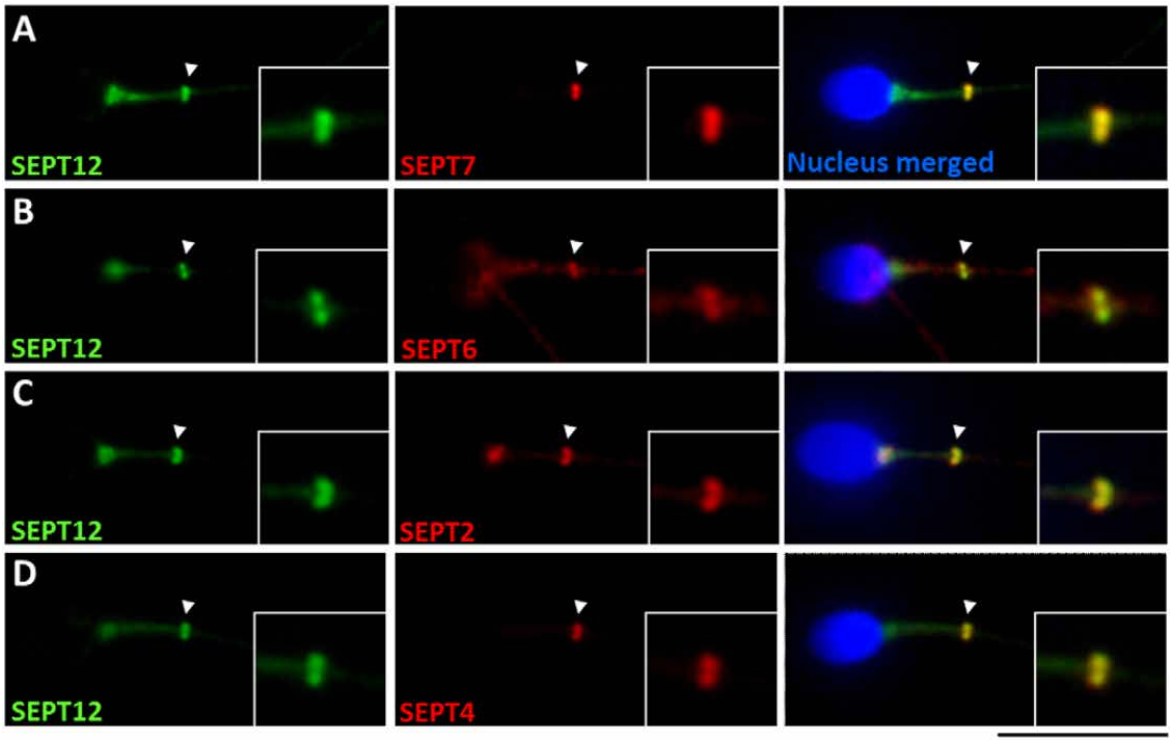

Figure 1.8 – Fluorescence images obtained by immunostaining of different septin subunits (SEPT12 green left and SEPT2/4/6/7 red middle) in fertile human sperm cells from Kuo et al. (2015)

Cell membrane remodelling and cell motility

Cellular membrane remodelling is a very important process for some major cellular functions. From motility, to environment sensing, cells need to control the shape of their membrane. One key process in which membrane remodelling is essential is the exocytosis. In exocytosis, SEPT5 has been identified to interact with syntaxin, a protein responsible for the formation of the SNARE complexes. By inhibiting the activity of syntaxin, SEPT5 regulates the vesicle secretion (Beites et al., 1999, 2005).

Septins can also directly reshape membranes. In septin deficient T cells, blebbing occurs very frequently during both cell migration on glass and mitosis (Gilden et al., 2012). Blebs consist of spherical bulges of plasma membrane that form due to the intracellular pressure when the connection between the plasma membrane and the cytoskeleton is disrupted. In T cells, during cell crawling on glass coverslips, septins accumulate near the site of retraction of the previous leading edge when cells change direction. The septins then merge back into the septin collar. To decipher whether septins are involved in preventing the emergence of blebs and in their retraction, cells were submitted to osmotic shocks. When exposed to hypotonic medium, cells react in a two step manner. First, they rapidly expand as water flows in. Then a regulatory volume decrease step happens. During this second step, the hydrostatic pressure at the membrane increases, which can cause its detachment from the cortical actomyosin

leading to the emergence of blebs. In septin knockdown cells, the reduction of the volume after the initial expansion was slower, showing that septins are involved in the retraction of blebs.

Septins are essential for the migration of many cell types, including epithelia, fibroblasts, lymphocytes and neurons (Dolat et al., 2014; Shinoda et al., 2010; Tooley et al., 2009; Füchtbauer et al., 2011). Depending on the cell type and mode of migration, septins regulate differently the organisation and contractility of actomyosin on stress fibres and/or plasma membrane. They regulate the formation of membrane protrusions and recruit Rho signalling effectors and kinases which control mechanotransduction. In kidney cells, during the cellular transition from epithelial to mesenchymal, the SEPT2/6/7/9 complex localises at the actin transverse arc, a contractile network of curved actin stress fibres (Dolat et al., 2014). In SEPT2 depleted cells, this network is severely disrupted, leading to shorter lifetime for nascent focal adhesions. Studies suggest that, in particular, SEPT9 isoform 1 may protect actin fibres from depolymerisation and stabilise the actin transverse arc (Smith et al., 2015). Interestingly, SEPT9_i1 is overexpressed during the transition from epithelial to mesenchymal. Overexpression of some other isoforms of SEPT9 such as SEPT9_i2 and SEPT9_i3 can lead to the opposite effect, reducing migration (Verdier-Pinard et al., 2017).

1.1.3 Interactions with the cytoskeleton

Septins have been shown to colocalise with other cytoskeletal proteins *in vivo*. Studies have focused on the interaction between septins and two of the main component of the cytoskeleton, actin and microtubules. Due to their important interactions as well as the type of structure that septins can create, septins are considered to be the fourth element of the cytoskeleton.

Actin

Septins have been widely observed at places where actomyosin networks are present (Kinoshita et al., 1997; Xie et al., 1999). They have been shown to be crucial for the maintenance and activity of these networks as seen in Figure 1.9 A and B. They act as scaffolds for actin binding proteins and effectors. On fungal cell membrane, septins interact indirectly with actin through myosin II. Myosin is connected to septins through Bni5 and to actin by the families of proteins BAR (Bin/amphiphysin/Rvs) and ERM (ezrin/radixin/moesin) (Finnigan et al., 2015; Garabedian et al., 2020; Oh et al., 2013). In animals, it was observed that septins can interact both directly and indirectly with actin (Hu et al., 2012; Kinoshita et al., 1997, 2002). Septins were notably found to bind to branched actin networks nucleated by Arp2/3 in axons of sensory neurons (Hu et al., 2012). Septins are known to interact with stress fibres (Dolat et al., 2014). Septins seem to be also binding to the plasma membrane underneath the stress fibres indicating a potential role for linking the membrane to the actin stress fibres (Martins et al., 2022).

To investigate the ability of septins to bind actin directly, *in vitro* reconstituted actin filaments were mixed with drosophila septins (Pnut-Dsep1-Dsep2) and human septin complexes consisting of SEPT2/6/7/9. In both experiments septins associated with the actin filaments, cross-linking them to create curved, circular or linear bundles (Figure 1.10 A) (Mavrakis et al., 2014). The curved and linear bundles correlated respectively with oligomeric or polymerised septins. However their direct role in the organisation, branching and capping of actin networks in vivo has yet to be elucidated.

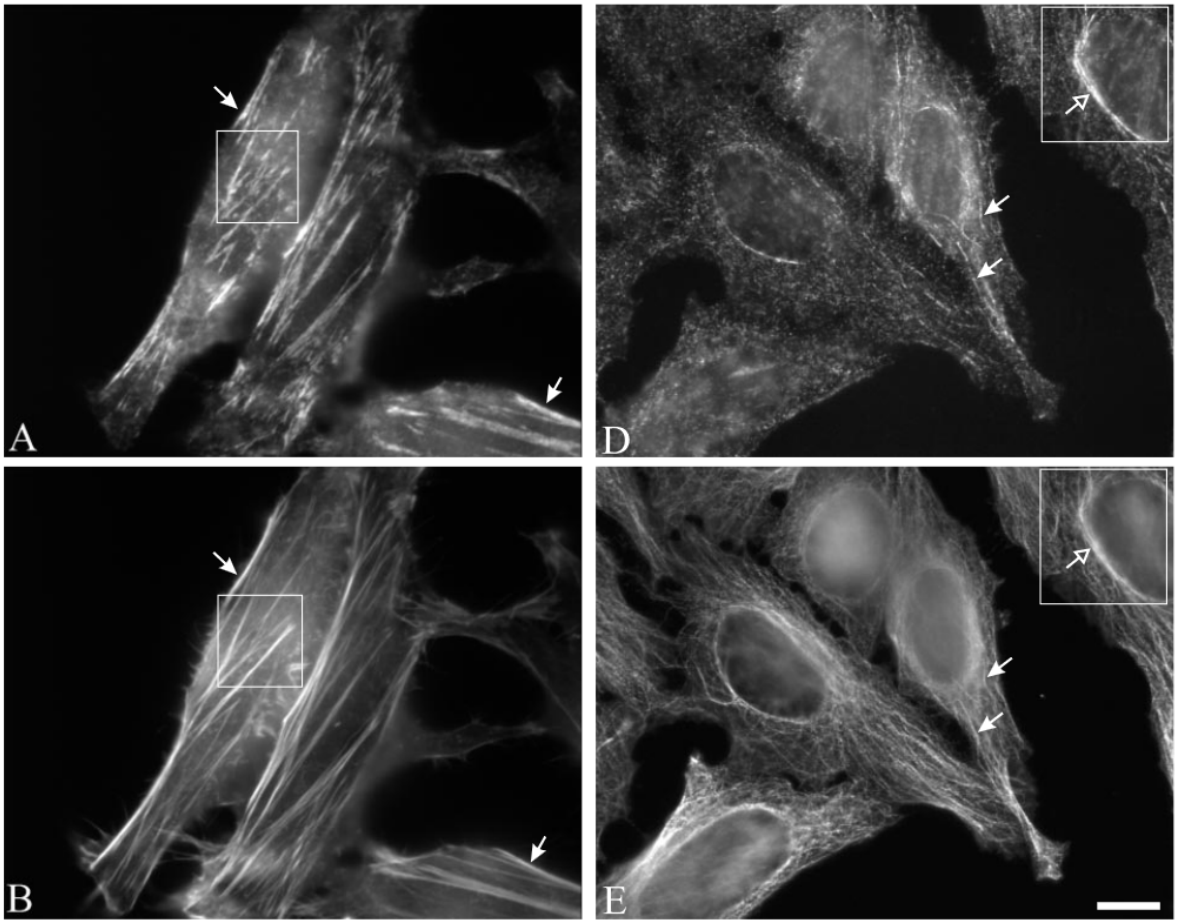

Figure 1.9 – Fluoresence images of Hela cells marked for cytoskeleton components. (A) and (D) anti-septins antibody, (B) phalloidin which tags the actin cytoskeleton, (E) anti-α-tubulin antibody. Those images show the colocalisation of septins with the cytoskeleton, from Surka et al. (2002). Scale bars are 10 µm.

Microtubules

Septins are associated to microtubules in a variety of cell types including epithelial cells, neurons and platelets in which they colocalise with subsets of microtubules such as perinuclear, Golgi-nucleated, subcortical and axonal microtubules (Bowen et al., 2011; Spiliotis et al., 2008; Ghossoub et al., 2013; Sellin et al., 2014; Martinez et al., 2006). They also associate with spindle pole, central spindle and midbody microtubules in dividing cells (Surka et al., 2002; Menon et al., 2014; Zhu et al., 2008). It has been shown that SEPT9_i1 can bind and recruit unpolymerised tubulin to microtubules (Nakos et al., 2019a). An *in vitro* study mixing SEPT9 subunits and microtubules has shown that SEPT9 promotes bundling and elongation of microtubules (Bai et al., 2013; Nakos et al., 2019b). Different isoforms of SEPT9 interact specifically with microtubules. Through dimerisation, SEPT9 is able to both recruit new tubulin to the microtubule but also reduce the rate of catastrophe. Combination of SEPT2/6/7 and SEPT9 leads to two different result depending on their state. In the minimal oligomeric state – described in further details in section 1.2.2 – they promote elongation through a stabilisation effect, but in the polymerised state, the microtubules paused or grew in a stunt manner, likely because their plus end is constrained in these conditions. Septin complexes bind

to perinuclear and polyglutamylated microtubules in epithelial cells (Spiliotis et al., 2008). On perinuclear microtubules, septins promote the persistent growth of plus-end, leading it to the cell periphery and apex, contributing to the establishment of the apical microtubule network (Bowen et al., 2011). To understand the role of SEPT9 on the polymerisation of microtubule, SEPT9 and tubulin were mixed *in vitro* and observed by fluorescence microscopy – Figure 1.10 B. After SEPT9 addition, microtubules made longer fibres. It was shown recently that microtubules interact exclusively with the isoform 1 of SEPT9 (Kuzmić et al., 2022).

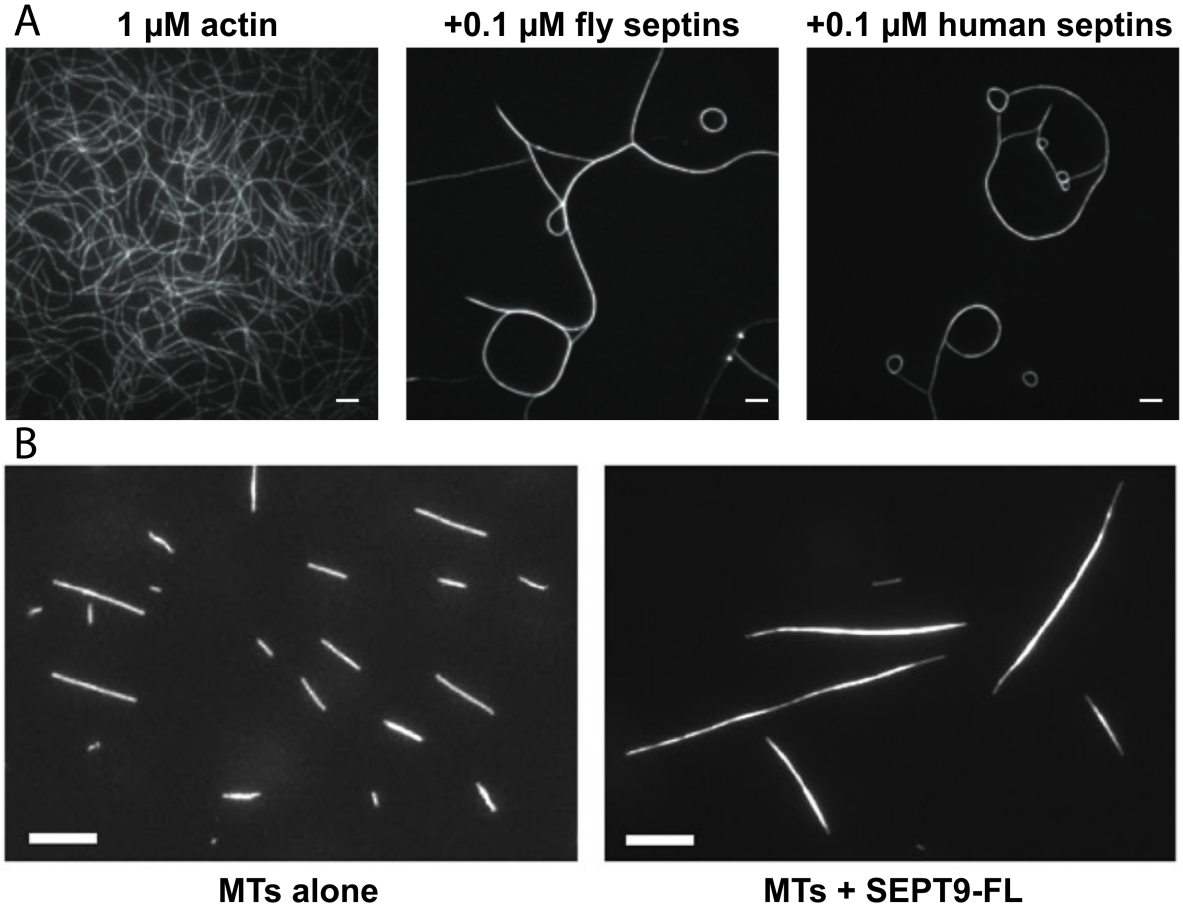

Figure 1.10 – (A) Fluorescence images of *in vitro* reconstituted actin filaments in the absence of crosslinkers or with septins, from Mavrakis et al. (2014). Scale bars are 5 µm. (B) Fluorescence images of microtubules before and after mixing with SEPT9, from Bai et al. (2013). Scale bars are 10 µm.

Septins also play a role in the regulation of microtubule associated motors and their cargo. Septins were among the first identified microtubule associated proteins to be able to selectively regulate the motility of different kinesin motors and select the destination of their cargo (Radler, 2020; Atherton et al., 2013; Janke and Magiera, 2020). Septins can also interact with some motors – dynein and kinesin-2/KIF17 – recruiting the motor or competing with its cargo (Kesisova et al., 2021).

1.1.4 Septins in pathologies

Due to the wide variety of functions, a defect in septin expression can have intricate consequences, leading to many potential pathologies. The involvement of septins in pathologies has been established but the exact role of septins is still under discussion. The pathologies in which septins have been the most studied are cancers and neuropathologies.

Cancer

The first studies relating septins to cancer showed the importance of the SEPT9 gene (Kalikin et al., 2000; Osaka et al., 1999). Further studies discovered that other septin genes were involved in the development of cancers, such as SEPT2 and SEPT4 (Kissel et al., 2005; Montagna et al., 2015; Marcus et al., 2016). SEPT9 and its isoforms have been identified to have altered levels of expression in various malignant tumours, including colorectal cancers, ovarian cancers and breast cancers (Tóth et al., 2011; Connolly et al., 2011; Scott et al., 2006). Abnormal methylation of the SEPT9 gene was detected in many cancer types, especially in colorectal cancer, with a hypermethylation of the promoter of the gene inhibiting the expression of SEPT9 (Tóth et al., 2011). A diagnosis test was developed, detecting this hypermethylation in blood (Grützmann et al., 2008). However, the detection in blood requires the release of DNA from cancer cells by apoptosis and necrosis which happens mainly at later cancer stage. In precancerous and early cancer the detection rate is only of 15% and 45% respectively with a high specificity (Nian et al., 2017). Combined with other methods, it can help detect early cancers. Interestingly, in breast cancers, SEPT9 is overexpressed leading to a reduction of apoptosis in cancer cells. This effect disappeared when SEPT9 was silenced (Montagna et al., 2003), hinting to another effect of septins which can lead to cancer development.

SEPT4 was also detected with abnormal levels of expression in many cancer types including kidney, brain, skin, prostate, lung and colorectal cancers (Kissel et al., 2005) (Montagna et al., 2015). This observation lead to the development of a diagnosis test for urothelial cancer by measuring the level of an isoform of SEPT4 in urine (Warren et al., 2011).

Finally, due to the interaction of septins with cytoskeleton and their importance in cell motility, some studies focused on their role in metastatic cancer cell motility. Indeed, it has been detected that in MCF7 breast cancer cells, the isoform 4 of SEPT9 was overexpressed leading to an increased cell motility (Chacko et al., 2005). It was shown that in detached cancer cells, microtentacle formation was highly septin dependent, showing the importance of septins in the metastatic state of cancer cells (Østevold et al., 2017).

Neurological disorders

Additionally to their role in the misfolding of myelin which can lead to neuropathologies, septins are involved in other neurological disorders. They were first associated to Parkinson disease (PD) after SEPT5 was found to interact with Parkin, a ubiquitin ligase whose mutation is related to juvenile PD (Zhang et al., 2000). The overexpression of SEPT5 also leads to cytotoxicity in rat neurons leading to an impaired motor function (Son et al., 2005). SEPT4 was also related to PD after it was found in the

cytoplasmic α-synuclein inclusions markers for PD and Lewy bodies dementia (Ihara et al., 2003). Abnormal levels of expression of septins can also be found in Alzheimer disease with an overexpression of SEPT5 and a reduced expression of both SEPT2 and SEPT3 (Musunuri et al., 2014). SEPT2 and SEPT4 can self-assemble into large amyloid filaments and are found in neurofibrillary plaques and tangles, structures associated to Alzheimer disease (Pissuti Damalio et al., 2012; Garcia et al., 2007).

1.1.5 Septin organisation in situ

In vivo, septins often organise into higher order structures. One of the best example is the structure that septins create during the yeast cell division. The first direct observation of the septin structure in yeast was achieved in 1976 when 10 nm thick filaments separated regularly by 28 nm were identified at the bud neck during cytokinesis (Byers and Goetsch, 1976) – Figure 1.2. Due to the resolution needed to distinguish those filaments individually, electron microscopy and super resolution techniques have been privileged.

The first observation using fluorescence microscopy showed that septins formed an initial ring at the place where the bud would emerge which would elongate and form an hourglass shaped structure. Upon the late stages of cytokinesis, prior to the contraction of the actomyosin ring, this structure would split in two rings, one on each side of the contraction site.

To assay the structure of the filaments, Vrabioiu and Mitchison (2006) used the polarisation of the light emitted by a dipole. They were able to show that during the ring splitting, the average direction of the filaments change, going from filaments parallel to the mother bud axis to filaments orthogonal to this axis. However, they were only able to recover an average effect. Later studies using electron microscopy allowed for better insight into the structure.

The first study that resolved the structure of septins at the bud neck used freeze substituted yeast (Bertin et al., 2012). Cells were quickly frozen at high pressure and later slowly brought back to 0°C before being embedded in resin. Electron Tomograms obtained from sections cut into the resin embedded cells showed that the septin structure would consist of orthogonal filaments, some going parallel to the mother-bud axis and other orthogonally as can be seen in Figure 1.11 A and B. However septins couldn't be specifically distinguished as no staining was available. With this method, it is possible to recover the 3D structure of the cell. 3D reconstruction allowed for the recovery of striking features of the architecture of the structure. During the hourglass phase, it was discovered that septins form a mesh of orthogonal filaments as highlighted in Figure 1.11 C. The filaments parallel to the mother bud axis were already known, but a new set of filament was also observed, orthogonal to the first one. Interestingly, it was also observed that septins do not sit directly on the membrane, there is a few nanometres (10-20 nm) gap between septin filaments and the plasma membrane. The origin for this distance and the identity of the electron dense filaments connecting septins to the plasma membrane is unknown.

The second study used spheroplasts to perform scanning electron microscopy (Ong et al., 2014). Spheroplasts are cells from which the plasma membrane is removed. The spheroplasts are fixed on a substrate. Removing the membrane can damage some of the structure of the cell, but it allows metal deposition on the sample, and associated with SEM, it allows good signal to noise ratio and good resolution. This experiment

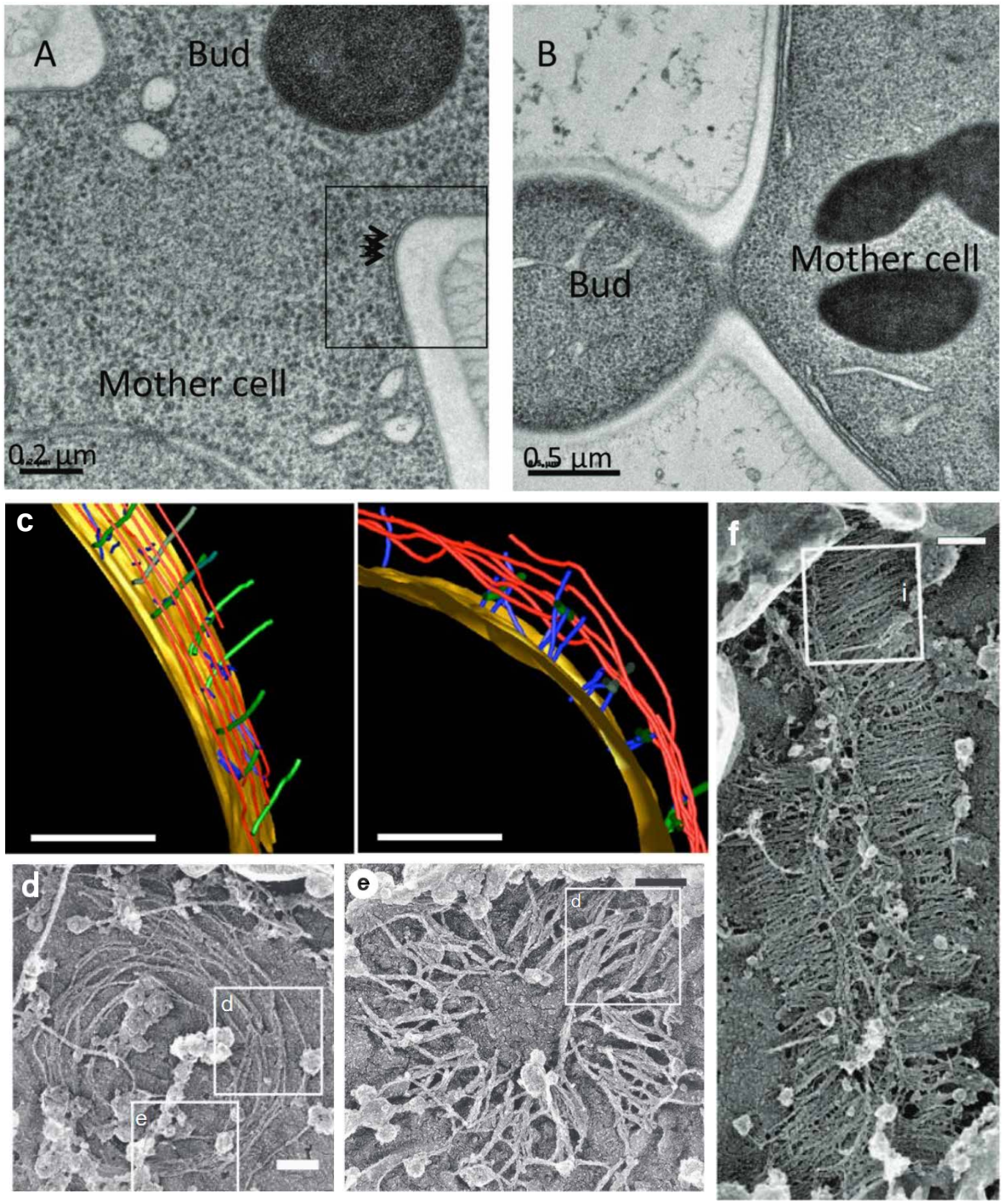

Figure 1.11 – Electron microscopy cross sections of yeast cells embedded in resin (A) medial section, arrows pointing at cross sections of the filaments and (B) grazing section. (C) Tomograms obtained from yeast cells embedded in resin during the hourglass stage. Scale bar is 100 nm. (D) Scanning electron microscopy image of a yeast spheroplast after ring splitting. Scale bar is 50 nm. (E) Scanning electron microscopy image of a yeast spheroplast in the early hourglass stage. (F) Scanning electron microscopy from a spheroplast from yeast during the hourglass stage. A, B, C From Bertin et al. (2012), D, E, F From Ong et al. (2014).

was performed on dividing yeast cells, allowing the observation of the structure at each step in the cytokinesis. The obtained images are compiled in Figure 1.11 D, E and F. They show that at the onset of division, septins exist as rather short paired filaments (400 nm) radially orientated. Filaments grow during cytokinesis and the long paired filaments orient parallel to the mother bud axis. During this step, a second set of filaments also emerges, orthogonal to the first one. Finally, upon splitting of the septin structure into two rings, only the circumferential filaments remain. The mechanisms behind the evolution of the structure made by septin filaments remain unknown, but key proteins for proper architecture of the structure have been identified.

Two key proteins identified are Bud3 and Bud4 (Sanders and Herskowitz, 1996; Chant and Pringle, 1995). Bud3 is a Rho Guanine nucleotide Exchange Factor and Bud4 is an anilin-like protein. They colocalise with septin filaments during the hourglass and double ring steps, except for the central part of the hourglass were the myosin-II filaments are densely present. A scanning electron microscopy study showed that the knockdown of either Bud3 or Bud4 as well as mutations change drastically the structure of septin filaments (Chen et al., 2020). Both proteins interact directly with septins with their central region and also interact with one another through their C-terminal domain (Finnigan et al., 2016). It was observed that the knockdown of Bud3 lead to fragmented septin structure that would eventually disappear. In the case of Bud4 knockdown, upon ring splitting, the mother side ring was absent and only the ring present on the daughter side was briefly observed. Strikingly, in double knockdown cells, only a faint single ring on the daughter side was observed and quickly disappeared. However, the formation of nascent septin ring at the onset of cytokinesis was not impacted.

Scanning electron microscopy on spheroplasts after either Bud3 or Bud4 knockdown allowed for a better understanding of their role in the organisation of the structure of septin filaments (Chen et al., 2020). Cells were observed during the transitional stage of the hourglass. Images are displayed in Figure 1.12 with coloured septin filaments. In wild type cells the network of septin filaments is clearly visible. In Bud3 knockdown cells, the circumferential filaments were lost and only filaments running along the mother bud axis are visible. In Bud4 knockdown cells, a clear asymmetry was observed in the structure with one side similar to the wild type, while in the other side the number of axial filaments was greatly reduced and circumferential filaments were absent. In later stage after ring splitting, in both conditions, the number of filaments forming the rings and their density was reduced. Also visible lateral connections in wild type cells were not observed in the knockdown conditions. These observations show the importance of the Bud3 and Bud4 proteins to create the septin mesh and/or stabilise it.

Considering the importance of septins in many cellular processes, there was a need for better understanding of the biophysical properties of the septin family.

1.2 In vitro studies

To better understand the variety of roles that septins perform in cells, *in vitro* approaches have been used to analyse the biophysical properties of septins. Such approaches rely on the combination of purified septins and biomimetic systems. They allow the perfect control of the experimental conditions and the determination of specific properties for each individual component of the system.

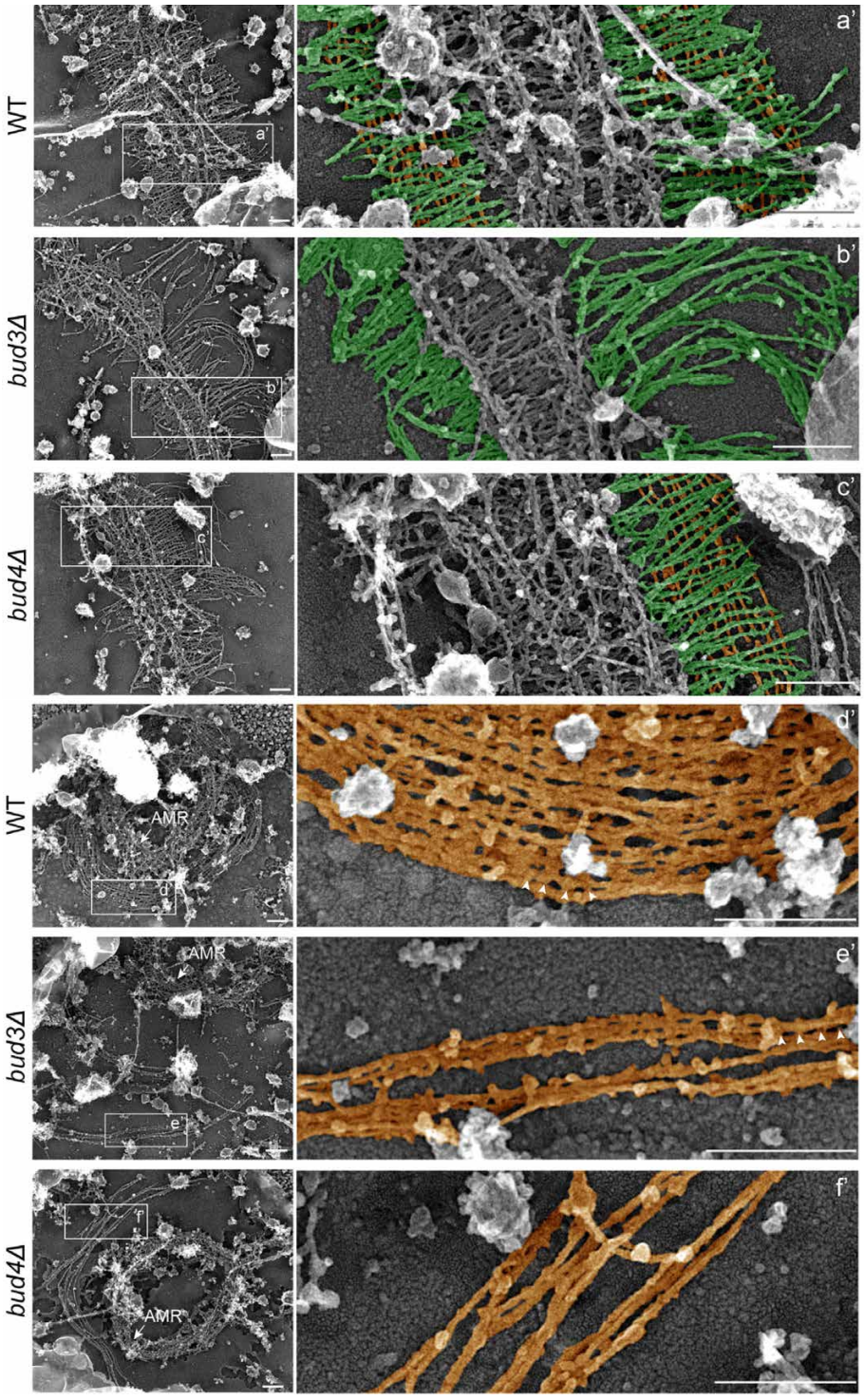

Figure 1.12 – SEM images obtained on spheroplasts at different stages. Top images correspond to the transitional hourglass structure, bottom images correspond to the double ring stage, from Chen et al. (2020). Scale bars are 200 nm.

1.2.1 Primary sequence of septins

There are 5 mitotic budding yeast septins, cdc3, cdc10, cdc11, cdc12 and shs1. They share a similar structure with three main regions, the N-terminal domain, the GTP-binding domain and the C-terminal domain. The length of each of these domains

depends on the septin subunit. The N-terminal domain is an intrinsically disordered domain that promotes interactions with other N-terminal domains of septins (Garcia et al., 2006; Sirajuddin et al., 2007). It also possesses a polybasic region at the frontier with the GTP-binding domain. This region binds to phospholipids and has a high specificity for PIP_2 (Zhang et al., 1999). Finally, the N-terminal region can associate with the C-terminal region of neighbouring septins and create NC interfaces allowing the formation of oligomers (Sirajuddin et al., 2007).

The GTP-binding domain is the largest and most conserved domains among septins. Although all septins possess this domain, in most septins the hydrolysis of GTP is slow and some such as the SEPT6 group even lack this activity (Zent and Wittinghofer, 2014; Abbey et al., 2019). The role of GTP hydolysis in septins is still unclear but growing evidence suggests that GTP-binding and hydrolysis could stabilize the interaction with GTP-binding domains of other septins. The state of the bound nucleotide might affect the step by step oligomerisation process. The consequence is that the GTP and GDP levels can control the length and rigidity of septin filaments (Khan et al., 2018). The GTP-binding domain also includes a septin specific region, the septin unique element (SUE) which is highly conserved and differentiates them from other small GTPases (Cao et al., 2007; Pan et al., 2007). The function of this unique region has yet to be understood.

Finally, septins possess a C-terminal domain which length is strongly dependent on the septin subunit ranging from more than one hundred residues to about a dozen. It is predicted to be a coiled coil and plays a role in the oligomerisation process by interacting with the N-terminal of other septins. They are also responsible for pairing of filaments and emergence of higher order structures (Bertin et al., 2008) (Sala et al., 2016).

1.2.2 Ultrastructural assembly

Thanks to their subunit-subunit interactions, septins can assemble into higher order structures. These structures are all made of hetero octamers or hexamers that can further assemble into filaments and other higher order structures. The first crystallographic structure of septin assembly is displayed in Figure 1.13. It was obtained for a human hexamer and wrongly determined the following palindromic assembly: SEPT7/SEPT6/SEPT2/SEPT2/SEPT6/SEPT7 (Sirajuddin et al., 2007). Actually, the correct order is SEPT2/SEPT6/SEPT7/SEPT7/SEPT6/SEPT2 as shown in (Mendonça et al., 2019). However the subunit-subunit contacts are not changed. This structure revealed the nature of the interfaces involved in the assembly as well as relative positions of different domains. Interestingly, even though septins assemble into a palindromic oligomer, this oligomer has a central planar symmetry rather than an axial symmetry.

Mitotic yeast septins form an hetero octamer made of 4 pairs of different septin subunits. To study their organisation, yeast septins were purified and observed by negative staining electron microscopy at salt concentrations above 150 mM (Bertin et al., 2008). The resolution allows for the observation of individual subunits, and their order can be recovered by labelling selectively only one septin subunit with a tag such as GFP or MBP. The obtained arrangement of the hetero octamer was a palindromic sequence: cdc11/cdc12/cdc3/cdc10/cdc10/cdc3/cdc12/cdc11. The fifth mitotic yeast septin, shs1, can replace cdc11 in the octamer. Septins interact through

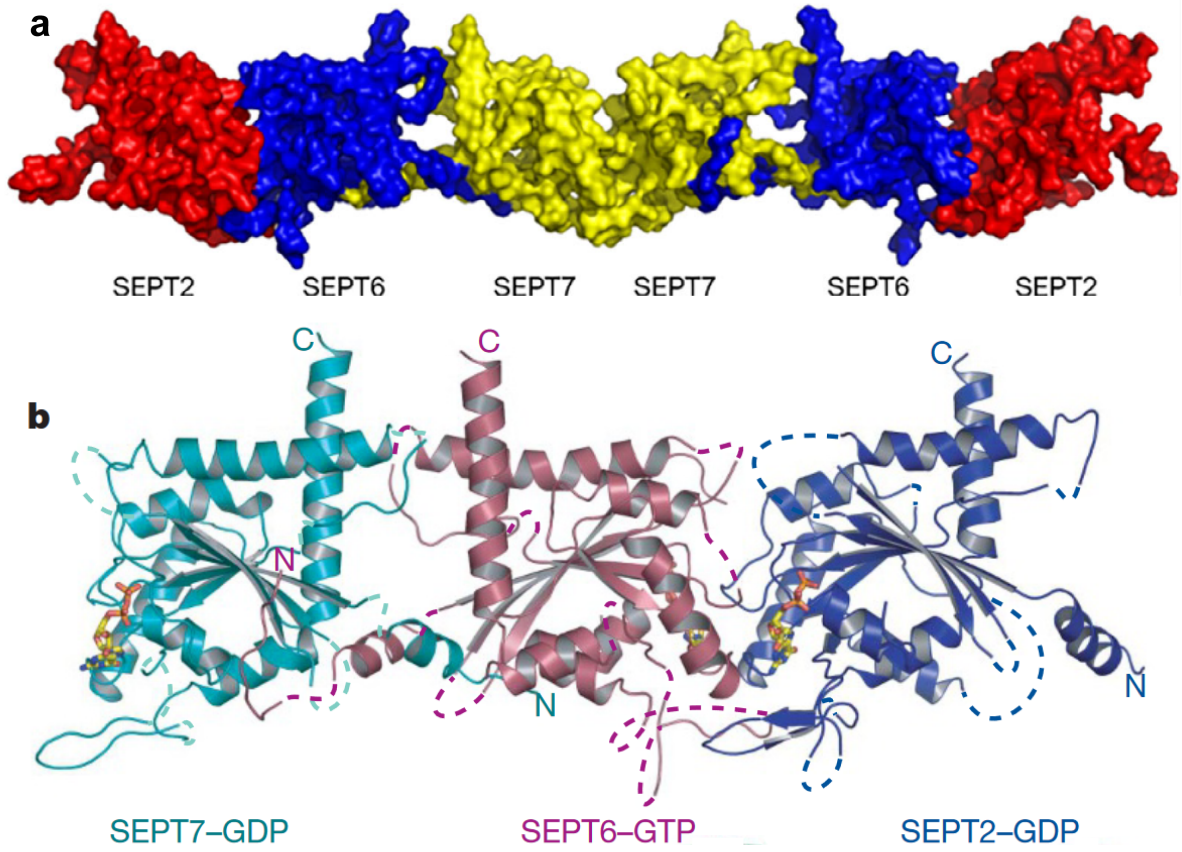

Figure 1.13 – (a) Surface representation of the hexameric assemblies. From Mendonça et al. (2019). (b) Ribbon model of the trimeric assembly from X-Ray crystallography. From Sirajuddin et al. (2007).

either NC interfaces or G interfaces and the specificity of these interaction allows for the controlled structure of the hetero octamer. The octamer is 32 nm long and 4 nm wide. Upon the reduction of salt concentration or addition of lipid membranes, octamers can further assemble into filaments by end to end interactions. These filaments were first observed in negative staining microscopy after their assembly in solution (Bertin et al., 2008). Filaments of a few micrometres in length were observed and always existed as pairs of filaments (Figure 1.14). The distance between the paired filaments ranges from 15 to 25 nm apart, and some electron densities were observed between paired filaments. The pairing of filaments would later be attributed to the C-terminal coiled coils, interacting with the coiled coils of the neighbouring filament, forming the pairs. Similar experiments were repeated on lipid monolayers (Bertin et al., 2010), and long paired filaments were observed to interact laterally and create sheets of filaments (Figure 1.14 B and C). Increasing the salt concentration to 300 mM did not affect the ability of complexes to associate into filaments on lipid membranes, showing that the presence of a lipid membrane favours the formation of septin filaments.

The substitution of the cdc11 subunit by shs1 induces the assembly of rings instead of flat sheets of filaments (Garcia et al., 2011). The octameric complex is very similar to the one with cdc11 but filaments form bundled rings with a diameter of about 500 nm and width of about 100 nm. The ratio of cdc11 and shs1 Was varied. For a ratio of shs1 to cdc11 of 2:1, filaments still formed paired filaments, but increasing the ratio led to the formation of rings as was observed by electron microscopy (Figure 1.14 D-I).

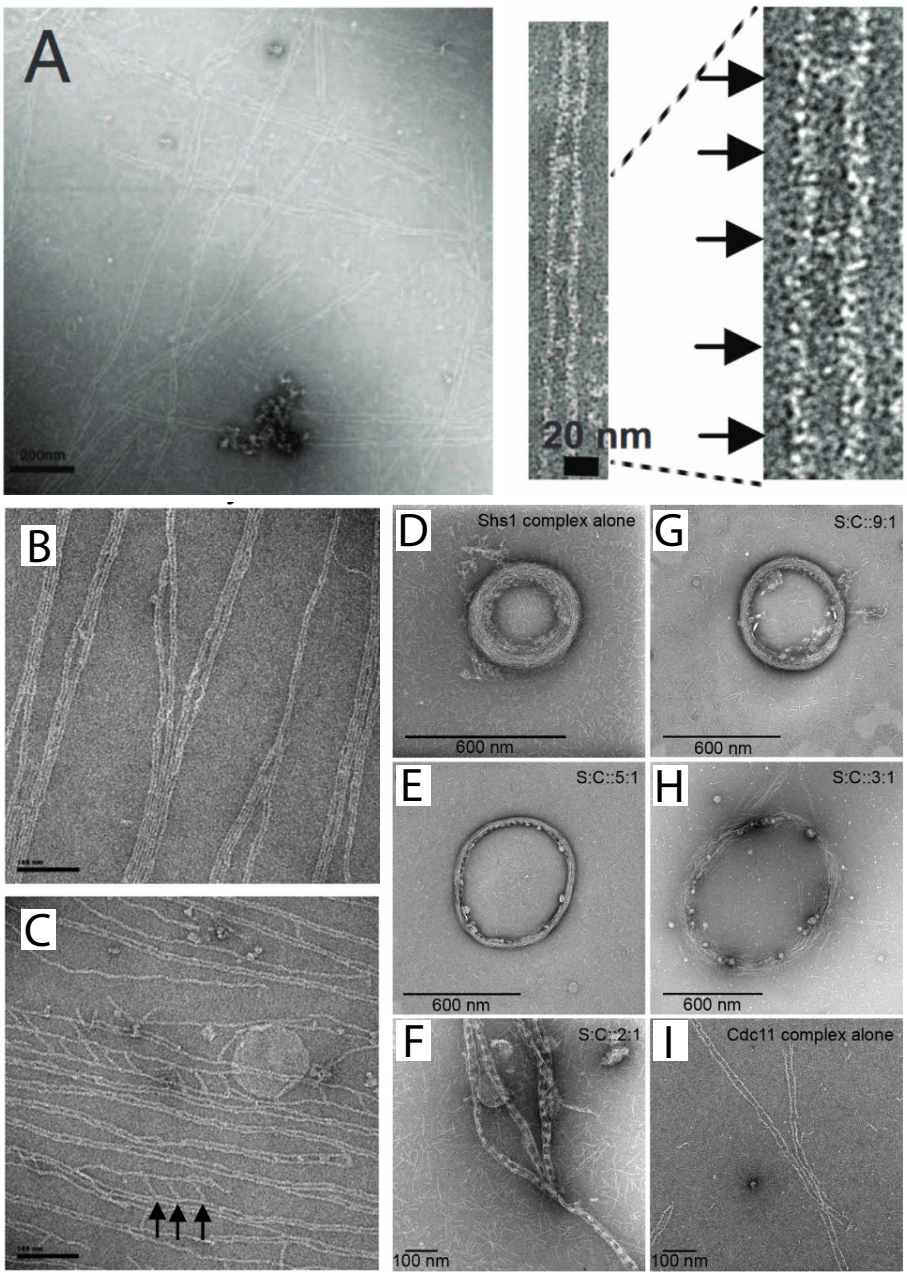

Figure 1.14 – Negative staining electron microscopy images from septin filaments. (A) Filaments formed in solution, on the right, zoom on a paired filaments showing the presence of densities between paired filaments (pointed by arrows). From Bertin et al. (2008). (B) Filaments formed on a lipid monolayer containing 20% PI(4,5)P_2. (C) Filaments formed on a lipid monolayer with overnight incubation. Arrows point at orthognal connections of about 35 nm in length between parallel paired sets of filaments. From Bertin et al. (2010). (D) to (I) Filaments with different ratio of shs1 to cdc11. From Garcia et al. (2011).

Later studies were focused on the mechanisms of septin assembly. Fluorescently labelled septins were added on supported lipid bilayers and filament formation was followed by TIRF imaging (Bridges et al., 2014; Woods et al., 2021). It was observed that septins assemble in an isodemic manner rather than cooperative. Because complexes

are palindromic, growth can happen at both ends. Two filaments can also interact end to end and anneal and form a single filament.

1.2.3 Orthology of septins

Septins were discovered in yeast Saccharomyces Cerevisiae before orthologs were found in all eukaryotes. Further studies allowed the classification of both fungal septins and animal septins into subgroups by respectively phylogenetic analysis and primary sequence analysis (Momany et al., 2001). However, initial studies comparing fungal to animal septins concluded that no orthologous relations could be drawn between the two (Kinoshita, 2003b). Comparing a bigger set of model organisms showed that some subsets of fungal septins could be compared with animal septins (Pan et al., 2007). To look for septin orthologs, the sequence of cdc3 was used to interrogate GenBank to obtain a list of proteins with similar sequences. To select septin orthologs from the list of proteins, they looked for septin specific sequences in the GTP-binding domain. The final list of proteins contained 160 sequences from various organisms. From those sequences one stood out, the Gla protein from *Giardia lamblia*. Because it only possesses part of the sequence specific to septins it was not classified as septin, but as *Giardia lamblia* is a basal eukaryote, it could potentially show how septins evolved. Phylogenetic tree showed some similarity between some of the animal septins with some of the fungal septins.

Later studies focused on the animal septins allowed for the classification of the 12 or 13 septin genes -depending on the animal- in subgroups that have strong similarity. The different subgroups are the SEPT2, SEPT6, SEPT7 and SEPT3 (Kinoshita, 2003a; Mostowy and Cossart, 2012). Similarly to the yeast septins, they can assemble into palindromic octamers, either hexamers or octamers, depending on the presence of SEPT9 which is part of the SEPT3 subgroup. The hexamer complex is made of a palindromic assembly of SEPT2/SEPT6/SEPT7 with SEPT7 at the centre (Sirajuddin et al., 2007), the octamer is similar with two copies of SEPT9 inserted in the centre, similarly to the yeast cdc10 its most homologous yeast septin (McMurray and Thorner, 2019; Mendonça et al., 2019). Septins within the same subgroup can be exchanged within the assembly, this is known as the Kinoshita rule (Kinoshita, 2003a). However, some other assemblies that do not respect this rule have also been reported, they can even be homomeric as it was shown for SEPT2 (Mendoza et al., 2002; Sellin et al., 2014; Karasmanis et al., 2018). These hexamers and octamers can also further assemble into filaments in a fashion similar to yeast septins.

1.2.4 Interaction with lipids and membranes

Because septins localise often at the plasma membrane in vivo -see section 1.1.5- it was speculated that they would interact directly with lipids. This was supported by the observation that in cell fractionation, septins would co-fraction with the plasma membrane (Xie et al., 1999). Also, septins possess a polybasic domain that can possibly interact with lipids. Finally, a direct interaction was observed between the lipid membrane and four yeast septin subunits cdc3, cdc10c cdc11, cdc12 as well as the human SEPT4 (Zhang et al., 1999; Casamayor and Snyder, 2003).

To further investigate the interaction between septins and lipids, *in vitro* experiments using lipid biomimetic membranes were performed. Such experiments allow

for the control of the lipid composition of the membrane. Studying the interaction of septins with a lipid monolayer, it was shown that septins do not interact with a pure neutral DOPC monolayer (Bertin et al., 2010). The addition of PIP to molar ratios of up to 20% did not affect the interaction between septins and the membrane. The addition of small amount of either $PI(4,5)P_2$ or $PI(3,4,5)P_3$ in amounts as low as 2.5% promoted the interaction between septins and the lipid monolayer. Different organisations would be obtained depending on the phosphoinositide used. With $PI(3,4,5)P_3$ the filaments would be less organised displaying more aggregation. The specific $PI(4,5)P_2$ interaction was confirmed by experiments performed on GUVs (Beber et al., 2019a). In the absence of $PI(4,5)P_2$ in the lipid mixture, no interaction could be detected. GUVs with increasing amount of $PI(4,5)P_2$ were incubated with purified yeast septins and the density of septins was plotted against the molar fraction of $PI(4,5)P_2$ in the vesicle. With a composition chosen to mimic the lipid composition of the plasma membrane, the septin interaction with the lipid bilayer was highly sensitive to the molar ration of $PI(4,5)P_2$, to an extent where it is more sensitive than common probes used for $PI(4,5)P_2$.

1.2.5 Septins and curvature

Because septins often localise at regions of micrometric curvatures in cells, and most interestingly regions with both positive and negative curvature, several studies have analysed how septins can discriminate curvatures, or if other cues were necessary. The first study performed on curvature sensitivity of septins was performed using beads coated with lipid bilayers containing 25% PIP (Bridges et al., 2016). The beads were then incubated with fluorescently labelled purified yeast septin octamers containing cdc11. The ratio of fluorescence between the purified septins and the fluorescent lipids in the bilayer was obtained for beads with sizes ranging from 6.5 µm to 0.3 µm in diameter. The fluorescence images and the septin adsorption are displayed in Figure 1.15 A. The maximum ratio of intensity, corresponding to the maximum septin density was obtained on the surface of the 1 µm beads, corresponding to a curvature of $+2$ µm^{-1}. Changing the bulk concentration of septins would not change the relative density between the sizes of beads. However, they found that the interaction was highly salt dependent, and by lowering the salt concentration to 50 mM, the density would be similar on 1 and 5 micrometres beads. They also studied the ability of complexes to recognise the curvature by adding mutations to cdc11 to prevent the end to end interaction of distinct octamers. Septins would still bind preferentially to the 1 µm beads even though the interaction was now mediated by His-Ni^{2+} interaction. In a second study, they performed scanning electron microscopy to obtain the orientation of septin filaments on small rods. The images are shown in Figure 1.15 B. On small rods, septins aligned along the principal axis of the rod, to minimise their curvature. Increasing the diameter of the rod lead to a change in orientation with septins going progressively perpendicular to the main axis of the rod, following an effective radius of curvature of about $+2$ µm^{-1}, which confirmed septins preference for this curvature.

The model proposed for the curvature sensitivity of septins relies on the interaction of septins with the membrane through amphipathic helices (Cannon et al., 2019). Amphipathic helices are used by a wide range of proteins to recognise nanometric membrane curvature and some septins (cdc12, SEPT6) possess predicted amphipathic helices at the extremity of their C-terminal domain. Curved membranes display local defects

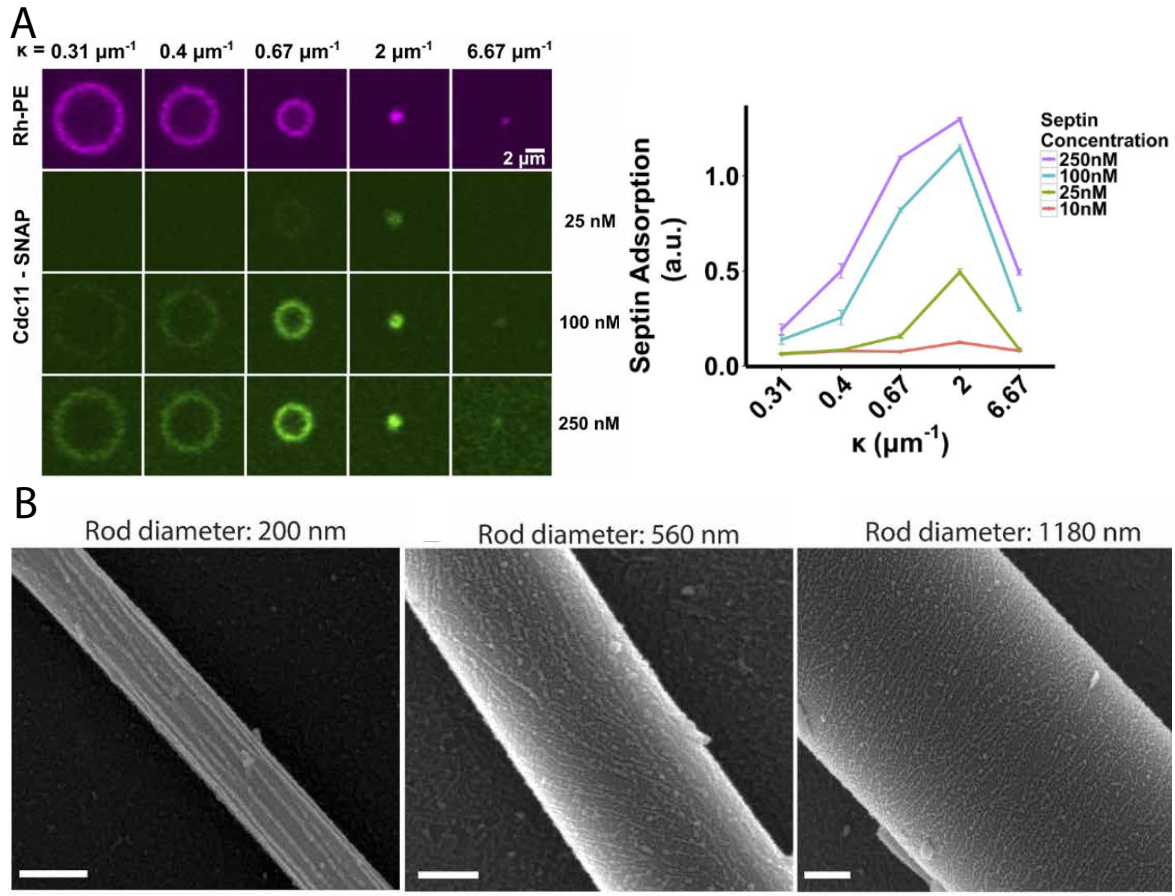

Figure 1.15 – (A) Beads coated with supported lipid bilayer and incubated with fluorescently labelled septins. Right: distribution of relative fluorescence intensity as a function of the bead size and septin concentration. From Bridges et al. (2016). (B) Scanning electron microscopy images of septins on lipid bilayers deposited on rods of varying diameters, from Cannon et al. (2019). Scale bars are 200 nm.

with a density increasing with the curvature. At a proper curvature, the typical space between the defects would correspond to the distance between amphipathic helices in the septin filament. To test this hypothesis, they truncated most of the C-terminus of cdc12 and observed that septins would lose their preferential curvature.

Later studies performed in our lab were run by using both vesicles and supported bilayers on wavy substrates (Beber et al., 2019b). The lipid composition was set to mimic the composition of the plasma membrane with a molar ratio of PI(4,5)P_2 that was optimised for septin interaction with the membrane. Upon incubation of septin on vesicles, a striking feature appeared. Septins would deform the vesicles creating spikes on their surface. Confocal images of these vesicles are displayed in Figure 1.16 A and B. The size and wavelength of these spikes were regular (analysis of the characteristics of the spikes is shown in Figure 1.16 B) displaying radii of curvature of -1.4 μm^{-1}. Septins were then incubated on lipid bilayers deposited on wavy substrates. This allows to screen both positive and negative curvatures simultaneously. Experiments were performed on a range of curvatures varying from -3 to +3 μm^{-1}. The obtained membranes coated with septins were first observed with fluorescent microscopy. It showed that septins would be enriched in regions with positive curvature. Their organisation

was also described using scanning electron microscopy; As can be seen in Figure 1.16 C, it appeared that septins organise very differently depending on the curvature. On the hills corresponding to the positive curvatures, septins aligned with the axis of zero curvature, while in the valleys, septins aligned with the axis of maximum curvature. This observation shows a preference for septins for negative curvatures with values of about -3 μm^{-1} and avoid positive curvature. The deformations observed on GUVs upon the addition of septins are very likely due to this preference for negative curvature. A model was proposed to explain this curvature preference, where septins try to maximise their area of contact with the membrane but have to bend accordingly to achieve this. There is therefore a balance between the energy of interaction and the bending modulus, related to the persistence length of the filament. This model does not specify the type of interaction between septins and the membrane and only on the filamentous nature of septins.

Finally a recent study using cryo-electron microscopy has revealed some interesting features in the structure of the human hexamer assembly (Mendonça et al., 2021). Most notably, they observed that the septin filament possess an intrinsic curvature. They observed on a single hexamer a deflection of the terminal subunit of 22 Å from the central axis. They estimated that such a deflection would lead upon assembly to rings of a few hundreds of nanometres. However, this estimation remains qualitative and does not take into account the possible bending at the interface of the hexamers.

1.2.6 Mechanical properties of septin filaments

The mechanical properties of septin filaments can be crucial in their role of stabilising the membrane and interaction with other cytoskeletal components. The first mechanical property of septin filaments which has been studied is their persistence length using techniques similar to those used for actin and microtubules. Filaments were formed and deposited either on lipid bilayers or passivated glass. They were then imaged with fluorescence microscopy to obtain their shape represented by the angle of its tangential vector along its length. Image of a filament and the corresponding fit of the correlation of the angle can be seen in Figure 1.17 A and B. The final value of persistence length varied from each experiment, with values ranging from 1 μm to 12 μm (Bridges et al., 2014; Beber et al., 2019b; Woods et al., 2021). Those values can be compared to actin, with persistence length of approximately 10 μm and microtubules which are much stiffer with persistence length of about 1 mm.

Considering the stiffness of septin filaments, and because their ability to deform membranes could depend on the mechanical strength of the septin network, a study performed in the lab measured both the elastic modulus and bending modulus on a membrane covered with septins (Beber et al., 2019b). To measure those two parameters, two different methods were used. The first technique relies on micropipette aspiration to obtain the elastic modulus (Figure 1.17 C). By monitoring the aspiration pressure inside the micropipette and the length of the aspirated tongue, one can obtain the elastic modulus of the membrane. Surprisingly, it was found that addition of septins would lower the elastic modulus going from 65 $mN.m^{-1}$ to 42 $mN.m^{-1}$. To obtain the bending modulus of the membrane associated with septins, they used a bead trapped in an optical tweezer to pull a tube from a GUV under tension (Figure 1.17 D). The bending modulus was not significantly changed and was measured to be close to 10 k_BT.

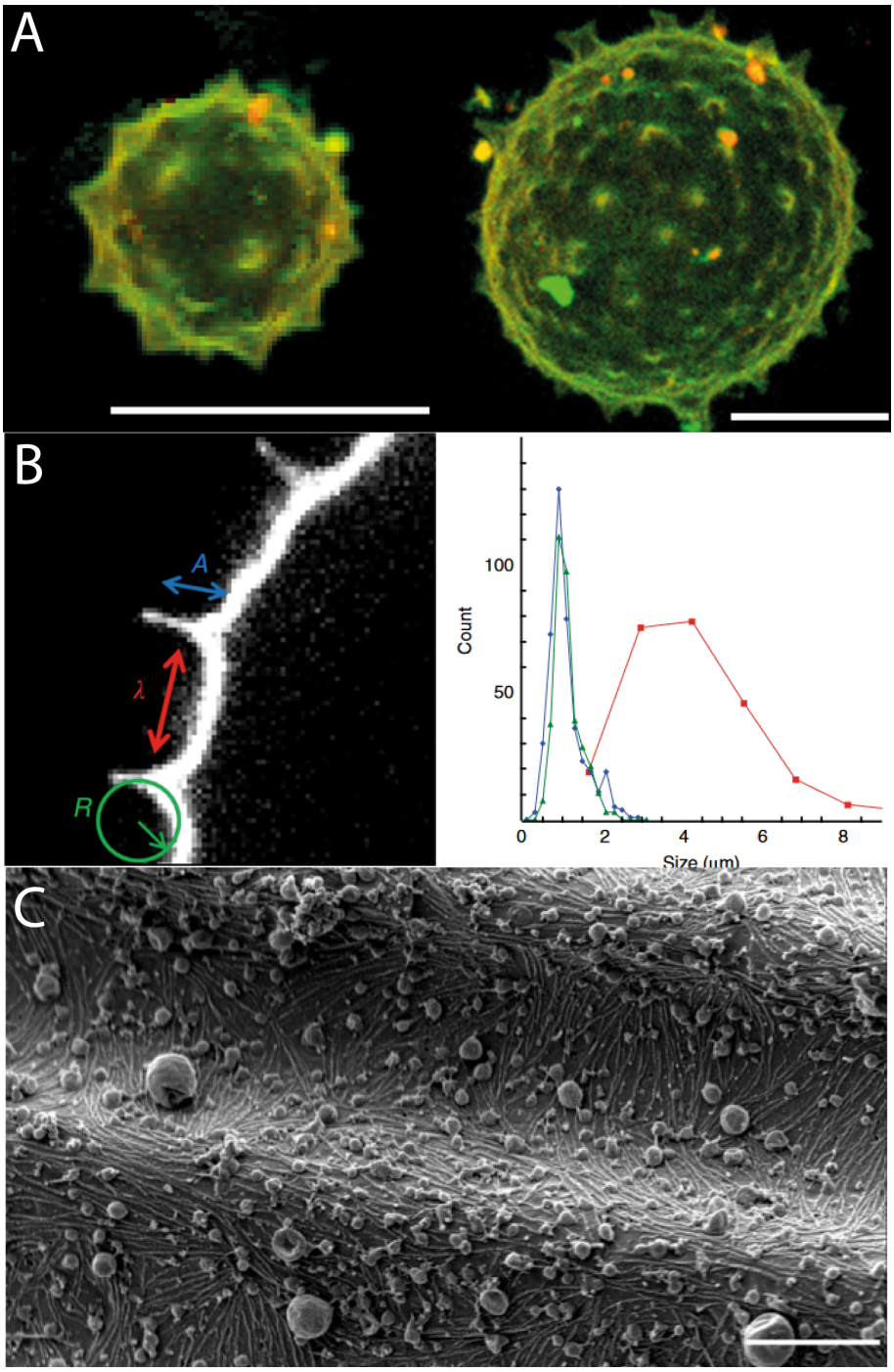

Figure 1.16 – (A) 3D reconstitution of GUVs coated with septins imaged with confocal microscopy. Scale bars are 10 µm.(B) Characterisation of the periodic deformations of GUVs by septins. (C) Scanning electron microscopy of a supported lipid bilayer deposited on a wavy substrate with septin filaments, from Beber et al. (2019b). Scale bar is 1 µm.

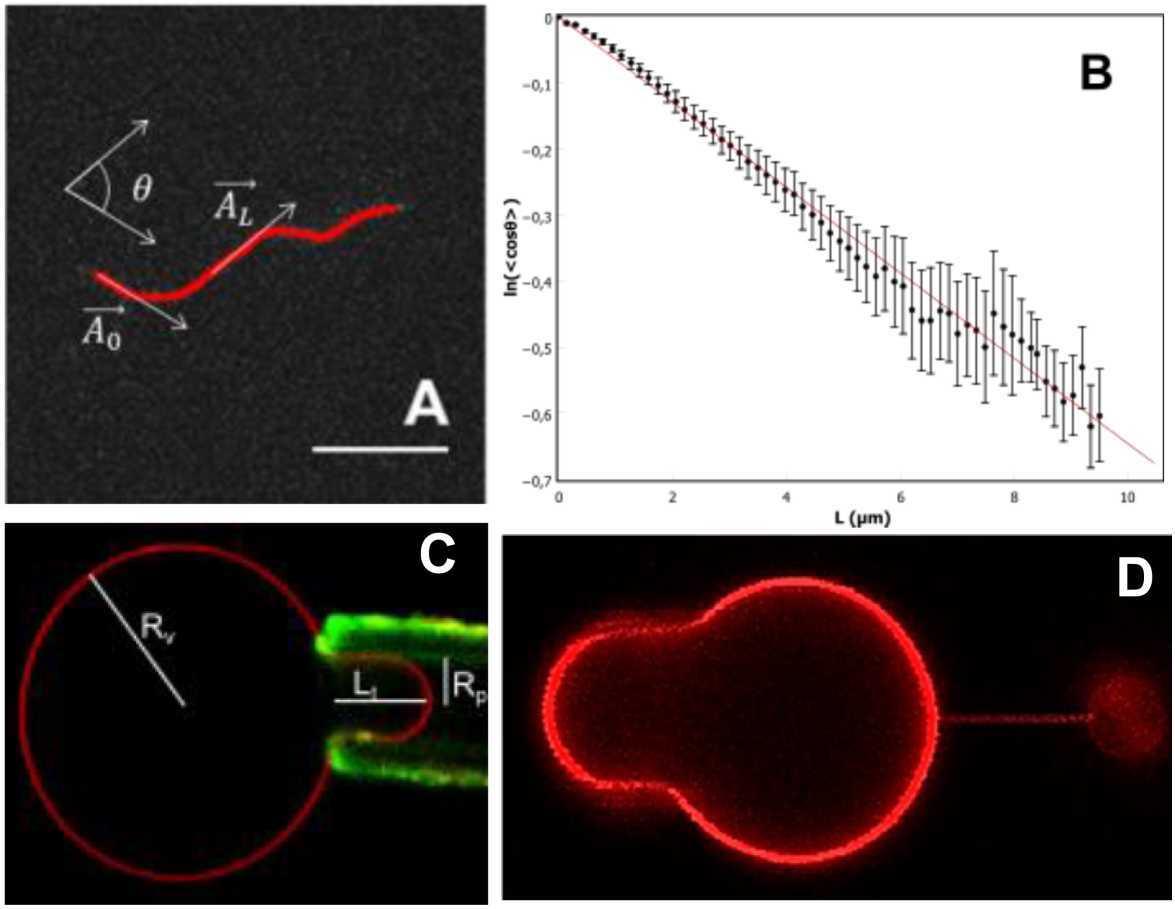

Figure 1.17 – (A) Septin filament deposited on a passivated glass substrate, in red is the contour used for analysis of the persistence length. (B) Logarithmic distribution of the angle between tangent separated by a distance L on the septin filament. The fit gave a persistence length of 7.8 µm. (C) Confocal image from micropipette aspiration on GUV. The micropipette is visible in green due to septins binding non specifically to glass. (D) Confocal image from tube pulling experiment, the GUV is held and out under tension by a micropipette on the left, while a bead is put in contact and pulled away from the GUV on the right. From Beber et al. (2019b).

1.3 Biological membranes

1.3.1 Composition and functions

Membranes are essential components of living organisms. They allow the separation of the cells from their environment and also the inner organisation into sub cellular compartments. They are mainly composed of proteins and lipids, with an average weight ratio of 1:1. Lipids are relatively small molecules combining a hydrophilic head (occupying about 0.5 nm^2) with two hydrophobic tails (about 2 nm long). They can form lipid bilayers which are the base of biological membranes. Lipid bilayers are made of two sheets of lipids with their heads facing outwards and the hydrophobic tails facing each other. Typical width of a lipid membrane is about 4 to 6 nanometres depending on the length of the hydrophobic tails. There are hundreds of lipids with various properties. However they all possess two states, a gel phase and a liquid phase. The transition can happen at temperatures ranging from -10°C to 90°C depending on the lipid. These

two phases can coexist and also lead to phase separation in membranes depending on the lipid composition and temperature (Shimshick and McConnell, 1973; Heberle and Feigenson, 2011). In biological membranes, this is believed to occur in some domains called "lipid rafts" of a few tens of nanometres in which some lipids – mainly cholesterol and sphingolipids – are strongly enriched (Lingwood and Simons, 2010). The diversity of both lipids and membrane associated proteins are responsible for the complexity of membranes. The caption in Figure 1.18 shows the complexity of a membrane in the cellular context.

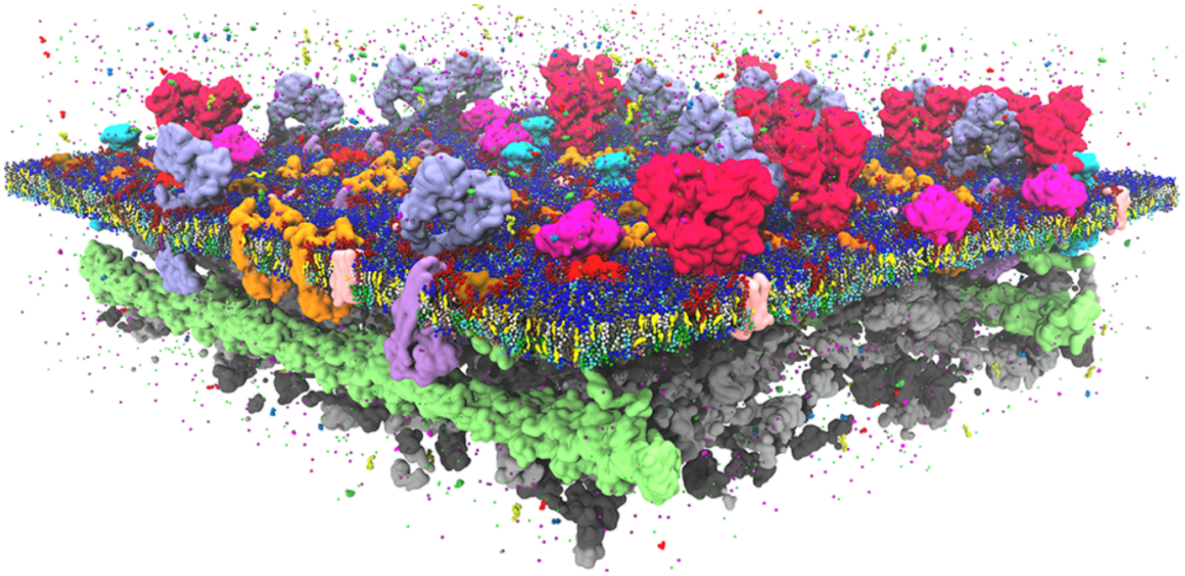

Figure 1.18 – Model of the plasma membrane showing the complexity, with a large variety of lipids, embedded and peripheric proteins as well as the underlying cytoskeleton. From Marrink et al. (2019).

Cells always interact with their environment via the plasma membrane. The plasma membrane is therefore essential in many processes such as mobility, signal transduction, communication with other cells, mechano-sensitivity. Despite its role as a separator, the membrane is permeable to a given extent to certain molecules. Membranes are slightly water permeable depending on the lipid composition. Additionally, some transmembrane proteins can control the fluxes of molecules through membranes. These proteins can either induce active or passive transport. Membranes can also serve as a recruitment platforms, increasing the local density of proteins. Membrane associated proteins can either bind to the lipid heads, or they can possess a transmembrane domain, which fully inserts inside the membrane. They can strongly change the physical characteristics of the membrane, starting with their curvature. It has been observed that some proteins with a nanometric intrinsic curvature can impose their intrinsic curvature to the membrane upon binding to the membrane (Peter et al., 2004).

1.3.2 Diffusion along biological membranes

Biological membranes are highly dynamic. Both lipids and proteins diffuse laterally in cells. Clustering and segregation can happen in a dynamic manner. These dynamical processes are essential to many cellular functions. To understand the diffusion of membrane components, both theoretical and experimental studies have been

performed. There has been a strong effort to follow the dynamics of lipids by labelling peptides and proteins -often toxin subunits- that bind to specific lipids. The dynamics of receptors has also been under high interest. The first and well accepted model for the diffusion of lipids and transmembrane proteins was developed by Saffman and Delbrück (Saffman and Delbrück, 1975). They consider the lipid bilayer to be an infinite sheet of viscous liquid and the particle of interest is considered as a cylinder. The viscosity of the surrounding fluid is neglected implying that no shear stress is transmitted to the surrounding media.

The equations describing brownian motion in a 2D sheet of fluid are:

$$\overline{r^2} = 4Dt \ ; \ D = k_B T d \tag{1.1}$$

Where r^2 is mean square displacement as a function of time t, k_B is the Boltzmann constant, T the absolute temperature and d is the mobility, defined as the velocity per unit of force applied on the particle.

The computation of d cannot be achieved as there are no solution for slow viscous flow for steady translational motion in 2 dimensions. A finite mobility can be inferred, considering the inertia of the 2D fluid:

$$d = \frac{1}{4\pi\mu h}\left(log\frac{4\mu}{\rho U a} + \frac{1}{2} - \gamma\right) \tag{1.2}$$

Where ρ is the density of the fluid, μ is its viscosity, a is the radius of the cylinder, h is the thickness of the sheet, U is the steady translational velocity and γ is Euler's constant (equal to 0.5772). However, the obtained mobility depends on U and therefore on the force. The previous equation was derived considering the mobility independent of the force and is not valid any more. Three considerations can correct for this: (i) consider the sheet to be finite, (ii) take into account the surrounding fluid, (iii) use the Langevin equation considering the mobility obtained for unsteady flow. All three corrections could be implemented simultaneously, but it becomes analytically impractical. Moreover, as they add up reciprocally, each one was independently derived from the others.

(i) With a finite sheet size of radius R where $R \gg a$, the mobility becomes:

$$d_f = \frac{1}{4\pi\mu h}\left(log\frac{R}{a} - \frac{1}{2}\right) \tag{1.3}$$

Where the 1/2 term correspond to a no-slip boundary condition arround the object. It goes to zero if there is no tangential stress.

(ii) When considering the surrounding fluid with a viscosity of μ', the flow inside the fluid sheet is still considered to be two dimensional. Indeed, the structure of lipids does not allow shear across the membrane. A no slip boundary condition is considered between the membrane and the surrounding fluid. The mobility then becomes:

$$d_s = \frac{1}{4\pi\mu h}\left(log\frac{\mu h}{\mu' a} - \gamma\right) \tag{1.4}$$

Again, if a zero tangential stress boundary condition is considered, a +1/2 term has to be added inside the brackets.

Finally, considering the drag of an accelerated cylinder in a viscous fluid and inserting them into Langevin's equation, it can be found that the effective mobility varies as:

$$d = \frac{1}{4\pi\mu h}\left(log\frac{4\mu t}{\rho a^2} - 1 - \gamma\right) \tag{1.5}$$

It is important to note that this mobility is time dependent. Considering typical values in biological membrane, it appears that the dominant term for the mobility originates from the friction with the surrounding fluid. The theoretical values obtained with this model were experimentally tested using several models of transmembrane proteins. They compared the dependence of the diffusion coefficient on multiple parameters. Some studies found some strong disagreement with the theory of Saffman and Delbrück (Gambin et al., 2006), other studies obtained results that would agree with the Saffman Delbrück model (Peters and Cherry, 1982; Ramadurai et al., 2009). The later studies notably tested the size of the molecule as well as the viscosity of the surrounding media. The difference could be due to the difference of experimental procedures, and the effect of crowding. Noteworthy, the radius of the cylinder has a marginal effect on the diffusion coefficient, but the crowding has a strong impact (Ramadurai et al., 2009). Typical values of diffusion coefficients in biomimetic membranes are about 1 to 10 $\mu m^2/s$ for both lipids on transmembrane proteins. It depends strongly on the viscosity of the lipid mixture, which depends strongly on both the lipid composition and temperature.

In cells the diffusion of most membrane components was slower than in model systems. It can be explained by the presence of immobile molecules that affect the diffusion of other membrane components and by the clustering and formation of small domains in the membranes which prevent the free diffusion of membrane components.

1.3.3 Experimental methods to assay diffusion properties

To obtain experimentally the diffusion coefficient of membrane components, four main methods have been developed. The Fluorescence Recovery After Photobleaching (FRAP), the Fluorescence Loss In Photobleaching (FLIP), the Fluorescence Correlation Spectroscopy (FCS) and the Single Particle Tracking (SPT). All these methods rely on fluorescence microscopy and require tagging of the particle of interest with a fluorescent molecule. Their principle are shown in Figure 1.19 and 1.20.

The FRAP and FLIP techniques are closely related. In FRAP, a region of interest is photobleached and the recovery of fluorescence in this region is monitored as a function of time – see Figure 1.19 A. The time needed for fluorescence recovery depends on both the size of the region and the diffusion coefficient. Theories allowing the recovery of the diffusion coefficient have been developed for simple geometries (Axelrod et al., 1976; Soumpasis, 1983). In FLIP, a region of interest is continuously bleached, and the fluorescence is monitored in the rest of the sample – see Figure 1.19 B. FLIP experiments are often performed in cells, which contain geometries too complex for the recovery of the diffusion coefficient (Clay et al., 2014).

FCS relies on very fast acquisition of the fluorescence intensity recorded from fluorescent molecules diffusing in the illumination volume of a focused laser. Each time a fluorescent particle enters the illuminated region, it creates a burst of emission. Working at low concentrations, it is possible to obtain the typical time spent by a fluorescent particle in this small region by fitting the auto correlation of the fluorescence intensity signal – see Figure 1.20 A. Knowing the size of the illumination volume, one can obtain the diffusion coefficient of the particle. It can be further improved by changing

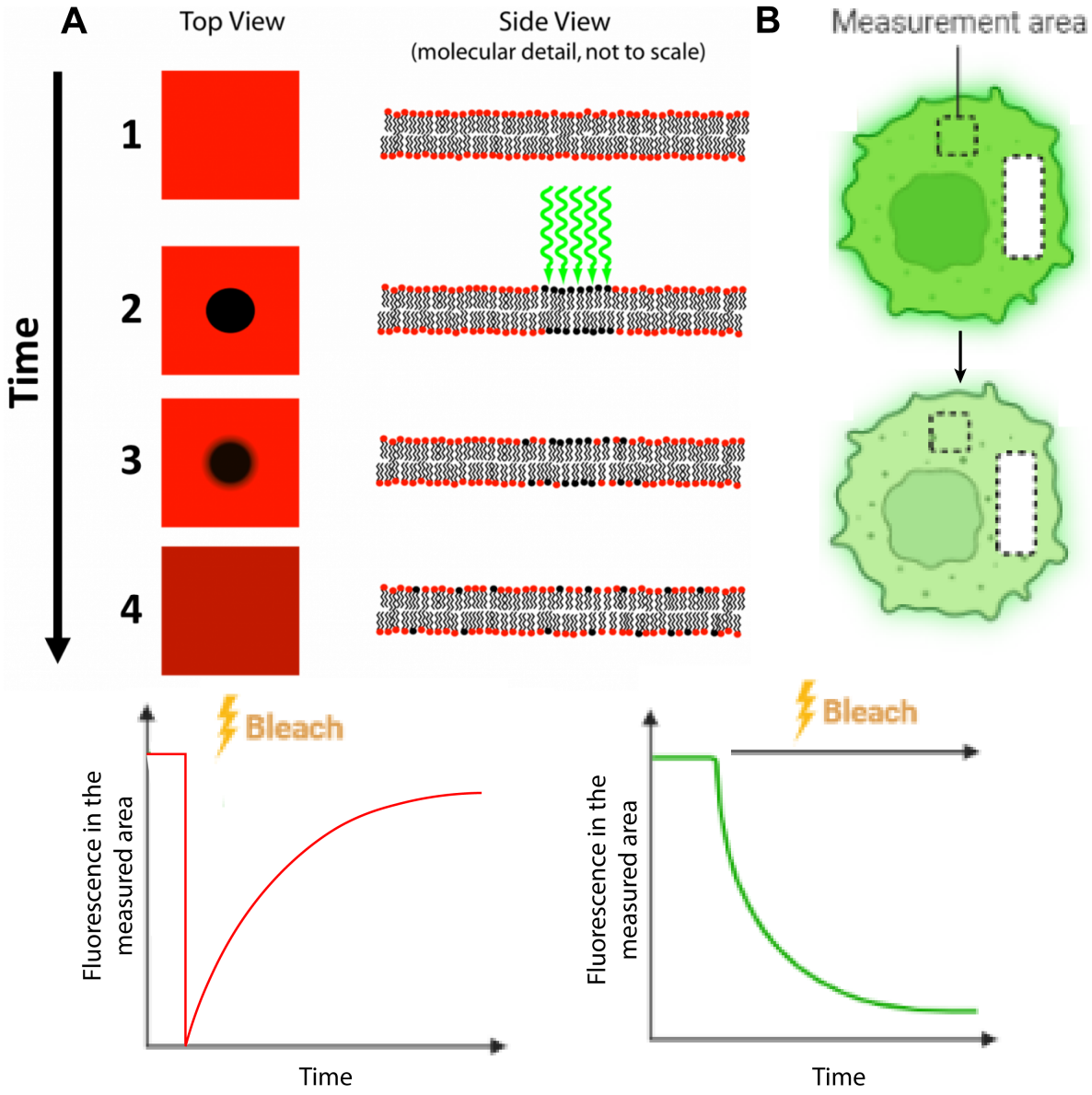

Figure 1.19 – (A) Sketch of a FRAP experiment on a lipid bilayer. A disk is homogeneously bleached by a pulse of high laser intensity. Diffusion of fluorescent molecules allows for the recovery of fluorescence within the photobleached region. From Photometrics website. (B) Sketch of a FLIP experiment on a cell. A region is constantly bleached and the fluorescence is recorded in another area. If the particles can diffuse, the overall fluorescence of the cell will decrease with time. Adapted from Biorender website.

the effective size of the focused beam, by spot variation, or using Stimulated Emission Depletion (STED). The principle of Spot variation is to under fill the back focal plane of the objective. By controlling the size of the beam at the BFP of the objective, it is possible to control the focal volume (Masuda et al., 2005; Wawrezinieck et al., 2005). STED works on the same principle as the LASER effect. By illuminating the fluorescent particles with a laser in the tail of the emission spectra of the molecule, it is possible to force the particles to emit at this exact wave-length which can later be filtered. It therefore combines two lasers, the first one to excite the fluorescence particles and the

second one to force the emission of the fluorescent molecules at a specific wavelength. The illumination pattern for this second laser is set as an annulus with a central minima which size is smaller than the focused beam of the excitation laser. the principle is displayed in Figure 1.20 B. The use for this technique will be discussed in the next section 1.3.4.

In SPT, the idea is to follow fluorescent particles and reconstruct their trajectory. A movie of dilute fluorescent particles is acquired with fast acquisition. By having fluorescent particles far apart, it is possible to assign detections in consecutive frames to individual particles. Their position can be computed with a better resolution than usually possible with optical microscopy using gaussian fitting of the 2D point spread function obtained on the camera. From the positions on consecutive frames, it is possible to recover the trajectory of each individual particle. The principle of the technique is shown in Figure 1.20 C. By fitting the Mean-Squared Displacement as a function of the lag-time, an estimate of the diffusion coefficient as well as the diffusion mode for each individual particle can be retrieved. This technique can also show spatial inhomogeneity in the diffusion behaviour of particles (Valentine et al., 2001). It is therefore a very powerful tool to look at diffusion of particles that interact in specific places (Borgdorff and Choquet, 2002).

1.3.4 Diffusion regimes in real membranes

Cells are crowded environment with strong inhomogeneities, affecting the diffusion of particles. Cells are out of equilibrium systems in which active transport can occur. As a consequence, diffusion diverging from brownian motion is often observed. Molecular motors transporting cargoes along cytoskeletal filaments have been extensively studied. They transport specific cargoes in a targeted fashion at speeds much faster than what brownian motion would allow. In this study, as I am interested in diffusion barriers, I will focus on diffusion modes that would slow down the rate of diffusion. Three types of diffusion have been described: the (i) “hopped diffusion”, the (ii) “trapped diffusion” and (iii) the “domain incorporation diffusion”. Each correspond to a different blocking mechanism leading to a macroscopic decrease of the diffusion coefficient. They are displayed in Figure 1.21. This figure also displays the evolution of the apparent diffusion coefficient with the size of the FCS spot. In the “hopped diffusion”, molecules are free to diffuse in the membrane but must cross some mesh with an energy barrier to overcome. In “trapped diffusion” the molecules diffuse freely until trapped in a specific location for a period of time. They are then released and diffusion freely again. Finally the “domain incorporation diffusion” is similar to the trapped “trapped diffusion” except that the molecule is now trapped in a domain in which it diffuses.

1.3.5 Biomimetic membranes

Because of the complexity of biological membranes it appeared that using biomimetic membrane would facilitate the study of membrane properties in a controlled environment. There exist various systems each generated by various methods improved over the years.

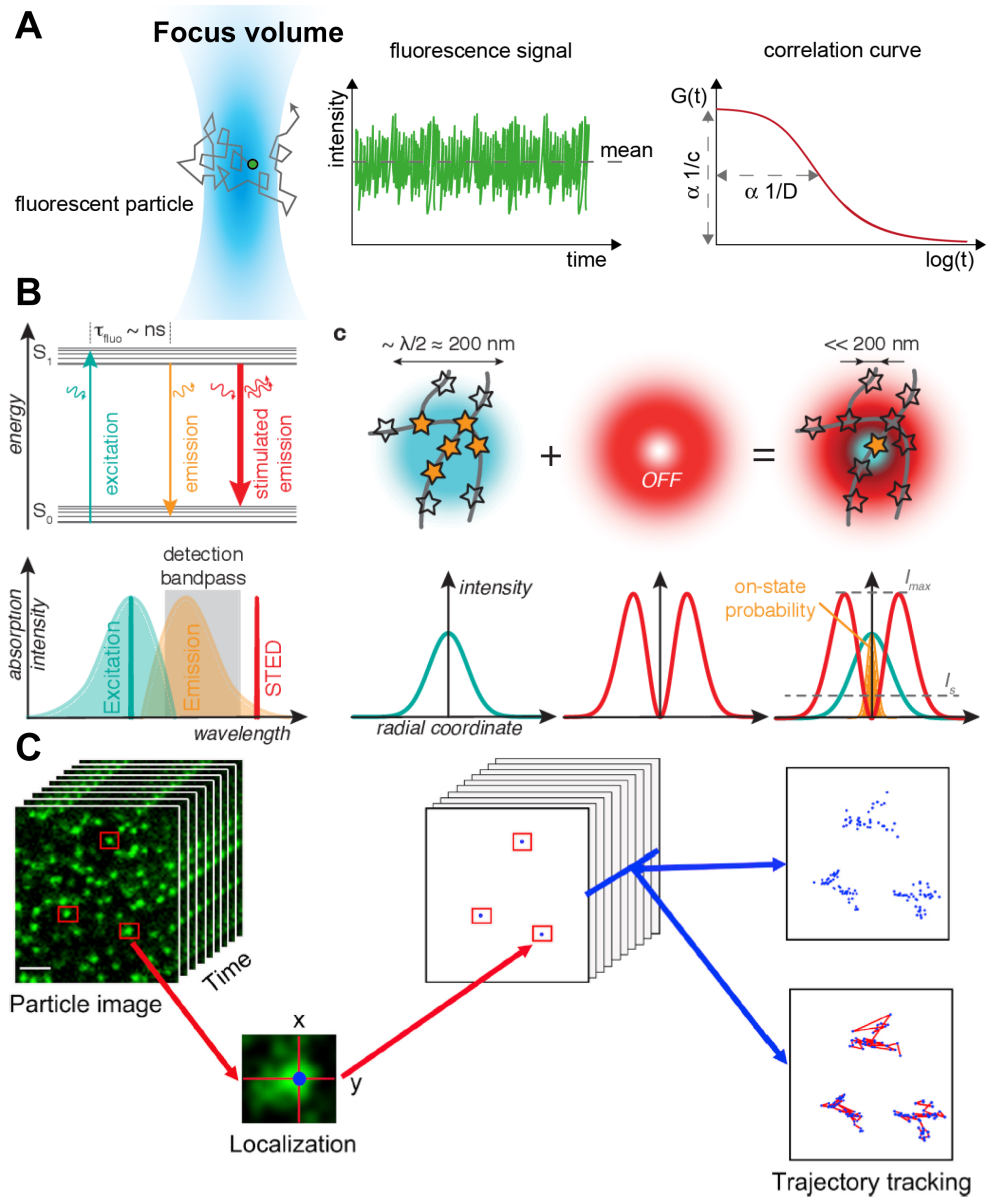

Figure 1.20 – (A) Sketch of FCS experiment performed on particles diffusing in three dimensions. The autocorrelation of the fluorescence signal gives access to the diffusion coefficient. From Bioquant group website (University of Heidelberg). (B) Principle of STED imaging, two lasers are used allowing for super resolution imaging. Left are the energy states of the fluorescent molecule with the energy of the two lasers used as well as the corresponding wavelength. Right is the comparison between a single focused laser used for confocal imaging and super resolution method using Sted. From (Jahr et al., 2020). (C) Sketch of SPT experiment. A movie of dilute fluorescent molecules is acquired and the postion of individual molecules is obtained. The trajectories can be recovered by linking positions in consecutive frames. From (Cui et al., 2018).

Vesicles

Vesicles are lipid bilayers arranged into a sphere. They isolate their interior from the surrounding media. Their size range from tens of nanometres to tens of micrometers, and therefore vesicles can be good models to mimic the plasma membrane but also

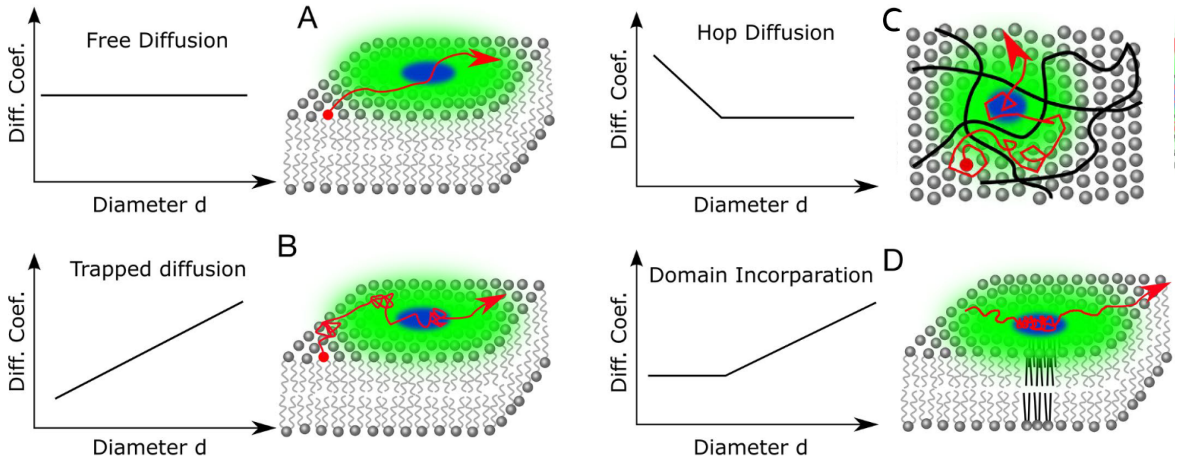

Figure 1.21 – Presentation of different types of diffusion behaviour and their features in STED-FCS. (A) Free diffusion also referred as brownian motion. (B) Trapped diffusion, the particle interacts transiently with immobile or slow diffusing binding partners. Diffusion coefficient increases with the diameter of the FCS spot. (C) Hop diffusion, the particle can diffuse freely within a mesh, and has a probability to cross this mesh. The diffusion coefficient decreases with the diameter of the FCS spot and then plateaus when the size is the spot becomes larger than the mesh size. (D) Domain incorporation diffusion, the particle gets transiently incorporated in a domain in which it diffuses at a different rate. The diffusion coefficient plateaus for FCS spot smaller than the typical size of the domain and then increases with increasing size of the FCS spot. From Schneider et al. (2017).

lipid cargoes. Unilamellar vesicles are often preferred, but most techniques generate also multilamellar vesicles. The multiple layers will affect the mechanical properties of the vesicle. They are classified considering their size and characteristics, either composition or number of lipid bilayers. Depending on the observation method and the membrane properties assayed, different models are used. One of the most common one is the Giant Unilamellar Vesicle (GUV). Its size ranges from a few micrometres to about 100 micrometres, similar to most cells and allows both their observation by optical microscopy and the measurement of their physical parameters by different micromanipulation techniques. GUVs were first produced by gentle hydration (Reeves and Dowben, 1969). A lipid film was deposited on a surface and rehydrated leading to the swelling and formation of vesicles. More recent techniques such as electro-formation and gel assisted swelling have been developed to increase the yield and the ratio of unilamellar vesicles. Small Unilamellar vesicles (SUVs) are vesicles with sizes ranging from 50 to 200 nm, allowing for other applications, notably cryo electron microscopy. SUVs are small enough to be embedded in vitreous ice section and allow electron transmission. They can be formed by extrusion, sonication of freeze thawing. Finally, in between there are Large Unilamellar Vesicles (LUVs) with sizes ranging from 200 nm to 1 µm which can also be observed with cryo electron microscopy. They are formed by either extrusion or vortexing rehydrated lipid films.

Flat membranes

Lipid membranes can display a high variety in sizes and substrates. The most common system is the supported lipid bilayer (SLB), which consists of a large lipid membrane deposited on a substrate of choice, usually glass but also mica or PDMS. Supported lipid bilayers are convenient systems. They are easy to handle, proteins can be added in the chamber and the observation can be performed using TIRF microscopy increasing the signal to noise ratio. The major drawback is the presence of a substrate interacting with the bottom layer which can alter some of the physical properties of the bilayer and impede the diffusion of some transmembrane proteins. To overcome this issue, protocols have been developed to create cushioned membranes, monolayers or even membranes floating between pillars (Richter et al., 2006). The different types of lipid bilayers are displayed in Figure 1.22. The usual protocol used to generate supported lipid bilayers is the fusion of small unilamellar vesicles on a hydrophilic substrate (Tamm and McConnell, 1985). The fusion process is mediated by electrostatic interactions between the vesicles and the substrate. Therefore, lipid charges, pH and ionic strength of the aqueous buffer are crucial to allow the fusion of the SUVs on the substrate. Similarly, the hydrophilicity of the substrate is essential, which makes the cleaning and activation steps crucial in the SLB formation process. Many studies have analysed the best conditions to create SLBs, depending on the substrate, the lipids and external conditions (Lin et al., 2010).

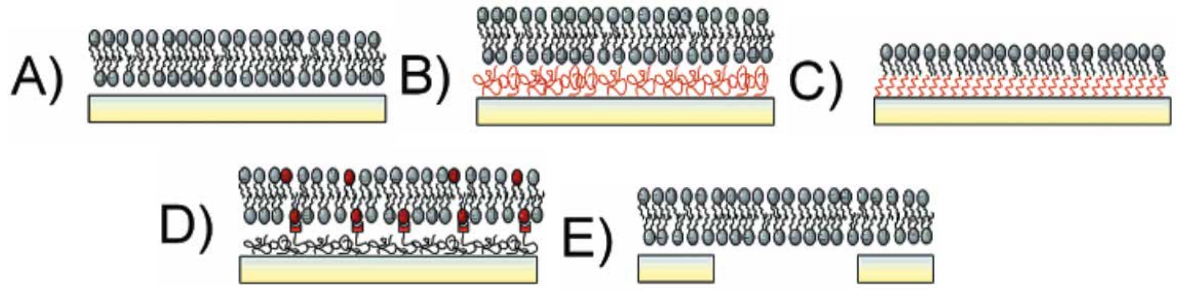

Figure 1.22 – Supported membranes : (A) Solid supported lipid bilayer (SLB). (B) Polymer cushioned bilayer. (C) Lipid monolayer assembled pre-grafted thiols or silanes. (D) Tethered lipid bilayer. (E) Suspended lipid bilayer. From Richter et al. (2006).

1.4 Diffusion barriers

One essential feature that cells have to perform is polarisation. Multiple strategies can exist and a major one is the creation of diffusion barriers. In cells, diffusion barriers can be generated on cellular membranes. Because septins assemble into filaments close to the membrane they were good candidates for proteins involved in the formation of diffusion barriers in cells. I will first present a few examples of known diffusion barriers before introducing the current knowledge about the role of septins in the establishment of diffusion barriers.

1.4.1 Compartmentalisation in cells

The internal compartmentalisation in cells by lipid membranes allowing each organelle to play some specific roles, with the possibility to exchange material with the rest of the cell either through pores or channels or by vesicular transport, has been thoroughly studied. However, many cell types including neurons, photoreceptors and epithelial cells also require compartmentalisation in order to fulfil their role. Cells are very dynamic environments, and this compartmentalisation rarely depends on long lived rigid macromolecular assembly. It depends on continuously remodelled interactions, allowing for cellular plasticity. It means that there is a need to control the transport and diffusion of cellular components in order to maintain the anisotropic distribution essential to partition the cell compartments. Diffusion barriers on membranes allow the formation of different domains. Such barriers can be found in continuous membranes such as the ER membrane and the plasma membrane.

The first example of such barrier is in the epithelial cells. Epithelia consists of a single layer of cells, bound to one another and delimiting body compartments. Their apical side faces the lumen while their basal side faces the internal organ. Their role is to control fluxes of molecules by both preventing the diffusion of free molecules between them and asymmetrically transport specific molecules through the cell sheet. To fulfil this role, epithelial cells are bound by tight junctions at the transition between the apical and basolateral membranes and running all around the junction. These junctions prevent the passage of molecules between cells but also help polarise the epithelial cells by preventing the lateral diffusion of lipids in the plasma membranes (Fölsch, 2008). It could therefore also prevent the lateral diffusion of some plasma membrane associated proteins. It was shown that this barrier is specific to lipids on the external leaflet of the plasma membrane while lipids in the inner layer or that can "flip flop" – transition from the inner to the outer leaflet and vice versa – can cross the barrier (Dragsten et al., 1981; Spiegel et al., 1985; van Meer and Simons, 1986). A sketch summarising the characteristics of this diffusion barrier is displayed in Figure 1.23 A and B.

Most vertebrate cells present a primary cilia. This cilia serves for both signalling and sensing (Singla and Reiter, 2006). It can later be modified into a more complex system as for photoreceptor cones. The ciliary membrane is continuous with the plasma membrane, however, it was shown that FP-GPI – a GPI anchored protein – is excluded in the ciliary membrane hinting at the presence of a diffusion barrier (Vieira et al., 2006). In the flagellum of *Chlamydomonas reinhardtii*, structure highly related to cilia, it appeared that the flagellum membrane and the rest of the plasma membrane have a distinct composition and proteins cannot freely exchange between the two domains (Musgrave et al., 1986). The presence of a diffusion barrier is also hinted by the presence of an electron dense ring at the base of the flagellum (Weiss et al., 1977). These findings suggest that the presence of a diffusion barrier is a common feature for all cilia derivates.

Studies performed on sperm cells have also shown the existence of a diffusion barrier. Sperm cells are partitioned and some certain proteins only locate in one of their compartments (Myles et al., 1981). For example, the CE9 integral membrane protein is located in the posterior tail in immature spermatozoa and can later diffuse into the mid piece after cleavage of its extracellular N-tail (Petruszak et al., 1991). The localisation of CE9 is perfectly delimited by the annulus between the mid piece and the tail, hinting that it can serve as a diffusion barrier (Cesario and Bartles, 1994). However, it is unclear how this cleavage allows CE9 to cross the annulus.

Diffusion barriers within neurons have been observed both at the initial segment of

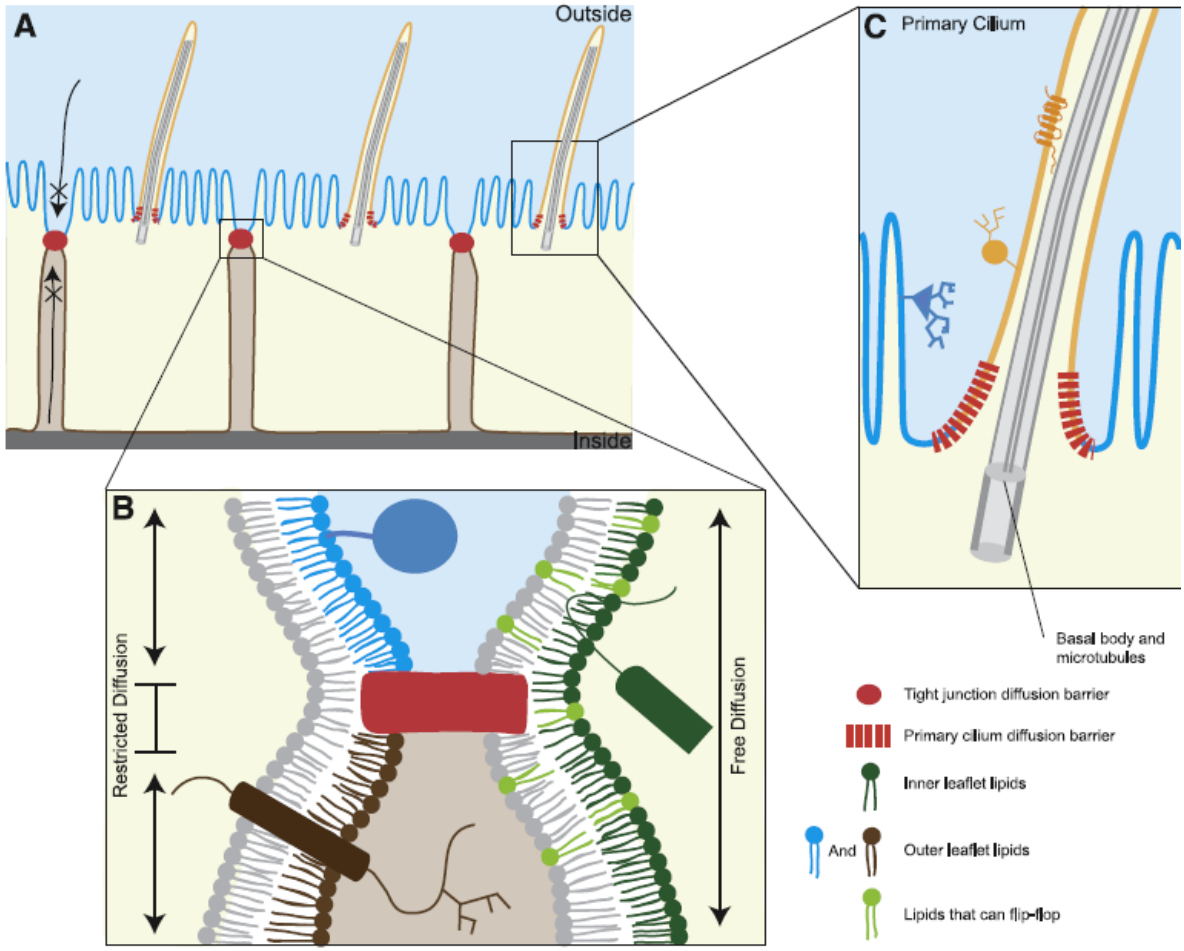

Figure 1.23 – Model of the plasma membrane showing the complexity, with a large variety of lipids, embedded and peripheric proteins as well as the underlying cytoskeleton. From Caudron and Barral (2009).

the axon as well as at the base of dendritic spines. Some proteins, such as Thy-1, are located specifically at the axonal membrane. The lateral mobility of proteins associated with Thy-1 is also reduced at the initial segment of the axon (Dotti et al., 1991). A very strong supportive observation for the existence of a diffusion barrier at the base of the axon was the diffusion of fluorescent lipids. It was observed that fluorescent phospholipids brought to the axonal membrane by vesicle transport would not diffuse into the rest of the membrane (Kobayashi and Simons, 1992; Nakada et al., 2003). In this case, actin depolymerisation leads to the loss of the diffusion barrier, with the loss of compartmentalisation for Thy-1. In dendritic spines, a similar barrier exist at their base. Spines dictate how strong a stimulus activates the neuron. They are dynamic, shrinking and forming back depending on stimulation (Valverde, 1967, 1971). They are therefore involved in memory. To achieve their function, their membrane as well as the cytosol need to be compartmented from the dendritic shaft. The diffusion of membrane targeted GFP as well as AMPA receptor is strongly reduced in the region of the neck of dendritic spines, supporting the existence of a diffusion barrier (Ashby et al., 2006). However, some proteins can still diffuse because the activation of a spine correlates with the reduction of threshold of activation of neighbouring spines. This reduction is explained by the diffusion of activated Ras from the activated spine to the

shaft (Harvey and Svoboda, 2007; Harvey et al., 2008).

Interestingly, as will be discussed later, septins have been later highlighted for their role in the establishment of diffusion barriers in cilia, sperm cells and neurons. However, their involvement in diffusion barriers was first discovered in Saccharomyces Cerevisiae.

1.4.2 Cell division in Yeast

Cell division in yeast Saccharomyces Cerevisiae is an highly asymmetric division, meaning that the daughter cell is created from a bud emerging from the mother cell, while the mother cell keeps a constant size (Pruyne et al., 2004). During cytokinesis, the cytoskeleton polarizes and transports exocytic vesicles to the bud, allowing its growth. Diffusion barriers located at the bud neck and helping retain cell polarity have been described for more than two decade. However, the molecular mechanisms governing their function are still poorly understood.

Three different barriers have been identified, one at the nuclear envelop, one at the endoplasmic reticulum membrane and one at the plasma membrane (Barral et al., 2000; Takizawa et al., 2000; Luedeke et al., 2005; Shcheprova et al., 2008). The first one to be identified was the one associated to the plasma membrane. Takizawa et al. (2000) discovered that Ist2, a protein linking the plasma membrane with the endoplasmic reticulum is only present in the bud, where it can freely diffuse as shown by Fluorescence recovery experiments – Figure 1.24 A. However in temperature sensitive mutants for cdc12 – in which temperature rise induces septin collar disassembly – Ist2 localises also in the mother cell after temperature rise as shown in Figure 1.24 B.

A study performed simultaneously focused on the diffusion of the polarisome and the exocyst complexes. To grow asymmetrically, the cell concentrates the polarisome and the exocyst complexes to the bud in an actin dependent manner (Tarassov et al., 2008). Both complexes can freely diffuse within the bud but cannot diffuse to the mother cell. This was observed by imaging and photobleaching several proteins of these complexes -Spa2 for the polarisome and Sec5p and Sec3p for the exocyst (Barral et al., 2000). In mutants similar to those used in the study on Ist2, both complexes are free to diffuse as displayed in Figure 1.24 C. Finally, after ring splitting, both complexes are confined into the neck region where they can still freely diffuse (Dobbelaere and Barral, 2004). All these results demonstrated the importance of septins in forming a diffusion barrier at the bud neck.

The endoplasmic reticulum is a continuous network of tubules which was shown by fluorescence imaging and photobleaching experiments on GFP targeted to the lumen of ER (Luedeke et al., 2005). It crosses the bud neck during cell division and all ER-membrane associated proteins studied so far -translocon subunit Sec61p, SNARE Sec22p and the HMG-CoA reductase Hmg1p- cannot diffuse through the bud neck. In septin deficient cells, this diffusion barrier is lost.

Budding yeast cells undergo a closed mitosis, meaning that the nuclear envelop remains intact through the anaphase. During anaphase, proteins associated with the inner nuclear membrane can freely diffuse through the bud neck. On the contrary, proteins associated with the outer nuclear membrane such as Nsg1p and Npup49p cannot cross the bud neck (Shcheprova et al., 2008). In septin mutants as well as mutants with defective bud neck organisation, the effect on the lateral diffusion at the bud neck was lost.

These observations show the key role of septins in the compartmentalisation of the

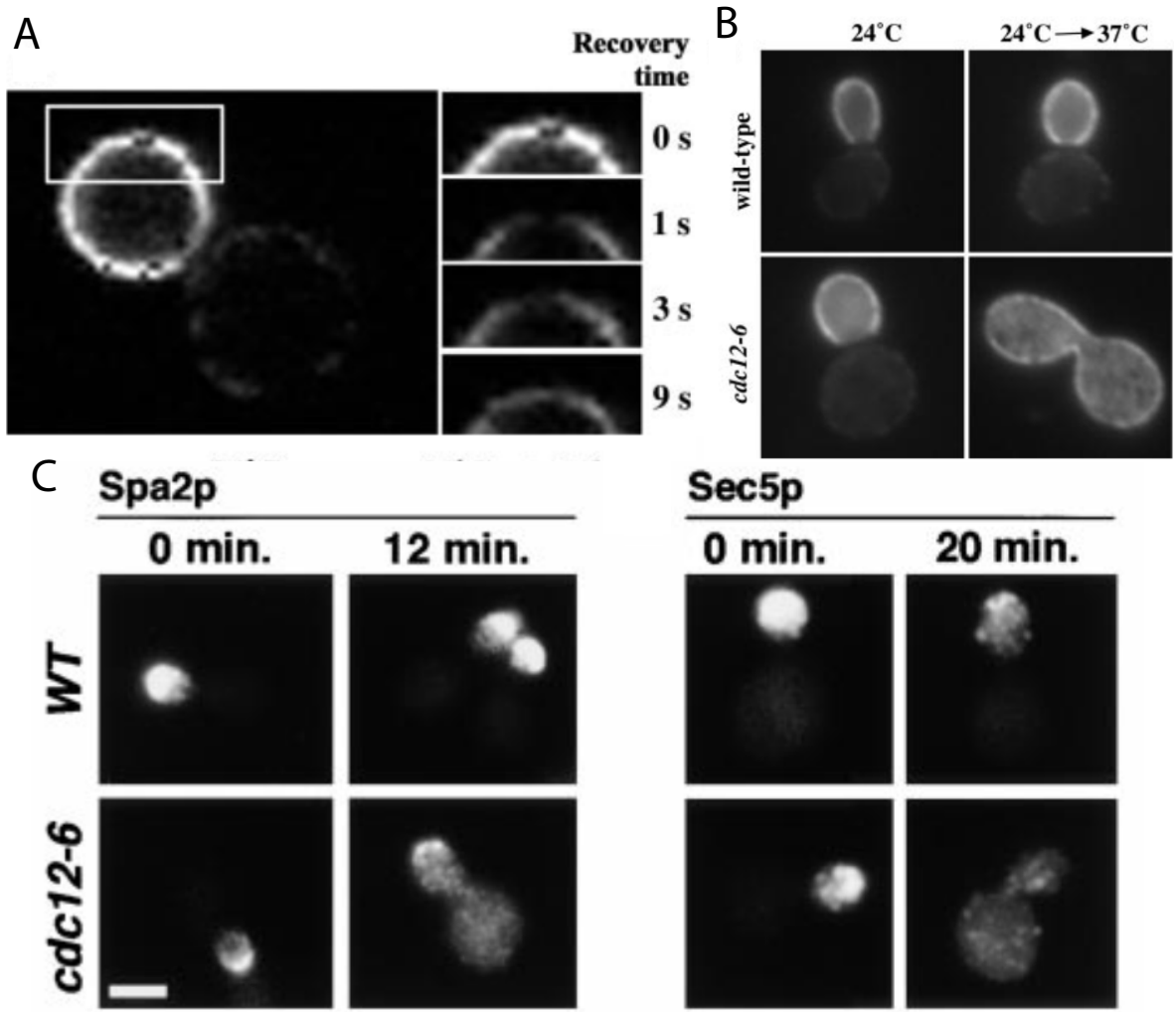

Figure 1.24 – (A) Fluorescence recovery experiment of Ist2, plasma membrane protein in the bud during cytokinesis. (B) Fluorescence images of Ist2 in yeast cells during cell division in wild type and temperature sensitive mutant. From Takizawa et al. (2000). (C) Fluorescence images of components of the polarisome -Spa2p- and the exocyst -Sec5p- in yeast cells undergoing cell division in wild type and temperature sensitive mutant. From Barral et al. (2000).

bud during cytokinesis. However, the mechanisms underlying this compartmentalisation are still poorly understood. Septin filaments could act as a physical barrier, make a scaffold to recruit other proteins that would lead to this compartmentalisation or be implicated in a cascade of events leading to the formation of diffusion barriers.

1.4.3 In other organisms

Since the discovery of the role of yeast septins in the establishment of diffusion barriers, similar implication has been reported in other organisms.

Septins were first shown to be involved in the emergence of diffusion barriers in mouse sperm cells. Looking at the distribution of basigin in both cauda and caput sperm cells, it was observed that in cauda, basigin locates exclusively at the tail – Figure 1.25 A– and in caput sperm basigin localises exclusively at the mid piece – Figure 1.25 B.

The labelling of SEPT4 showed that the distribution of basigin is compartmented at the septin annulus (Kwitny et al., 2010). In SEPT4 knockdown sperm cell, the distribution is homogeneous within the whole sperm cell for both caput and cauda spermatozoa – Figure 1.25 C.

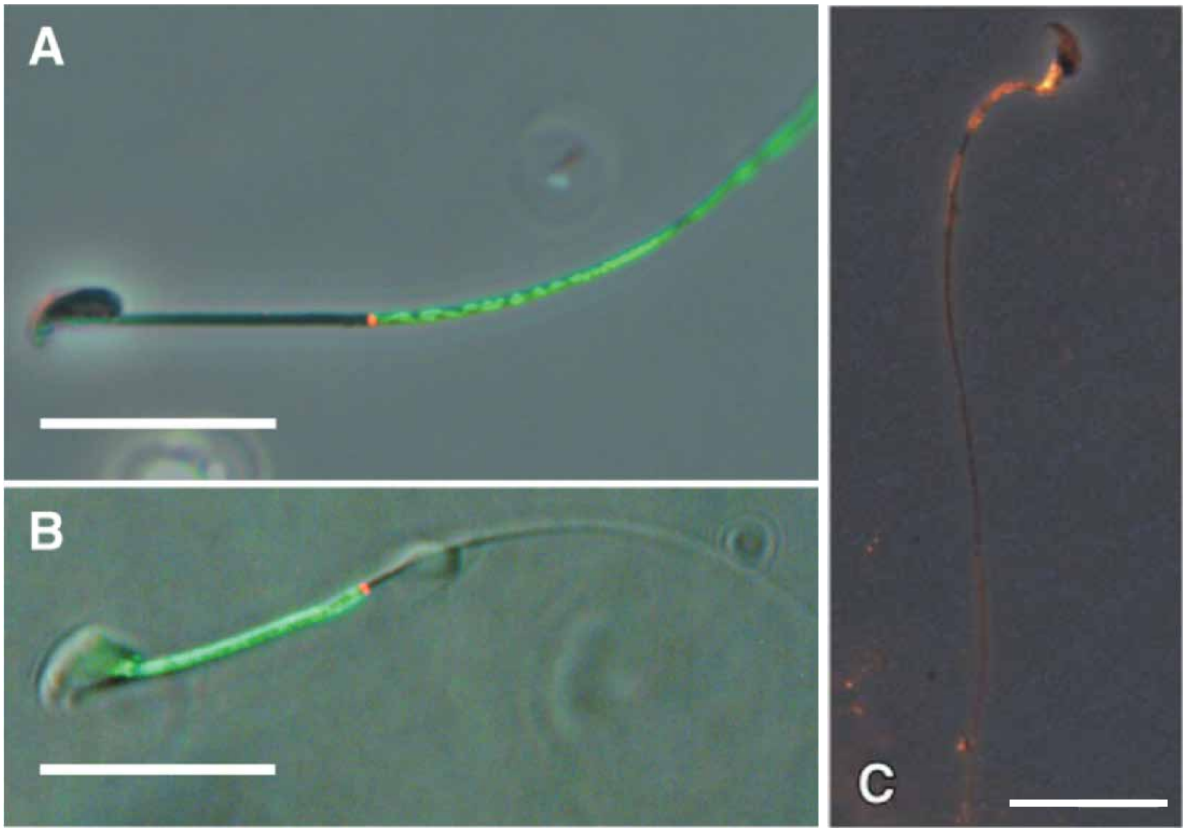

Figure 1.25 – Overlay of fluorescence images of SEPT4 (red) and basigin (green) with transmission light images of (A) caput, (B) cauda and (C) Sept4 knockdown caput sperm cells. Scale bars are 20 µm. From Kwitny et al. (2010).

A study performed in cilia cells also showed the involvement of septins in creating diffusion barriers at the base of primary cilia. The ciliary membrane is continuous with the plasma membrane, and there is no physical separation of the cytosol at the base of primary cilia. However, some proteins such as Sonic hedgehog locate specifically in the primary cilia. Signal transduction in the primary cilia depends on the presence of particular proteins including membrane bound proteins. The diffusion of four of them has been investigated: two G-protein coupled receptor, serotonin receptor 6 Htr6 and somatostatin receptor Sstr3, the membrane anchored tail of fibrocystin PKHD1 and the Shh signal transducer Smo (Hu et al., 2010). All those proteins were labelled with GFP. Fluorescence recovery experiments (FRAP) were performed to observe their lateral mobility. When bleaching half of the cilia, the fluorescence would recover and a reduction of fluorescence in the second half was observed, with the total fluorescence in the cilia being constant. To investigate the role of the septin collar at the base of the primary cilia, the SEPT2 gene was silenced. This resulted in a dramatic reduction of the number of primary cilia in the cell population, only 10-15% of cells having a shortened cilia. Images and analysis from the photobleaching experiments of the whole cilia for both Htr6 and Smo are displayed in Figure 1.26. In the parental strain, no

visible recovery was recorded. For the silencing RNA strain, some recovery could be observed. For all four proteins, the amount of fluorescence recovery after bleaching of the cilia was very significantly increased, highlighting the role of septins in the formation of a diffusion barrier at the base of primary cilia. However these results have not bee repeated yet.

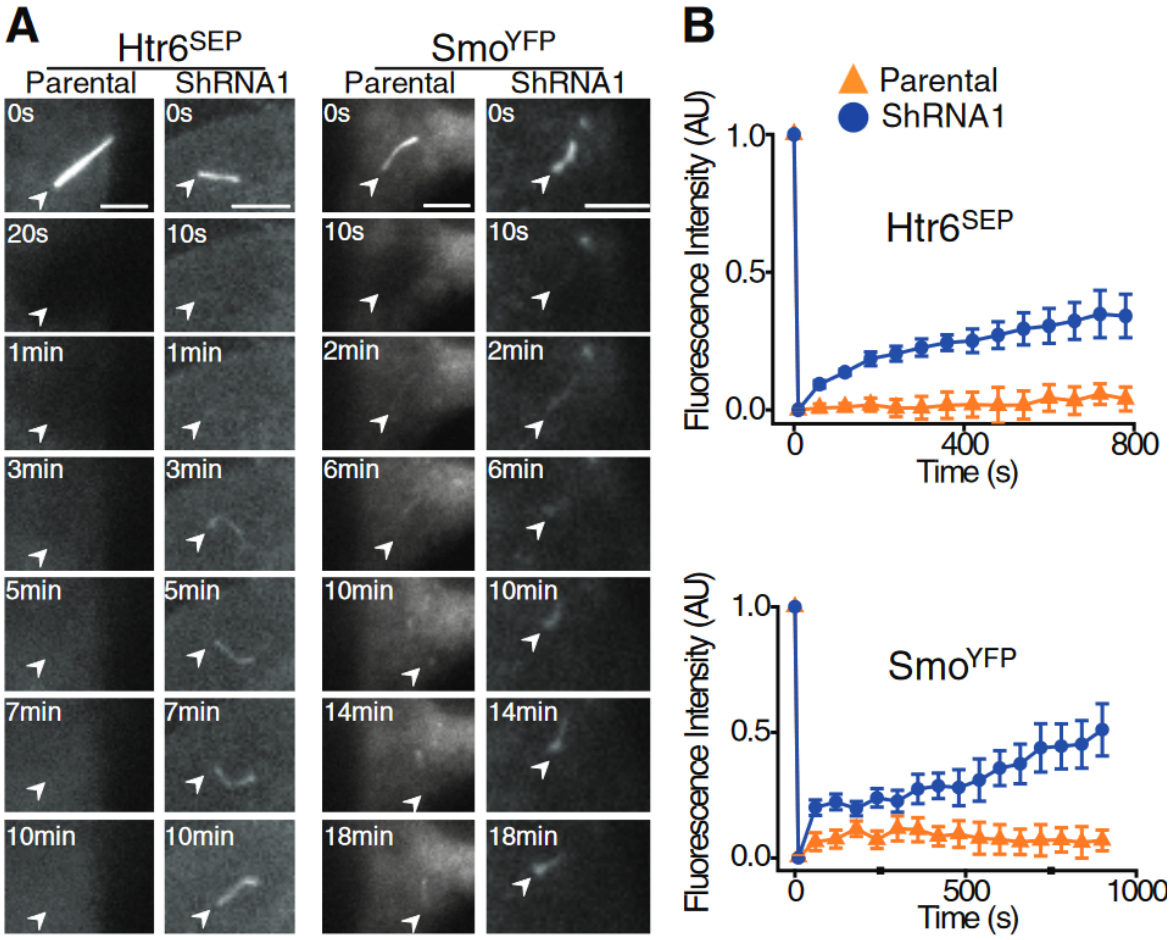

Figure 1.26 – (A) Fluorescence recovery after photobleaching the whole cilium in parental and silenced septin cells. Scale bars are 5 µm. (B) Average fluorescence recovery curves. From Hu et al. (2010).

Most excitatory synapses are localised at the end of spines, protrusions expanding from the dendritic shaft. Typically, the spine head where the synapses are present is separated from the shaft by a long neck. This neck helps regulating the exchange of molecules from the spine head to the dendrite which is critical for the synapses. Considering that septins locate at the base of the spines, their role in controlling the lateral diffusion of membrane proteins has been investigated. Studying the lateral diffusion of AMPARs is important for the strength of synaptic transmission and plasticity of the synapse. It was observed that in SEPT7 positive spines, the lateral diffusion of GluA2 containing AMPARs was slower (Ewers et al., 2014). Performing Fluorescence recovery experiment, it was observed that the transmembrane and the inner leaflet associated proteins have a slower diffusion in septin positive spines, and knockdown of septins lead to higher diffusivity of those proteins.

Recently, a study assayed the diffusion of $PI(4,5)P_2$, a phosphoinositide responsible

for recruiting and activating numerous proteins and complexes involved in many cellular functions such as the regulation of ion channels, endo and exocytosis etc. The distribution and mobility of this lipid has therefore been studied and it was hypothesised that the PI(4,5)P_2 was segregated into pools to achieve different functions (Hammond, 2016). The mechanism for this segregation is not understood completely. Higher densities of PI(4,5)P_2 were observed in regions specific to the regulation of exocytosis, caveolae and clusters of signalling K-Ras4B. It was reported that the synthesis of PI(4,5)P_2 is located at lipid rafts, structures of a few nanometres in diameter with short life expectancy. On the other hand, PI(4,5)P_2 regulates transport, signalling and other functions on ranges of hundreds of nanometres and for time scales up to several minutes, scales much larger and longer than the lipid rafts. By targeting the free PI(4,5)P_2 with the C-terminal region of Tubby, Tubby$_c$, labelled with Photo-activalble mcherry, PAmcherry1, it was possible to follow single PI(4,5)P_2 lipids at the inner ventral plasma membrane of HeLa cells (Pacheco et al., 2022). They studied the diffusion of PI(4,5)P_2 in different structures such as ER-PM contact sites, clathrin-coated structures, adhesion sites, spectrin dense regions and septin dense regions. They found that only in the latter two diffusion of PI(4,5)P_2 was impaired with a stronger effect for the septin dense regions than for the spectrin dense regions.

Those studies have shown the involvement of septins in establishing diffusion barriers, but the mechanisms responsible for this diffusion barrier are still unknown.

1.4.4 Examples of diffusion barrier mechanisms

Septins are not the only diffusion barrier in cells. Other diffusion barriers have been identified for which the mechanisms are well understood.

Because of the importance of micro-domains on the plasma membrane, many studies have focused on the diffusion of different lipids and membrane associated proteins. One well documented model is the "pickets and fence" model, consisting of a mesh of actin filaments and trans membrane proteins linking the actin and the membrane. A sketch of this structure is displayed in Figure 1.27. This structure leads to the well studied "hop movement" of transmembrane proteins. It was also observed that phospholipids were confined in regions that are not lipid rafts. A study performing Single particle Tracking measured the diffusion of DOPE, a lipid that is not associated with lipid rafts, and of TfR, a transmembrane protein (Fujiwara et al., 2016). It is important to note that only the DOPE in the outer leaflet of the plasma membrane could be labelled in this protocol. It was observed that all of them showed typical hopping diffusion with compartments of size similar to the dimensions of the actin mesh as confirmed by electron microscopy. This shows the importance of the cytoskeleton mesh on the diffusion of membrane proteins. To further study the effect of the actin fence, additional cytosolic domains were added to TfR. The initial size of the cytoplamsic domain of TfR was 67 amino acids. The Halo Tag protein was added in single or multiple copies, to obtain a final size of up to 1000 amino acids. Finally those where compared with ACP-TM a conjugation of the acyl carrier protein with a transmembrane domain, resulting in a transmembrane protein with a cytosolic domain of 10 amino acids. Comparing the diffusion coefficient of these different models, it appeared that a significant difference was observed with two halo proteins, and even bigger with three Halo tag proteins, when the cytosolic domain reaches 1000 amino acids. Because the addition of only one Halo tag protein did not change the diffusion coefficient, it shows that for the diffusion

of TfR, pickets play a more crucial role than the cytoskeleton mesh.

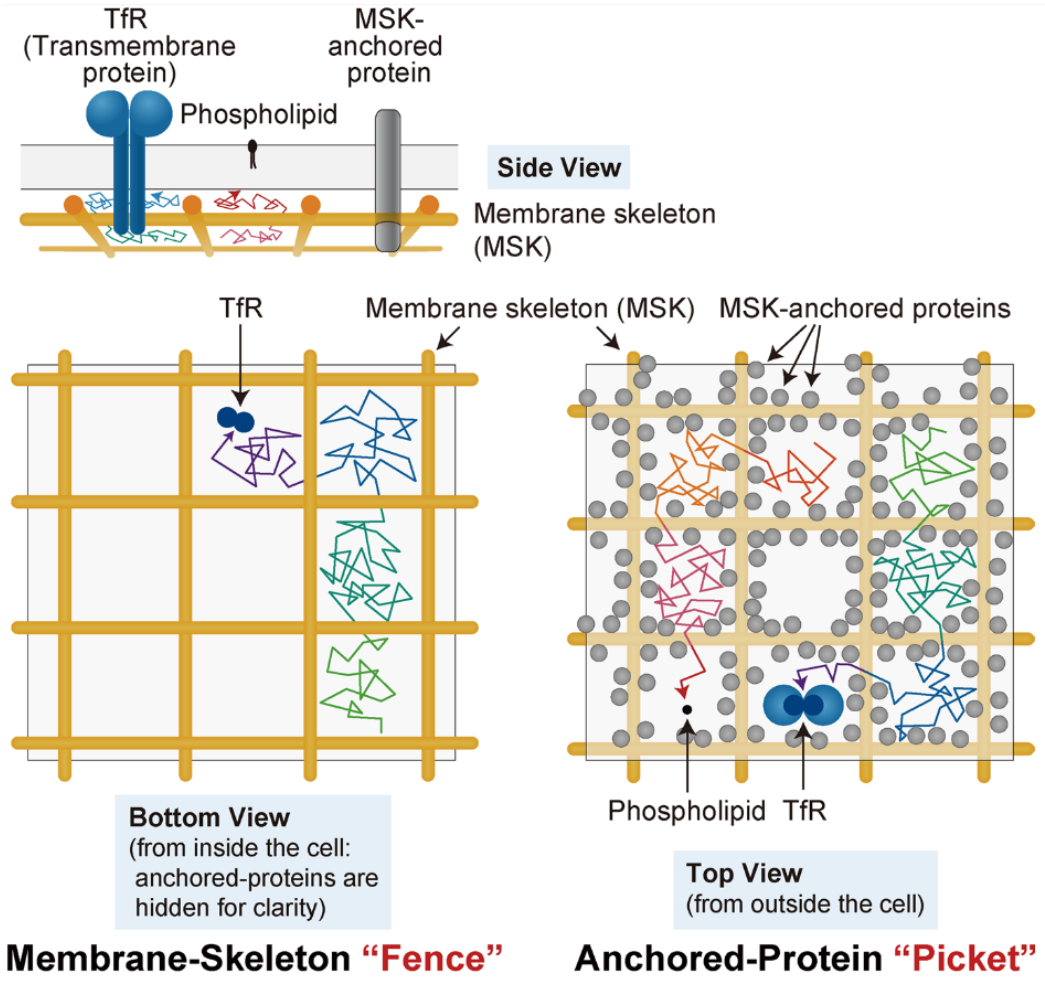

Figure 1.27 – Schematic representation of the picket and fence model of diffusion barrier. From Fujiwara et al. (2016).

The emergence of physical obstacle to the diffusion of membrane components can also be due to the oligomerisation or clustering of proteins. Both oligomerisation and clustering of membrane bound proteins are very important in many processes. During these processes, the interacting proteins will diffuse as one bigger molecule. In a bilayer free of diffusion barrier their diffusion coefficient will be reduced as predicted by the Saffman-Delbrück model (Ramadurai et al., 2009). However, in cells the diffusion coefficient was smaller than expected (Iino et al., 2001), likely due to the effect of the diffusion barriers created by the cytoskeleton and most likely the important decrease of the hoping rate through the pickets described before. It would therefore locally increase the crowding which can result in a smaller hopping rate for other membrane bound proteins and even lipids.

Partitioning of the membrane components can also happen because of the divergent characteristics of different lipids and proteins. Lipid rafts are good examples for such partitioning with the emergence of metastable saturated lipid and cholesterol rich nanometric assemblies (Lingwood and Simons, 2010). Because some proteins interact specifically with specific lipids, the emergence of such micro-domains can impact the diffusion of all membrane components. This has been proposed as the mechanism for

the diffusion barrier at the ER membrane during yeast cell division (Clay et al., 2014). Clay et al. (2014) observed that the establishment of the diffusion barrier was strongly dependent on the sphingolipid synthesis. The exclusion of a vast majority of ER membrane proteins at the bud neck led the authors to conclude that sphingolipids might create a specific domain in this region and exclude most proteins.

Finally, the curvature of the membrane can help enrich some proteins and induce their accumulation at specific places while they would not be able to cross other regions of different curvature. Indeed, some transmembrane as well as membrane binding proteins can recognise specific membrane curvature or even induce some curvature to the surrounding membrane (Peter et al., 2004). Besides, some lipids are more rigid and are less likely to enter regions of high curvature. The length of the lipid tails can also vary. This length can dictate the thickness of the bilayer, and prevents certain transmembrane proteins to enter specific regions (Bigay and Antonny, 2012). When lipids with short length are accumulated – this is the case for the Golgi membrane – the region will be very unfavourable for long transmembrane proteins as well as long tailed lipids.

1.5 Summary of the PhD project

The main goal of my project was to study the role of septins in establishing diffusion barriers. This role has been suggested by various *in vivo* studies. Looking at the localisation of various essential proteins in the specialisation of some cellular sub compartment, it has been observed that septins are often involved in their segregations to specific domains in cells. Those observations have been carried out in many different organisms and cell types. However, in all these reports, no mechanism has been proposed. The first reported diffusion barrier involving septins is established during *Saccharomyces Cerevisiae* cell division. The *Saccharomyces Cerevisiae* septins are the most studied septins and therefore constitute a good model.

To understand the mechanism from which septins could establish diffusion barriers and to determine whether septins could affect directly the diffusion of membrane-bound components, we decided to use an *in vitro* approach. The advantage of this approach is the control of all the biophysical parameters of the system. I used biomimetic membranes combined with purified yeast septins and model membrane components. We wanted to study the effect of the geometry (dimensions of extra membrane size) of membrane bound proteins on their diffusion in the presence of a septin mesh. I studied the diffusion of two different lipids to assess the role of septins on the diffusion of lipids, and four different models mimicking membrane bound proteins.

Additionally, following the project of a former student in the lab, I studied the role of septins in the mechanics of lipid membranes. It has been shown that septins are able to deform lipid membranes, implying that they must impose some deformation to lipid bilayers. However, the mechanical properties of septin meshes have until now escaped proper measurement, and results obtained previously in the lab were very counter-intuitive. I probed the mechanical properties of lipid membranes on top of which a septin mesh was generated.

Chapter 2

Material and methods

To study the role of septins in establishing diffusion barriers as well as their mechanical properties, I prepared biomimetic membranes and purified septins following the protocols that I present below. I will also present the different microscopy methods that I used to study the diffusion of membrane associated components. Finally, I will present the techniques used to study the mechanical properties of lipid membranes.

2.1 Septin purification

Yeast septins were purified from E.Coli extracts by Aurélie Bertin and myself following protocols described previously. Derivatives of pACYCDuet-1 (EMD Biosciences) and pETDuet-1 (EMD Biosciences) carrying respectively cdc3, cdc11 and GFP-cdc10, $(His)_6$-cdc12 were co-transformed into E.Coli BL21(DE3) by heat shock. The resulting co-transformants were plated on an agarose gel containing LB medium, chloroamphenicol and ampicilin. Colonies were then picked and were left to grow at 37°C in LB medium containing 34 mg/mL of chloroamphenicol and 50 mg/mL of ampicilin until they reached an optical density of $A_{600nm} = 1$. They were then induced with 500 mM of IPTG for 20h at 16°C. The cells were then harvested by centrifugation and resuspended in Lysis Buffer (300 mM NaCl, 2 mM $MgCl_2$, 40 mM GDP, 1 mM EDTA, 5 mM β-mercaptoethanol, 0.5% Tween-20, 12% glycerol, 50 mM Tris, Ph = 8). Cells were lysed using combination of lysozyme treatment ($0.5 mg.mL^{-1}$) and sonication in the presence of anti-protease and benzonase. The obtained lysate was centrifuged at 10,000 g for 30 min at 4 ° C. The septin complexes in the supernatant were captured by Ni^{2+} affinity using Ni-NTA agarose beads (Qiagen). After elution with 0.5 M imidazole, 0.5 M NaCl, 50 mM Tris (pH = 8), the eluate was desalted by passage into a PD-10 column (GE Healthcare) to a buffer containing 150 mM NaCl, 50 mM Tris (pH = 8). Two further steps of purification were performed. First, a size exclusion chromatography was performed using a Superdex 200 column (GE Healthcare) in the same buffer as previously. Then the fractions containing the complexes were pooled and submitted to anion exchange chromatography. To perform this second chromatography, the pooled fractions were first desalted using a PD-10 column into a 50 mM Tris (pH = 8) buffer. They were then injected into a Resource Q anion exchange column (GE Healthcare) and submitted to a linear salt gradient, starting from 0 to 0.5 M of NaCl. Typically, septin complexes eluted around 300 mM of NaCl. This concentration of salt prevents further polymerisation of the complexes. The fractions containing septins were aliquoted, flash frozen and kept at -80°C for later use. The concentration

of the samples was measured using a NanoDrop^{TM}. The extinction coefficient for the GFP-labelled octamer is $\epsilon = 291.000\ M^{-1}.cm^{-1}$. The typical yield was 1 mg per litre of culture. The quality of the proteins was analysed by running SDS-page gel displayed in Figure 2.1 C.

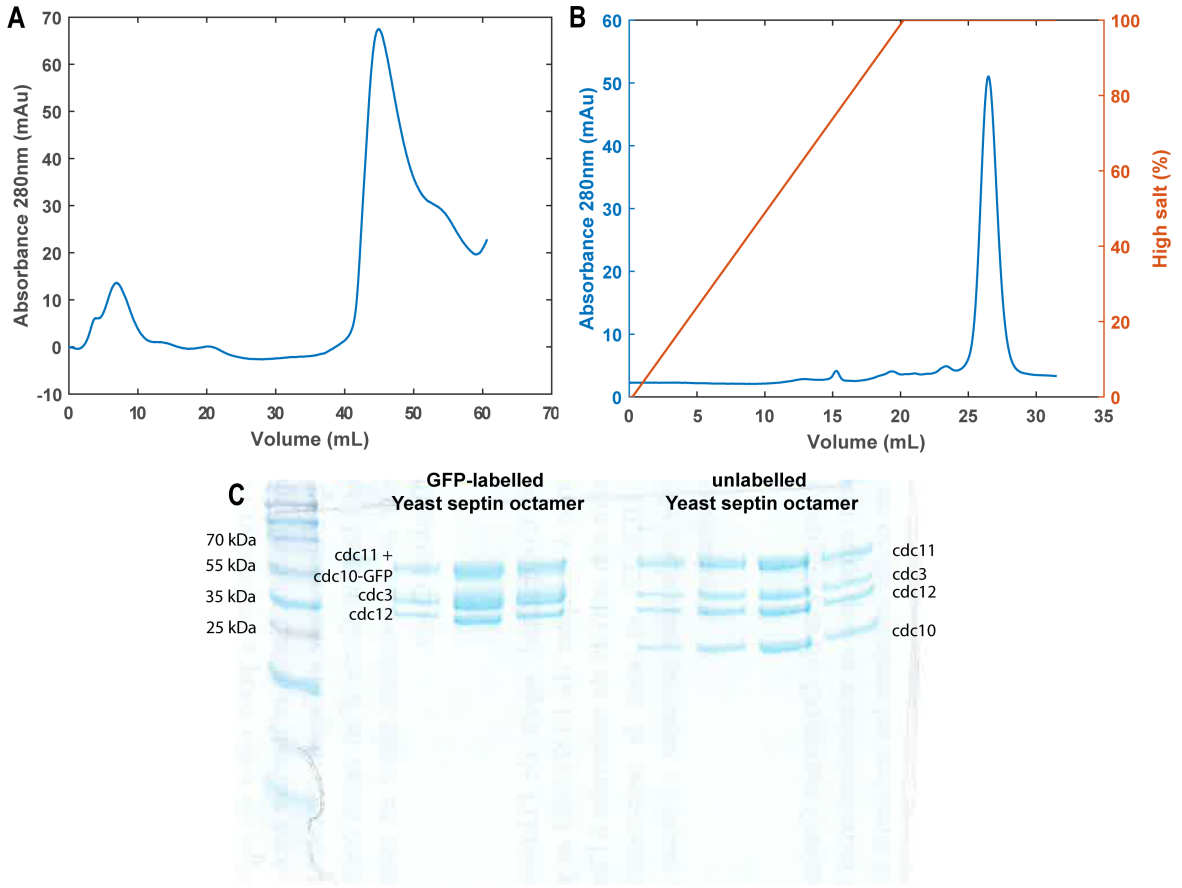

Figure 2.1 – Absorbance of the elution at 280 nm (maximum of proteins) during purification of GFP-labelled septins during size exclusion with superdex (A) and the anion exchange with Ressource Q (B). In (B) the percentage of 500 mM NaCl Buffer injected is also plotted to follow the salt concentration in the column and know at which salt concentration septins are eluted. The system presents a total dead volume of around 10 mL. Septins are usually eluted around 300 mM of NaCl. (C) SDS-page gel performed on the elution fractions after anion exchange. The ladder is in the left column. The group of columns to the left correspond to yeast septins with GFP-cdc10, the right columns correspond to the unlabelled yeast septins.

2.2 Formation of biomimetic membranes

I used both Giant Unilamellar Vesicles and Supported Lipid Bilayers as biomimetic membranes. Using those model systems allows for the control of the biophysical parameters, from lipid composition to concentration of proteins of interest. The lipid composition used in this study was optimised for PI(4,5)P_2 (referenced as PIP_2 in the following text) incorporation (Prévost et al., 2015) as it was shown that the yeast

septins have a strong specificity for this lipid (Bertin et al., 2010; Beber et al., 2019a). The lipid composition was 56.5% EggPC, 15% cholesterol, 10% DOPE, 10% DOPS, 8% brain-PIP_2 and 0.5% of the desired fluorescent lipid -either Bodipy-TR Ceramide, DPPE Atto532 or DHPE Oregon Green.

2.2.1 Formation of Giant Unilamellar Vesicle

Multiple techniques exist to generate Giant Unilamellar Vesicles: electro-formation, gel-assisted swelling and inverse emulsion. During my thesis, I used exclusively the electro-formation and the gel-assisted swelling methods, both methods being routinely used in the lab.

We used buffers containing salt -50 mM- to allow the proper incorporation of PIP_2 in the membrane. When using such salt concentrations, some of the techniques to form GUVs were ruled out as they do not work when using salt in the growing solution. Also, even though the inverse emulsion method using microfluidics has a very good yield and can be used with any buffer, it has the drawback of leaving oil in the lipid membrane, which will modify some of its physical properties and was therefore also ruled out for my project (Faizi et al., 2022).

The "Growth Buffer" (50 mM NaCl, 50 mM Sucrose and 10 mM Tris (pH = 7.8)) and the "Observation Buffer" (75 mM NaCl and 10 mM Tris (pH=7.8)) were prepared. Their osmolarities were controlled with a freezing point osmometer (Löser) and adjusted by adding small amounts of NaCl until their difference was less than 5%.

All lipids are kept in chloroform except for PIP_2 which is kept in a solution of 70% chloroform and 30% methanol. Powders were kept at -80 °C. Once solubilised in chloroform, lipids were stored in amber vials with an argon atmosphere at -20 °C for a period of time depending on their usage and stability. Because of the evaporation at each use, the aliquots of lipids were made in a fashion that the stocks will not be be used too many times – maximum about 10 times.

Electro-formation on platinum wires

The electro-formation method relies on the deposition of a lipid film on two electrodes facing each other in a chamber containing an aqueous solution. I used exclusively platinum wires as electrodes. The method is also commonly used with ITO plates, which gives a better final yield but for which only buffers containing no salt can be used. Some work has been published using ITO plates and growing buffer with salt, however the reproducibility between labs for such technique is quite poor. The advantage of the electro-formation using platinum wires method is that most of the vesicles are unilamellar with minimal defects (Beber et al., 2019a). The principle of the method is presented in Figure 2.2 A. Lipids are deposited on platinum wires which will serve as electrodes. After all the solvent is evaporated, a buffer is added to the chamber and an electrical field is applied between the electrodes. The lipid film swells in the presence of the electrical field and GUVs are generated.

I prepared GUVs by mixing lipids – following the composition presented above – at a concentration of 3 $mg.mL^{-1}$ in chloroform. I typically prepared 50 µL of the lipid mixture. I stored the mixture similarly to the lipid stocks and used it for up to 3 growths.

The Teflon growth chambers in which platinum wires were inserted were custom made. They consisted of three wells through which the wires go along the bottom of

the chambers – see Figure 2.2 B. Before lipid deposition, I cleaned both the chambers and the wires by sonication in a water bath sonicator. First, wires and chambers were disassembled, they were plunged in acetone in the water bath sonicator for 10 min. Then, wires were inserted in the chamber and the assembled wires and chambers were plunged in acetone, then ethanol then water and sonicated each time for 10 min. Between each step they were wiped thoroughly.

Once the chambers were clean, I deposited lipids droplets of about 0.1 µL along the wires. A total of about 5 µL was used for each chamber. The chambers were then placed under vacuum for 30 min to evaporate any trace of chloroform. The bottom of the chambers were then sealed with clean 22*40 mm glass coverslips using vacuum grease. The sides were sealed using paste from Vitrex. The wells of the chambers were filled with 1 mL of the "Growth Buffer" before the top was sealed with another 22*40 mm glass coverslip. The chambers were placed at 4°C and connected to AC generators at 500 Hz with voltage of either 250 mV for 16h growth or 350 mV for 6h growth. Chambers were designed to allow the direct observation of the lipid deposit on the wires at any point in the process with a long working distance 40x objective. The electro-formation process can thus be checked after each step -see Figure 2.2 C and D. After growth, the top coverslip was gently removed and GUVs were collected by gently aspirating at the vicinity of the wires with a cut pipette tip. GUVs must be used quickly after collection because it has been observed that PIP_2 is re-solubilised. Indeed, 3 to 4 hours after the collection of GUVs from the wire, almost no interaction is visible between septins and the membrane.

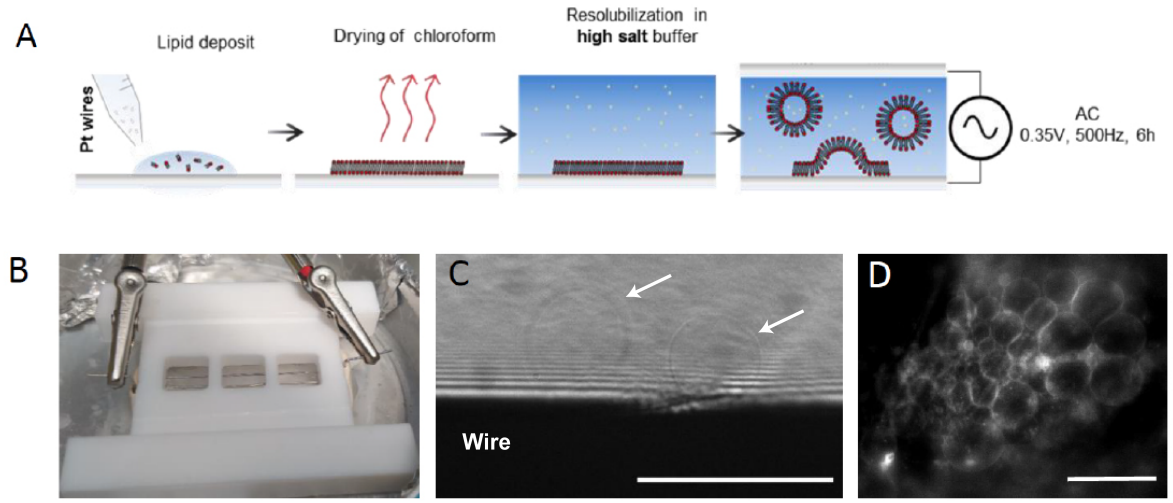

Figure 2.2 – (A) Scheme of the electro-formation on platinum wires process. (B) Picture of the custom made teflon chambers sealed with glass coverslips and Vitrex paste. The platinum wires are connected to a generator. (C) Image obtained with transmission light with a 40x long working distance objective. The dark bottom part is the wire, on top of which two GUVs are distinguishable (arrows). (D) Fluorescence image of the GUVs on the platinum wires obtained using 20x long working distance objective. Scale bars are 100 µm.

Gel-assisted swelling

I used the gel assisted swelling method to prepare quickly large amount of vesicles. Despite its simplicity and wide range of use, the obtained vesicles display more defects and tend to be more multilamellar than those obtained with electro-formation. The principle of the method is presented in Figure 2.3. A lipid film is deposited on a polymer gel. After total evaporation of the solvent, the film and the polymer gel are rehydrated resulting in the spontaneous swelling of the lipid films.

Initially, this method was developed using Agarose gel but polyvinyl alcohol (PVA) can be used as a substitute. I prepared the PVA gel by dissolving 5% PVA into a pre filtered solution containing 150 mM sucrose and 20 mM Tris (pH = 7.8). The solution has to be heated above 90°C for about 30 min for full dissolution of the PVA. The solution was kept at 4°C for up to 6 months. When new coverslips were made, they were placed at 60°C for 10 to 15 min. About 40 µL of gel was deposited on a clean 22*22 mm glass coverslip to create a very thin and even layer on the glass. The coverslips were placed at 60 ° C for 30 min and then stored at room temperature for up to two weeks.

I used the same lipid mixture as for the electro-formation method but at a concentration of 1 mg.mL^{-1}. 10 µL of the lipid mixture were spread on the gel-covered coverslips, which were then placed under vacuum for 30 min to remove any trace of chloroform. The chambers were then rehydrated with 0.8 mL of "Growth Buffer". The swelling happens very quickly. After a a couple of minutes, vesicles with a radius of more than 5 µm could be obtained. However, for a better yield about 1 hour of growth at room temperature is recommanded. Vesicles were collected with a pre-cut pipette tip, aspirating the solution in the vicinity of the gel.

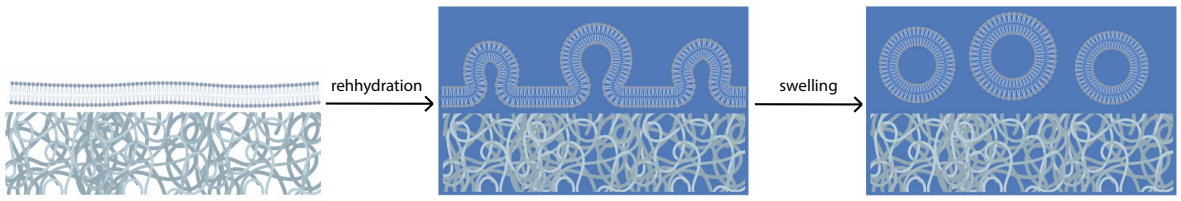

Figure 2.3 – Caption of the gel assisted swelling method. After drying, the lipids form a film on the polymer. Rehydration leads to swelling of the films that results in the formation of vesicles.

2.2.2 Formation of Supported Lipid Bilayer

Supported lipid bilayers are generated by the fusion of Small Unilamellar Vesicles on an hydrophilic substrate. Many protocols have been optimised for the formation of SLBs, they were summarised by Lin et al. (2010).

Formation of Small Unilamellar Vesicles

The principle of SUVs formation is presented in Figure 2.4. A solution of lipids in solvent is dried leading to the formation of a film which is rehydrated. After gentle vortexing, multilamellar vesicles and large vesicles are formed. The solution of vesicles is sonicated, breaking the large vesicles into SUVs.

SUVs were prepared by mixing 0.5 mg of lipids following the composition presented earlier (section 2.2). The lipid mix was then dried under gentle nitrogen flow before being placed under vacuum for 30 min to remove any trace of chloroform. The lipids were then rehydrated in 125 µL of 'SUV Buffer' containing 150 mM NaCl and 20 mM Citrate (pH = 4.8) for 30 min. The solution was vortexed for a few seconds until it became opaque and then sonicated in a water bath sonicator (Elmasonic s10) for 5 to 10 minutes until it becomes transparent again. The SUVs were then aliquoted in 25 µL aliquots which can then be stored for up to 4 weeks at -20°C.

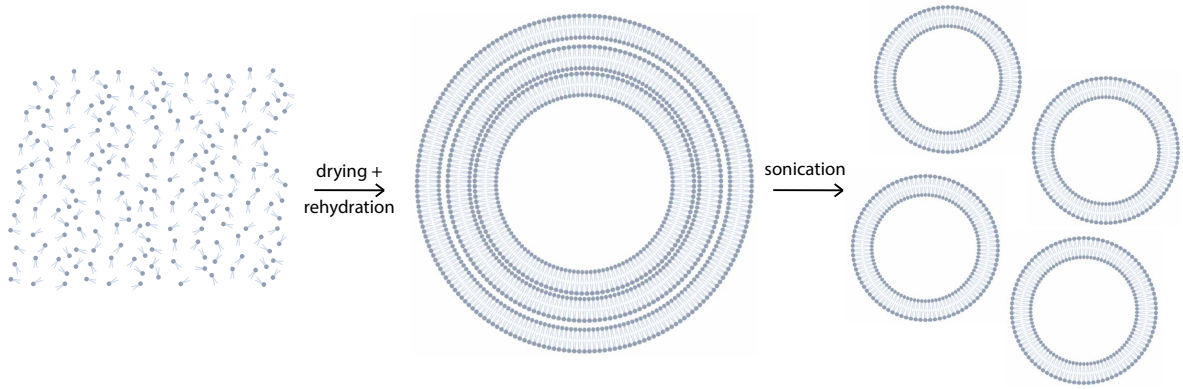

Figure 2.4 – Scheme of the SUV formation process, starting from a mixture of lipids in chloroform. After drying and rehydration, MLVs are formed and are then broke down into SUVs by sonication.

Fusion of SUVs to the substrate to form Supported Lipid Bilayers

There has been intensive work done to achieve better reproducibility of lipid bilayers. Multiple parameters are important to obtain good motility of the lipids in the supported bilayer. The cleaning and activation procedures for the bilayers are important. They can determine the final quality because even small traces of contamination on the substrate can prevent the formation of the bilayer or diminish its mobility. Addition of $CaCl_2$ in the buffer used for the fusion of the SUVs on the substrate can enhance the interaction between, them improving the fusion rate. However, it can also lead to the presence of small vesicles attached to the bilayer. Therefore, a careful use of $CaCl_2$ at small concentration can improve bilayers quality, but should be avoided if not necessary. Finally, the ability to fuse on the substrate also depends on the lipid composition because the interaction between the substrate and the lipids depends on their charge, and the fusion rate on the rigidity and viscosity.

During my thesis, I deposited lipid bilayers on both mica and glass depending on the studied lipid as will be explained in section 3.1.4. The glass coverslips were cleaned by sonication in a water bath sonicator using first acetone, then ethanol, then water. The coverslips were then activated by either plasma exposure for 2 min or by 10 min sonication in 1 M KOH.

When using mica, the mica was freshly cleaved into a very thin sheet and placed on top of a clean glass coverslip. The chambers were made using custom made teflon chambers -cylinders with 1 cm in height and with internal diameter of 6 mm- that were sealed on top of the glass coverslip or the mica using vacuum grease. For mica, the leakage was often an issue. I unsuccessfully tested adding NOA glue to stick the mica

on the glass coverslip. Finally, a careful cut and cleavage of the mica sheet to prevent small cracks on the edges and a very thin layer of mica (less than 50 µm) seemed the best strategy to perform this experiment. One aliquot of SUVs was thawed for each bilayer and diluted in 125 µL of "SUV Buffer" to reach a final lipid concentration of 0.7 mg/mL. The obtained solution is then added in the chambers and left to incubate at room temperature for 30 min. The chambers were then washed thoroughly by pipetting 5 times with the "SUV Buffer" and another 5 times with the "Observation Buffer". The washing steps are crucial for obtaining good bilayers. If the washing is not performed with strong enough flows, detachment of vesicles for the bilayer will not be efficient enough. On the contrary, if during pipetting bubbles are created, they will locally disrupt the bilayer. The obtained bilayers were used immediately. When septins were added, they were left to incubate for 30 min and then either observed with septins still in the solution or washed away with another 3 to 5 washes with "Observation Buffer".

2.3 Prepation of proteo-GUVs containing aquaporin

The principle of the incorporation is presented in Figure 2.5. The aquaporin stabilised in detergent is added to pre formed SUVs that are destabilised by the addition of detergent. The aquaporins are therefore able to incorporate in the SUVs and stabilise with detergent removal. The proteo SUVs were then mixed with other SUVs and the electro-formation protocol was applied to form proteo GUVs.

To study the diffusion of transmembrane proteins, I had to create membranes with incorporated proteins. I chose to use GUVs rather than SLBs to prevent any effect on the diffusion of the transmembrane proteins that might come from the friction with the substrate. The preparation of GUVs containing transmembrane protein has been widely studied and protocols to enhance the yields obtained have been proposed. However, the reproducibility is always challenging between different experiments because many parameters -effects from the geometry of the chamber, charges of the lipids, conditions during drying - are not fully understood. For this study, I chose the protocol using electro-formation on platinum wires. Other protocols exist, but for my purpose I needed unilamellar vesicles in high salt conditions and with minimal defects.

2.3.1 Purification of aquaporin

The aquaporin 0 (AQP0) was purified by Stéphanie Mangenot and John Manzi using bovine eye lenses. The bovine lenses were flash frozen in liquid nitrogen and stored at -80°C for later use. After slow thawing at 4°C in 10 mM Tris (pH = 8) 5 mM EDTA 5 mM EGTA and protease inhibitor mix, the nucleus and the cortex were separated. Only the cortex was then grinded with Potter-Elvehjem of smaller and smaller diameter. The obtained solution was then washed, ultra centrifuged (45 min at 55,000 rpm) and resuspended in a succession of different buffers, first : 10 mM Tris (pH = 8) 4 mM Urea, second : 10 mM Tris (pH = 8) 20 mM NaOH, third : 10 mM Tris (pH = 8). The solution was solubilised in 4% (w/w) Octyl β-D-Glucopyranoside (OG) for 3h at 4 °C. After ultra centrifugation (20 min at 200,000 g) the supernatant is added to an ion exchange mono-S column (Amersham Biosciences) pre equilibrated with Tris 10 mM (pH = 8) 1.5% OG. The protein is eluted with a gradient from 0% to 100 % of buffer containing Tris 10 mM (pH = 8) 350 mM NaCl 1.5 % OG. Fractions containing aquaporin were pooled together and injected onto a size exclusion column Superose 12

10 / 300 GL (GE Healthcare). Column was pre equilibrated with 10 mM Tris (pH = 8) 150 mM NaCl 1.5% OG. The protein was then concentrated using centricon with a size threshold of 3 kDa (Millipore). The final concentration was measured with a spectrophotometer UV-visible NanoDrop^{TM} looking at the absorbance of the protein solution at $\lambda = 280$ nm. The extinction coefficient of the aquaporin at this concentration is $\epsilon_{AQP0} = 1.39$ cm^2.mg^{-1}. The proteins were checked by running SDS-page gel.

2.3.2 Incorporation in SUVs

SUVs are prepared following the protocol in section 2.2.2. To incorporate the aquaporins into the SUVs, a detergent is added at a concentration comprised between R_{sat} corresponding to the beginning of the solubilisation of the SUVs and R_{sol} corresponding to the full solubilisation of the SUVs and the micellar state. I used Octyl β-D-Glucopyranoside at a concentration of 40 mM to the SUV solution. Aquaporins were then added with a weight ratio of proteins to lipids of 1:100. The solution was left at 4°C for 1 hour. To remove detergent, a total weight ratio of 20/1 Biobeads/detergent was used (Rigaud et al., 1998). They were first cleaned using methanol and rinsed with MilliQ water. The addition of Biobeads was performed in three steps with 1h incubation at 4°C between each of them. After each step, the supernatant was collected and the beads were discarded. After the last step, the proteo-SUVs solution was aliquoted, flash frozen and kept at -80°C for further use.

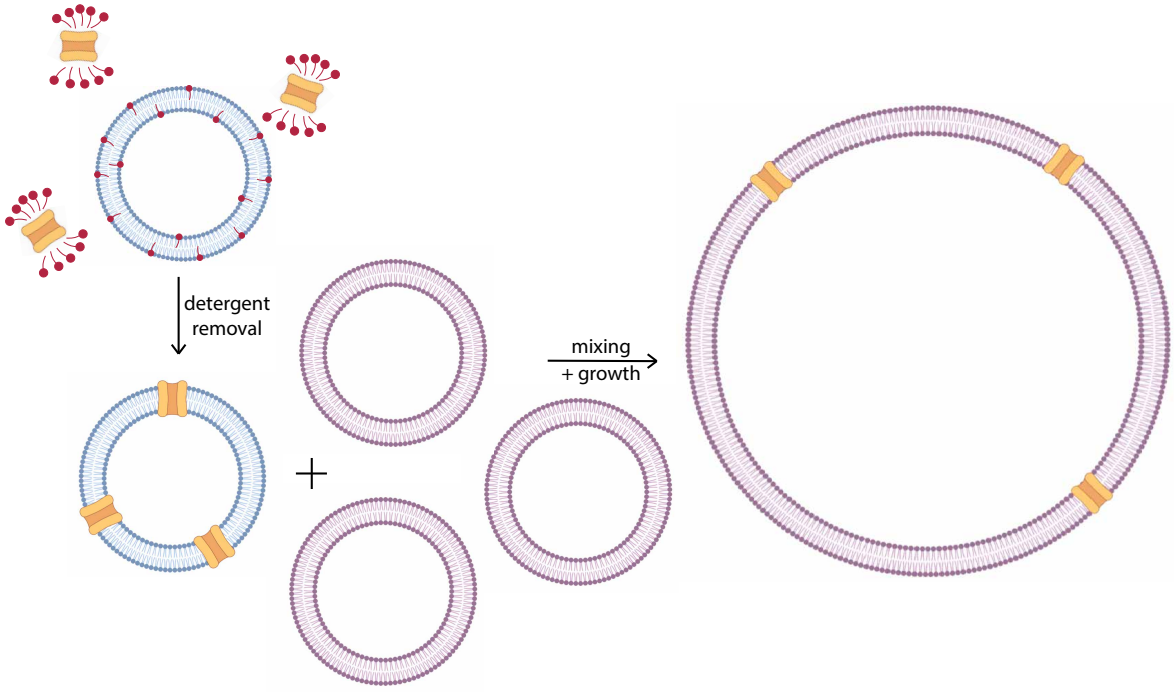

Figure 2.5 – Scheme of the formation of GUVs containing transmembrane proteins. Proteins kept in detergent are mixed with SUVs pre incubated with detergent. Upon removal of the detergent, proteins will incorporate in the membrane. The obtained SUVs are mixed with other SUVs containing desired fluorescent lipids before the electroformation protocol is applied. Schemes are not scaled, GUVs typically have radii 100 times bigger than SUVs.

2.3.3 Electro-formation of the proteo GUVs

SUVs containing aquaporins were mixed to SUVs containing fluorescent lipids. The ratio of SUVs used was adjusted to reach single molecule densities in order to perform single particle tracking on the aquaporins – the volumetric ratio was ranging from 1:100 to 1:500, see section Single Particle Tracking. After mixing, I deposited small drops of the SUV solution on the platinum wires using a pipette. The chambers were then left at room temperature for 30 min before closing and connecting them to AC generators similarly as in section "electro-formation on platinum wires".

The yield for proteo GUVs production is notoriously low. I tested different approaches to improve it. The deposition and the drying steps are crucial in order to obtain a maximum yield of GUVs. By decreasing the amount of salt in the SUV solution just before deposition, the formation of salt crystals was avoided which resulted in a more homogeneous deposition -see Figure 2.6. Finally, I changed the size of the drops deposited on the wire as well as their propensity to spread along the wires. To change the spreading, I placed the wires in an air plasma for 2 minutes before deposition of the drops. Finally, it appeared that the best conditions seemed to be bigger drops (0.2 mL) without air plasma treatment to prevent them from fusing together.

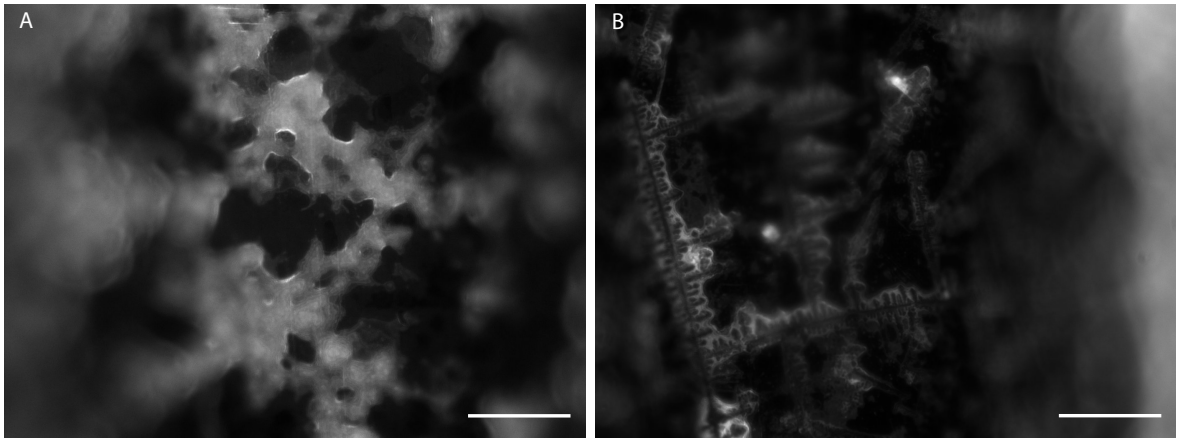

Figure 2.6 – (A) Fluorescence image of lipids after deposition and drying of proteo-SUVs on the platinum wire when the buffer is kept at low salt for the SUV mixture. The image was obtained with a 40x long working distance objective and a LED lamp associated to filters to recover the fluorescence. (B) Similar image when the SUV mixture contains 75 mM of NaCl. Upon drying, salt crystals form. When adding the 'Growth Buffer', these crystals dissolve and most of the lipids go back into solution. Scale bars are 100 µm.

2.4 Formation of wavy substrates

To assess the ability of septins to sense curvature, we used wavy substrates. Wavy substrates were prepared by Luca Pellegrino and Joao Cabral from Imperial College in London as described in Chiche et al. (2008). Briefly, PDMS slabs were prepared by mixing selected base to crosslinker with a ratio of 1:10. Solution was then degassed for 15 min under vacuum and casted on a glass plate at room temperature and left for 3h. The mixture was then thermally cured in a convection oven at 75°C.

Coupons of 2x3 cm^2 were cut from the cured PDMS slab with a thickness of 2.5 ± 0.2 mm. The coupons were clamped onto a strain stage and strained before oxydation. The oxydation was performed using a 40 kHz plasma chamber (Diener FEMTO) at an oxygen pressure of 1 mbar and a power of 20 W.

Upon plasma exposition, Si-CH_3 groups were changed to SiO_x, creating a layer with a thickness of about 10 nm with glass like properties. This region had different mechanical characteristics when compared to the bulk PDMS. Upon release of the strain, the mechanical frustration is released into vertical deformations resulting in a sinusoidal pattern with wavelength ranging from 0.1 to 10 µm. The adjustment of the strain, the power, the gas pressure and the irradiation allowed the fine tuning of the wavelength and the amplitude of the sinusoidal pattern. For the observation of the organisation of septins on such wavy substrates, we chose 3 $µm^{-1}$ for the curvature of the substrate. The wavelength was chosen to be around 2 µm in order to be higher than the typical size of a septin filament. The amplitude was therefore about 250 to 300 nm to obtain the desired curvature.

2.5 Observation and micromanipulation of GUVs

To study the interaction of septins on lipid membranes and the diffusion of different membrane associated components, I had to visualise and be able to manipulate the vesicles in a chamber suited for optical microscopy and allowing manipulation of the GUVs.

A 5 $mg.mL^{-1}$ solution of β-casein was prepared in the "Observation Buffer". It was used to passivate all glass surfaces to prevent bursting of GUVs on the surfaces due to strong interactions as well as to limit the interaction between septins and glass.

The chamber for observation consisted of two glass coverslips glued with vacuum grease on a spacer with a thickness of 1 mm while the sides were left open. A picture of the observation chamber is shown in Figure 2.7 B. The bottom coverslip was 30*11 mm, the top one 35*9 mm. The difference of width between the top and bottom is important to later insert the micropipette from the side. The solution of β-casein was injected in the chamber and left for 30 min to fully passivate the glass coverslips.

To manipulate the GUVs, I used micropipettes that can gently aspirate vesicles, allowing their manipulation. Micropipettes were made from glass capillaries pulled using a pipette puller P-2000 (Sutter Instruments). They were then forged using a MF-830 microforge (Narishige) to obtain the desired opening size (about one forth of the diameter of the vesicles corresponding to 5 to 10 µm). They were then filled with the β-casein solution with home made syringes using a thin glass capillary as a needle. The micropipettes were then connected to a water tank which can be moved vertically to control the pressure inside micropipettes. A picture of the experimental set-up with the water tank (arrow) is displayed in Figure 2.7 A. The micropipettes were then fixed on a micromanipulator (Narishige) and inserted inside the observation chamber. The micropipette inserted in the observation chamber can be seen in Figure 2.7 C. This setup allows the micropipette to stay immobile compared to the objective, while the stage can still move. Finally, using micropipette aspiration, it is possible to obtain the mechanical characteristics of the membrane as described in section 2.8.1.

The β-casein solution was removed after incubation and the GUV solution could be added after dilution in the "Observation Buffer". The ratio for dilution depended on the yield of growth. Typically a ratio of GUV solution to 'Observation Buffer' of 1:2 was

used for the electro-formation on platinum wires technique, and 1:10 for the gel-assisted method. After the sample injection in the observation chamber, the vesicles were left to sediment for 10 to 20 min before their observation. When septins were added, they were first diluted to reach the same osmolarity as in the "Observation Buffer" and mixed with the GUVs just prior to the injection in the observation chamber.

To observe GUVs, the focus was set at about 10 µm above the glass slide to have the best chance of observing vesicles with transmission light. Upon finding a GUV, the micropipette was brought in close proximity of the GUV and pressure inside the micropipette was lowered by bringing the water tank down a few millimetres up to one centimetre. After the GUV was captured by the aspiration of the micropipette, I gently lifted it from the glass coverslip by adjusting the height of the micropipette with the micromanipulator.

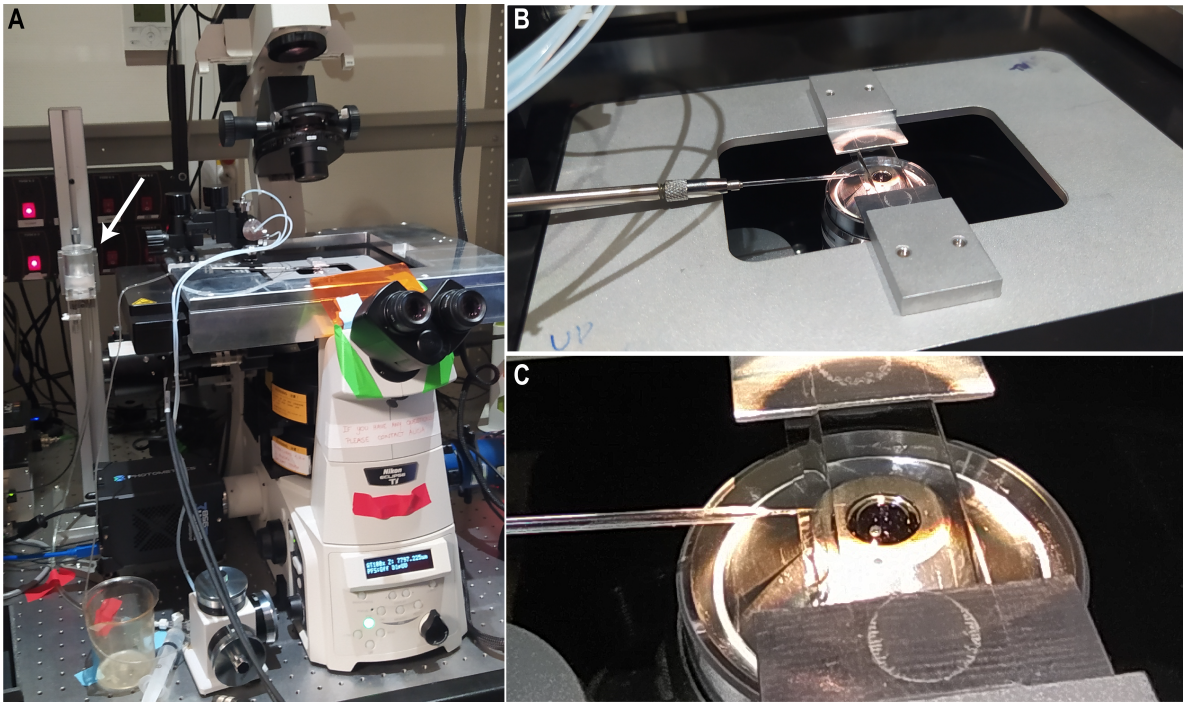

Figure 2.7 – (A) Picture of the experimental setup. On the left of the microscope, you can see the water reservoir (arrow) which can be moved vertically to control the internal pressure in the micropipette. (B) Picture of the observation chamber, with a micropipette inserted between the two glass slides. The micropipette is attached to a micromanipulator fixed on an aluminium frame. This frame is fixed on the static part of the microscope. (C) Zoom on the micropipette tip inserted inside the observation chamber.

2.6 Optical microscopy techniques

To visualise the membranes and the septins interaction with the membrane, I used different optical microscopy techniques. Fluorescence imaging is necessary to observe the dynamics of both membranes and proteins, however, many different techniques can be used. I used both confocal and Total Internal Reflection Fluorescence (TIRF) microscopy to observe respectively GUVs and SLBs. I present the methods below.

2.6.1 Confocal microscopy

Confocal microscopy allows better vertical sectioning of the sample as compared with wide field imaging, making it a good tool to obtain 3D reconstruction of objects. It is widely used to image GUVs. A laser is focused on the observation plane, and a pinhole is conjugated to the same focus point to filter the out of focus fluorescence signal. The signal is then collected by an avalanche photodiode. A schematic representation of a confocal microscope is displayed in Figure 2.8. The resolution is still limited by diffraction. It depends on the Point Spread Function and can be computed in wide-field microscopy using Rayleigh's criteria as:

$$d_{xy} = \frac{1.22\lambda}{2NA} \; ; \; d_z = \frac{2\lambda n}{NA^2} \tag{2.1}$$

Where λ is the wavelength of the emission light, NA the numerical aperture of the objective and n the refractive index of the medium between the sample and the lens.

In confocal microscopy on the other hand, the illumination is not homogeneous. To calculate the resolution, the Point Spread Function of the excitation should also be considered. The final intensity profile is the multiplication of both the excitation and emission PSF. In theory, it is therefore possible to reduce the resolution limit in all directions by a factor of about $\sqrt{2}$. In practice, the pinhole is not infinitely small and a improvement by a factor of 1.3 is more realistic.

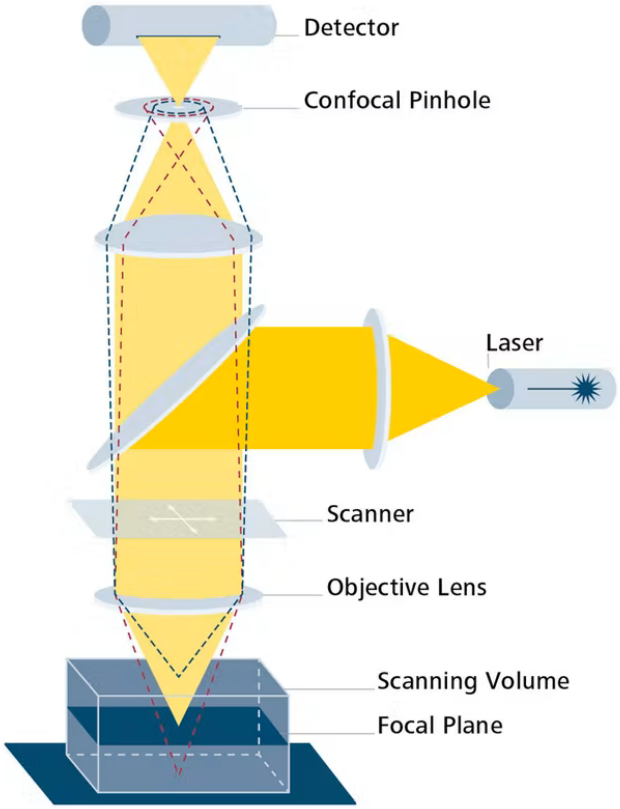

Figure 2.8 – Schematic representation of a confocal microscope. A laser is used for illumination and focused in the sample point. Galvo mirrors allow fast scanning of the sample. The fluorescence signal is recovered and the out of focus background is filtered through a pinhole. Image from Zeiss.

As opposed to wide-field imaging where the whole sample is illuminated at once, the confocal method relies on point by point scanning of the sample. The improvement in signal to noise ratio is a trade-off to the slower acquisition. It is therefore poorly suited to recover dynamics. One way to solve this issue of slow scanning is to use spinning disk microscopy. The general principal of out of focus background rejection is the same, but the acquisition is parallelised using an array of micro-lenses on a rotating wheel. A similar wheel containing pinholes conjugated to the array of focused points is synchronised with the first wheel. The fluorescent signal is now collected on a camera. A schematic representation of a spinning disk confocal microscope is displayed in Figure 2.9. With this technique, the acquisition time for an image can be decreased to about 10 ms. Both techniques were used to image GUVs, but only spinning disk was used to perform fluorescence recovery experiments as it could reach the exposure time necessary for such technique -see section 2.6.3.

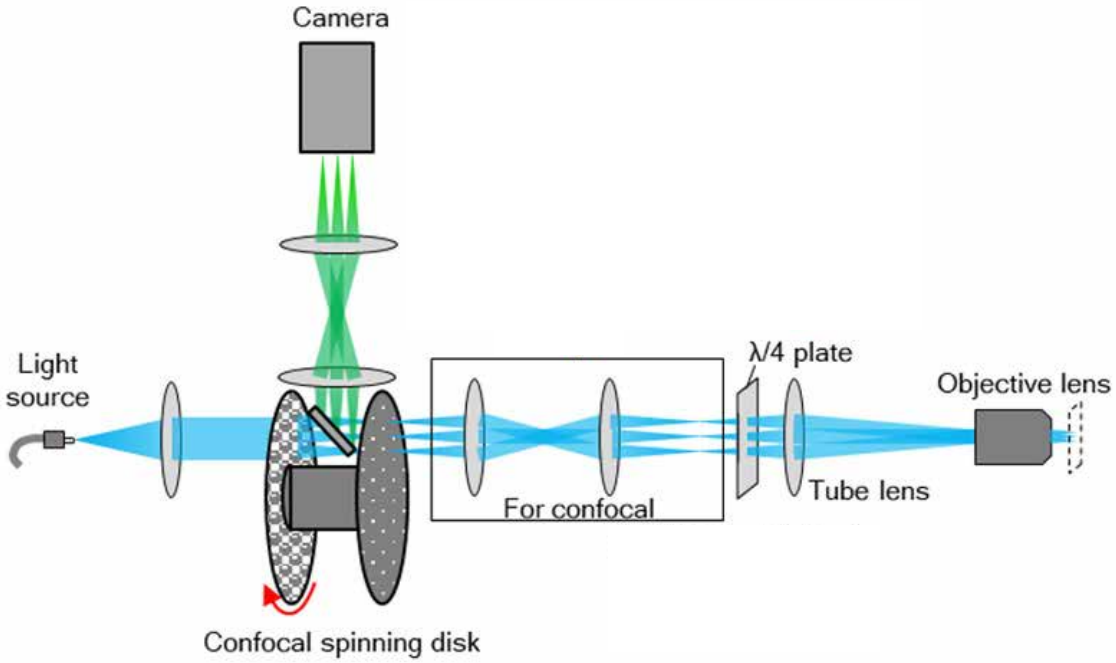

Figure 2.9 – Schematic representation of a spinning disk microscope. A laser is collimated and illuminates a rotating wheel containing an array of micro-lenses. This wheel is synchronised with a wheel containing pinholes. A set of lenses (the $\lambda/4$ wave-plate is often used for changing the polarisation of the illumination light) then collimates all the laser beams to illuminate the back focal plane with an angle from the axis of the objective. This angle will create an xy deflection of the focus point in the plane of the sample. The illumination signal is then collected by the objective, goes through the same set of lenses and the wheel containing the pinholes. The signal is then recorded on a camera to reconstitute the image.

Assuming a uniform binding of septins on the membranes, I approximated the density of septins from the measured fluorescence signal in the corresponding channel. To this end, some calibration is required. A solution of GFP at a known concentration is imaged with the same parameters – laser power, gain, exposure time etc. – as the ones used for imaging the septins in the experiment. I then imaged in the same con-

ditions GUVs with a fluorescent lipid at a known molar ratio and a solution of SUVs with the same fluorescent lipid at a known final concentration. Those calibrations were performed at different concentrations to make sure that the fluorescent signal varied linearly with the concentration in the range of interest. The two solutions are used to convert the signal in the lipid channel into similar density for the protein channel. The density in the protein channel can therefore be computed as:

$$D_{sept} = \frac{S_{sept}}{I_{sept}} \tag{2.2}$$

Where D_{sept} is the septin density, S_{sept} is the signal in the septin channel and I_{sept} is the intensity per unit of density on a vesicle. This intensity can be obtained using the conversion factor and the intensity per unit of density of the lipids:

$$I_{sept} = I_{lipids} * f \tag{2.3}$$

Where I_{lipids} is the intensity of chosen fluorescent lipids per unit of density and f is the conversion factor computed as:

$$f = \frac{\sigma_{sept}}{C_{sept}} * \frac{C_{lipids}}{\sigma_{lipids}} \tag{2.4}$$

Where σ is the signal from the bulk solution and C the concentration in the bulk solution respectively. In the imaging conditions and range of concentration, this conversion factor was independent of the concentration of both lipids and septins.

The confocal microscope consisted of an Nikon TE-Eclipse inverted microscope with three laser lines ($\lambda = 488$ nm; $\lambda = 561$ nm and $\lambda = 647$ nm) combined with a Nikon-C1 confocal head. FRAP could only be performed by successive scans in an appropriate region and was therefore slow (more than a few seconds to bleach a region of 10 μm^2). Micropipette holders were mounted on the stage of the microscope and associated to water tanks to control pressure inside the micropipettes.

I used a spinning disk confocal microscope from the Nikon imaging centre. It consisted of Nikon TE-Eclipse inverted microscope with four laser lines ($\lambda = 405$ nm; $\lambda = 488$ nm; $\lambda = 561$ nm and $\lambda = 647$ nm) combined with a CSU-X1 (Nikon) spinning wheel and a Prime95B camera (Photometrics). Removable micropipette holder and water tank were added to the microscope by Oleg Mikhajlov, student in the lab. It was also equipped with a FRAP head.

2.6.2 TIRF microscopy

To observe the supported lipid bilayers I used Total Internal Reflection Fluorescence (TIRF) microscopy. TIRF is a powerful technique to look at objects very close to a surface, making it very useful for imaging membranes in contact with the coverslip. A schematic representation of a TIRF microscope is displayed in Figure 2.10. It relies on the principle that above a critical incident angle, the light won't propagate in the aqueous buffer and only an evanescent wave at the interface between glass and water will appear. The energy of the evanescent wave goes as :

$$E(z) = E_0 * exp(-z/d) \tag{2.5}$$

Where z is the vertical distance from the interface, E_0 the energy at the interface, and d is the penetration depth. This penetration depth depends on the incident angle θ_i, the wavelengthλ, and the refractive indexes n_1 (the coverslip) and n_2 (the sample).

$$d = \frac{\lambda}{4\pi}(n_1^2 sin^2(\theta_i) - n_2^2)^{-1/2} \tag{2.6}$$

By changing the angle of illumination, it is possible to control the penetration depth. Increasing the angle will lead to a very sharp decay of the illumination intensity from the glass coverslip. However, there is a compromise to be made with the intensity transmitted in the media which is also reduced for the higher angles.

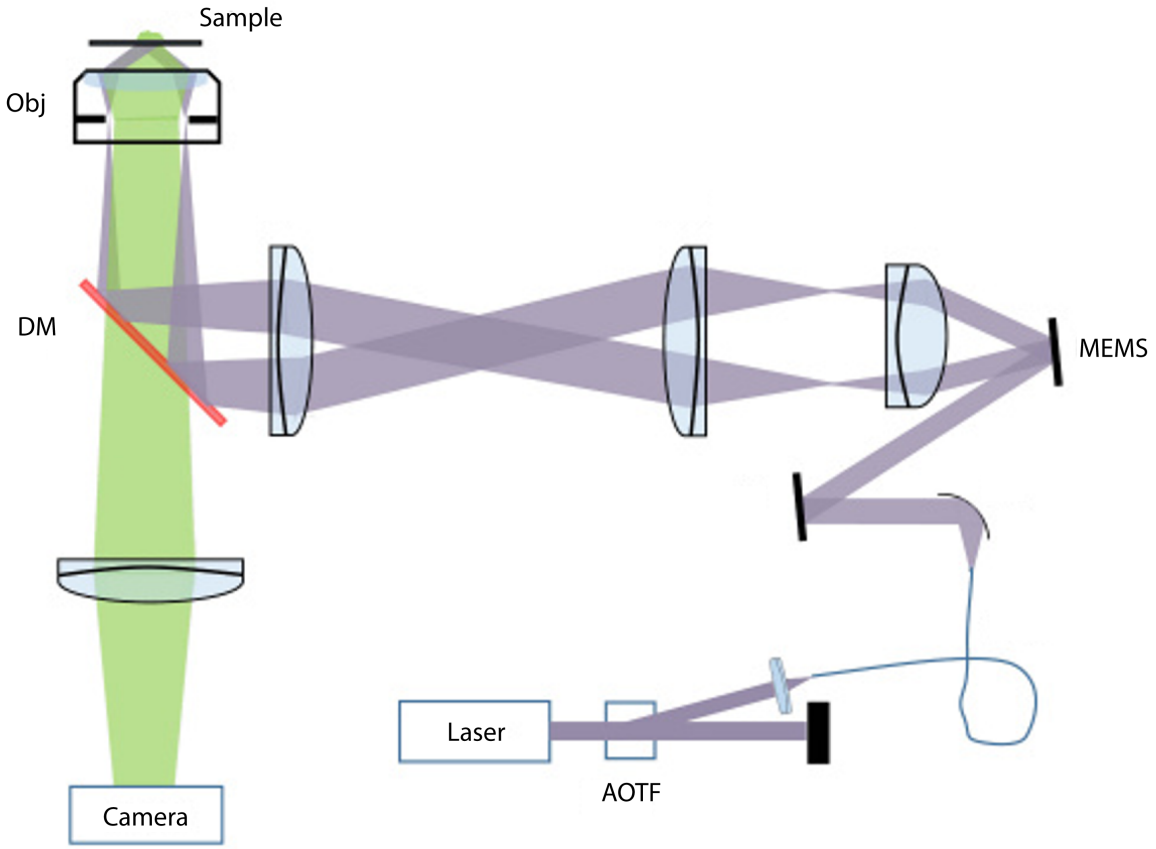

Figure 2.10 – Schematic representation of a TIRF microscope. A laser (controlled by an AOTF) is focused by a set of lenses in the back focal plane of the objective. The light then comes out at a single angle from the objective depending on the position of the focused point in the BFP. If the angle is higher than a critical angle the illumination light is reflected at the surface between the glass coverslip and the sample, and only an evanescent wave propagates in the sample. The fluorescence signal from the sample is then recorded on a camera.

The microscope used for the TIRF imaging was an Olympus IX71 wide-field microscope equipped with a 60x, 1.45 NA oil immersion objective for TIRF microscopy. The microscope is equipped with an optical bench combining four laser lines ($\lambda = 405$ nm; $\lambda = 488$ nm; $\lambda = 561$ nm and $\lambda = 633$ nm). The lasers output powers are controlled with an AOTF (acousto-optical tunable filter). It was also equipped with a commercial FRAP head controlling galvo-mirrors to control the excitation pattern in the sample

and therefore to bleach specified regions. The camera, filters, and laser lines were controlled with Metamorph, and the ILAS2 add-on allowed control of the TIRF and FRAP modules.

2.6.3 Fluorescence Recovery After Photobleaching

To study the diffusion of lipids in biomimetic membranes I used Fluorescence Recovery After Photobleaching. It uses a very intense laser burst in a defined region in order to photobleach the fluorescent molecules present in this region. The fluorescence in the region is then recorded as a function of time. How quickly the signal recovers depends on the diffusion coefficient of the fluorescent particles.

The FRAP experiments were performed using both the spinning disk confocal microscope and the TIRF microscope. The control of the FRAP module was done with the ILAS2 software combined with Metamorph. I used different time intervals to sample the recovery of the fluorescence. Directly after the laser burst, the time intervals were set to the acquisition time to detect the fast kinetic of the initial recovery. It was later increased by a factor 5 to obtain the final kinetics of the recovery. For the bleaching step, I used the maximum laser intensity to shorten the time needed to fully bleach the region of interest (ROI). The laser was focused in the plane of observation and scanned within the region of interest to uniformly photobleach the molecules. The number of scans required was optimised to achieve full bleaching with minimal time. Typically, I used bleaching times of 200-300 ms. Longer times would lead to important diffusion of the fluorescent molecules around the ROI while bleaching. The photobleached molecules would therefore diffuse in the surrounding region affecting the concentration of fluorescent molecules. This will affect the kinetics of fluorescence recovery in the region of interest. I used bleaching times of 50 to 200 ms depending on whether the experiment was performed on a GUV or a SLB. See Figure 2.11 for a typical movie of a FRAP experiment on a SLB.

The analysis was performed using a custom made Matlab routine to correct for the background fluorescence as well as the bleaching of the whole sample due to the exposure for observation. The bleaching due to the observation can be corrected using the fluorescence intensity of a region far enough which was not affected by the laser burst. The theory for analysing FRAP recovery curves has been thoroughly described even though the best way to fit FRAP data is still debated. The most simple solution and still often used, is to fit the data with an exponential decay function -see Figure 2.12 A. In this study, the bleached area is assumed to have been homogeneously bleached, and therefore have homogeneous initial fluorescence intensity. In this case the fluorescence as a function of time goes as :

$$F(t) = A\ exp\left(-\frac{2\tau}{t}\right)\left[I_0\left(\frac{2\tau}{t}\right) + I_1\left(\frac{2\tau}{t}\right)\right] \tag{2.7}$$

Where I_0 and I_1 are the modified Bessel functions, A is the mobile fraction and τ is the characteristic time of the recovery. It is directly linked to the diffusion coefficient by :

$$D = \frac{r^2}{4\tau} \tag{2.8}$$

Where D is the diffusion coefficient, and r is the radius of the disk where bleaching occurred. The fit obtained with this equation gave good results at long time scale but

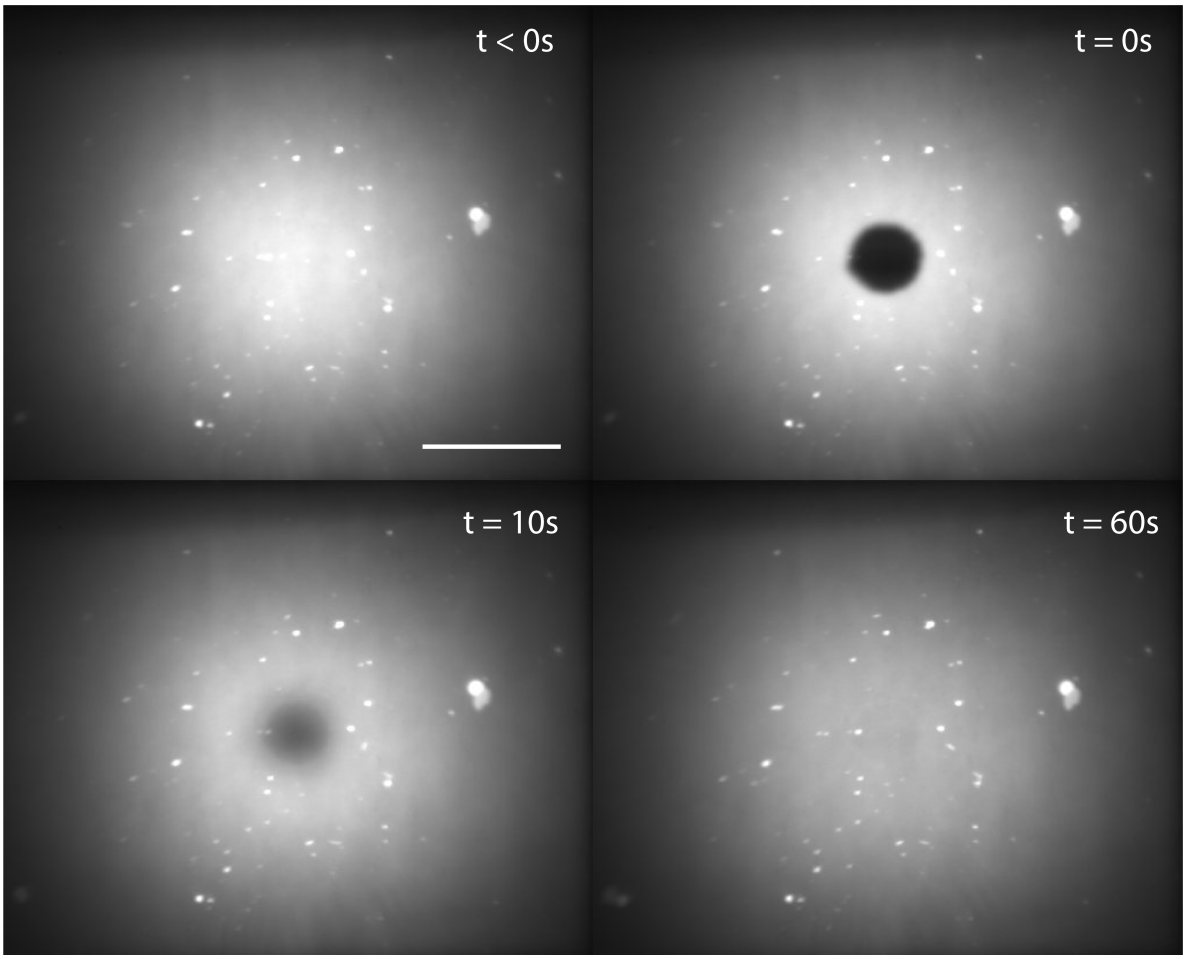

Figure 2.11 – Images from a FRAP experiment performed on a SLB. The full movie duration is 60 seconds, scale bar is 50 μm.

poorly performed on the shortest time scale -see Figure 2.12 B (insert). At the first time point after photobleaching, the fluorescence intensity is not exactly homogeneous in the bleached area. At the edges, particles enter and exit the ROI faster than the photobleaching step. It results that the fluorescence intensity is smoothened at the edges of the ROI even at the first time point after photobleaching. The effect on the average fluorescence in the ROI is more important for small ROI.

I thus had to take into account the effect from the edges of the photobleached region. As this effect depends on the surface of the bleaching region, I decided to always use the same size of ROI for one given set of experiments. To simplify the analysis, I considered that just after the bleaching step, the intensity in the bleached region was homogeneous. This homogeneous intensity could not be recorded as the initial recovery on the edges is faster than the acquisition step. I considered that the intensity in the centre of the region would not have been affected by the recovery on the edges, I therefore used the value of the central intensity as my initial homogeneous intensity. In this condition, the exponential fit is even less satisfying – Figure 2.12 C – but the fit using equation 2.7 gives good result on the full curve as can be seen in Figure 2.12 D.

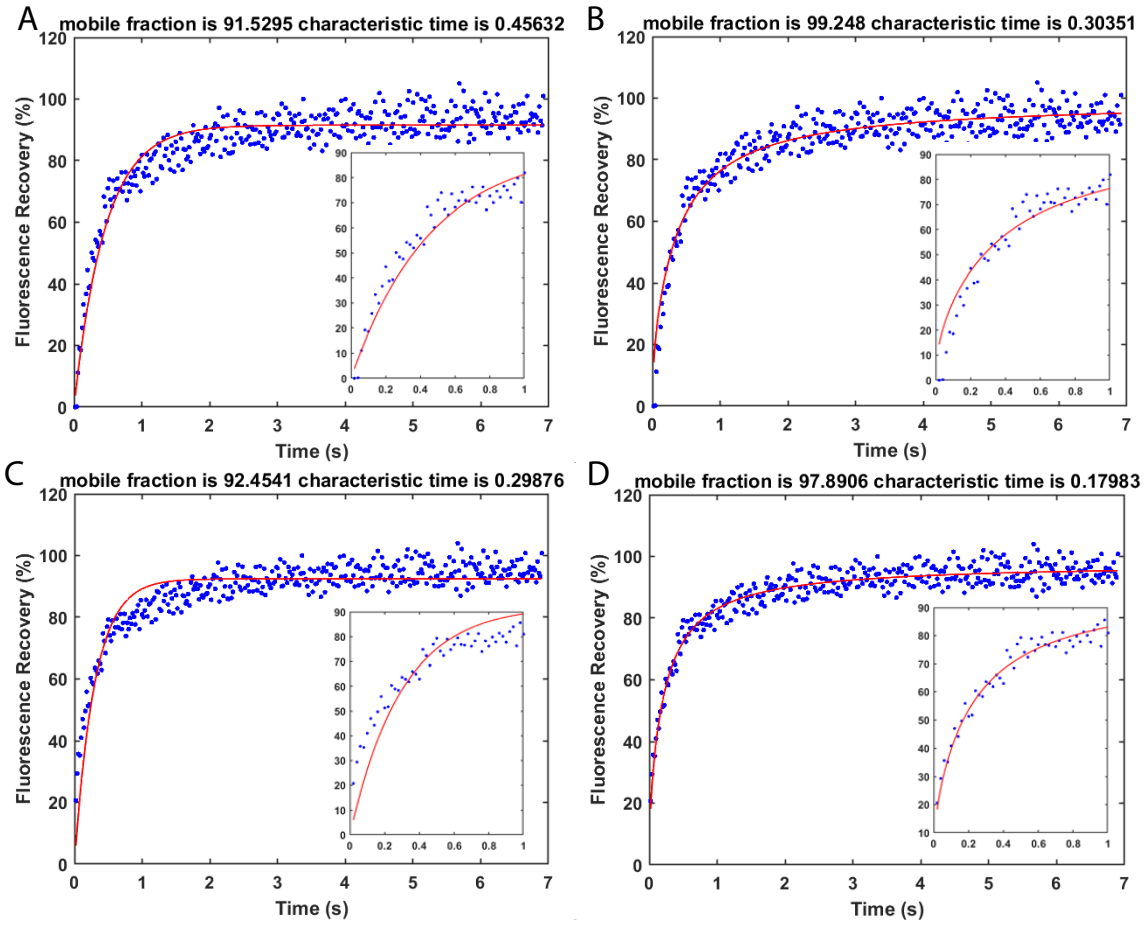

Figure 2.12 – Comparison of fitting models for FRAP experiments performed on GUVs with spinning disk. Acquisition time is uniform and set to 20 ms which allows good recovery of the initial points. Inserts are zoom on the first second of the recovery. (A) and (B) The effect of the edge is not considered. (A) Fitting performed with a standard exponential decay curve. This fitting recovers poorly the long time scale behaviour observed. (B) Fitting performed using equation 2.7. It is not able to fit properly the early time points. (B) and (C) The effect of the edges and early recovery is taken into account. (C) Fitting performed with the standard exponential fitting. It is not able to fit properly the early and late time points. (D) Fitting performed using equation 2.7. It accurately fits the experimental data.

2.7 Single Particle Tracking

To study the diffusion of model membrane associated proteins, I worked at low densities and therefore chose to use Single Particle Tracking (SPT). It allows to overcome the optical resolution barrier, and obtain more detailed information on the diffusion behaviour as compared with FRAP. Single particle tracking relies on the low density of the fluorescent particles. If the density is low enough, the probability for two objects to be closer than the resolution limit due to diffraction is very low. By finding the centres of the peaks made by each individual fluorescent particle, it is possible to localise them with a precision below the diffraction limit. Finally, by linking the positions between each frame, tracks can be reconstituted and the diffusion behaviour of the particles can be obtained.

2.7.1 Setup optimisation for SPT

To perform single particle tracking on mimetic membranes such as vesicles and lipid bilayers, it is necessary to optimise the signal to noise ratio. I used a Nikon TI-Eclipse microscope equipped with a TIRF arm from Nikon. It possessed three laser lines ($\lambda = 488$ nm; $\lambda = 532$ nm and $\lambda = 638$ nm). Lasers were controlled with a Digital to Analog Converter (DAC). The calibration of the laser power output as a function of the applied voltage was performed. When performing SPT experiments, it is essential to maximise the Signal to Noise Ratio (SNR). The fluorescence signal is linear as a function of the intensity of the excitation beam until it reaches a saturation regime. To maximise the signal, the power of the laser should be high enough to reach this saturation regime. The maximum laser power per unit of area out of the objective in each laser line was respectively 1200 W/cm^2; 1300 W/cm^2 and 900 W/cm^2. For observation of GUVS, wide field had to be used.

Finally, the camera used to collect the signal is important. The localisation precision depends on the SNR, which in turns depends on the camera. Two factors are involved in the SNR, the quantum efficiency, ie the probability for one photon to be detected (which depends on the wavelength of emission of the fluorophore), and the background noise of the camera. Finally, the speed of the camera is also important as it will set the smallest time between consecutive images which is essential to track particles.

I tested different top of the range cameras to determine which would be best suited to perform single particle tracking in our conditions. As the localisation of the particle relies on the fitting of the PSF, it is important to chose a pixel size that allows good sampling of the PSF. If the pixel becomes too small, the number of photons recorded on each pixel is decreased, and as a consequence, the SNR is also decreased. Considering that I track my fluorescent particles with the 638 laser line, I aimed at a sampling size of about 100 nm which corresponds to a real pixel size of about 10 µm with our 100x, NA=1.49 objective. Three cameras were selected for comparison, the Hamamatsu Orca Fusion, The Photometrics Prime95B and the Andor Ultra 888. To obtain comparable results, the three cameras were conjugated to a system of lenses and mirrors to compensate for the difference in pixel size and allow similar imaging conditions. I made sure that the optical path for each camera would be similar in order to remove the effect from addition of lenses and mirrors in the comparison – see Figure 2.13.

I tested the cameras at different laser powers on fluorescent beads to compare the sensitivity and the noise coming from the cameras. I decreased the power until the beads are barely detectable and compared for which power value this limit was reached. At the same law intensity illumination, beads would still be detected with the Prime95B and the Ultra888 but not with the Orca Fusion. I then compared the signal to noise ratio of the cameras at a slightly higher value than the limit of laser intensity of the Orca Fusion. To estimate the signal to noise of the cameras, I took blank images to obtain the background value of the pixels and the noise of each cameras. I then imaged the beads at the same laser intensity for each camera and compared the signal on the same 10 beads by summing the signal on a 5 by 5 box. I converted all the values on the equivalent photon count. The Prime95B had the lowest background noise with a standard deviation of the blank image of only 1 photon. The Orca Fusion on the other hand had a standard deviation of 2 photons. When comparing the signal to noise of the cameras, the Ultra 888 and the Orca Fusion had similar results at the compared laser intensity while the SNR on the Prime95B was increase by about 30%. Also, it can record frames fast enough and has the advantage of having the perfect pixel size

without having to add any lens to our setup. I thereby chose to use the Prime95B. I show in Figure 2.13 (right) images of beads acquired on the different cameras at the laser intensity used for the comparison of SNR.

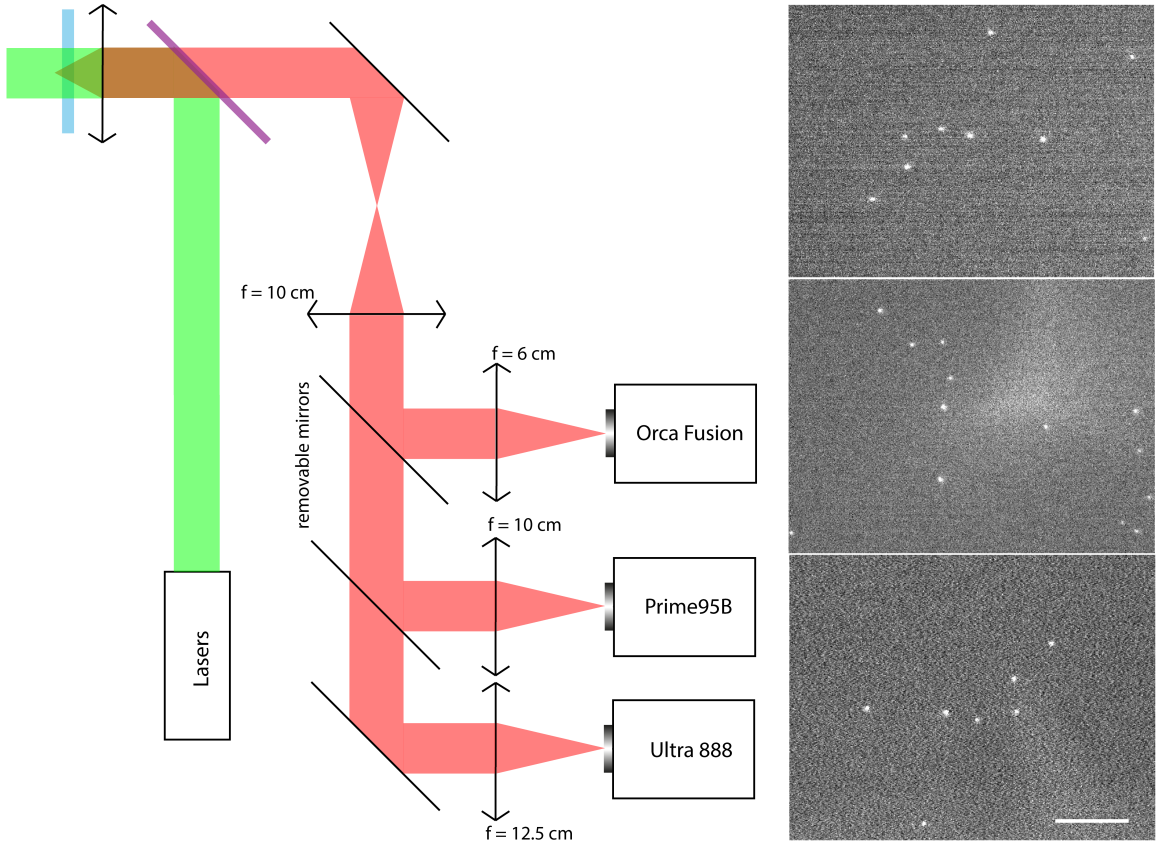

Figure 2.13 – Left: Schematic representation of the montage used to compare cameras. Mirrors were placed on magnetic bases, which allowed removal of mirrors without changing the overall alignment. This allowed fast switching form one camera to the other. Right: Images acquired on the cameras using fluorescent beads and 1 mW of 647 laser. Top to bottom are Orca Fusion, Prime95B and Ultra 888. Scale bar is 10 µm.

The filters and dichroic mirrors were optimised for the fluorophores used in this study. The septins were tagged with GFP and imaged through a filter set optimised for the imaging of GFP while having minimal signal from the 532 fluorophore. For labelling the lipids I had to change the fluorescent dye. Indeed, Bodipy TR ceramide is a very common dye for membranes but its excitation and emission spectra are centred respectively at 595 and 620 nm. This induces some leakage in the 638 nm channel which will prevent observation of single particles. I chose DPPE Atto532, which is shifted to the blue by about 60 nm. This shift prevents leakage in the 638 nm laser line. To ensure that the leakage in the 488 nm laser line would be minimal, I used a excitation filter in this laser line with a cut at 520 nm. The GFP has very little excitation at 532 nm. The fluorescent particles used for tracking are Atto647N, a bright small fluorescent molecule, and QD655 conjugated to streptavidins (Invitrogen). I used filter sets from either Chroma or Nikon (Atto647N) optimised for each particle that I detail in table 2.7.1.

Fluorescent molecule	Excitation filter	Dichroic mirror	Emission filter
GFP (488)	ZET488/10x	ZT491rdc	ET520/20m
DPPE Atto 532	ZET532/10x	ZT532rdc	ET575/50m
Atto647N	620CWL (590-650)	660LP	700CWL (663-738)
QDots 655	ZET488/10x	AT505DC	ET670/50m

Table 2.1 – List of filter sets used for each fluorescent molecule for the single particle tracking experiment.

2.7.2 Preparation of the samples

I performed Single Particle Tracking experiments on four different fluorescent particles: DSPE-PEG-Cy5, aquaporins labelled with Atto647, streptavidin-Atto647N and Quantum Dots. The different steps required to perform single particle for each particle are detailed below.

Cleaning procedure

To perform Single Particle experiments, it is crucial to remove any contaminant from the sample. I had to thoroughly clean the glass slides used for the observation chamber and I also had to filter of the buffers to prevent contamination from external fluorescent particles. The glass slides were cleaned by sonication with acetone then ethanol then water each step for 10 min before drying under a flow of pressurised nitrogen with a filter to prevent oil deposits on the glass coverslips. A later plasma cleaning procedure was sometimes used but did not further reduce the noise on the camera when imaging a control sample with no fluorescent particle in the 638 nm laser line. It is important to note that most contaminant particles emit in the blue or green. When compared, the background was much higher in the other two laser lines and the plasma cleaning step decreased very noticeably the number of detectable molecules in the absence of sample.

I tested Single Particle Tracking on lipid bilayers containing DSPE-PEG-Cy5. I made SLBs with a small percentage of these fluorescent lipids and observed them on the single molecule microscope with either wide-field or TIRF illumination. However, the presence of contaminants giving single molecule signal was observed. Upon removal of the fluorescent lipids the signal was still present but only if a lipid bilayer was formed. The coverslip was checked at each step and no fluorescence was observed until the addition of SUVs if the coverslip was activated beforehand. Tests were run using different syringes and batches of lipids and no difference was observed. I switched to GUVs, and in this case no contamination was observed, but the signal from the fluorescent probes was also reduced. The overall signal to noise ratio was improved with a smaller chance to detect undesired fluorescent molecules in our sample.

Optimisation of the density of single particles

When performing Single Particle Tracking, the density of fluorescent molecules has to be optimised. It is necessary that molecules do not come in close proximity (less than the size of the PSF) and that they do not cross trajectories which could result in miss assignment of the positions during the tracking step. The optimum imaging density therefore depends on the size of the PSF, the diffusion coefficient and the acquisition time. I used three different samples for single particle tracking to study the diffusion of different membrane associated particles. For each system, the density has to be optimised.

I performed some tests to optimise the density of single particles for each sample. I started with aquaporin. I prepared the SUVs to a ratio of protein to lipid of 1:100 w:w in order to have a density higher than required for SPT. I could then dilute the proteo SUVs (containing aquaporins) with SUVs that did not contain aquaporin. By mixing with other SUVs, I could change the fluorescent lipids and their amount without having to make a new preparation of SUVS containing aquaporin. The ratio of proteo SUVs and fluorescent SUVs had to be optimised for each new preparation of aquaporin. I started by screening the dilution from 1:1 to 1:1000, and later screened to get a density ideal for single particle tracking. Such density depends on multiple parameters: the diffusion coefficient, the exposure time and the PSF. Ideally, one would like to detect only single molecules and assign their position to a trajectory with no ambiguity. Molecules have thus to be apart enough. The probability of two molecules being about 250 nm apart should be considered. However, the more stringent restriction is that two trajectories should not come too close one another. To reduce errors, the lower the density the better. However, there is a cost in the sampling of the diffusion media and statistics as fewer molecules and therefore fewer trajectories will be recorded. This effect is not too important in the case of a lipid bilayer, but becomes significant for vesicles because the surface being imaged is rather small and to image a new surface means finding a new vesicle with close to no defect. I worked at densities of about 1 fluorescent particle per 5 μm^2 which corresponded with my preparation protocols to dilution of 1:100 to 1:500 of proteo-SUVs to SUVs with fluorescent lipids.

For the Quantum Dots and streptavidin labelled with Atto647N the density was optimised by changing both the density of DSPE-PEG biotin lipids and the incubation concentration and time of either the Quantum Dots or the streptavidin. The concentration of either Quantum Dots or streptavidin had to be kept under 100 pM to prevent high concentrations of free floating fluorescent molecules. Due to the very high difference in diffusion coefficient, it was easy to differentiate the small fraction of free-floating particles with the particles bound to the membrane. The concentration used for Quantum Dots was 50 pM and 20 pM for streptavidin. The molar ratio of DSPE-PEG2k-biotin was optimised at 0.004% for Quantum Dots and 0.002% for streptavidin. Both where incubated with vesicles after electro-formation for 1 hour at 4°C under gentle mixing. With this protocol only the lipids of the external leaflet of the GUVs will be labelled and therefore all the fluorescent particles will face the side where septins interact. The vesicles where then transferred in the observation buffer where they would also be incubated with septins.

2.7.3 Analysis of SPT experiments

The films were analysed using a home built Matlab script SlimFast to obtain the localisations and to assign them to trajectories. A snapshot from a SPT experiment is displayed in Figure 2.14 A with detected particles indicated by red dots. It allowed to choose different parameters to ensure that a minimum amount of false detections and wrong affiliations to trajectories happened. To verify both, the evalSPT software was used. It allows the visualisation of the trajectory on the movie to detect if errors in the localisation and tracking procedures occurred. If so, I would change parameters on the SlimFast software or lower the density of fluorescent molecules in later experiments.

To compute the diffusion coefficient of the trajectories, the mean squared displacement (MSD) was computed as a function of the time step. Considering brownian motion and particles diffusing in 2 dimensions, the formula to obtain the diffusion coefficient is :

$$MSD(t) = 4Dt \tag{2.9}$$

Where D is the diffusion coefficient, t the time step used to compute MSD. To fit experimental data, one has to consider effects coming from the imperfect precision of localisation as well as the motion blur (Vestergaard et al., 2014). The formula then becomes :

$$MSD(t) = 4Dt + 4(\sigma^2 - 2D\Delta tR) \tag{2.10}$$

Where the second term accounts for the precision of localisation σ and the motion blur R. This motion blur coefficient is usually equal to 1/6 unless the shutter of the camera isn't open during all of the time step Δt.

Another effect to consider is the possibility of anomalous diffusion. In this case the mean squared displacement is:

$$MSD(t) = 4Dt^{\alpha} + 4(\sigma^2 - 2D\Delta t^{\alpha}R) \tag{2.11}$$

Where α is a coefficient accounting for anomalous diffusion. It is equal to 1 for brownian motion, but can be different from 1 for either super diffusive($\alpha > 1$) or sub diffusive ($\alpha < 1$).

However, some issues may occur from statistics. Indeed, for one trajectory, the mean squared displacement considers that the data is not correlated when it is in fact strongly correlated (Vestergaard et al., 2014). It means that the addition of more points to the fit can actually reduce the precision of the data, but it will be accurate. It means that in a population of trajectories the estimated diffusion coefficients will be spread out, but their average will be close to the true value. A low number of points are actually needed for optimal fitting – one is ideal if the uncertainty on the localisation is null. I chose to use the first five points of the curve which often give a good fit to the model – see Figure 2.14C.

To obtain the anomalous diffusion coefficient, I performed a linear fitted the MSD as a function of lag-time in a log-log scale. The number of points considered to perform the fit is essential. In my conditions, as particles can quickly diffuse out of the region in focus, I had to limit the number of considered points. To obtain the anomalous diffusion coefficient, I decided to fit on the first ten points of the curves.

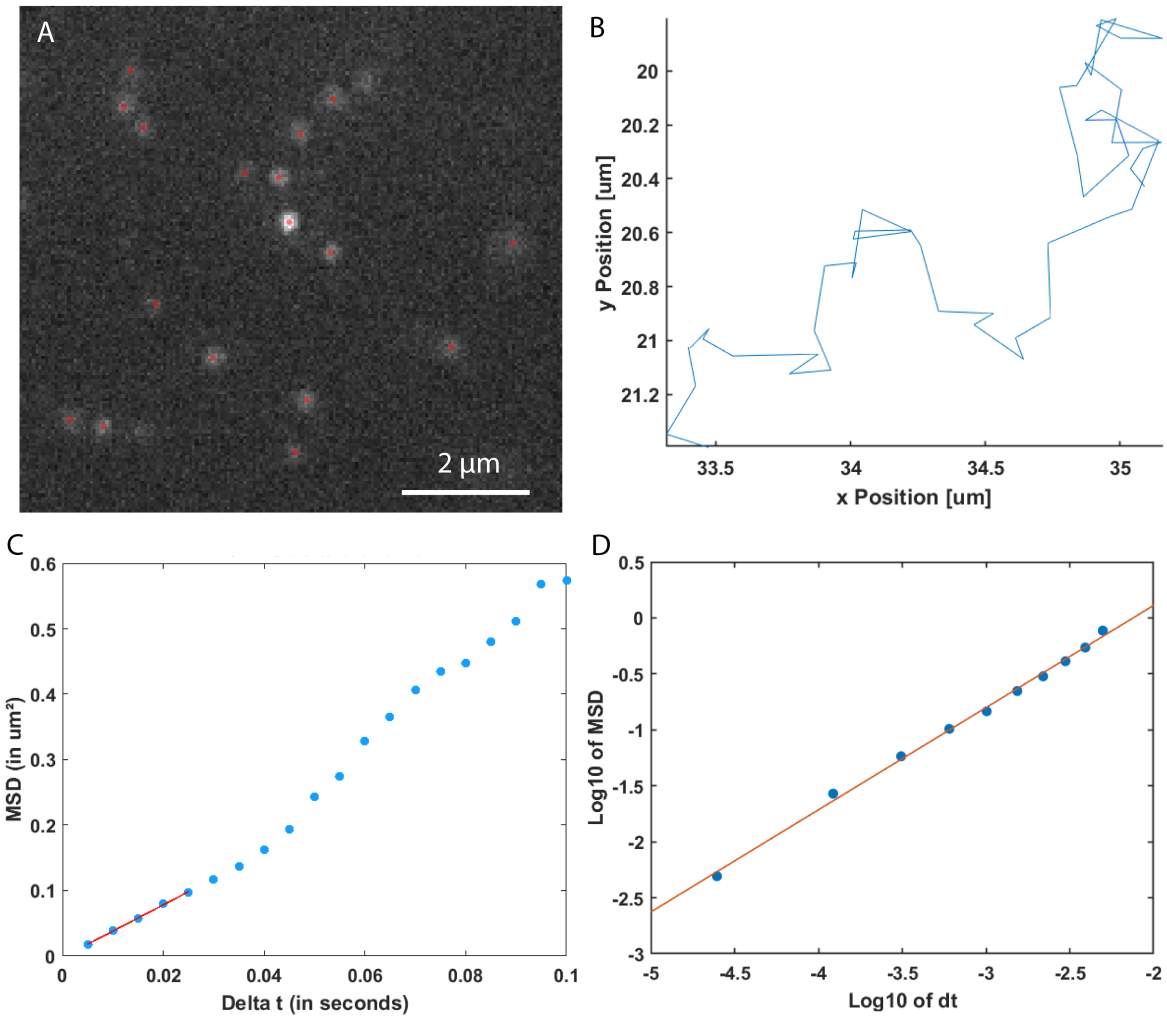

Figure 2.14 – (A) Raw image from an acquisition movie. Fluorescent molecules are quantum dots, acquisition time is 5 ms. The red dots correspond to detections of single particles by the SlimFast software. (B) Trajectory for one molecule after the tracking algorithm of the SlimFast software is applied. (C) Mean squared displacement as a function of the lag-time for a trajectory of about 100 time points. The linear fitting is applied on the first five points of the plot. (D) Mean squared displacement as a function of the lag-time in log-log scale. The fit performed to obtain the anomalous diffusion coefficient considers the first ten time points.

2.8 Obtention of mechanical properties

To study the mechanical properties of lipid bilayers, different approaches have been used. The most common approach is the micropipette aspiration. In this particular study, it failed to reasons detailed in section 4.2. I therefore used indentation by an Atomic Force Microscope tip.

2.8.1 Micropipette aspiration

The micropipette aspiration technique is a common method used to study the mechanical properties of lipid membranes. It can be used on GUVs to obtain the elastic and bending modulus of biomimetic membranes. It relies on recording the deformation

of a vesicle due to the aspiration by a micropipette. By recording the pressure inside the micropipette and measuring the length of the lipid tongue aspirated inside the micropipette, it is possible to recover both the elastic and the bending modulus of the membrane.

To perform micropipette aspiration, it is important to limit the interaction of lipids with the micropipette by passivating it. Also, after the capture of the vesicles, they are pre stretched to unfold defects in the lipid bilayer. Then by studying the GUV at different tension regimes, it is possible to recover independently the bending and the elastic modulus. The Helfrich Hamiltonian describes the membrane mechanics:

$$H = \iint \left(\frac{\kappa}{2}(C - C_0)^2 + \sigma\right) \, dS \tag{2.12}$$

Where σ is the tension of the membrane, κ is the bending modulus of the membrane and C and C_0 are respectively the curvature and the intrinsic curvature of the membrane. Performing Fourier analysis on this hamiltonian it is possible to obtain the relative area variation dA_{ent} due to fluctuations:

$$dA_{ent} = \frac{k_B T}{8\pi\kappa} ln\left(\frac{\pi^2/a^2 + \sigma/\kappa}{\pi^2 L^2 + \sigma/\kappa}\right) \tag{2.13}$$

Where L is the macroscopic length of the membrane, a few micrometers in the case of a GUV, and a is the microscopic length of the membrane, typically 1 nm. An extra elastic term has to be added to obtain the total change in area dA.

$$dA = dA_{ent} + \frac{\sigma}{K_A} \tag{2.14}$$

With K_A the elastic area compressibility modulus. The exact fitting of this equation is complicated in experimental setups. Therefore, two distinct regimes are derived. A low tension regime in which entropic fluctuations play an important role and an elastic regime in which the membrane has been unfolded and only the elastic deformation is considered.

2.8.2 AFM Experiments

The principle of the AFM indentation method is presented in Figure 2.15 A. A cantilever with a tip is pressed on an object of interest. The deflection of the cantilever is recorded giving a measure of the force applied and the vertical position of the tip.

AFM experiments were performed on a combination of a Nanowizard 4 microscope (JPK) and an inversed TIRF microscope (Zeiss) equipped with an oil immersion objective (100x, NA 1.40). A 1.5x telescope was added to obtain a final 150x magnification and a corresponding pixel size of 107 nm. Four laser lines were present (405 nm, 488 nm, 561 nm, 640 nm) combined into a single beam. The intensity was tuned with an acousto-optic tunable filter. The camera used for imaging fluorescence was an EM-CCD iXion Ultra897 (Andor Technologies). For the AFM acquisition, the microscope was equipped with a piezo Tip Assisted Optics (TAO) to perform sample displacement in x, y, z with a range of 100x100x10 μm. To ensure the stability of the sample during acquisition, the microscope was also equipped with a home made auto focus system. To create it, 4% of the laser power of the 640 nm laser was redirected to the sample glass coverslip interface reflected by the surface and guided into a home-made QPD to

follow the transverse displacement and correct them with the TAO. The lasers, filters and camera were controlled with a custom made LABVIEW script.

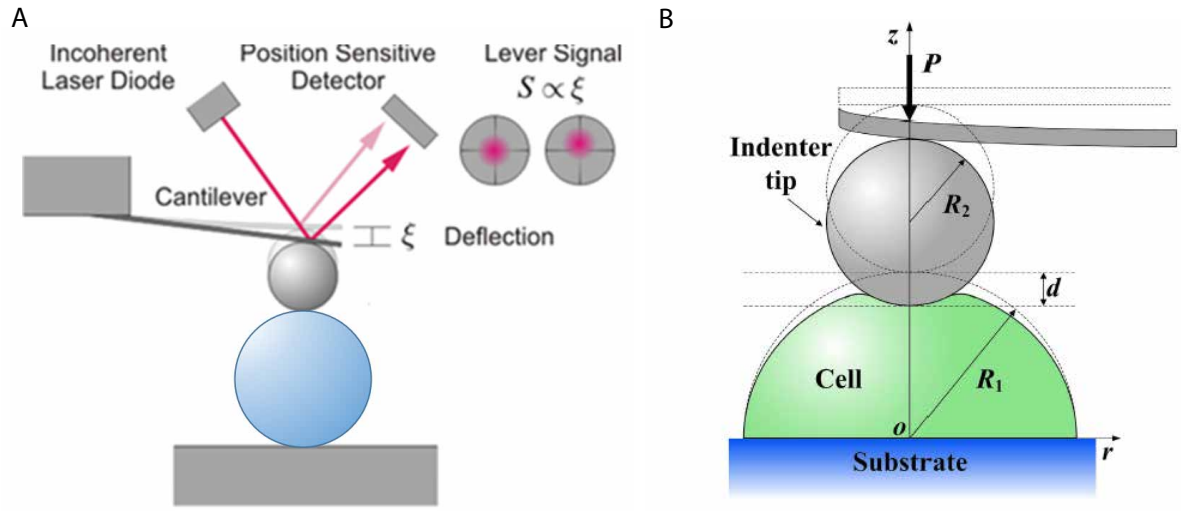

Figure 2.15 – (A) Schematic representation of the indentation procedure. (B) Hertz contact model representation.

The GUVs were prepared with the gel assisted swelling method. To prevent lateral displacement, the GUVs had to be bound to the glass substrate. Multiple methods for binding were used. Strong interactions could result in bursting the GUVs on the glass substrate, leaving only lipid bilayers. I tested coating with polylysine which left only the smallest vesicle intact. We used a small amount of $MgCl_2$ (20 µL) at a concentration of 10 mM that was then diluted and washed away before addition of vesicles which lead to strong binding but very little bursting. A higher concentration lead to bursting of all GUVs within 2 to 3 minutes. GUVs were incubated for 20 min with septins and later injected in the observation chamber. After another 20 min of sedimentation, the chamber was rinsed with the "Observation Buffer" to remove the excess of septins that would otherwise bind to the AFM tip.

The tips used for the AFM indentation experiments were CP-PNPL-SiO from sQude with diameters of either 1.7 µm or 5.1 µm. The tips were cleaned with air plasma treatment and kept in dessicated atmosphere. The cantilevers were characterised by their frequency spectra in solution which gives their rigidity constant. The fluorescence imaging allowed fast scanning of the sample to find GUVs and proper alignment of the AFM tip with the vesicle of interest to indent it at its centre. The vesicles were selected for their unilamellarity and their dimension. When indenting, the force displacement curves were obtained during both the descent and the ascent of the tip to observe if some of the energy was lost by viscosity, and if the tip detached properly from the GUVs. This issue was more important when septins were added as they adhere to the tip. Experiments are performed fixing the maximum force applied by the lever. This maximum can be set up to 15 nN. This value is fixed by the highest deflection of the cantilever that can be recorded on the detector. The speed used for the vertical displacement of the tip was 1 $\mu m.s^{-1}$.

2.8.3 AFM analysis

The analysis of the AFM curves was performed using the JPK software for correcting the drift and obtaining the force applied from the vertical deflection. To recover the mechanical characteristics of the GUVs from the force/indentation curves, the Hertz contact model was used first – see Figure 2.15 B. It allows the recovery of the Young's modulus of the GUV.

$$F = \frac{4}{3} E^* R^{0.5} \delta^{1.5} \tag{2.15}$$

However, it is poorly fitted for characterisation of a vesicle. Indeed, a vesicle is not an elastic ball, but a fluid sphere, with different mechanical parameters: its elastic area compressibility, its bending modulus and its tension. Therefore, the theory developed in Schäfer et al. (2015) was better suited to our system. To analyse my experiments, the conical shape of the AFM tip is replaced by a sphere which changed some terms in the system of equations.

We kept the hypothesis that were made in the model. First, the pressure and tension are assumed to be homogeneous across the membrane. Second, the bending energy of the membrane is considered negligible compared to the compressibility and tension terms. The Young-Laplace's law can be applied:

$$\Delta P = T \left(\frac{1}{\rho_1} + \frac{1}{\rho_2} \right) \tag{2.16}$$

Where ρ_1 and ρ_2 denote the principal radii of curvature at any point of the surface. The membrane was decomposed into three different regions displayed on Figure 2.16. The first region is the region of contact between the AFM tip and the vesicle. In this region, the geometry of the vesicle is imposed by the shape of the tip. The second region is the membrane free of any contact. Its shape can be determined using the Young-Laplace law and considering continuity of the membrane. The third region is the contact region with the substrate, where the membrane is flat.

The final shape of the vesicle can be described knowing three radii – see Figure 2.16- R_0, the maximum radius of the vesicle, R_i, the radius of the contact surface, and R_1 the radius of the contact with the AFM tip. An AFM tip with a radius of R_p was considered. The height of the indentation h, and the contact angle θ were calculated.

$$h = R_p - \sqrt{R_p^2 - R_1^2} \tag{2.17}$$

$$\theta = arctan \left(\frac{R_1}{\sqrt{R_p^2 - R_1^2}} \right) \tag{2.18}$$

To compute the shape of the sphere, the variable $u = sin(\beta)$ was used to facilitate computation. For the free contour it follows the following equation :

$$A = \frac{R_0}{R_0^2 - R_1^2} \; ; \; B = -\frac{R_i^2 R_0}{R_0^2 - R_1^2} \tag{2.19}$$

$$u(r) = Ar + \frac{B}{r} \tag{2.20}$$

For the part going from R_1 to R_i where the height is maximal, u goes as :

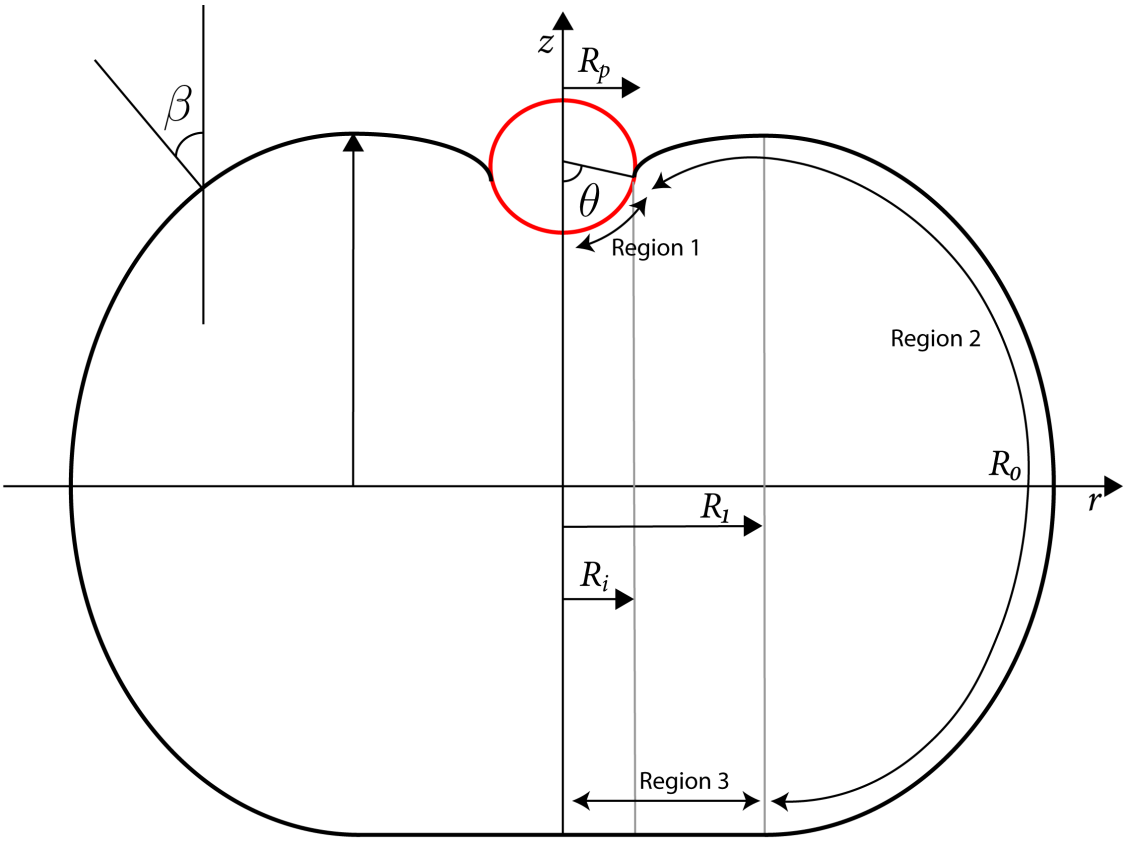

Figure 2.16 – Representation of the model used to numerically solve the system of equation and obtain the tension and area compressibility of the vesicles.

$$A_2 = \frac{R_1 sin(\theta) + B + AR_0^2}{R_i^2 - R_1^2} \; ; \; B_2 = -(A_2 R_1^2 + R_1 sin(\theta)) \tag{2.21}$$

$$u_2(r) = A_2 r + \frac{B_2}{r} \tag{2.22}$$

Then u can be linked to the height of the vesicle by the following equation :

$$\frac{\mathrm{d}z}{\mathrm{d}r} = tan\beta = \frac{u(r)}{\sqrt{1 - u(r)^2}} \tag{2.23}$$

To obtain the shape of the vesicles which depends on the three radii, a system of three equations must be solved numerically. This system corresponds to to the force equilibrium and the conservation of the volume. The conservation of the volume leads to the following equation :

$$V = 2\int_{R_i}^{R_0} \frac{\pi r^2 u}{\sqrt{1-u^2}}\mathrm{d}r + \int_{R_1}^{R_i} \frac{\pi r^2 u_2}{\sqrt{1-u_2^2}}\mathrm{d}r - \pi R_i^2 z(R_i) - \pi h^2 \left(R_p - \frac{h}{3}\right) \tag{2.24}$$

Where V is the initial volume of the vesicle. For the force equilibrium, the force on each side of the vesicle was calculated as a function of the three radii and has to be equal to the applied force f. This leads to two equations :

$$f_{bot} = \frac{\pi R_0 R_i^2}{R_0^2 - R_1^2}\left(T_0 + K_A\frac{\Delta S}{S}\right) \tag{2.25}$$

$$f_{top} = 2\pi(A_2 R_1^2 + R_1)\left(T_0 + K_A\frac{\Delta S}{S}\right) \tag{2.26}$$

With T_0 the tension prior to indentation and K_A the area compressibility modulus. Finally the indentation can be recovered using geometric considerations:

$$\delta = 2R_v - \left[2\int_{R_i}^{R_0}\frac{u}{\sqrt{1-u^2}}\mathrm{d}r + \int_{R_1}^{R_i}\frac{u_2}{\sqrt{1-u_2^2}}\mathrm{d}r - h\right] \tag{2.27}$$

After solving the system of equations for each force increment, the force indentation curve can be reconstructed for a given set of tension and area compressibility modulus. I used a Matlab routine provided by Professor Andreas Janshoff. For the numerical stability, the system was first solved at high forces, and the obtained values of the radii were used as initial parameters for the next step with a smaller force. Fitting of the experimental data provided the tension and the area compressibility of the vesicle.

If the indentation is done fast enough, the volume should be conserved as the leakage of water through the membrane is a slow process. However, if performed too fast, dissipation by viscosity could happen. This dissipation is visible on the force-displacement curves as an hysteresis between the part of increasing indentation and the part of the decreasing indentation. For all experiments the difference between the two parts was small enough to neglect the viscosity.

Chapter 3

The role of septins in establishing diffusion barriers

Septins have been shown to be involved in the establishment of diffusion barriers *in vivo*. However, the mechanism through which septin establish these diffusion barriers is still poorly understood. I studied the ability of septins to generate diffusion barriers in *in vitro* reconstituted systems. I performed both FRAP and SPT experiments on SLBs and GUVs to assess the diffusion of different membrane components in the presence of septins.

3.1 Diffusion of lipids

It has been proposed that diffusion barriers in cells could be created by the immobilisation of certain lipids in the membrane, leading to a crowding effect that would prevent the diffusion other lipids as well as the diffusion of transmembrane proteins. To test if this mechanism is involved in the formation of diffusion barriers by septins, I tested the effect of the addition of septins on the diffusion of different lipids in model bilayers. I started with markers of the membrane to study the overall fluidity of the lipid bilayer and then focused on PI(4,5)P_2, with which septins interact specifically.

3.1.1 Validation of the system

First, I had to make sure that the in vitro models were behaving properly and in particular that the lipid bilayers were fluid. This is particularly important for SLBs. I prepared both GUVs and SLBs with a lipid mixture mimicking the plasma membrane and most importantly containing PI(4,5)P_2 to allow septins to bind to the membrane. GUVs were prepared with both electro-formation and PVA methods. I then imaged the GUVs using confocal microscopy, and measured the interaction with purified GFP-septins. Confocal images of a vesicle incubated with septins can be seen in Figure 3.1 A. My results are similar to the ones previously reported in the team using this lipid mixture (Beber et al., 2019a). This test was repeated for each new batch of purified septins to make sure that they were able to bind properly to the GUVs. I performed similar tests with supported lipid bilayers and incubated the obtained bilayers with GFP-tagged septins for 30 min. I later washed away the solution to remove unbound septins. I then imaged septins with TIRF microscopy to ensure that they would bind

to the supported lipid bilayers. Images of a SLB with septins bound can be seen in Figure 3.1 B.

For the supported lipid bilayers, I had to make sure that the bilayers were fluid. Indeed, the presence of a substrate can alter the fluidity of the bilayer. To check the fluidity of the bilayer the most common and straightforward technique is to perform Fluorescence Recovery After Photobleaching. The details are presented in Section 2.6.3. For a supported lipid bilayer, both the diffusion coefficient and the mobile fraction are equally important. The substrate can affect the diffusion coefficient by adding some extra friction on the bottom layer. Defects and unfused vesicles can create immobile fraction as well.

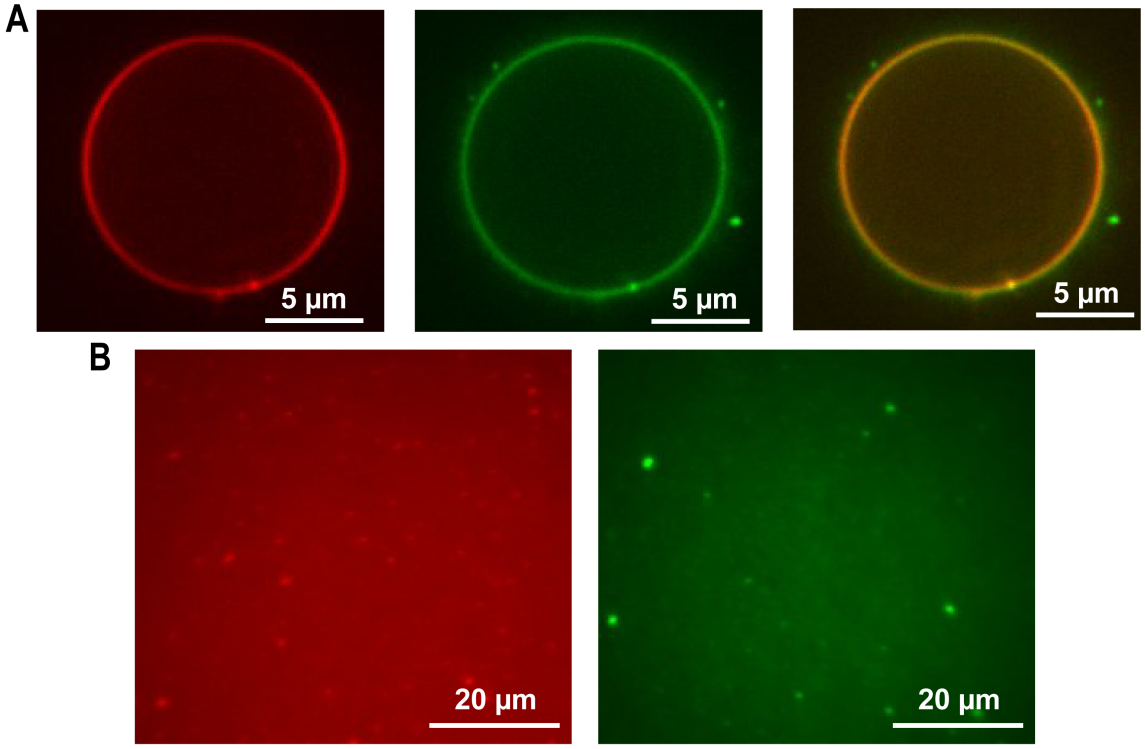

Figure 3.1 – Binding of septins on the different systems used in this study. (A) Confocal images of a GUV containing Bodipy-TR ceramide (red) and incubated with 200 nM GFP-labelled septins (green). (B) Supported lipid bilayer on a glass substrate observed with TIRF microscopy.

I prepared glass coverslips by first cleaning them with bath sonication using acetone, ethanol and water. A final step of either air plasma activation or KOH activation is carried out. The bilayers contained 1% of Bodipy-TR ceramide, a marker for lipid membranes that I used to study the overall fluidity of the bilayer. I imaged the bilayers with TIRF microscopy and performed FRAP experiments to recover the diffusion coefficient and the mobile fraction of the Bodipy-TR ceramide. Snapshots from a FRAP experiment as well as the intensity corresponding to the photobleached region are displayed in Figure 3.2. The diffusion coefficient obtained was $D_{Bdpy-TR} = 1.36 \pm 0.07\ \mu m^2/s$. This value is within the range of diffusion coefficients reported for bilayers containing similar fraction of cholesterol (15% here), a lipid that strongly impacts the viscosity of the bilayer.

The mobile fraction of Bodipy-TR ceramide was above 90% in all bilayers experi-

ments, reaching 95 to almost 100%. When compared to literature, those values are in the high range of mobile fractions – reported values range between 75 and 95% – for supported lipid bilayers, indicating that the amount of defects in the bilayers that I produced was low enough.

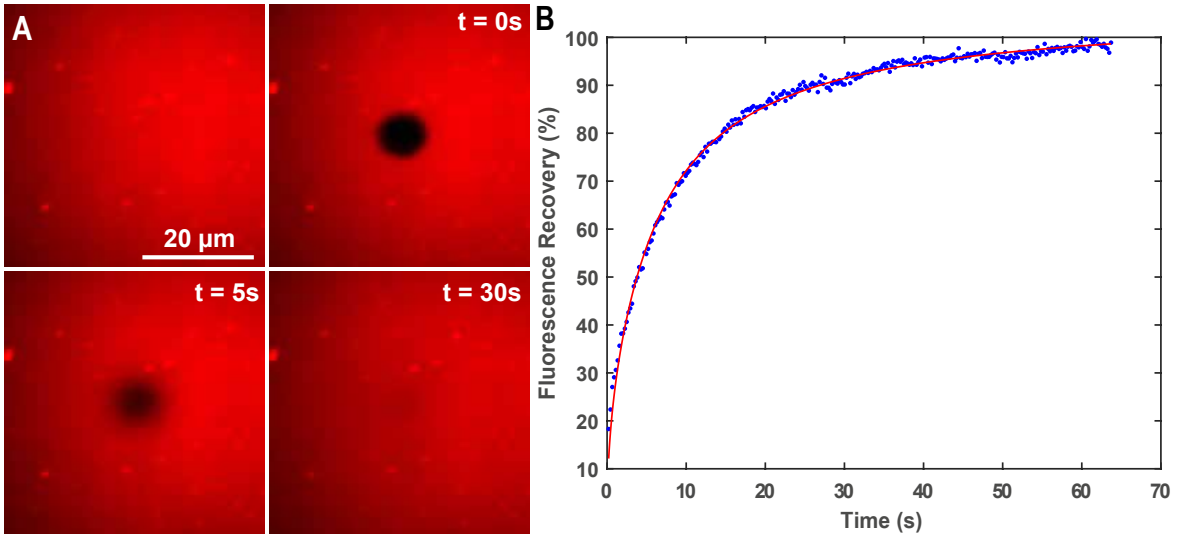

Figure 3.2 – Fluorescence recovery experiment on Bodipy-TR ceramide in a lipid bilayer deposited on glass. (A) Snapshots obtained with TIRF microscopy during the fluorescence experiment with t = 0 corresponding to the bleaching step. (B) Fluorescence intensity – in percentage of the maximum intensity – in the bleached region as a function of time after correction for overall bleaching. It shows that the mobile fraction is high with a diffusion coefficient of $D_{Bdpy-TR} = 1.36 \pm 0.07\ \mu m^2/s$ in good agreement with literature.

3.1.2 Diffusion of septins

Before testing the effect of septins on the diffusion of different lipids, I studied the dynamics of septins themselves on the biomimetic membranes. I wanted to make sure that septins would create a mesh stable enough to create a diffusion barrier, but were still able to diffuse on the substrate at low density.

To measure the dynamics of septins in the filament state, I performed FRAP experiments on GFP-tagged septins added at concentrations of 200 to 300 nM on both GUVs and SLBs. Snapshots of a FRAP experiment on septins bound to a GUV as well as the fluorescence intensity in the photobleached region are displayed in Figure 3.3. In all the tested conditions, no recovery of fluorescence was detected, even when unbound septins were still present in solution and even after more than 10 min. I could therefore conclude that septins were making a dense stable mesh preventing septins from diffusing on the membrane. This showed that the membrane was saturated by septins. More importantly, it would hence be possible for this mesh to create stable diffusion barriers.

To check that individual septin protomers are able to diffuse on membranes, I checked the diffusion of septins at lower densities on the membrane. To perform this experiment I used septins that were tagged by reaction of one cysteine from the septin octamer with a Atto647N maleimide. I used a molar ratio of maleimide-Atto647N to

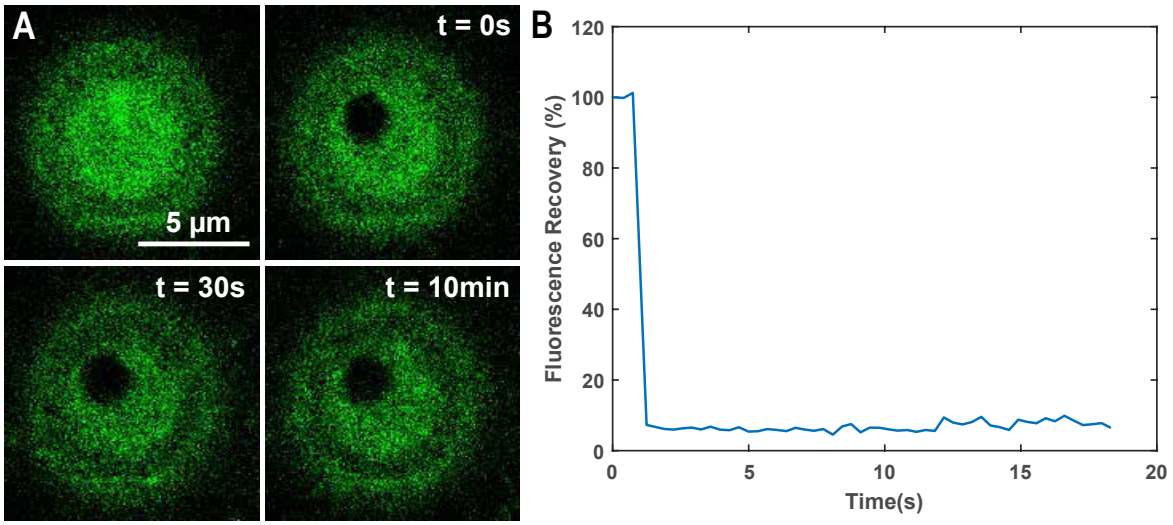

Figure 3.3 – Fluorescence recovery experiment on GFP-tagged septins interacting on a GUV. (A) Snapshots obtained with confocal microscopy at the bottom of the GUV. (B) Fluorescence intensity – in percentage of the maximum intensity – in the bleached region as a function of time after correction for overall bleaching. The experiment shows no recovery in the septin signal even in the time scales of minutes.

septins of 1 to 10. The free dyes were washed away, and the concentration of the obtained septins was checked using a NanoDrop. The proteins were observed in law slat condition with negative staining electron microscopy to ensure that they could assemble normally into filaments. The obtained septins were diluted in a buffer containing 150 mM NaCl and 10 mM Tris (pH = 7.6) to prevent the formation of filaments in solution. I incubated the septins with a supported lipid bilayer at a concentration of 50 pM, and observed them using TIRF microscopy.

After less than a minute, I could observe some octamers binding, and the density on the bilayer reached a plateau after about 5 min. I imaged the septins with 10 ms exposure time which was enough to obtain good signal to noise ratio. A snapshot from one movie is displayed in Figure 3.4 A. On the snapshot, trajectories of the visible particles are overlapped and colour coded. The single octamers of septins could be tracked and I obtained a precision of localisation of about 30 nm for septin octamers on a supported lipid bilayer. The distribution of precision of localisation for each trajectory is displayed in Figure 3.4 B.

The diffusion coefficient of septins followed a distribution which displayed multiple populations of trajectory – Figure 3.4 C. The populations have average diffusion coefficients of respectively 1.0; 0.11 and 0.006 $\mu m^2/s$. The fastest population corresponded to free diffusing particles, while the slowest population corresponded to immobile septin octamers. The last population corresponded to trajectories with a mix of free diffusion and immobilisation. I wanted to see if this behaviour would have an effect on the anomalous diffusion coefficient, to see whether some sub diffusive characteristics could be obtained. The heatmap corresponding to the distribution of anomalous coefficient with diffusion coefficient is plotted in Figure 3.4 D. The anomalous coefficient was centred around 1 for each population of trajectory. I could not detect any anomalous diffusion in this experiment.

To study in more details the different populations, I looked at single trajectories.

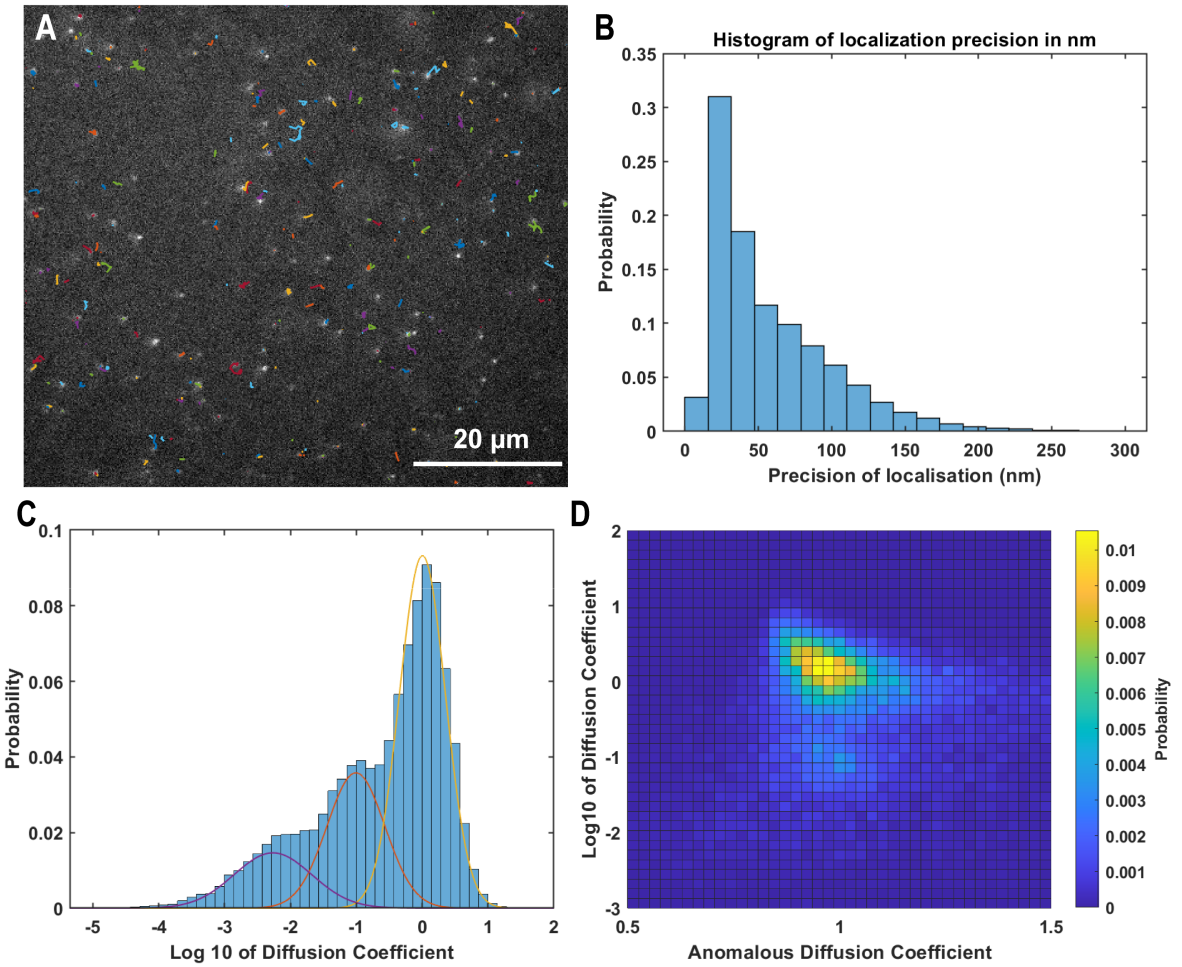

Figure 3.4 – Single Particle Tracking experiment performed on octamers of septins – labelled with Atto647N – in 150 mM NaCl to prevent formation of filaments and interacting on a lipid bilayer. (A) Snapshot of the septin octamers obtained with TIRF microscopy with 10 ms exposure time. Trajectories of septin octamers are overlapped and colour coded. (B) Distribution of the precision of localisation of septin octamers during the experiment. The maximum is located at around 30 nm. (C) Distribution of the diffusion coefficient of septin octamers in logarithmic scale. Three peaks can be distinguished corresponding to diffusion coefficients of 0.006; 0.11 and 1.0 $\mu m^2/s$. (D) Heatmap of the distribution of anomalous diffusion coefficient and diffusion coefficient. No anomalous diffusion was detected.

Trajectories from the fast diffusing and intermediate diffusing populations are displayed in Figure 3.5 A and C respectively. The trajectory A corresponds to brownian motion as could be seen from the distribution of jump sizes but also the homogeneous distribution of angles between consecutive jumps – displayed in Figure 3.5 B.

In the case of the trajectory from the average moving population, there is some clear inhomogeneity in the diffusion, with the diffusion stopping at different times and places before the septin octamer starts diffusing again. This behaviour is reflected in the distribution of angles between consecutive jumps that shows a maxima at 180 °. The trajectory displayed in Figure 3.5 C is an example of a long trajectory. In most cases, the septin octamers in the population of intermediate diffusion coefficient would initially diffuse before stopping and the fluorescent dye would bleach before they start

diffusing again. The dye would typically bleach after about 1 second. The reason for the stops is unknown, and multiple factors could play a role. The septins might find a defect in the bilayer – an unfused vesicle for example – or find some other unlabelled or photobleached septin octamers and bind to them transiently.

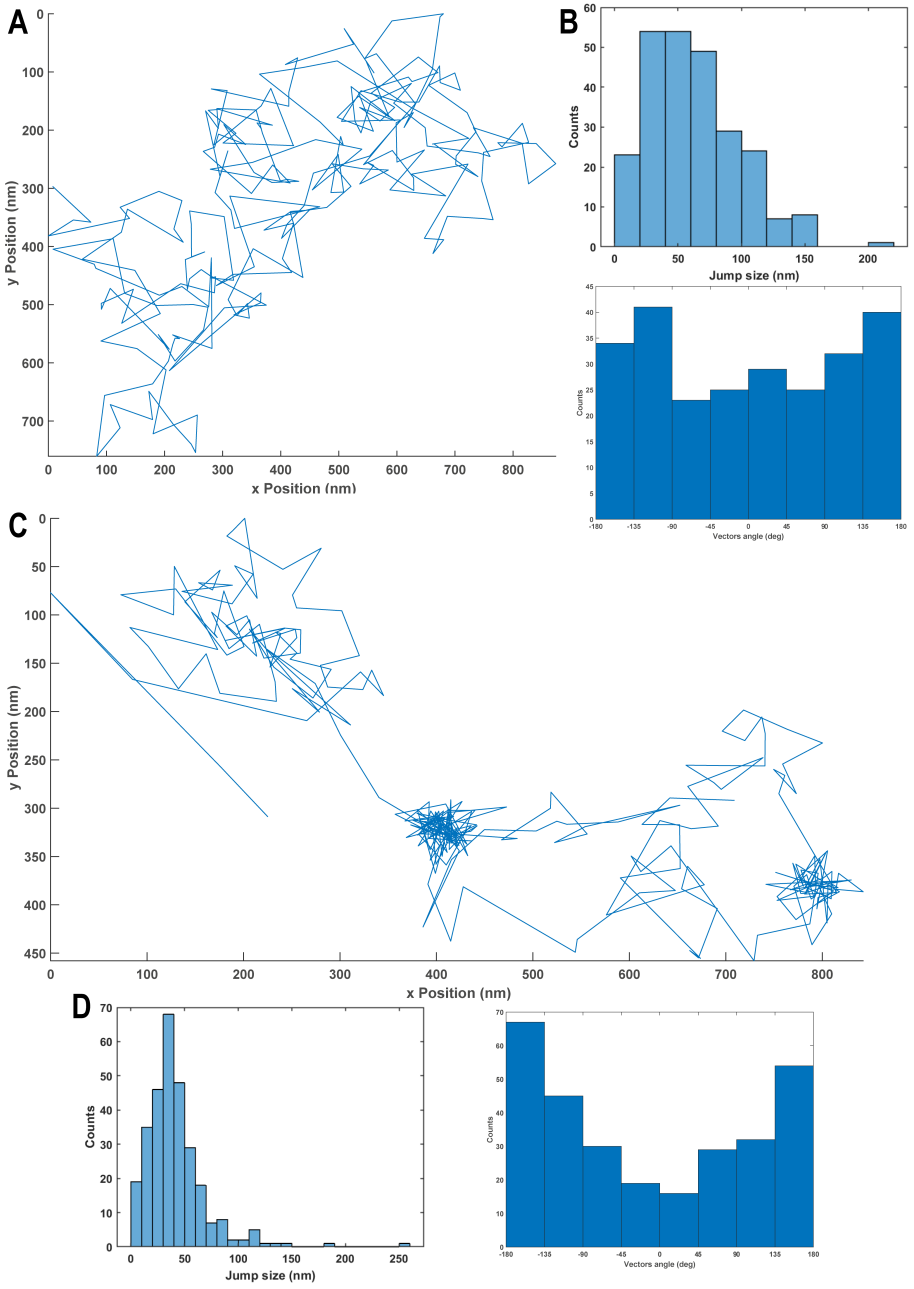

Figure 3.5 – Trajectories obtained from the Single Particle Tracking experiments performed on septin octamers. (A) An example of a trajectory displaying characteristics of Brownian motion. (B) Distribution of jump sizes and distribution of angles between consecutive jumps. (C) Trajectory displaying a mix of brownian motion with places with lower diffusivity. The octamer is trapped in some small regions and can then diffuse again. (D) Ditribution of jump sizes and distribution of angles between consecutive jumps. The distribution of angles between consecutive jumps shows a high anisotropic behaviour with a maximum around 180°. This type of trajectory was rare, representing less than 5% of all trajectories.

The completely immobile population could result from septins interacting with glass. Indeed, it has been observed that septins have a strong affinity for glass. In case the bilayer displays local defects with holes leaving small areas of glass available for binding, septin octamers could locate at those defects and would be unable to diffuse.

Because septins were able to display dynamic properties on supported lipid bilayers, I concluded that septin protomers behave normally on these biomimetic membranes and therefore they should therefore be able to self-organise properly. I then measured the fluidity of the bilayer in the presence of septins.

3.1.3 Diffusion of non specific lipids

To measure the impact of the septin mesh on the fluidity of the lipid bilayer, I compared the diffusion coefficient of Bodipy-TR ceramide in a control supported lipid bilayer (without septins) with the same lipid bilayer after addition of septins. I performed FRAP experiments on supported lipid bilayers after incubation with GFP-tagged septins. The septins were incubated for 30 min at 300 nM to ensure that a dense mesh of septin filaments could be formed on the membrane. The fluorescence in the photobleached region during a FRAP experiment is displayed in Figure 3.6 A. In all the experiments, the mobile fraction was similar to the control experiment, indicating that septins do not block the diffusion of lipids in the bilayer. Additionally, the diffusion coefficients – displayed in Figure 3.6 B – obtained from different lipid bilayers are similar to the one obtained in the control experiment, $D = 1.40 \pm 0.12\ \mu m^2/s$. I concluded that septins do not affect the fluidity of the lipid bilayers. These results corroborate with observations from micropipette aspiration experiments which showed that lipids are able to flow under a septin mesh. These experiments will be further discussed in section 4.2.

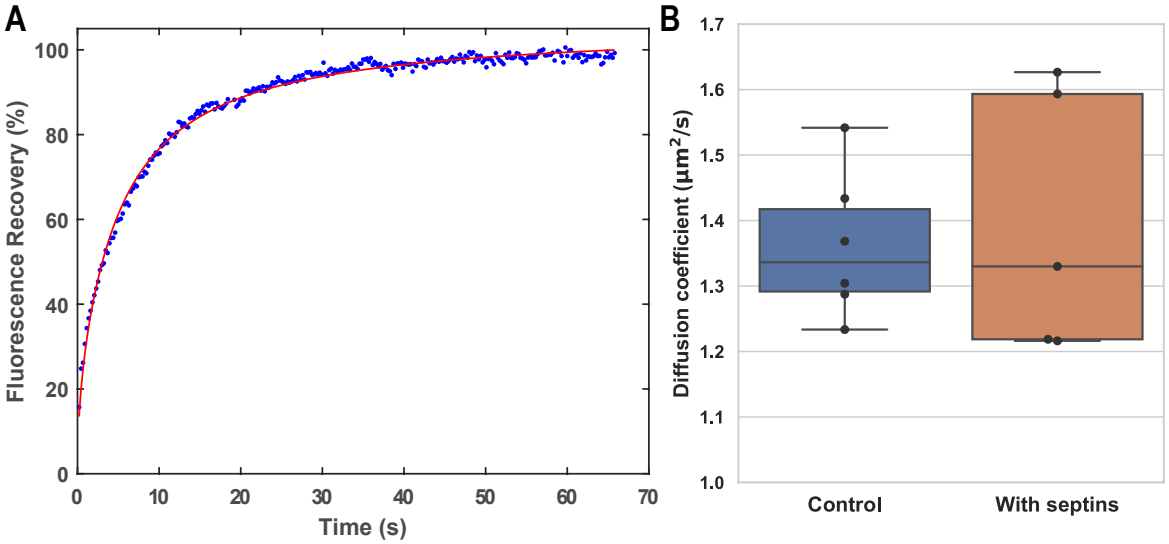

Figure 3.6 – Fluorescence recovery experiment performed on Bodipy-TR ceramide incorporated in a SLB on which septin are interacting. (A) Fluorescence intensity in the bleached region as a function of time. (B) Diffusion coefficient obtained from FRAP experiment on Bodipy-TR in control experiments without septins and when septins are added. No significant difference was observed.

3.1.4 Diffusion of PI(4,5)P_2 in SLBs

Because septins do not affect the overall fluidity of the lipid bilayers, I investigated the diffusion of PI(4,5)P_2 in the presence of septins. PI(4,5)P_2 is the lipid responsible for the interaction between septins and the membrane. To study the diffusion of PI(4,5)P_2, I used commercially available fluorescently labelled PI(4,5)P_2 in which one of the tail is replaced by Texas Red. Because the head is unchanged, septins should/can bind to the lipid similarly as for the purified PI(4,5)P_2. I generated supported lipid bilayers, removing 3% of the PI(4,5)P_2 – leaving thus 5% – in the lipid mixture and adding 2% of TR-PI(4,5)P_2. The reasoning is that when only 5% of PI(4,5)P_2 are present in the membrane, septins do not bind very efficiently to the lipid membrane. Therefore, this composition should maximise the binding of septins to the fluorescent PI(4,5)P_2 without increasing the molar ratio of fluorescent lipids above a few percent.

I prepared the lipid bilayers on glass substrates and performed FRAP experiments in the absence of septins. Snapshots from a FRAP experiment as well as the intensity corresponding to the photobleached region are displayed in Figure 3.7 A and B. The mobile fraction of TR-PI(4,5)P_2 was low, around 50%. This mobile fraction probably corresponds to the fraction of lipids in the upper layer of the SLB which is not in contact with the glass substrate. The PI(4,5)P_2 in the layer in contact with glass is most likely unable to diffuse. Because PI(4,5)P_2 is a highly negatively charged lipid (charge is -3.9 at pH 7.4) positively charged ions must bridge the electrostatic interaction with glass. To achieve PI(4,5)P_2 diffusion, those ions have to be transported. This can induce a very important friction as glass displays some rugosity at the atomic scale. Similar observations have been reported (Braunger et al., 2013), and different methods have been proposed to recover the mobility of PI(4,5)P_2. I tried removing Ca^{2+} ions by washing the bilayers with EDTA with no success. I also worked in more acidic conditions using Citrate buffer at a pH of 4.8 but the mobile fraction never exceeded 50%.

To obtain good fluidity of PI(4,5)P_2 in the control experiment, I changed the substrate. I chose mica, as it is less negatively charged than glass and atomically flat. Even if the head of the PI(4,5)P_2 interacts with positively charged ions, they would be able to diffuse along the mica. When I deposited the SUVs, I used freshly cleaved sheets of mica. No cleaning or activation process was necessary to observe lipid bilayers on the mica. However, the bilayers displayed many defects, mostly holes with micrometric sizes suggesting that the lipid mica interaction is weaker than the lipid glass interaction. These holes are pointed with arrows in the snapshots from a FRAP experiment displayed in Figure 3.7 C. The FRAP experiment were performed far enough from any of those holes and a trace is displayed in Figure 3.7 D. The mobile fraction of TR-PI(4,5)P_2 on the mica substrate was about 95%, showing that the PI(4,5)P_2 incorporated in the bottom layer was able to diffuse. The diffusion coefficient obtained was $D = 1.55 \pm 0.25\ \mu m^2/s$, value similar to the one obtained for Bodipy-TR ceramide in SLB on glass. I then added septins to these lipid bilayers and observed strong reshaping of the lipid bilayer which prevented the measurement of the diffusion coefficient. I will describe in details this observation in section 4.1.

3.1.5 Diffusion of PI(4,5)P_2 in GUVs

To remove any diffusion artefact from the substrate and prevent the disruption of the lipid bilayer upon the addition of septins, I chose to use Giant Unilamellar Vesicles

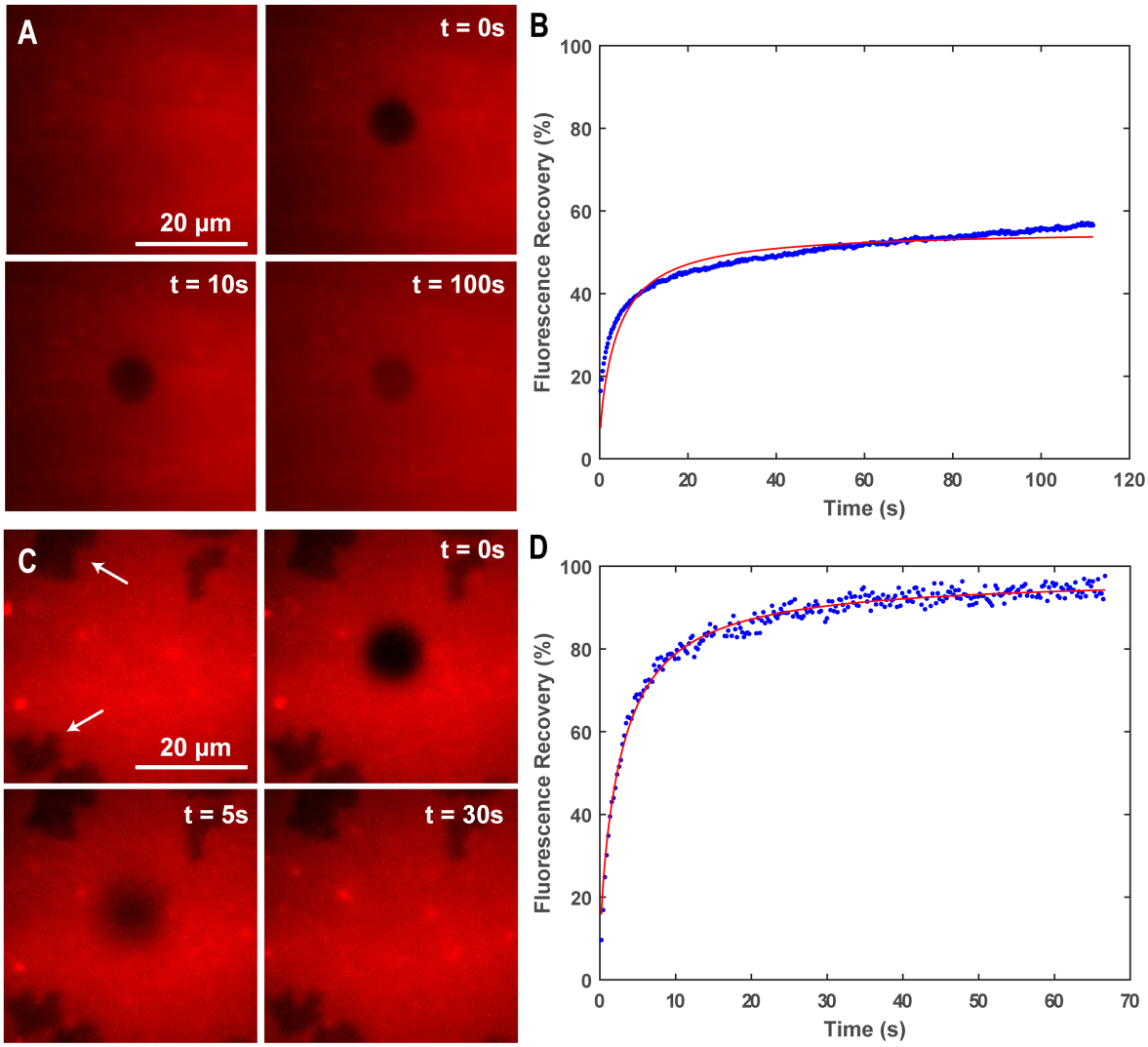

Figure 3.7 – Fluorescence recovery experiments performed on PI(4,5)P_2 tagged with Texas Red, incorporated in SLB deposited either on glass (A and B) or mica (C and D). (A) Snapshots obtained with TIRF microscopy, even after a few minutes, the bleached zone can still be distinguished. (B) Fluorescence intensity of the bleached zone as a function of time after overall bleaching correction. It shows that more than half of the lipids diffuse much more slowly than expected. (C) Snapshots obtained with TIRF microscopy, some defects are visible before the start of the experiment (arrows), but the bleached zone cannot be distinguished after less than a minute. (D) Fluorescence intensity of the bleached zone as a function of time after overall bleaching correction. The mobile fraction is about 95%.

as a model system for biomimetic membrane. The vesicles were manipulated with micropipettes. Using micropipettes I could lift the vesicles from the glass coverslip to prevent any GUV substrate interaction that would affect the diffusion of the TR-PI(4,5)P_2. I imaged the GUVs using spinning disk confocal microscopy to achieve simultaneously optical sectioning of the GUV and fast acquisition, essential for the FRAP experiment.

The FRAP experiments were performed on the bottom of the GUVs which is close to a flat surface for ROIs small compared to the radius of the vesicle. Snapshots from a

FRAP experiment are displayed in Figure 3.8 A. The photobleached region fits within the region of the GUV inside the focal volume. I used regions of 1 µm in radius, small enough to be able to correct for the photobleaching. Photobleaching results from the observation and can be corrected by monitoring the fluorescence intensity in another region of the GUV. I assayed GUVs made from both electro-formation on platinum wires and gel assisted swelling on PVA and compared the diffusion coefficients. The distribution of diffusion coefficients of TR-PI(4,5)P_2 for both growing methods are displayed in Figure 3.8 B. The PI(4,5)P_2 in the GUVs formed via gel assisted swelling showed significantly lower diffusion coefficient than those formed with electro-formation. This difference might come from polymers incorporated in the membrane as suggested by previous work (Faizi et al., 2022). I therefore decided to use GUVs prepared by electro-formation exclusively.

The diffusion coefficient of TR-PI(4,5)P_2 is $D = 1.7 \pm 0.1\ \mu m^2/s$, a value similar to the one obtained in SLBs on mica and a mobile fraction of 100 %. I then incubated the GUVs with GFP-tagged septins, and measured their effect on the diffusion of PI(4,5)P_2. From the distribution of diffusion coefficient, I obtained $D = 1.6 \pm 0.1\ \mu m^2/s$. The difference in diffusion coefficient is not significant enough to conclude. To further detail the effect of septins on the diffusion of PI(4,5)P_2, I plotted in Figure= 3.8 C the diffusion coefficient for the GUVs coated with septins against the density of septins on the GUV. The density of septins is expressed in fraction of the surface occupied by septin considering that one septin octamer occupies 4x32 nm^2. This fraction can reach above one as septins can bundle. Some effect might be detectable at fractions above 1 but such densities are rare and might not be relevant *in vivo*. Also, even though the diffusion coefficient might be affected, the mobile fraction is still about 100% as can be seen in Figure 3.8 D where the fluorescence in the photobleached area is displayed as a function of time for a vesicle with fraction of septins of 1.75.

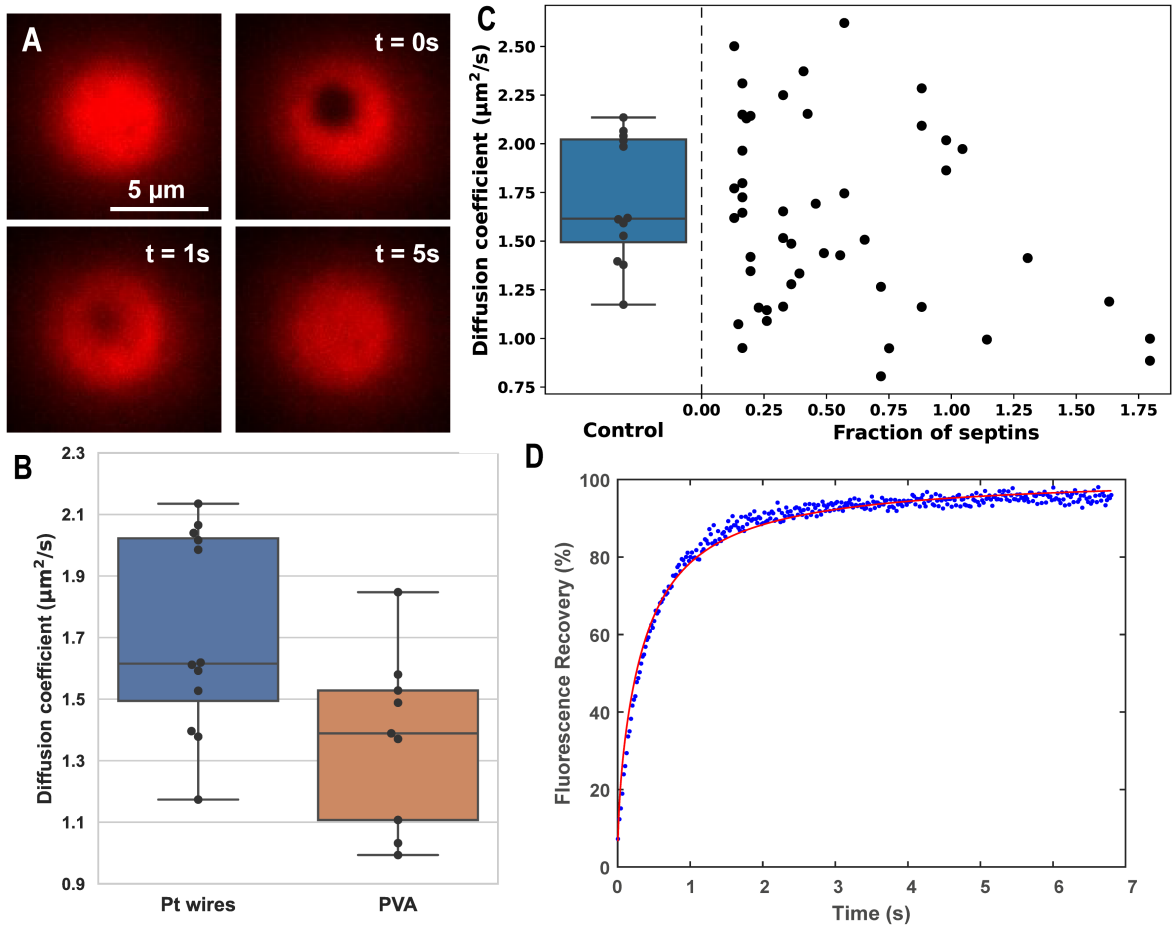

Figure 3.8 – Fluorescence recovery experiments performed on PI(4,5)P_2 tagged with Texas Red, incorporated in GUV. (A) Snapshots obtained using spinning disk confocal. (B) Diffusion Coefficient of PI(4,5)P_2 in the control case and as a function of the septin density on the GUV expressed as the faction of surface occupied by septin filaments. No clear effect was observed. (C) Diffusion coefficient of PI(4,5)P_2 in GUVs produced either by electro-formation or gel-assisted swelling. As some difference was observed, only the electro-formation method was used for the study. (D) Fluorescence intensity of the bleached zone as a function of time after overall bleaching correction. The mobile fraction was always above 95% even in the presence of septins.

Summary

- **Septins octamers diffuse on membranes and polymerise, generating immobile networks**
- **Lipids that do not interact specifically with septins can diffuse freely under the septin mesh**
- **Septins do not significantly immobilise PI(4,5)P_2, a lipid interacting specifically with septins**

3.2 Diffusion of model membrane proteins

Because septins do not seem to affect the diffusion of lipids in biomimetic membranes, I decided to use model objects to mimic membrane associated proteins. I wanted to model transmembrane proteins as well as proteins with different cytosolic sizes. I started by studying a simple model for a membrane associated protein by imaging a DSPE lipid associated to a PEG polymer and labelled with Cy5. I then used different systems to perform Single Particle Tracking on objects with defined geometries. I used three models, aquaporin, streptavidin and Quantum Dot to assay the effect of septins on the diffusion of objects with different size external to the membrane. Single Particle Tracking allowed the recovery of the characteristics of each individual trajectory and the obtention of more refined properties of the diffusion of my models of proteins.

3.2.1 Diffusion of DSPE-PEG2k

To mimic a protein anchored at the membrane with a cytosolic domain, I chose to use DSPE-PEG2k-Cy5. This lipid can be incorporated easily in the lipid mixture, and can be imaged by fluorescence microscopy. Its domain dimension, external to the membrane, corresponds to the gyration radius of the PEG polymer which depends on the length of the polymer chain and the size of the Cy5. For a PEG2k chain the gyration radius is equal to 3.7 nm, while the Cy5 is a small molecule, less than 1 nm in size. I added 1% of this lipid to my lipid mixture. I decided to use GUVs as a model membrane to prevent the interaction of the polymer chain with the substrate. I prepared GUVs by electro-formation and performed FRAP experiments on the DSPE-PEG2k-Cy5 lipids using a spinning disk confocal. Snapshots from a FRAP experiment are displayed in Figure 3.9 A.

The diffusion coefficient of the DSPE-PEG2k-Cy5 in the absence of septins was $D = 2.4 \pm 0.2\ \mu m^2/s$ and the mobile fraction was 100%. After septins addition at concentration of 300 nM, the diffusion coefficient was reduced to $D = 1.55 \pm 0.15\ \mu m^2/s$. To decipher whether an effect of the septin density could be recovered I plotted in Figure 3.9 B the diffusion coefficient of DSPE-PEG2k-Cy5 as a function of the fraction of the membrane occupied by septins. Some correlation can be observed between the septin density and the diffusion coefficient. The high septin density corresponds to low diffusion coefficient for the PEG lipid. Interestingly, the mobile fraction was still 100% even at the highest septin density.

This initial result suggested that septins could slow down the diffusion of membrane components with a domain external to the membrane but they did not prevent them from diffusing. However, this system was not ideal for multiple reasons. The first reason is that I am not able to distinguish between lipids from the inner leaflet and lipids from the outer leaflet. Because septins are only present on the outer leaflet, the inner leaflet lipids should be able to diffuse normally. The second reason is that at 1% DSPE-PEG2k-Cy5, the PEG will cover almost half of the lipid membrane, which might reduce the ability of septins to polymerise. The third reason is that at molar ratios required to perform FRAP, some crowding effect will start to appear in the diffusion behaviour. The PEG polymer chains will start to interact with one another. This effect becomes more important as the size of the particle of interest increases. Last, with FRAP, one cannot recover some of the refined properties of the diffusion that each particle experiences such as the “hop diffusion”.

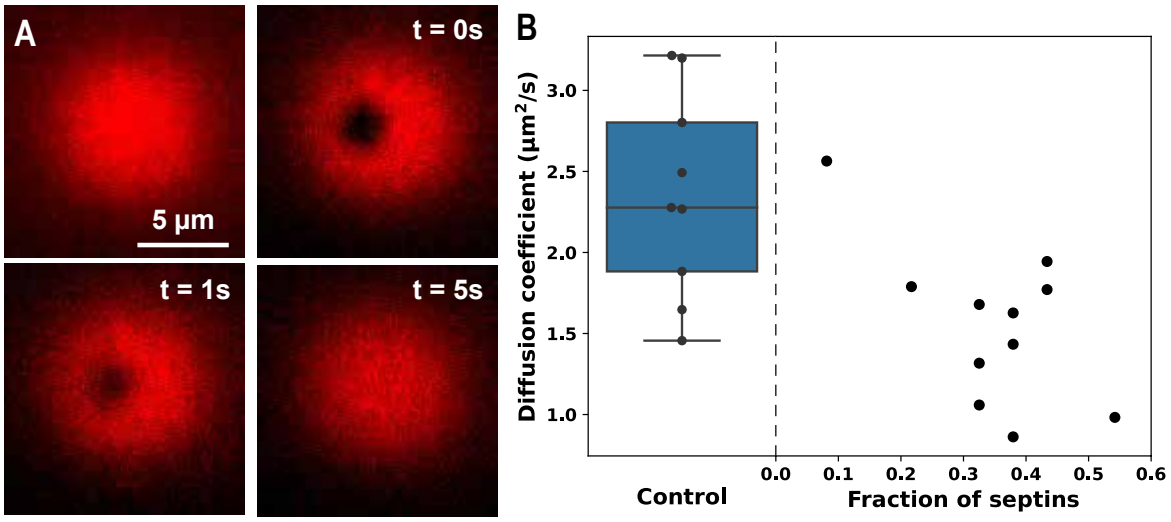

Figure 3.9 – Fluorescence recovery experiment performed on DSPE-PEG2k-Cy5 lipid incorporated in a GUV produced by electro-formation. (A) Snapshots obtained using spinning disk confocal. (B) Diffusion coefficient in the control and as a function of the septin density. A drop of diffusion coefficient can be observed when septin density increases.

3.2.2 Presentation of the SPT experiments

To overcome these issues, I decided to use Single Particle Tracking (SPT) with different models of membrane associated proteins. These models will allow to track particles on the outer leaflet of the vesicle exclusively and to work at low densities to neither affect the binding of septins to the membrane nor introduce crowding effect and recover the properties of single trajectories.

I have performed Single Particle Tracking experiments on GUVs made by electro-formation. The use of GUVs as opposed to SLBs will prevent any effect from the substrate on the diffusion of my models of proteins. I captured the vesicles using micropipettes to also prevent any contact with the glass coverslip. Using wide-field imaging, I was able to obtain trajectories of particles diffusing at the bottom of GUVs. The experimental setup is sketched in Figure 3.10 A. Trajectories obtained using this experimental setup are displayed in Figure 3.10 B.

To mimic different types of membrane associated proteins, I used three different model systems. The idea of those models is to study the influence of the size of the domain external to the membrane on the ability of septins to create diffusion barriers. Those models were chosen to mimic the proteins known to be blocked in vivo by diffusion barriers established by septins. Reported proteins include exclusively membrane associated proteins and most of them include a cytosolic domain of varying size with few exceptions (CD4, Sstr3).

The models are displayed in Figure 3.10 C. I studied three models, each corresponding to a type of membrane associated protein. (i) To study whether proteins deprived of cytosolic domain could sense the formation of a diffusion barrier by septins, I used aquaporin, a water channel that has no cytosolic domain. (ii) To mimic proteins with a rather large cytosolic domain, I used streptavidin, a tetramer commonly used for its specific interaction with biotin. The tetramer of streptavidin is about 6 nm in size.

I used DSPE-PEG-biotin lipids to anchor the streptavidin to the membrane. (iii) Finally, many proteins reported as being blocked by the diffusion barriers are involved in complexes such as the exocyst and the polarisome. To mimic such complexes, I used Quantum Dots, which are covered with streptavidin. The total size of the particle made of Quantum Dot and streptavidins is about 17 nm. I used the same biotinylated lipids to bind the Quantum Dots to the membrane.

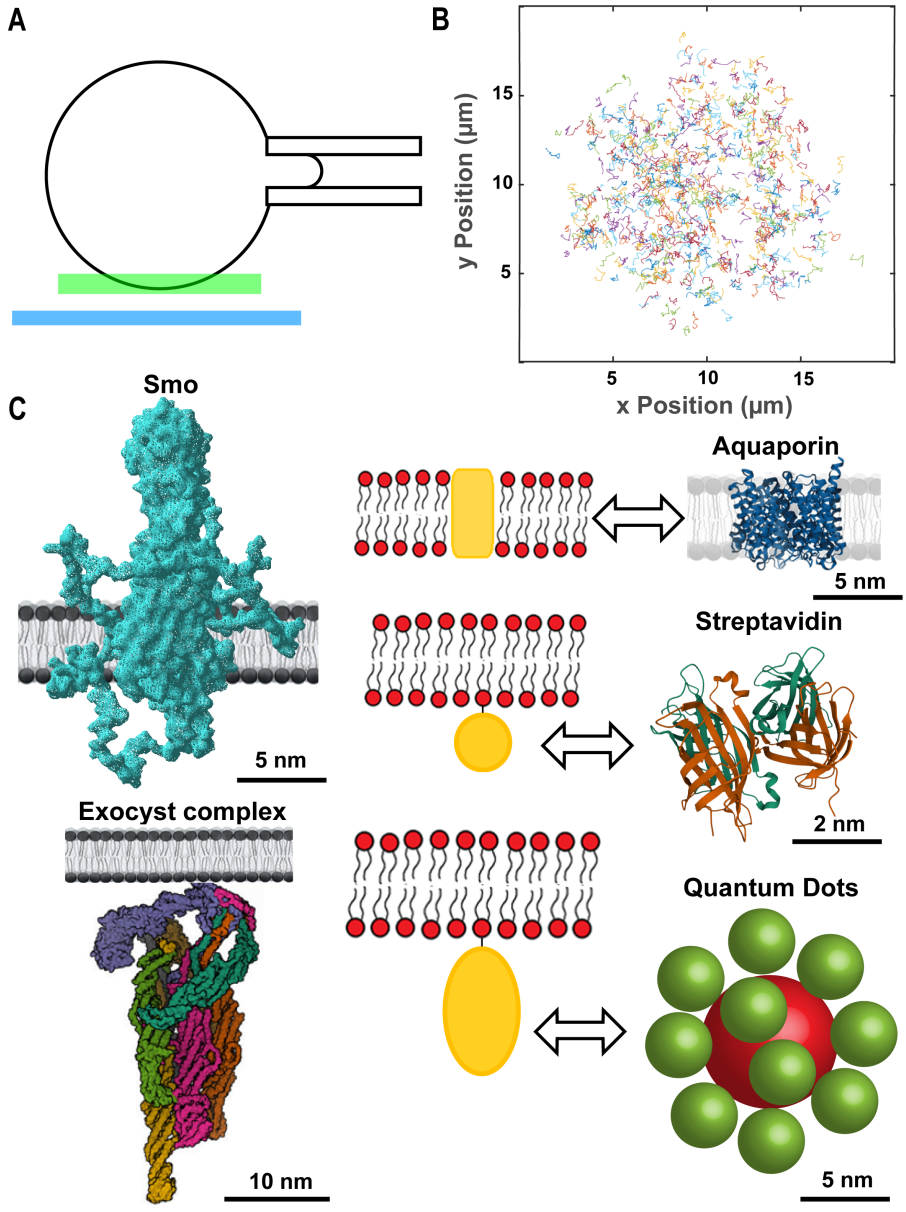

Figure 3.10 – (A) Scheme of the setup, a GUV is caught by micropipette aspiration, lifted from the glass coverslip and the bottom plain is imaged to perform SPT. (B) Trajectories obtained from the bottom of a GUV, with different colours to distinguish the individual trajectories. (C) (left) Structure of proteins (Smo and the Exocyst complex) that have been reported to be blocked by septin dependent diffusion barriers. (right) The different models used in the SPT experiment to mimic different types of membrane associated proteins: transmembrane proteins with no cytosolic domain using aquaporin(top), proteins with a cytosolic domain using streptavidin (middle) and complexes associated to the membrane using Quantum Dots (bottom).

Because my SPT experiments were performed on GUVs, I had to correct for the geometry on which my particles were diffusing. A sketch of the geometry is shown in Figure 3.11 A. The positions of the particles are recorded on the camera which only gives the position in the focal plane, while the position on the axis orthogonal to the focal plane is lost – Figure 3.11 B. First, I estimated the error made by not correcting for the different geometry. This error depends on the position on the GUV. It is minimal at the very bottom of the GUV and increases with the distance from the centre. Typically, for a GUV of size R = 5 µm, the error on the edges of the focal plane will reach about 15%. To avoid having to perform this correction, it is possible to use exclusively big vesicles (R ¿ 10 µm). Indeed, the correction is inversely proportional to the radius of the vesicle. It is also possible to limit the region of interest to the centre of the vesicle. However, it is also possible to fully calculate the correction which enables the study of more vesicles and bigger region of interest which allows more trajectories to be analysed.

To correct for the spherical shape, no transformation exist that keeps the distances between all points equal. It is equivalent to making a flat map of the Earth. However the distance between points can be easily computed as:

$$d = R\ \theta \tag{3.1}$$

Where d is the distance between two points, A and B, on the sphere, θ is the angle at the centre of the sphere separates which those two points, and R is the radius of the sphere. Therefore, only the angle separating the two points has to be computed. This is done knowing the position of the projection of the centre of the sphere on the focal plane. The vertical position of the points can then be recovered from the equation of a sphere which allows for the calculation of the scalar product:

$$\overrightarrow{OA}.\overrightarrow{OB} = R^2 cos(\theta) \tag{3.2}$$

I performed this correction for all the SPT experiments performed on GUVs.

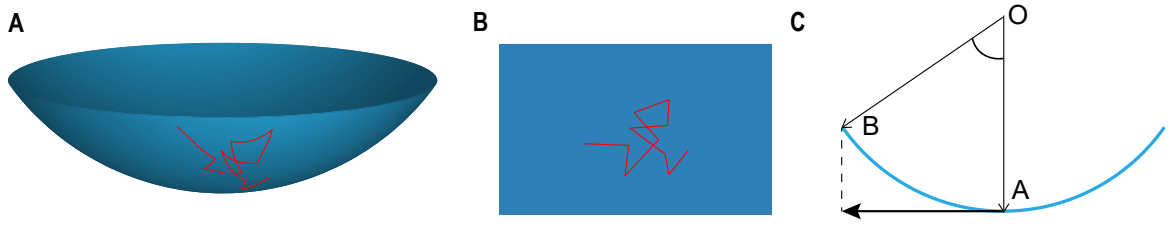

Figure 3.11 – Correction for the calculation of distances for the single particle experiment. (A) Trajectories follow the shape of the vesicle while the camera only gives the projection on a plane (B). The calculation for the actual distance can be performed by looking at the length of the arc between the two position (C).

3.2.3 Diffusion of aquaporin, model for transmembrane protein

The first model protein I studied was the aquaporin, a water channel that possesses no cytosolic domain. It was therefore a good model to study the diffusion of transmembrane proteins without any known specific interaction with septins. Aquaporin is a tetramer making a barrel with a diameter of 6 nm. The aquaporin was labelled

with Atto647N via a cysteine maleimide conjugation. When performing SPT, I had to ensure that aquaporins were correctly inserted in the GUV and that the density was optimised for the reconstruction of trajectories. Experimental conditions are described in the section 2.7.1. For this experiment, I labelled the membrane with DPPE Atto532. Indeed, Texas red has a maximum of excitation around 591 nm and its emission spectra extends beyond 700 nm, giving high background signal in the 647 laser line, preventing single particle observation.

After the incorporation of aquaporins in GUVs, I imaged the vesicles on the microscope previously optimised for single particle imaging. The GUVs were captured using micropipette aspiration, and gently lifted from the glass coverslip. The signal on the equatorial plane of the GUV was recorded to ensure that the vesicle is unilamellar. I then focused at the bottom of the GUV using the signal from the fluorescent lipids. Often, the focus would be slightly offset, which meant that the correction of the sphere geometry was crucial. I then used maximum laser power and tried exposure times corresponding to those used for the camera test – section 2.7.1. I used 10 ms exposure time, which seemed the best compromise between the blur of motion and the amount of photons received per molecule. I recorded movies for 20 s after which most of the Atto647N molecules were bleached. A snapshot from one of the SPT experiment is displayed in Figure 3.12 A. The single molecules appear much dimmer than in the experiment performed on SLB, which is normal when going from TIRF to wide-field imaging. The loss of signal is also combined with an increased background. The precision of localisation is hereby about 100 nm as compared with 30 nm achieved on the supported bilayer. The distribution of precision of localisation for individual trajectories is displayed in Figure 3.12 B.

The diffusion coefficient for aquaporin in the absence of septins was 2.4 $\mu m^2/s$ (N = 6 preps; 19 GUVs). This value is in good agreement with published values and also with the value obtained for the diffusion of lipids. Upon addition of septins, the average diffusion coefficient was reduced to 2.0 $\mu m^2/s$ (N= 6 preps; 25 GUVs). The distribution of diffusion coefficients are displayed in Figure 3.12 C. The difference in average diffusion coefficient value results from a population of very slow diffusing particles when septins were added (highlighted in Figure 3.12 C). To study in more details this "immobile" population, I performed additional analysis.

I first plotted the accumulation of detections of single molecules during a full movie on each GUV. They are obtained by performing the detections of single particles on each frame of the movies, then the xy positions of all the detections are plotted in a single image. The map obtained from the experiment on aquaporin when septins were added to the vesicles is displayed in Figure 3.12 D. If the particles can explore the whole surface of the vesicle, the map should be homogeneous. Indeed, in the control experiment, all the maps were rather homogeneous. In the presence of septins, most maps were still homogeneous, sometimes with a bright spot which would correspond to an immobile particle, detected multiple times at the same position during the movie.

To estimate the proportion of immobile or very slow diffusing trajectories I chose a threshold of diffusion coefficient to sort out the mobile trajectories from the immobile ones. I chose this threshold to have minimum immobile trajectories in the control experiment but still be sensitive to changes in the diffusion coefficient. I chose 0.1 $\mu m^2/s$, because it corresponds to the lowest values of the distribution in the control experiment. I thus obtained a fraction of immobile trajectories of 6% in the presence of septins. However, this percentage does not reflect the percentage of immobile particles. Indeed,

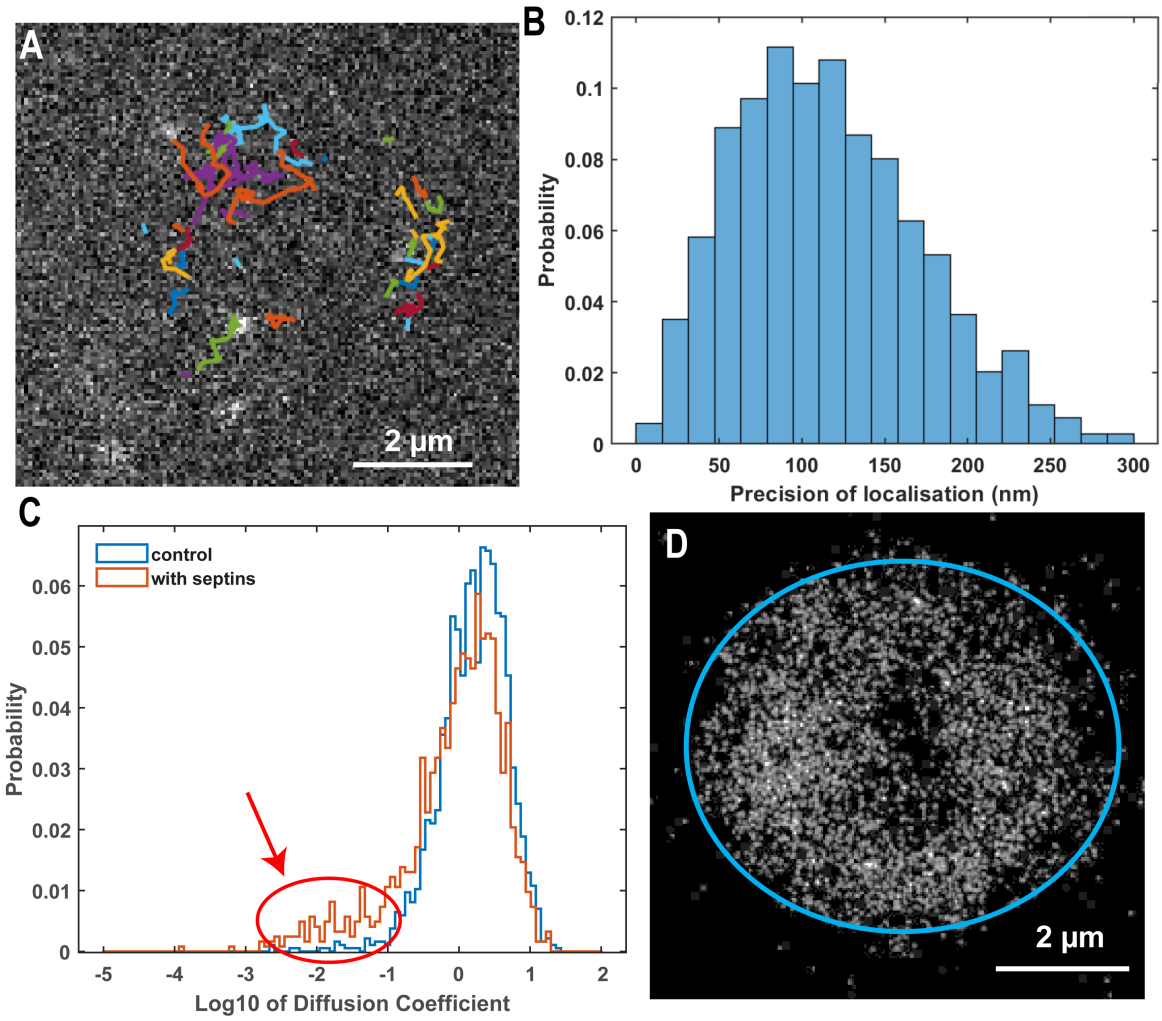

Figure 3.12 – Single Particle tracking experiment performed on aquaporin labelled with Atto647N incorporated in GUVs. (A) Snapshot of the aquaporins at the bottom of a GUV, exposure time is 10 ms. Trajectories obtained from the visible aquaporins are overlapped with the snapshot. One aquaporin protein could give multiple trajectories as it would sometimes not be detected. Different trajectories are colour coded to distinguish them. (B) Distribution of the precision of localisation of the aquaporins. The peak is located at about 100 nm. (C) Accumulation of localisation of Single Particles during a 20 s movie. On each frame all the detections are recorded, and the image is created by indicating all the detections during the full movie as a single dot. (D) Distribution of the diffusion coefficient of single trajectories in the control experiment and in the presence of septins. The mean diffusion coefficient is not affected but for a population of trajectories with very low diffusion coefficient – lower than 0.1 $\mu m^2/s$.

the mobile particles will on average give shorter trajectories as they can diffuse out of the observation region, and new particles can come in the volume.

One way to estimate the ratio of mobile to immobile particles is by accounting for the length of each trajectory. Considering that the whole vesicle is illuminated homogeneously, the ratio of mobile to immobile particles is conserved during the experiment. Therefore, by weighting each trajectory with its length, it is possible to obtain the ratio of immobile particles. Performing this analysis, I obtained obtained an immobile frac-

tion of 2 ± 0.4 % for the control experiment and 15 ± 3 % when septins are bound to the membrane. The distribution of immobile fractions for individual GUVs is displayed in Figure 3.13 A.

To assay the possibility that trajectories could display anomalous diffusion, I plotted in Figure 3.13 B the heatmaps of the diffusion coefficient and the anomalous diffusion coefficient for individual trajectories in both the control experiment and after addition of septins. The distribution was more disperse in the experiment with septins as compared with the control, but the mean anomalous diffusion coefficient was also equal to 1, and no population with anomalous coefficient lower than 1 was detected. This shows that no anomalous diffusion was detected even in the presence of septins. Regarding the very slow diffusing population, the alpha coefficient is not relevant for immobile particles.

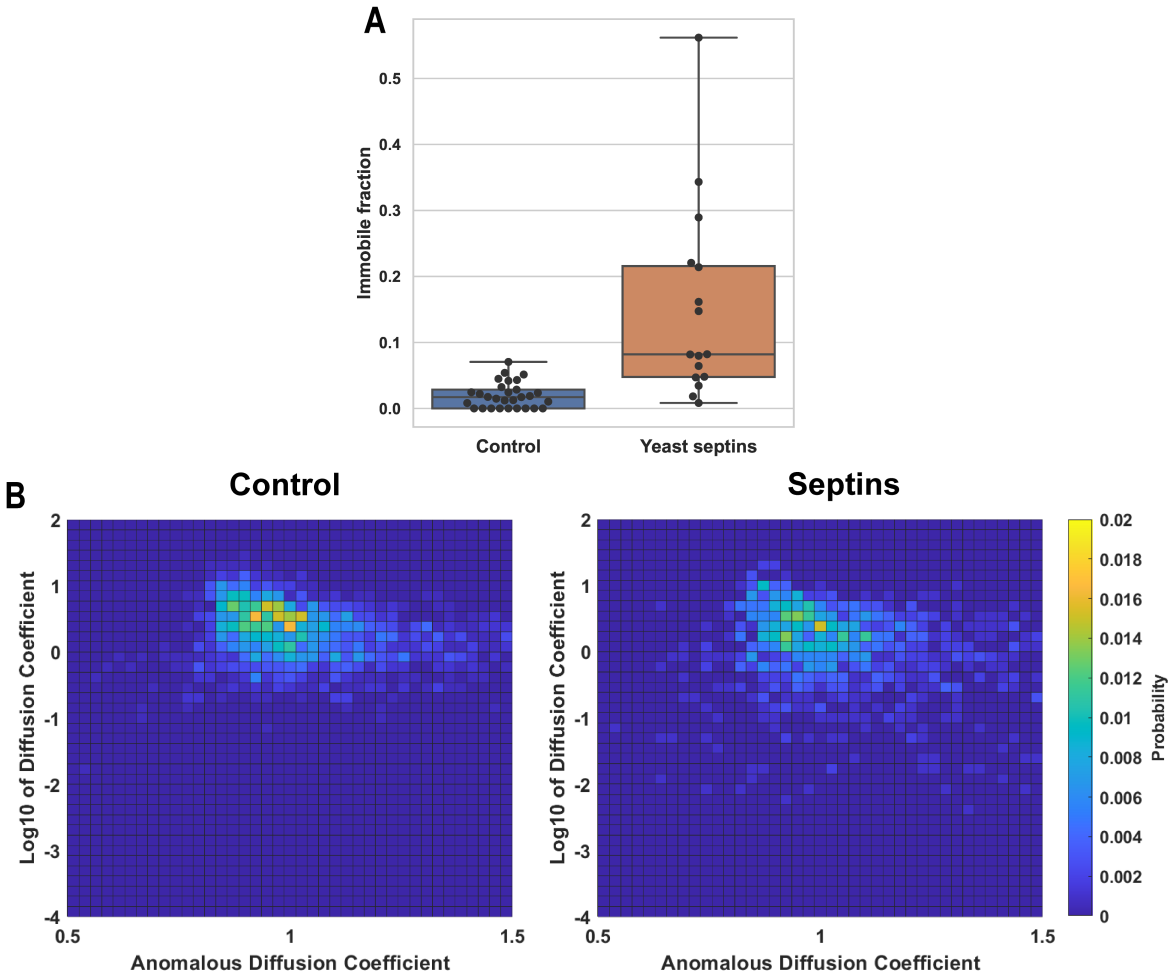

Figure 3.13 – (A) Immobile fraction of particles in the SPT experiment on aquaporin. Each dot represents a single GUV. The threshold for distinguishing immobile particles was chosen to have less than 2% of immobile particles in the control experiment. (B) Heatmaps of the distribution of anomalous diffusion coefficient and diffusion coefficient in the control experiment and when septins are bound to the membrane. No anomalous diffusion was detected.

Multiple factors could explain this immobile population. Upon the addition of septins in the sample, many small vesicles will adhere on the septin filaments bound to the membrane. If some aquaporins are located in one of these small vesicles, they will be unable to diffuse. Also septins can sometimes generate local deformations such as

invaginations or tubes. These deformations could strongly reduce the apparent diffusivity of some of the membrane components. Overall, I considered this population too small to interpret this observation as the formation of a significant diffusion barrier. I concluded that upon the addition of septins, the aquaporins were still able to diffuse in the bilayer, similarly to the lipids.

3.2.4 Diffusion of Quantum Dots, model for protein complexes

I then studied the diffusion of membrane bound objects displaying a large cytosolic domain. These model systems were meant to mimic protein complexes that are anchored to the plasma membrane and are blocked by diffusion barriers established by septins. A good example of such complex is the yeast exocyst, a complex responsible for the fusion of vesicles with the plasma membrane which is localised exclusively in the daughter cell during cell division. This complex stands out from the membrane by about 30 nm. To study objects of similar sizes, I used Quantum Dots 655, conjugated to streptavidins. The streptavidins passivate the Quantum Dots, and allow their binding to biotin. I added 0.004% of DSPE-PEG-biotin lipids to the lipid mixture, and grew GUVs by electro-formation on platinum wires. The GUVs were collected after overnight growth and left to incubate with Quantum Dots at concentration of 100 pM for 1 hour at 4°C. This guarantees that the Quantum Dots are located on the outer leaflet of the vesicle membrane. When adding septins, I mixed the GUVs (already coated with the Quantum Dots) with yeast septins at concentrations of 200 nM directly in the observation chamber. I captured the GUVs and observed them with fluorescence microscopy.

In this experiment, the vesicles did not have to be necessarily unilamellar because Quantum Dots can exclusively interact with the outer leaflet of the external bilayer. However, to ensure that there would not be an effect from the friction with inner bilayers, I used unilamellar vesicles exclusively. I imaged the Quantum Dots to focus on the bottom of the vesicle, because they are much less sensitive to photobleaching as compared with Atto647N. By using Quantum Dots, I could therefore focus more precisely than using the fluorescent lipids. Because Quantum Dots are brighter than Atto647N, I could also reduce the exposure time to 5 ms. A snapshot acquired with 5 ms exposure time from a 20 s movie is displayed in Figure 3.14 A. The precision of localisation in this experiment was about 60 nm, better than for the Atto647N. The distribution for each individual trajectory is displayed in Figure 3.14 B. I checked that I did not record any unbinding event from the vesicle, indicating that the Quantum Dots are indeed anchored to the lipid membrane.

I plotted the distribution of diffusion coefficient for each single trajectory in the control experiment and after addition of yeast septins in Figure 3.15 A. The diffusion coefficient is plotted in log scale. In the control experiment, I obtained a diffusion coefficient of 2.0 $\mu m^2/s$ (N=3 preps; 9 GUVs). It is important to note that despite the size of the Quantum Dots, the drag they create is negligible compared to the one coming from the lipids in the bilayer. A free floating Quantum Dot is expected to have a diffusion coefficient of about 20 $\mu m^2/s$. When septins were bound to the membrane, the diffusion coefficient was reduced tenfold to 0.22 $\mu m^2/s$ (N=3 preps; 10 GUVs). The distribution of diffusion coefficients in the presence of septins displayed a long tail towards the very low diffusion coefficients, with many trajectories having diffusion coefficients below 0.1 $\mu m^2/s$.

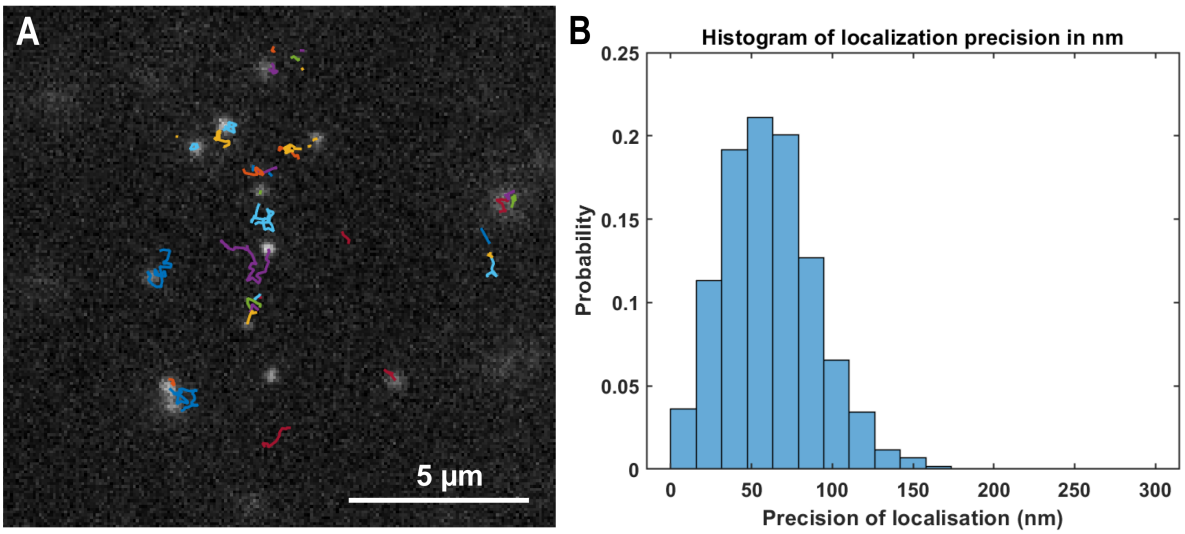

Figure 3.14 – Single Particle Tracking experiment on quantum dots with streptavidin bound to DSPE-PEG-biotin incorporated in a GUV. (A) Snapshot of the quantum dots, exposure time is 5 ms. Trajectories obtained from the visible Quantum Dots are overlapped with the snapshot. One Quantum Dot protein could give multiple trajectories as they blink rapidly. Different trajectories are colour coded to distinguish them. (B) Distribution of precision of localisation, peak is around 60 nm.

To estimate the proportion of the population corresponding to immobile or very slow diffusing particles I applied the same strategy as for the aquaporin, with a threshold for immobile fraction set at 0.1 $\mu m^2/s$. I obtained an immobile fraction for the control experiment of 1.3 ± 0.2 %. In the presence of septins, the immobile fraction significantly increased to 55 ± 7 %. The distribution of immobile fractions of particles of individual GUVs is plotted in Figure 3.15 B. When removing this population of immobile particles, the average diffusion coefficient is still much lower than in the control experiment, indicating that the diffusion of all the particles is reduced by the addition of septins on the vesicle.

I plotted the accumulations of localisations for both the control experiment and after the addition of septins. Two maps constructed by accumulation of localisations during 20 s movies in the presence of septins are displayed in Figure 3.16 B and C. In the control experiment, the maps showed a uniform disk – Figure 3.16 A – as expected for particles free to diffuse on the membrane. Upon the addition of septins, the maps are completely changed. They display both bright points (yellow arrows), and linear traces (white arrows). Each point and linear trace corresponds to a single Quantum Dots giving multiple detections in the same region during the 20 s movie. The points correspond to the immobile fraction, and the lines to the mobile fraction. These maps show that all Quantum Dots are constrained to diffuse in small regions. It is unclear why some Quantum Dots are immobile while others can still diffuse. However, Quantum Dots diffusing along lines clearly show constrained diffusion. They are most likely trapped between two parallel sets of septin filaments. The width of those lines is limited by the precision of localisation (60 nm), indicating that the sets of septin filaments are closer than the precision of localisation. Images obtained from electron microscopy show that in the range of concentrations used for this experiment, septin filaments are typically separated by less than 30 nm. The linear regions were typically a few micrometres long,

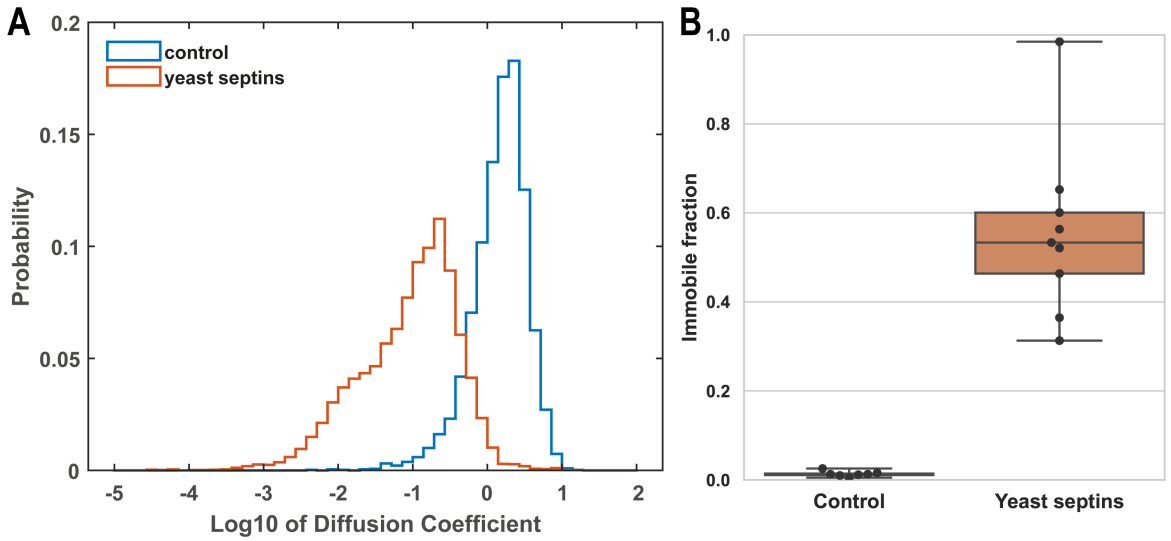

Figure 3.15 – (A) Distribution of diffusion coefficients in log scale of quantum dots in the control experiment and when yeast septins interact on the membrane. (B) Immobile fraction of quantum dots in the control experiment and when septins interact on the membrane.

and showed similar orientations for regions close to one another. They reveal a typical nematic organisation for septin filaments bound to the vesicle.

To study the diffusion mode experienced by Quantum Dots, I plotted in Figure 3.17 the heatmaps of the diffusion coefficient and the anomalous diffusion coefficient for individual trajectories in both the control experiment and after addition of septins. As expected for the control experiment, the distribution shows one population with an anomalous diffusion coefficient close to 1, corresponding to free brownian motion. In the presence of septins, the distribution was more dispersed, especially for the immobile particles, for which the anomalous diffusion coefficient is not relevant. For the population displaying some diffusion, the anomalous diffusion coefficient was still centred around 1. Therefore, no anomalous diffusion was detected.

Considering particles freely diffusing in one dimension, the diffusion coefficient would have been simply divided by a factor of 2. However, the diffusion coefficient of the trajectories diffusing in the linear region is divided by a factor of more than 4 compared with the control experiment. This reduction does not result from the boundaries limiting the length of the trajectories because this would be detected in the anomalous diffusion coefficient. This reduction in the diffusion coefficient indicates that septins also add friction to the Quantum Dots as expected from its size, similar to the typical distance between septin filaments.

From those observations, I concluded that Quantum Dots were not able to cross septin filaments. Septins would therefore be able to act as diffusion barriers for large protein complexes of more than 15-20 nm above the membrane.

3.2.5 Diffusion of streptavidin, model for cytosolic domain

Because septins were able to block the diffusion of Quantum Dots, mimicking large protein complexes, I wanted to assay their effect on the diffusion of models with smaller domain external to the membrane. Some of the proteins that have been reported to

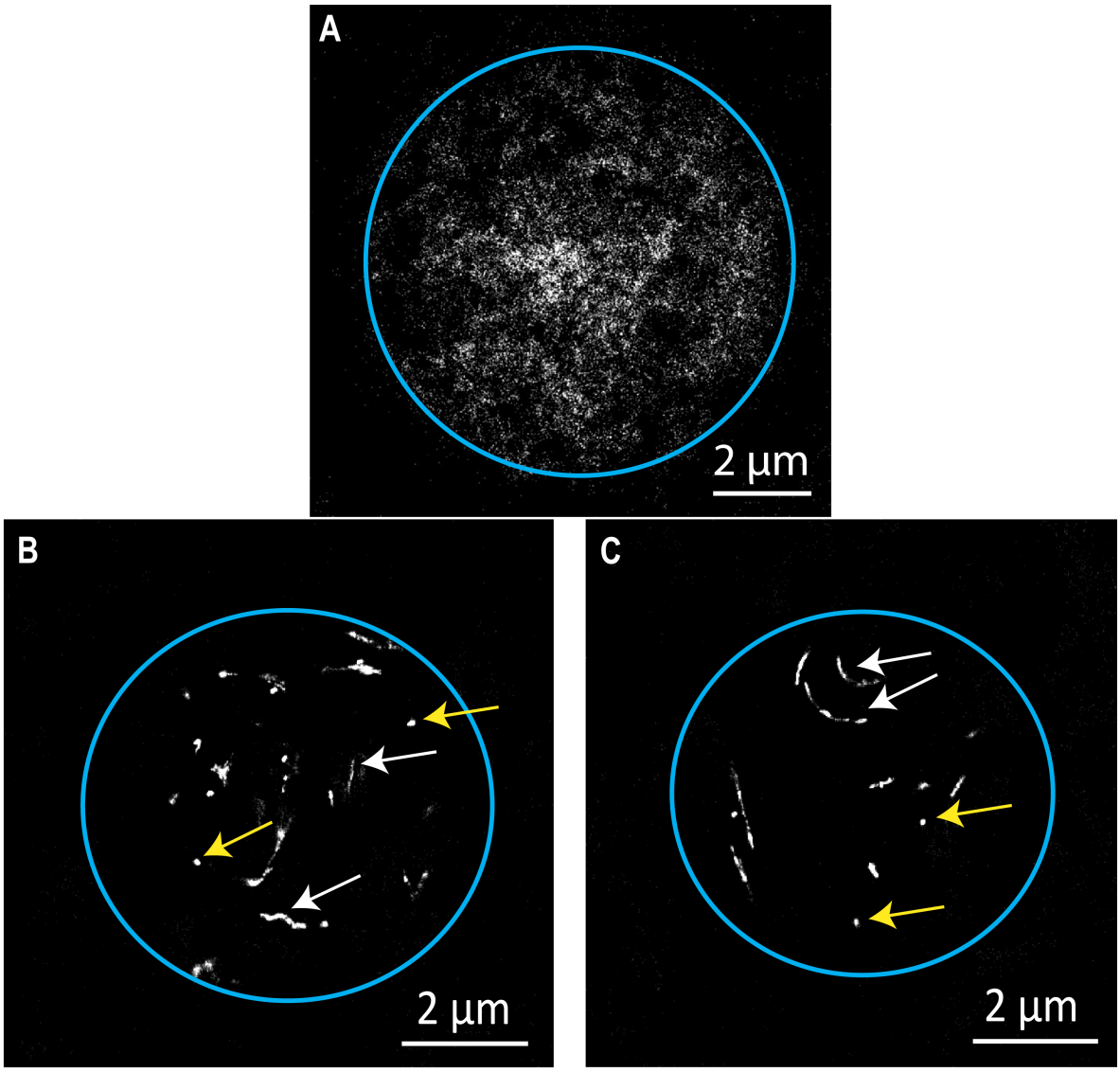

Figure 3.16 – Accumulations of quantum dots during 20s movies. (A) From the control experiment. (B) and (C) after the addition of septins. Long linear traces (arrows) correspond to a single quantum dots diffusing in a linear region during the movie.

be arrested by diffusion barriers established by septins have cytosolic domains smaller than 5 nm – such as the Smo protein in cilia. I thereby decided to assay the ability of septins to form a diffusion barrier for molecules with a cytosolic domain of similar size. I therefore chose streptavidin as a model. Streptavidin forms a tetramer with a size of 5 to 6 nm, and can bind to biotin. I used the same biotinylated lipids as the ones used for the Quantum Dots to anchor the streptavidin to the membrane, and used streptavidin labelled with Atto647N. I optimised the density of streptavidin bound to the membrane as described in section 2.7.1. I used 0.001% of DSPE-PEG-biotin in the lipid mixture, and DPPE Atto532 to replace Bodipy-TR as explained in the aquaporin experiment. After electro-formation of the GUVs, I incubated the streptavidin-Atto647N with the GUVs at concentration of 20 pM for 1 hour at 4°C. The streptavidin can only interact with the outer leaflet of the vesicle.

The septin incubation and subsequent observation was performed similarly as for the Quantum Dots experiment, except that the focus on the bottom of the vesicle was

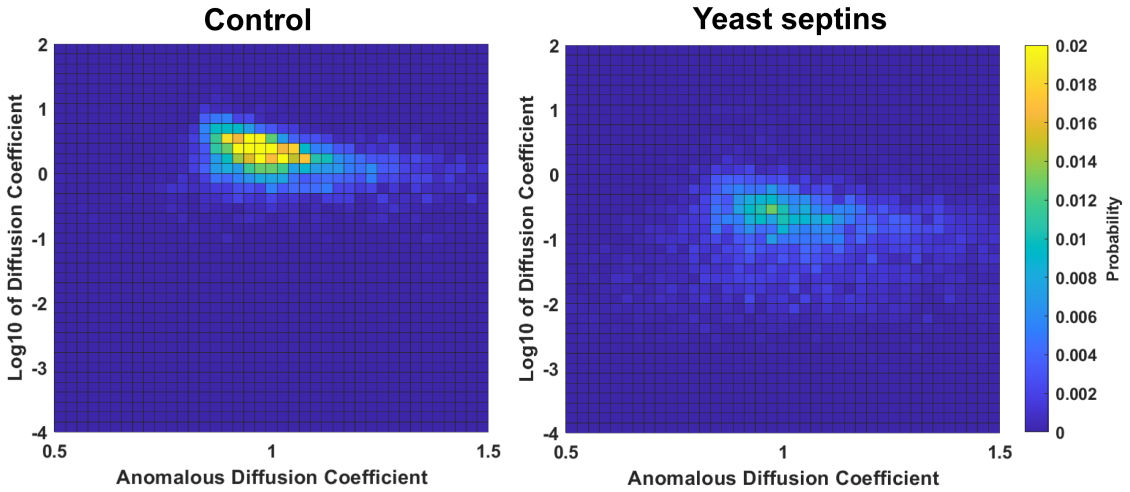

Figure 3.17 – Heatmaps of the distribution of anomalous diffusion coefficient and diffusion coefficient obtained for Quantum Dots in the control experiment and when septins are bound to the membrane.

performed using the DPPE Atto532 signal in order to preserve the Atto647N from photobleaching before the experiment. I used an exposure time of 10 ms optimised for the Atto647N on the aquaporins. A snapshot from a 20 s movie is displayed in Figure 3.18 A. The precision of localisation obtained with this system was 100 nm, similar to the one obtained with aquaporin. The distribution of precision of localisation is displayed in Figure 3.18 B. I did not observe any unbinding event of the streptavidin, indicating that the streptavidin is stably anchored to the membrane similarly to the Quantum Dots.

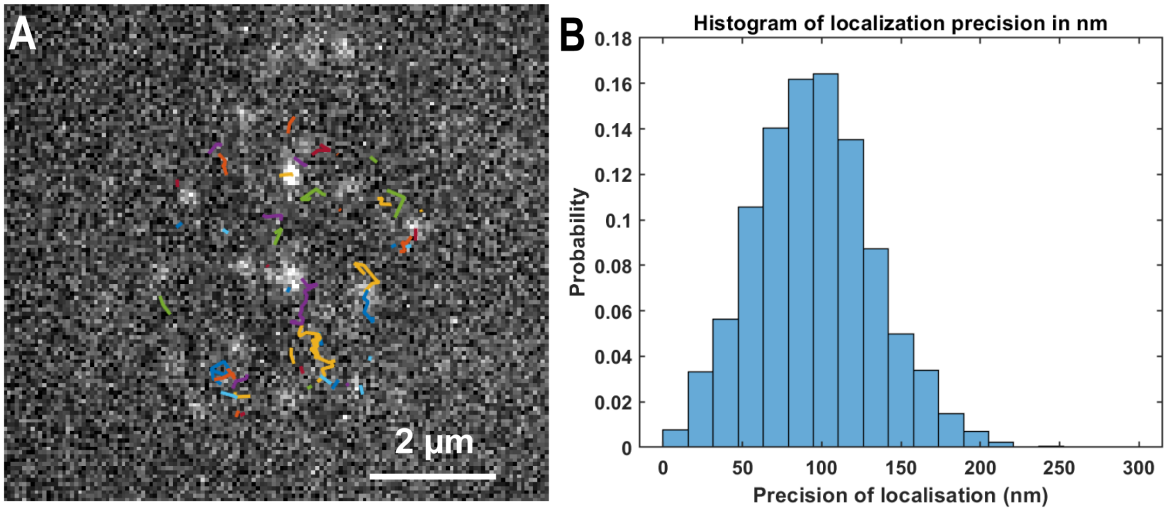

Figure 3.18 – Single Particle tracking experiments performed on streptavidin labelled with Atto647N and bound to DSPE-PEG-biotin lipids incorporated in GUVs. (A) Snapshot of the streptavidins at the bottom of a GUV, exposure time is 10 ms. Trajectories obtained from the visible streptavidins are overlapped with the snapshot. One streptavidin protein could give multiple trajectories as it would sometimes not be detected. Different trajectories are colour coded to distinguish them. (B) Distribution of the precision of localisation of trajectories. Peak is at 100 nm.

Diffusion behaviour of streptavidin

The distribution of diffusion coefficient for the streptavidin anchored to one lipid in the membrane in the control experiment and after addition of septins is displayed in Figure 3.19 A. The diffusion coefficient obtained for the streptavidin in the absence of septins was 1.8 $\mu m^2/s$ (N = 2 preps; 7 GUVs), similar to the one obtained with Quantum Dots. In the presence of septins, the distribution of diffusion coefficient displays a long tail towards the very slow diffusing or immobile particles. The average diffusion coefficient is therefore reduced to 0.56 $\mu m^2/s$ (N = 3 preps; 9 GUVs). Removing the slow diffusing trajectories, the average diffusion coefficient was still only equal to 0.71 $\mu m^2/s$, indicating that the diffusing particles were diffusing more slowly than in the control experiment. Two maps generated by the accumulation of detections during a movie in the presence of septins are displayed in Figure 3.19 C and D. A map obtained from a controlled experiment is displayed in Figure 3.19 D for comparison. The maps from the control experiment were homogeneous disks as expected when no septins are present. In the presence of septins, the maps showed an homogeneous background with bright spots (pointed by arrows). Those bright spots correspond to immobile streptavidins, and the homogeneous background to streptavidins able to explore the full surface of the vesicle. In this experiment no immobile point was ever detected to suddenly diffuse, and vice versa.

The immobile fraction of streptavidin was evaluated using the same strategy as described earlier. The immobile fractions for each GUV in the different experiment are displayed in Figure 3.20 A. The immobile fraction for the control experiment was 2 ± 0.2 %. The fraction reached 40 ± 7 % after the addition of septins. The immobile fraction was therefore quite important, close to the values obtained for Quantum Dots. I was not able to explain the the existence of this immobile fraction.

I then plotted the heatmaps of the distribution of the diffusion coefficient and the anomalous diffusion coefficient for each individual trajectory in Figure 3.20 C. As expected, the distribution in the control experiment is centred around 1 for the anomalous diffusion coefficient. In the presence of yeast septins, the distribution is more spread, but still centred around one, indicating that no anomalous diffusion could be detected in this experiment.

After comparing those results with the ones obtained with Quantum Dots, I can draw the conclusion that while some streptavidins are immobile, some were able to diffuse through the septin network. However, better quantification was necessary for the characterisation of the diffusion of streptavidin. In addition, I performed different control experiments to ensure that all the detections were only streptavidins bound to the vesicle.

As a first control I removed the DSPE-PEG-biotin lipid from the membrane, to ensure that streptavidin did not bind non specifically to lipids or septins. Working under experimental conditions similar to the real experiments, I did not observe any streptavidin bound to the vesicle in the absence of septins. In the presence of septins, only one to two streptavidins were found per GUV. Therefore the probability of having one of them on the bottom of the GUV – the only part imaged during the SPT experiment – was low.

I also replaced the GFP-tagged yeast septins by unlabelled septins to ensure that the GFP tag is not responsible for either blocking or allowing the diffusion of streptavidin. The distributions of diffusion coefficients for the dark septins and the GFP-tagged septins are displayed in Figure 3.20 B. No significant difference was observed between

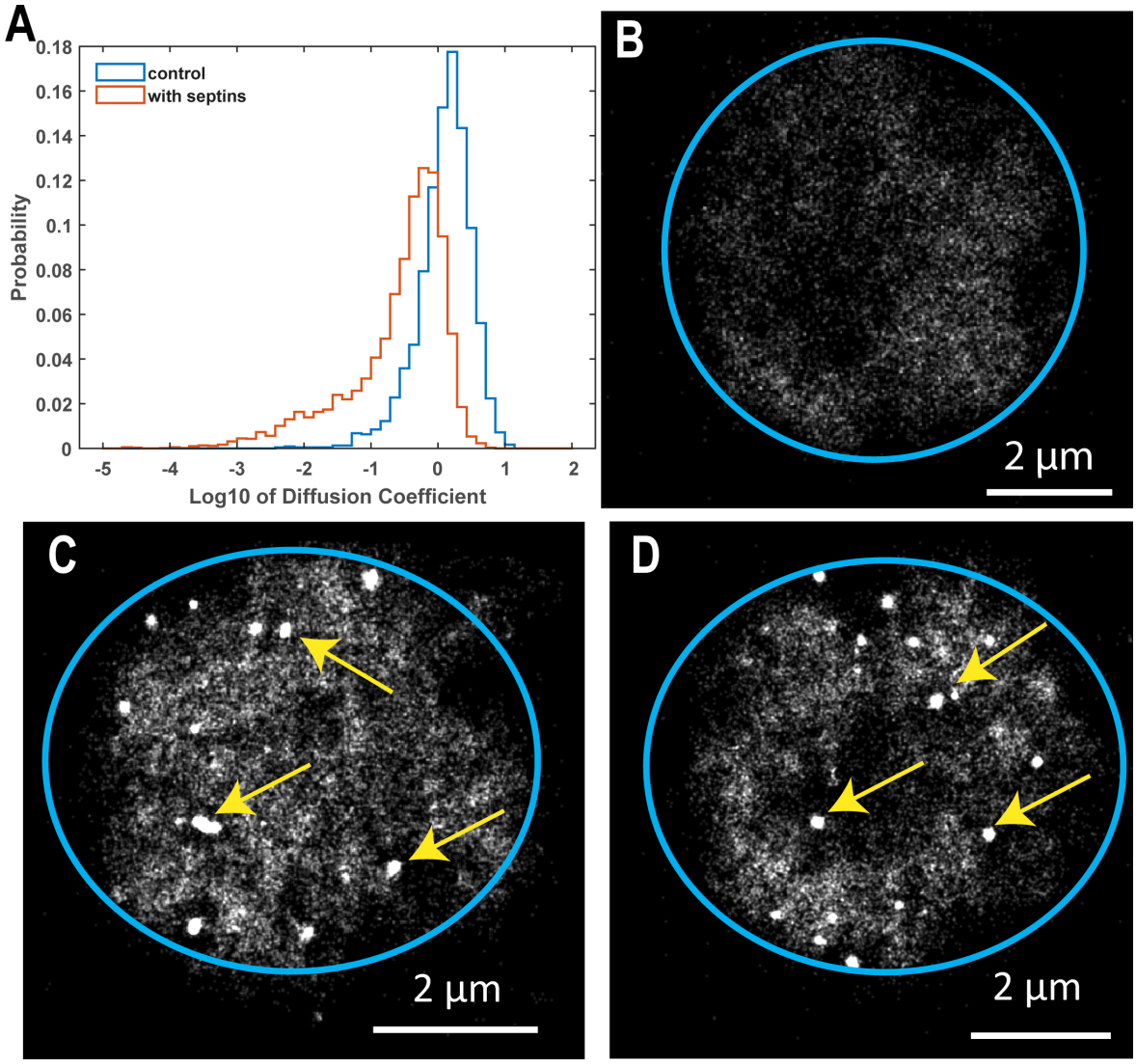

Figure 3.19 – (A) Distribution of diffusion coefficients obtained for streptavidin in a logarithmic scale in the control experiment and with yeast septins bound on the vesicle. (B), (C) and (D) Accumulation of detections during 20s movies. (B) From the control experiment, (C) and (D) after the addition of septins. The bright spots correspond to immobile streptavidin that give multiple detections at the same localisation while the other points correspond to particles that can explore the whole vesicle.

the dark and the GFP tagged septins. Finally, the immobile fraction was 27 ± 6 %, a value lower than for the GFP-tagged septins. It is thus possible that GFP plays a slight role in immobilising some of the streptavidins.

Influence of the tension of the membrane

The observation that streptavidin could cross septin filaments was surprising. Considering the size of streptavidin, it is hardly imaginable that it can diffuse across a filament juxtaposed to the membrane. One plausible explanation is that fluctuations of the membrane can open gaps through which the streptavidin is able to diffuse. Another possibility is that by applying tension on the GUV to capture them, I could create defects in the septin mesh, allowing the diffusion of streptavidin.

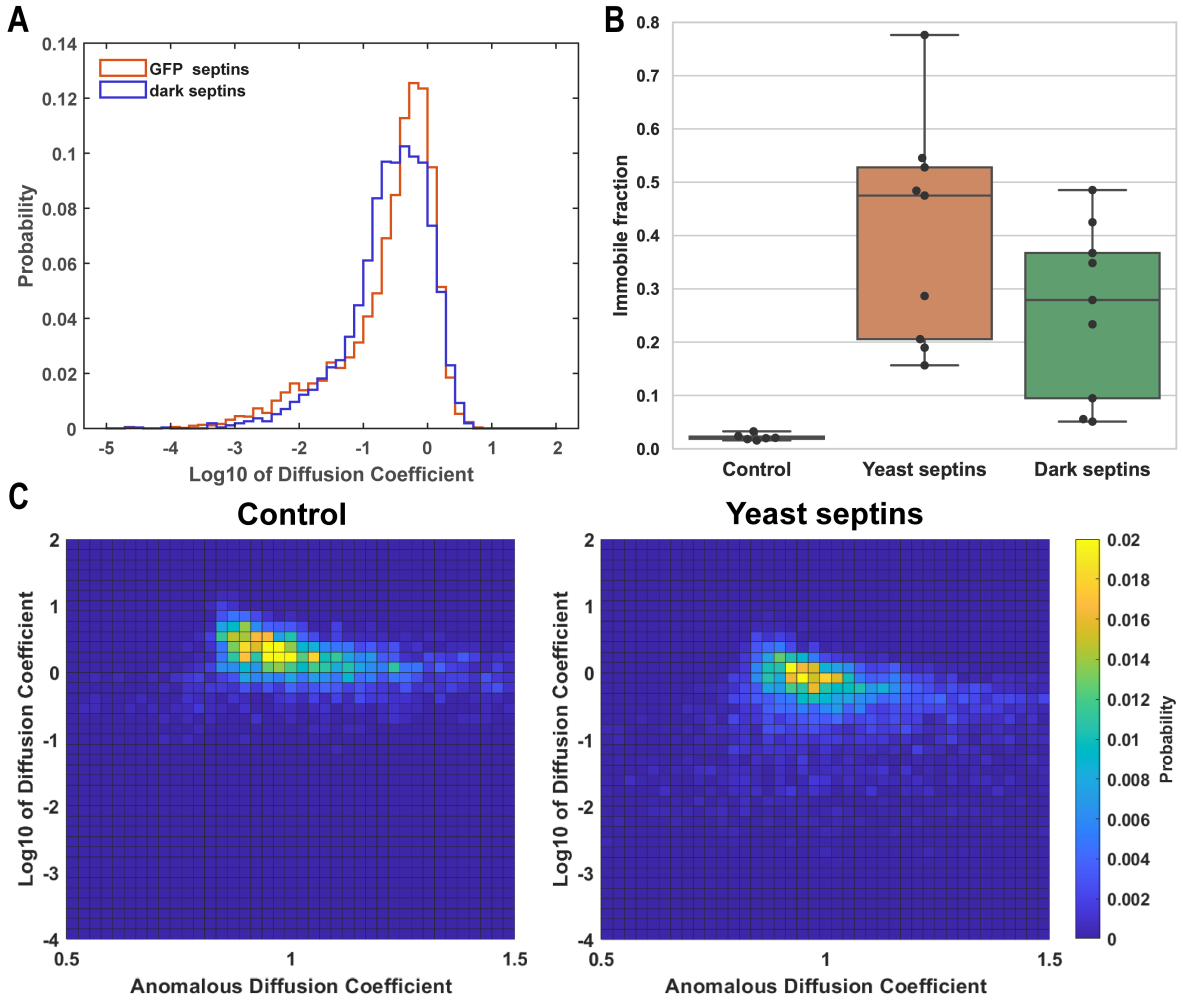

Figure 3.20 – (A) Comparison of the immobile fraction of streptavidin in the control experiment and in the presence of yeast septins. A control using non labelled septins was also performed.(B) Distribution of diffusion coefficient of single trajectories of streptavidin for the GFP-tagged yeast septins and for the control with unlabelled septins. (C) Heatmaps of the distribution of anomalous diffusion coefficient and diffusion coefficient in the control experiment and when septins are bound to the membrane.

To test both hypothesis, I changed the tension in the membrane. To obtain lower tension, I did not use micropipettes to avoid imposing any tension. I imaged the vesicle not at the plane in contact with the glass but about 1 µm above the plane of contact with the glass. The correction for the geometry was necessary in this situation as I was imaging an annulus of membrane further from the centre. By not aspirating the membrane, I did not perturb the septin network. To increase the tension and therefore reduce the amount of local fluctuations, I applied an osmotic shock to the vesicles corresponding to 20% of the initial salt concentration. I incubated the vesicles in a hypo-osmotic solution containing only 60 mM NaCl and 7.5 mM Tris (pH = 7.6) after the addition of septins. I equilibrate the vesicles for 20 min. I then captured the vesicles with a micropipette and imaged them. The distribution of diffusion coefficients for the low tension, increased tension and control with yeast septins are displayed in Figure 3.21 A.

The diffusion coefficient obtained in the experiment with no aspiration, and thus

at low tension, was 0.30 $\mu m^2/s$ (N=4 preps; 12 GUVs). The slower diffusion coefficient obtained might be the consequence of local deformations that septins can induce at the membrane, which are smoothened upon micropipette aspiration. With increased tension, the diffusion coefficient was 0.18 $\mu m^2/s$ (N=3 preps; 6 GUVs). The diffusion coefficient was significantly reduced in this condition. The immobile fraction of streptavidin for individual GUVs was compared for each condition in Figure 3.21 B. The immobile fraction when the GUVs were not aspirated with micropipette was 36 ± 7 %,and 53 ± 7 % for the higher tension experiment. Increasing the tension would therefore slightly increase the immobile fraction, but most importantly it reduced the diffusion coefficient of the diffusing population. It is possible that increasing the tension decreased the ruffling and the fluctuations which might reduce the rate at which streptavidin can cross septin filaments. However, even with increased tension, streptavidin was able to explore all the vesicle, indicating that they could still cross under septin filaments.

The maps of localisations' accumulation during 20 s movies for each GUV were similar to the control using yeast septins. The streptavidins were still able to go through septin filaments in both the low tension regime and the high tension regime. I plotted the heatmaps of the distribution of the diffusion coefficient and the anomalous diffusion coefficient for each individual trajectory in Figure 3.21 C. In both the low and high tension regimes, the distribution of anomalous diffusion coefficient was spread but centred around 1. No population showed abnormal diffusion.

Overall, the change in membrane tension did not change importantly the diffusion behaviour of streptavidin in the presence of septins. Streptavidins were still able to cross septin filaments. The main hypothesis was now that there is a gap between the septins and the membrane. The existence of a gap is not contradictory with the ability of septins to bind to lipid membranes. Indeed some septins possess coiled coil domains that are up to 10 nm long. These coiled coils could interact with the membranes and let septin filaments 'float' above the membrane. This idea is also supported by the presence of sequences corresponding to amphipathic helices at the tip of the coiled coils of some of the septin subunits.

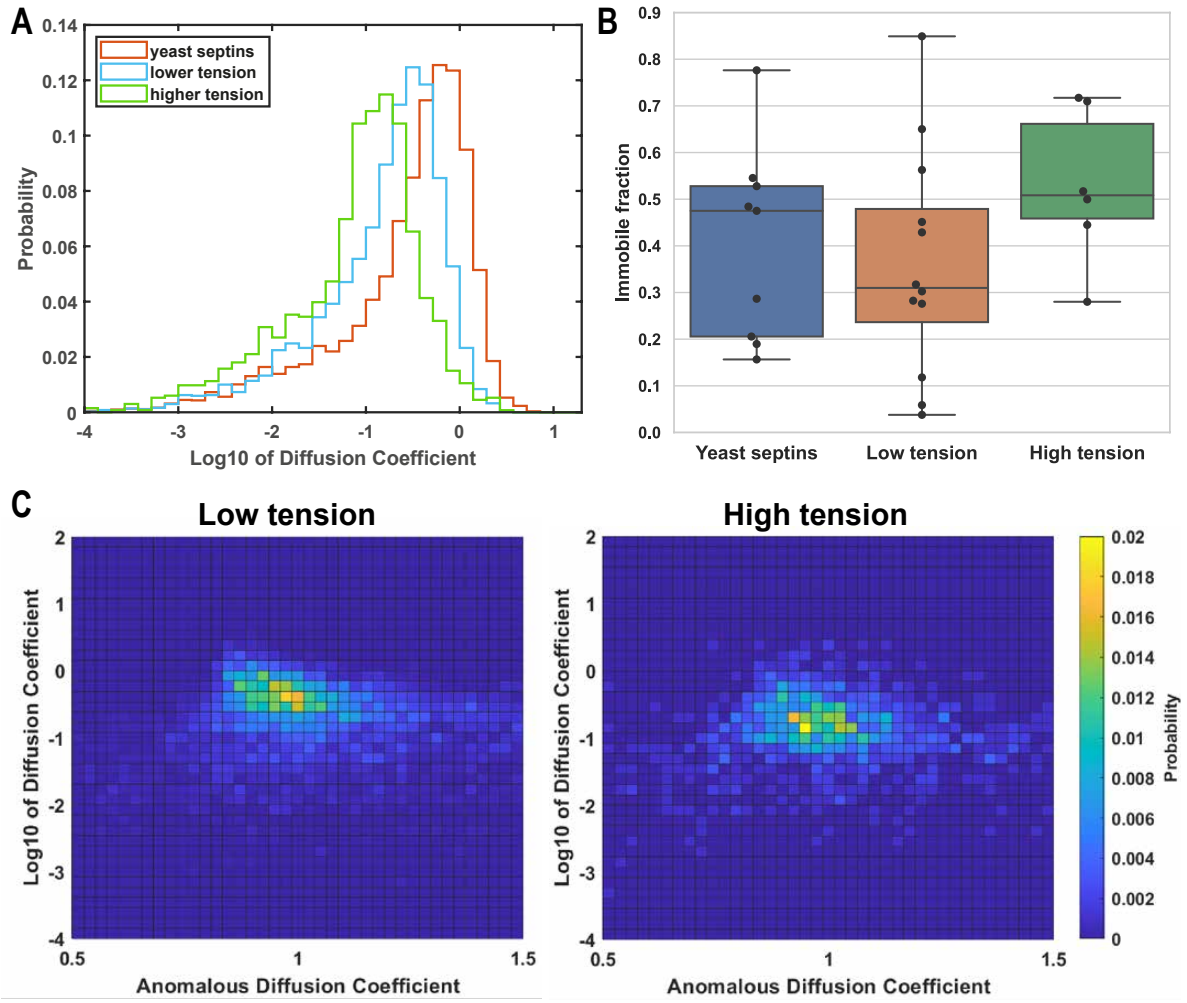

Figure 3.21 – (A) Distribution of diffusion coefficient for single trajectories of streptavidin bound to DSPE-PEG2k-biotin in the presence of yeast septins with either lower or higher tension in the membrane. (B) Immobile fraction of streptavidin in presence of yeast septins at either lower or higher tension. (C) Heatmaps of the distribution of anomalous diffusion coefficient and diffusion coefficient for higher or lower tension.

Summary

- **Aquaporin, model for transmembrane protein, can diffuse freely in presence of septins**
- **Quantum Dots anchored to the membrane, models for large protein complexes, cannot cross septin filaments and diffuse along lines**
- **Streptavidin and PEG Cy5, both model of proteins possessing a cytosolic domain, are able to diffuse in the presence of septins**

3.3 Effect of cross linked network

3.3.1 Cross-linking septin networks

When adding purified yeast septins on membranes, parallel arrays of filaments have been most frequently observed, while in vivo, we know that septins can form orthogonal meshes (Ong et al., 2014). I wanted to generate and assay septin network more similar to those that have been reported in vivo. I used two different systems to create those orthogonal mesh in vitro, one using yeast septins combined with the Bud proteins, and one using human septins that consistently self-organise into orthogonal meshes.

In vivo, yeast septins have been reported to create diffusion barriers in the course of cell division. It has been reported that Bud3 and Bud4 proteins are essential to maintain and control the architecture of septin filaments (Chen et al., 2020). Aurélie Bertin performed cryo electron microscopy assays, mixing purified yeast septins with either Bud3, Bud4 or both and adding them to LUVs. The experiments were performed at 40 nM of Bud proteins and 100 nM of septins. It was observed that the addition of Bud3 lead to the formation of orthogonal meshes while Bud4 resulted in bundling of septin filaments. Images obtained from cryo electron microscopy in solution are displayed in Figure 3.22 A and B.

As the diffusion barrier is conserved in mammal septins, I was interested in studying the ability of human septins to create diffusion barriers in vitro. Koyomi Nakazawa, a post-doctoral fellow in the lab has performed scanning electron microscopy experiments on human septin octamers consisting of SEPT2/SEPT6/SEPT7/SEPT9. Images are displayed in Figure 3.22 C. Interestingly, she observed that at concentrations higher than 50 nM, human septins would spontaneously form two layers of filaments orthogonal to one another. The mesh size was about 30 nm, corresponding to the length of one octamer – see analysis in Figure 3.22 D. No more than 2 layers have been observed.

3.3.2 SPT in the presence of crossed linked septin networks

For the single Particle experiments, I decided to focus on Quantum Dots and streptavidin, the two systems for which the addition of yeast septins altered the diffusion behaviour. I decreased the yeast septin concentration to 100 nM with 40 nM of either Bud3 or Bud4. The septins had a much higher affinity with the membrane than without Bud proteins. Higher septin concentrations lead to the formation of big bundles and meshes in solution, that could interact with vesicles. The human septins were also incubated at concentration of 100 nM. The SPT experiments were performed similarly as for yeast septins.

Diffusion of Quantum Dots

I first studied the diffusion of Quantum Dots anchored to the membrane when crossed linked yeast septin networks are interacting with the membrane. The distribution coefficient for single trajectory of Quantum Dots is plotted in Figure 3.23 A for yeast septins with either Bud3 or Bud4 and compared to the control experiment and yeast septins alone. The average diffusion coefficient of Quantum Dots in the presence of yeast septins and Bud3 was 0.035 $\mu m^2/s$ (N=3 preps; 9 GUVs) and 0.14 $\mu m^2/s$ (N=2 preps; 7 GUVs) when yeast septins and Bud4 were present.

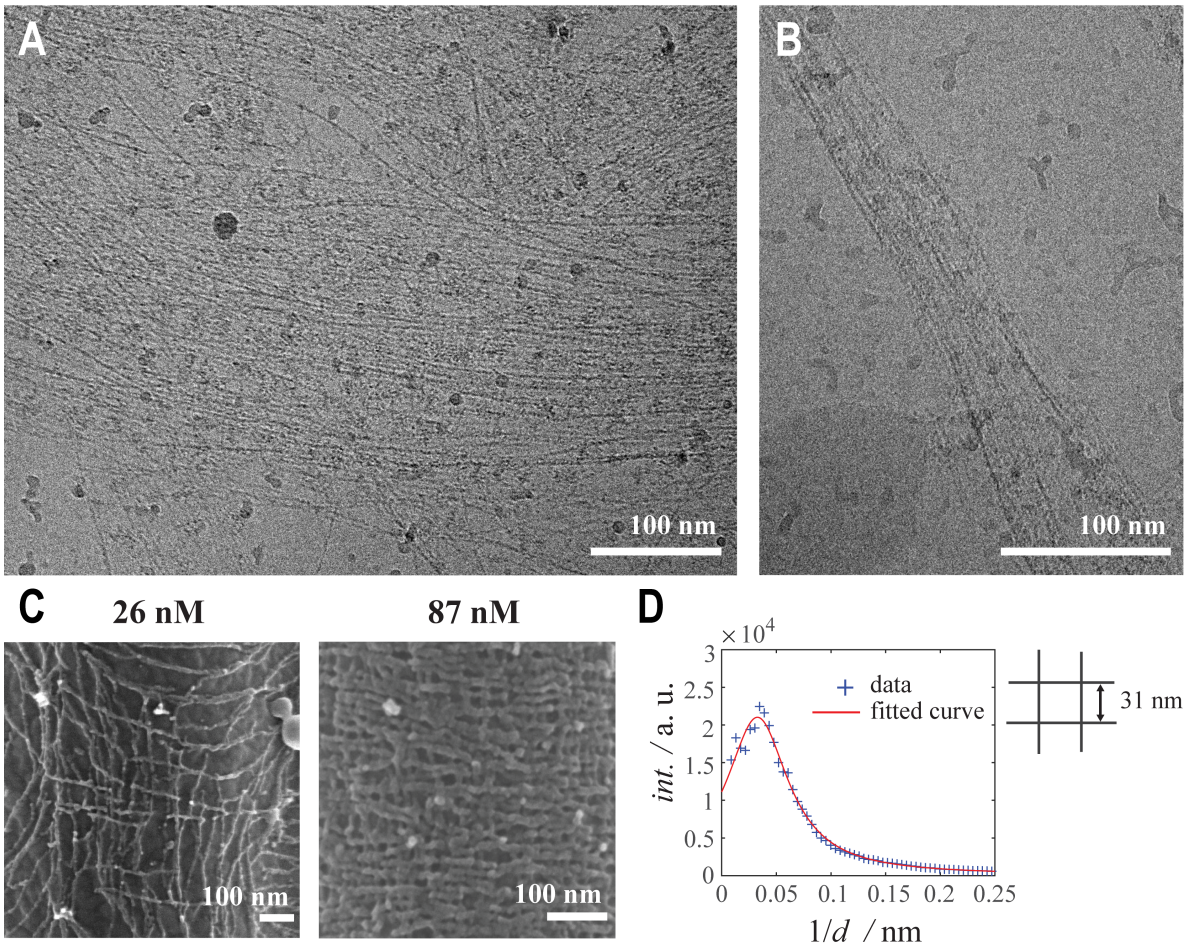

Figure 3.22 – (A) and (B) Images from cryo electon microscopy performed on yeast septins (100 nM) in solutions mixed respectively with Bud3 and Bud4 (40 nM). (C) Scanning electron microscopy performed on human septin octamers interacting on lipid bilayers at two different concentrations. (D) Distribution on the typical distance between human septin filaments incubated on a lipid bilayer at a concentration of 87 nM.

When Bud4 was added to yeast septins, the average diffusion coefficient was slightly reduced, and the distribution of diffusion coefficients was shifted. A map of accumulation of localisations over a 20 s movie is displayed in Figure 3.23 D. This map was obtained at a density of Quantum Dots too high to perform Single Particle Tracking, and this experiment was not kept for analysis of the diffusion coefficient. However, it shows that the Quantum Dots diffuse along lines similarly to the experiment with yeast septins alone. It also gives a more detailed view of the organisation of filaments on the membrane, with spots where nematic defects are most likely present (red circles and arrow in Figure 3.23 D). The addition of Bud4 is most likely bundling the septin filaments, as observed in cryo electron macroscopy, allowing the Quantum dots to diffuse between septin bundles.

With Bud3 and yeast septins, both the distribution and the average diffusion coefficient showed significant differences. The distribution was wide but with a single peak corresponding to immobile particle. This observation was confirmed by the map of localisations' accumulation displayed in Figure 3.23 E. The maps showed exclusively bright spots, corresponding to immobile Quantum Dots localised over many frames at the same position.

I then studied the effect of a human septin mesh on the diffusion of Quantum Dots. The human septins were labelled with GFP, I could therefore visualise the binding of human septins to the vesicles. The distribution coefficient for single trajectories of Quantum Dots is plotted in Figure 3.23 B for the experiment with human septins and compared with the yeast septins and the control. The average diffusion coefficient of Quantum Dots when human septins were added was 0.031 $\mu m^2/s$ (N=3 preps; 7 GUVs). Similarly to the experiment with yeast septins and Bud3, the distribution of diffusion coefficients consisted in only one main peak corresponding to immobile Quantum Dots. This observation was confirmed by the maps showing the accumulation of localisations during each movie, one is displayed in Figure 3.23 F. All maps displayed only bright spots, showing that Quantum Dots were unable to diffuse.

The immobile fraction of Quantum Dots for individual GUVs and for all the different conditions with septins are compared in Figure 3.23 C. As expected, the immobile fraction for the experiments with either the yeast septins with Bud3 or the human septins was always about 100 %. For the condition with yeast septins and Bud4, the immobile fraction was 71 $\pm$ 10 %. This fraction was higher than with yeast septins alone, as expected from the reduction in the average diffusion coefficient.

I plotted the heatmaps for the distribution of diffusion coefficient and anomalous diffusion coefficient for all three conditions in Figure 3.24. In all maps the distribution was spread out. Indeed, for immobile particles, the anomalous diffusion coefficient is not relevant. For the experiment with yeast septins and Bud4, the anomalous diffusion coefficient was still centred around 1, and no population of trajectories displayed anomalous diffusion lower than 1. I therefore concluded, that Quantum Dots were diffusing in constrained regions but with no anomalous diffusion.

In all three tested conditions, the ability of septin filaments to block the diffusion was not altered by the addition of either Bud3 or Bud4 or by using human septins, only the shapes of the constrained regions were changed.

Diffusion of streptavidin

To test if they could alter the diffusion of smaller particles, I studied the diffusion of streptavidin with crossed linked networks. Because I did not observe significant difference upon Bud4 addition to the septins, I focused on Bud3 with yeast septins and human septins. The experiments were performed using the protocol used for streptavidin and yeast septins alone. I incubated the GUVs with either 100 nM yeast septins and 40 nM Bud3 or only 100 nM human septin. The distribution of diffusion coefficients for single trajectories are displayed in Figure 3.25 A and B and compared to the experiment with yeast septins alone and the control experiment. The average diffusion coefficients of streptavidins when yeast septins and Bud3 were added to the membrane was 0.47 $\mu m^2/s$ (N=4 preps; 17 GUVs), and 0.46 $\mu m^2/s$ (N=5 preps; 12 GUVs) when human septins were added. Both conditions displayed distributions very similar to the one obtained from the experiment with the yeast septins alone.

Similarly, the maps displaying the accumulations of localisations for both conditions were very similar to the ones obtained with only yeast septins – Figure 3.25 C and D. They presented an homogeneous background with some bright spots (pointed by arrows). The bright spots corresponded to immobile streptavidins, while the background corresponded to streptavidins that were able to explore the whole surface of the GUVs. The fraction of immobile particles was obtained using the same strategy as described previously. The immobile fraction for individual GUVs are displayed in Figure 3.25 E.

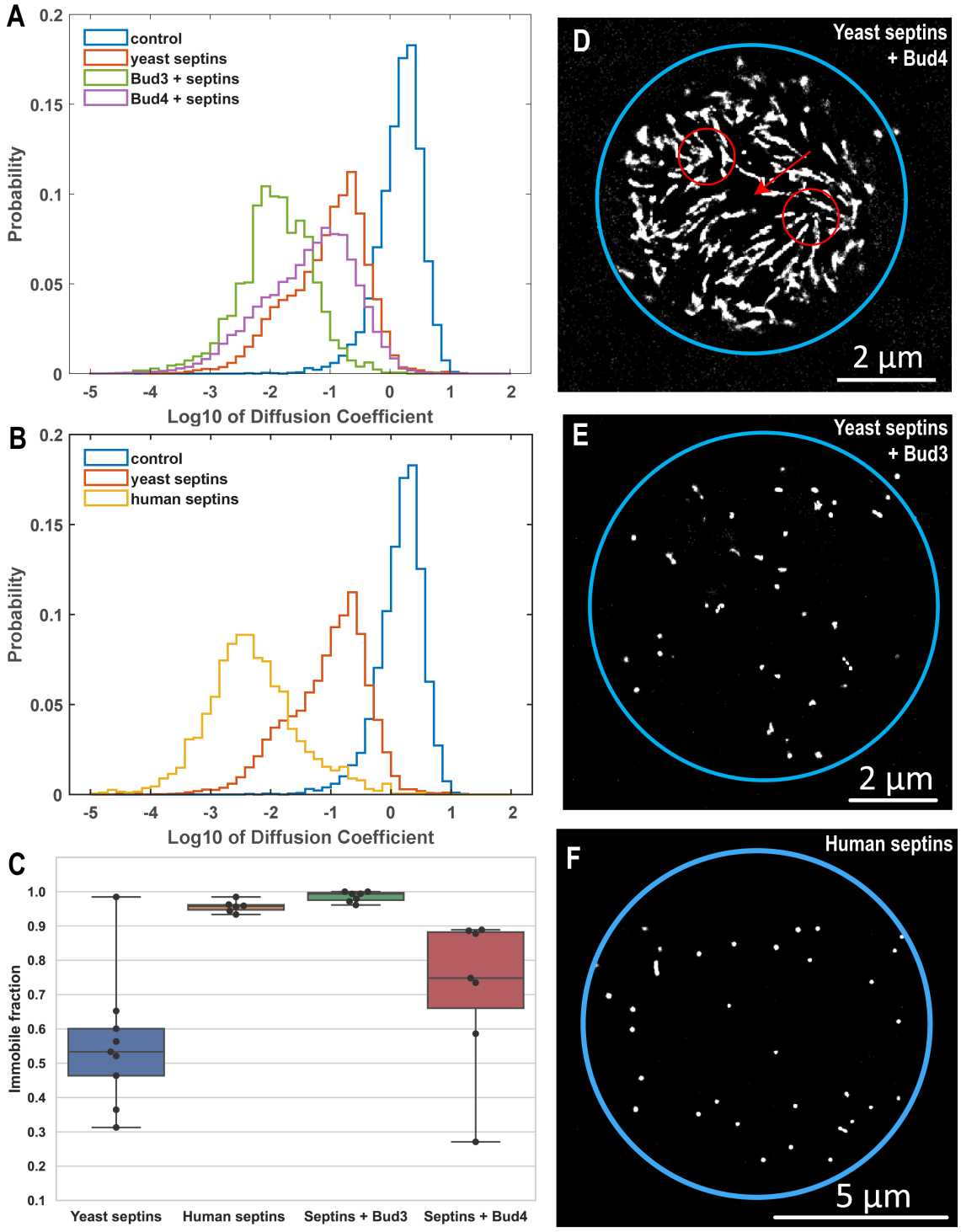

Figure 3.23 – (A) and (B) Distribution of diffusion coefficient of single quantum dots in log scale for the control experiment, yeast septins bound to the membrane and different crossed-linked septin networks. (C) Immobile fraction of quantum dots for different crossed linked septin network compared to the case of yeast septins alone. (D, E and F) Accumulation of detections of quantum dots along 20s movies for respectively Bud4 + yeast setpins, Bud3 + yeast septins, and human septins. (D) Red circles correspond to +1/2 nematic defect, red arrow points at a -1/2 nematic defect.

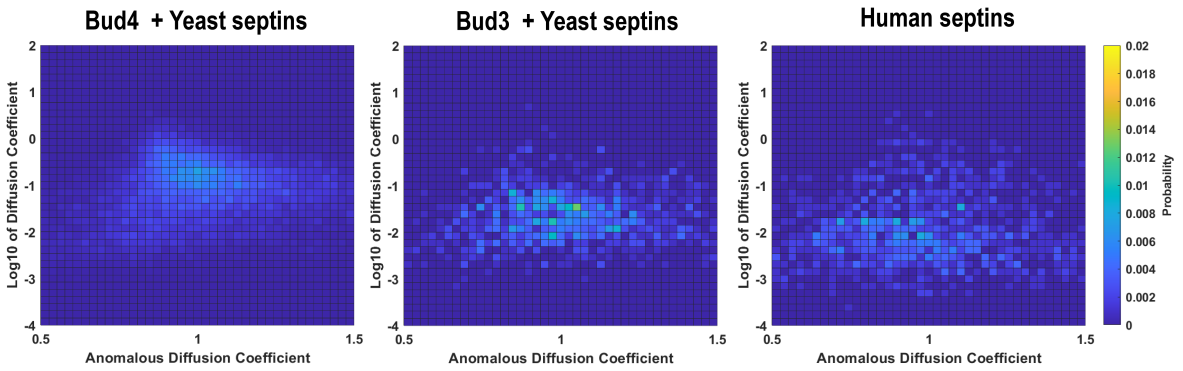

Figure 3.24 – Heatmaps of the distribution of anomalous diffusion coefficient and diffusion coefficient for quantum dots bound to the membrane in presence of different crossed-linked septin networks.

The immobile fraction for the experiment with yeast septins and Bud3 was 28 ± 5 % and 44 ± 10 % for the experiment with human septins. When removing those immobile particles the average diffusion coefficients in the experiment with respectively yeast septins and Bud3 and human septins were 0.60 $\mu m^2/s$ and 0.67 $\mu m^2/s$. These values are close to the 0.71 $\mu m^2/s$ obtained for the mobile fraction in the experiment on streptavidin with the yeast septins alone. Finally, the heatmaps of the distribution of diffusion coefficients and anomalous diffusion coefficients for both conditions showed no anomalous diffusion, similar to the experiment with yeast septins alone.

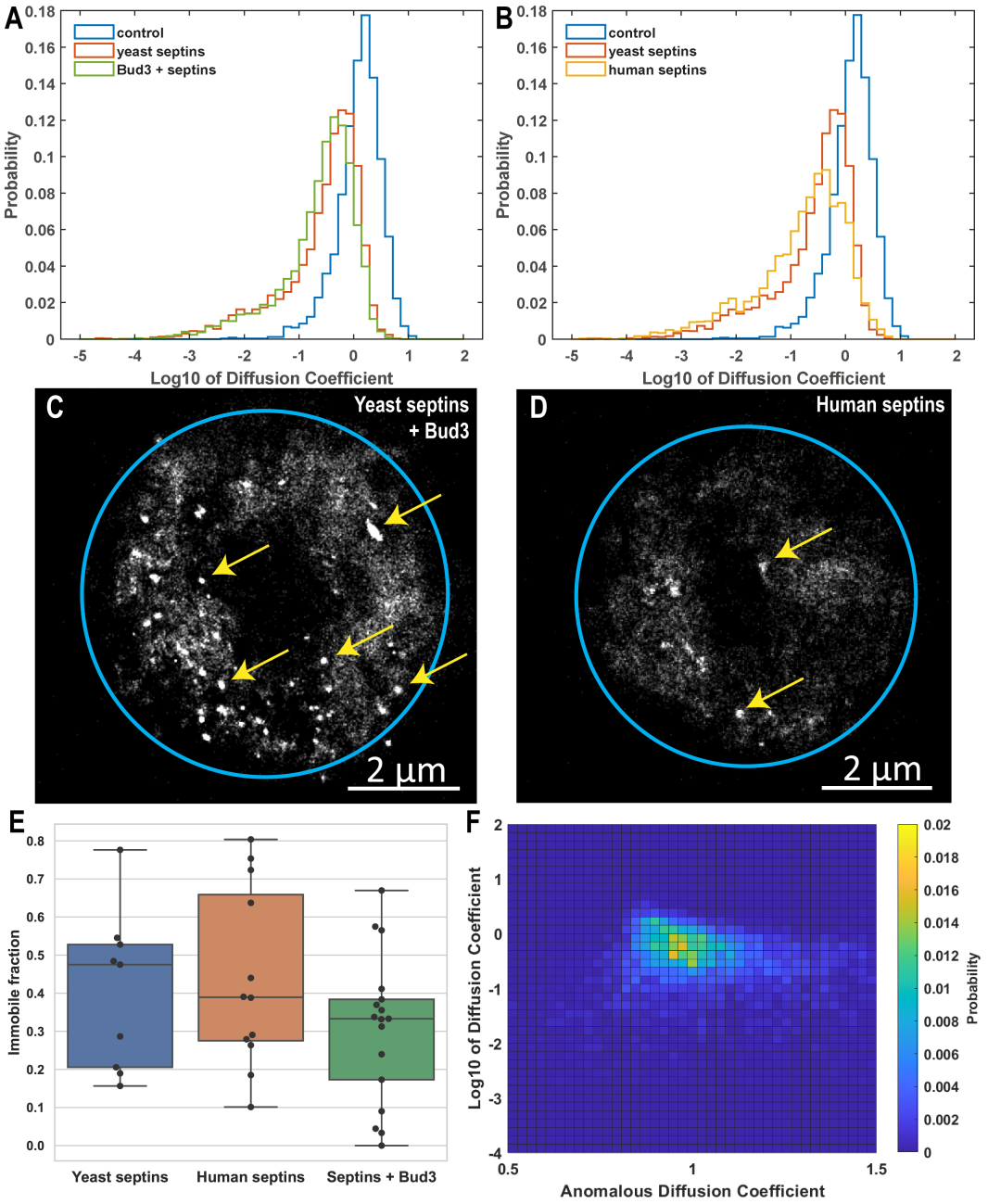

Figure 3.25 – Single Particle Tracking of streptavidin in the presence of different crossed-linked septin networks. (A and B) Distribution of diffusion coefficient of single streptavidins in log scale for the control experiment, yeast septins bound to the membrane and different crossed-linked septin networks. (C and D) Accumulation of detections of quantum dots along 20s movies for respectively Bud3 + yeast septins and human septins. (E) Immobile fraction of streptavidin for different crossed-linked septin networks compared with yeast septins alone. (F) Heatmap of the distribution of anomalous diffusion coefficient and diffusion coefficient for streptavidin when yeast septins and Bud3 are added on the GUV.

3.4 Conclusion

I showed using FRAP that *in vitro* septins do not prevent the diffusion of both non-specific lipids and PI(4,5)P_2. I then assayed the diffusion of models of membrane bound proteins to invest whether septin filaments would sterically prevent the diffusion of proteins. Performing SPT experiments, I showed that aquaporin – a transmembrane protein – can freely diffuse in the presence of septins. Conversely, Quantum Dots bound to the membrane were unable to cross septin filaments. Finally, streptavidin bound to a lipid displayed a slower diffusion after the addition of septins but were still able to diffuse across the whole membrane. A schematic representation of the trajectories obtained for the models of membrane proteins is displayed in Figure 3.26 A.

To account for these observations, I propose that there is a gap between the septin filaments and the membrane, allowing the diffusion of both streptavidin bound to a biotinylated lipid and DSPE-PEG2k through a septin network. A representation of the membrane with the different models of proteins and septin filaments is displayed Figure 3.26 B. Septins might interact with the membrane through the amphipathic helices localised at the end of their coiled coils domains (Cannon et al., 2019). The coiled coils have the right length to generate the spacing that my results suggest.

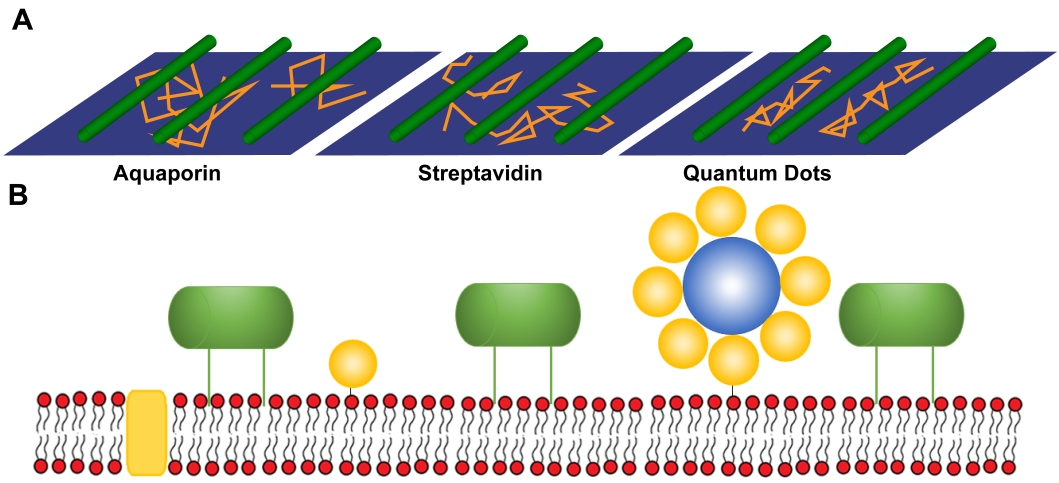

Figure 3.26 – (A) Schematic representation of trajectories of the different models of membrane proteins in the presence of septin filaments. (B) Schematic representation of the different models of proteins and septin filament connected to the membrane through their coiled coils.

Summary

- **Addition of Bud3 to yeast septins induces the formation of orthogonal meshes *in vitro***
- **Quantum Dots were fully immobilised in the crossed linked network, showing that filaments in both direction block their diffusion**
- **Streptavidins were still able to explore the full vesicle, indicating that cross linking the network did not change its ability to cross septin filaments**
- **Similarly to yeast septins, human septins blocked the diffusion of Quantum Dots but streptavidins were able to diffuse**

Chapter 4

Mechanical properties of septin networks

The role of septins on the mechanics of membrane is still poorly understood. Studies have managed to obtain the persistence length of single septin filament, but the measurements performed on membranes were not satisfying. Septins have been shown to be able to deform membranes. The ability of septins to deform membranes depends on their curvature sensitivity but also their intrinsic mechanical characteristics. Finally, septins have been reported to mechanically stabilise the membrane in vivo. Therefore an *in vitro* study investigating the mechanical properties of a membrane with septins filaments bound appeared relevant.

4.1 Membrane reshaping

While I was performing the experiment on the diffusion of PI(4,5)P_2 in lipid bilayers deposited on mica I observed a strong reshaping of the membrane. upon addition of septins. I prepared lipid bilayers from SUVs containing TR-PI(4,5)P_2, and incubated them on mica as described in section 3.1.4. I obtained bilayers with good fluidity, but displaying holes with bare mica. To adress the effect of the addition of septins on the diffusion of PI(4,5)P_2, I added 300 nM of purified yeasts septins labelled with GFP. The bilayers, initially flat, were completely remodelled after a few minutes. Snapshots from a movie recorded seconds after the addition of septins are displayed in Figure 4.1. Before the addition of septins to the solution, the bilayer displayed some defects, with both holes and small vesicles on the bilayers. Shortly after the addition of septins, bright tubes started to appear, and elongated (some in the z-direction) within few minutes. In the meantime, the holes expanded. After about 10 minutes, almost no bilayer was left, and only lipid tubes could be observed. Septins were observed to localise on both the lipid tubes and the mica. In places where lipid bilayer could still be observed, the density of septins was reduced. The diameters of the tubes were ranging from 1 to 2 µm. The addition of septins at concentrations of 30 nM also led to deformations of the membrane but at smaller scale. The membrane would display small spheres on the edges of the holes with radii ranging from 1 to 1.5 µm.

These observations were supported by AFM imaging performed on supported lipid bilayers deposited on mica by collaborators. They observed that the addition of septins would disturb the lipid membrane, leading to its detachment. They also observed swelling from the centre of some membrane patches. Those experiments were performed

at lower septin concentrations, with a maximum concentration used of 30 nM.

This behaviour only occurred for lipid bilayers deposited on mica because the interaction of lipid bilayers seemed weaker with mica than with glass. Indeed, before the addition of septins, the presence of holes in the lipid bilayer reflected a weaker interaction between the SUVs and the mica leading to poor fusion efficiencies. Also, the initial holes can allow the binding of septins to mica for which it has a strong affinity and compete with the lipid bilayer-mica interaction. The binding of septins to mica seemed to be the main factor for bilayer detachment in the AFM imaging study. These results have been published in Nanoscale (Vial et al., 2021).

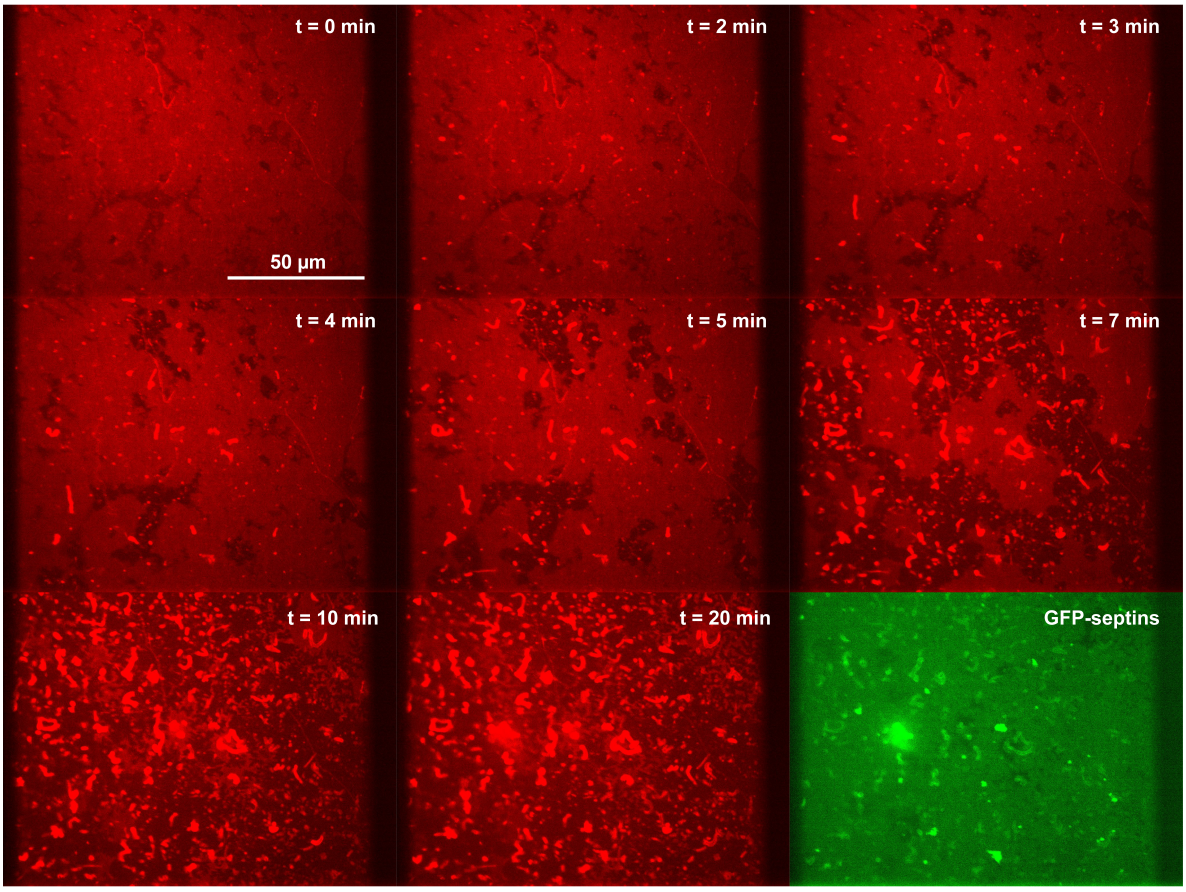

Figure 4.1 – Snapshots from a movie showing deformation of a lipid bilayer by addition of septins. The lipids were labelled with PI(4,5)P_2-TR (red) and deposited on mica. GFP-tagged septins (green) were added at a concentration of 300 nM. Bilayer was quickly disrupted and tubes going out of the membrane plane were observed.

After observing this deformation, I wanted to study in more details the mechanical properties of septin meshes, which seem crucial in many functions of septins.

4.2 Micropipette aspiration

Micropipette aspiration is a method commonly used to obtain the bending and the elastic modulus of a lipid membrane (Kwok and Evans, 1981). Vesicles are aspirated with a micropipette in which the pressure is controlled by displacing vertically a water tank. The length of the aspirated tongue is recorded as a function of the pressure inside

the micropipette. Depending on the tension regime in the vesicle, one can obtain either the bending modulus in the low tension regime, or the elastic modulus in the high tension regime.

Previous experiments have been performed using micropipette aspiration to obtain the elastic modulus and the bending modulus of a system consisting of septins filaments bound to a lipid membrane (Beber et al., 2019b). These experiments were performed on GUVs incubated with purified yeast septins labelled with GFP. The GUVs were captured and pre stretched to smooth out the membrane and remove possible defects. The pressure would then be released and septins were locally injected to bind to the lipid membrane. Surprisingly, the addition of septins did not change significantly the elastic modulus and the bending modulus. During the experiment, septins never localised on the tongue, the part of the membrane being aspirated by the micropipette even when it was being elongated.

To make sure septins were initially evenly distributed on the surface of the vesicle, I wanted to repeat the experiment using GUVs pre incubated with septins before capturing them with a micropipette. I used the same lipid mixture as in the previous study (Beber et al., 2019b), incubated the GUVs made by electro-formation with 200 nM septins for 30 min before performing the micropipette aspiration experiment. Confocal images from the micropipette experiment are displayed in Figure 4.2 for two different GUVs A (top) and B (bottom). The experiment was repeated five times and all vesicles showed similar behaviours.

The density of septins bound to the membrane was three times higher in vesicle B than in vesicle A. The septin density on both vesicles was homogeneous before micropipette aspiration as displayed for vesicle B. The pressures indicated correspond to the pressure difference between the observation chamber and the micropipette. During aspiration, the pressures are positive. In both cases, there was a threshold in the pressure applied to start aspirating the vesicle. This threshold depended strongly on the septin density, about 30 Pa for vesicle A and 150 Pa for vesicle B. Upon increasing the applied pressure, the tongue got slightly elongated as can be seen for vesicle A at a pressure of 90 Pa when compared to 30 Pa. However, during all the experiments, the septins were always excluded from the tongue, the portion of the membrane aspirated inside the micropipette.

When reaching a critical value, the vesicles would undergo very strong deformations, with the tongue getting elongated very abruptly. This critical pressure was reached at 100 Pa in vesicle A and 200 Pa in vesicle B. The tongue was still depleted from septins, and if the pressure was not released, the vesicles were fully aspirated inside the micropipette. I suspect that this observation occurs either because septins detach from the membrane or because the filamentous network is altered, allowing the membrane outside of the micropipette to deform. The second hypothesis is more likely because the density of septins increases when the critical pressure is reached. These observations were consistent with septins creating a rigid filamentous network on the membranes. Finally, upon releasing the pressure, the tongue was pushed back from the micropipette, and the vesicle would lose its initial sphericity, and display wrinkles – see vesicle A – or larger deformations.

Recovering the mechanical properties of the septin mesh seems complicated. Indeed, the usual theoretical considerations that allow the obtention of both the bending and elastic modulus would not be possible. The system is no longer a single sheet of fluid undergoing elastic deformation. It is a rather more complicated system and developing

a model to account for all the effects of the inhomogeneously distributed septin filaments and their physical state seemed daunting. I therefore chose a different strategy and used Atomic Force Microscopy (AFM) to probe the mechanical properties of the membrane.

4.3 AFM using Hertz contact

I decided to perform AFM indentation experiment to assay the role of septins in the mechanical properties of membranes. I used a cantilever with a tip of a known geometry to apply a force on an object. The deflection of the tip is recorded to determine both its vertical position and the force applied, knowing the rigidity of the cantilever. It is therefore possible to obtain the deformation of the object of interest for a given force. Depending on the object, different models describing the contact can be used to recover the mechanical properties, such as the Young's modulus. The most common contact model used is the Hertz contact. It considers a spherical tip exerting pressure on a homogeneous and elastic half ball which is well adapted to the geometry of a cell attached to a surface. The model gives a relation between the indentation and the force which varies as $F \propto d^{3/2}$. The full equation is written in section 2.8.3. This equation is valid for ratio of radii of the object to the tip smaller than 5 and bigger than 1/5.

I performed AFM indentation experiment on GUVs incubated with GFP labelled yeast septins. The GUVs were prepared by gel assisted swelling on PVA. The GUVs were then deposited on a glass coverslip covered with polylysine to ensure strong binding of the vesicles on the coverslip. Septins were added to the GUVs directly in the observation buffer, left for 30 min to ensure full interaction. The excess of septins was then rinsed away. This rinsing was crucial to prevent any attachment of septins on the AFM tip. The AFM setup was combined with a Fluorescent optical microscope, which allowed the visualisation of vesicles and the alignment of the tip with the vesicle. The tip was then lowered using a piezo at a constant rate, and the force indentation curves could be recovered. A curve obtained for a GUV in the absence of septins is displayed in Figure 4.3 A. A fit using a Hertz contact model is also displayed in red. It shows that the real force indentation curve did not follow the expected 1.5 power law. Focusing on the early deformations (first points on the graph), I was able to fit the data with the model as displayed for the first micrometre of indentation on the same vesicle in Figure 4.3 B.

I decided to only use the first 200 nm of indentation because even for small vesicles, the fitting was satisfying. I plotted in Figure 4.3 C the distribution of apparent Young's modulus for individual GUVs in both the control experiment and after the addition of septins. The Young's modulus for the control experiment was 3.4 ± 0.4 kPa, and was increased to 11 ± 2 kPa in the presence of septins. However, because the geometry in the model considers a volumetric object instead of a surface, a strong dependency on the size of the vesicle can occur.

To decipher whether differences in size could explain the difference of apparent Young's modulus, I plotted in Figure 4.3 D the distribution of Young's modulus as a function of the radius of the GUV for both the control experiment and in the presence of septins. For both conditions, the apparent Young's modulus decreased with increasing radius. With septins, the vesicles were on average smaller than in the control experiment. This effect resulted from the extra rinsing steps required after the addition of septins. Pipetting induces important shear flows on the surface of the coverslip. The shear flow disrupts the larger vesicles. The intact vesicles can be split in two

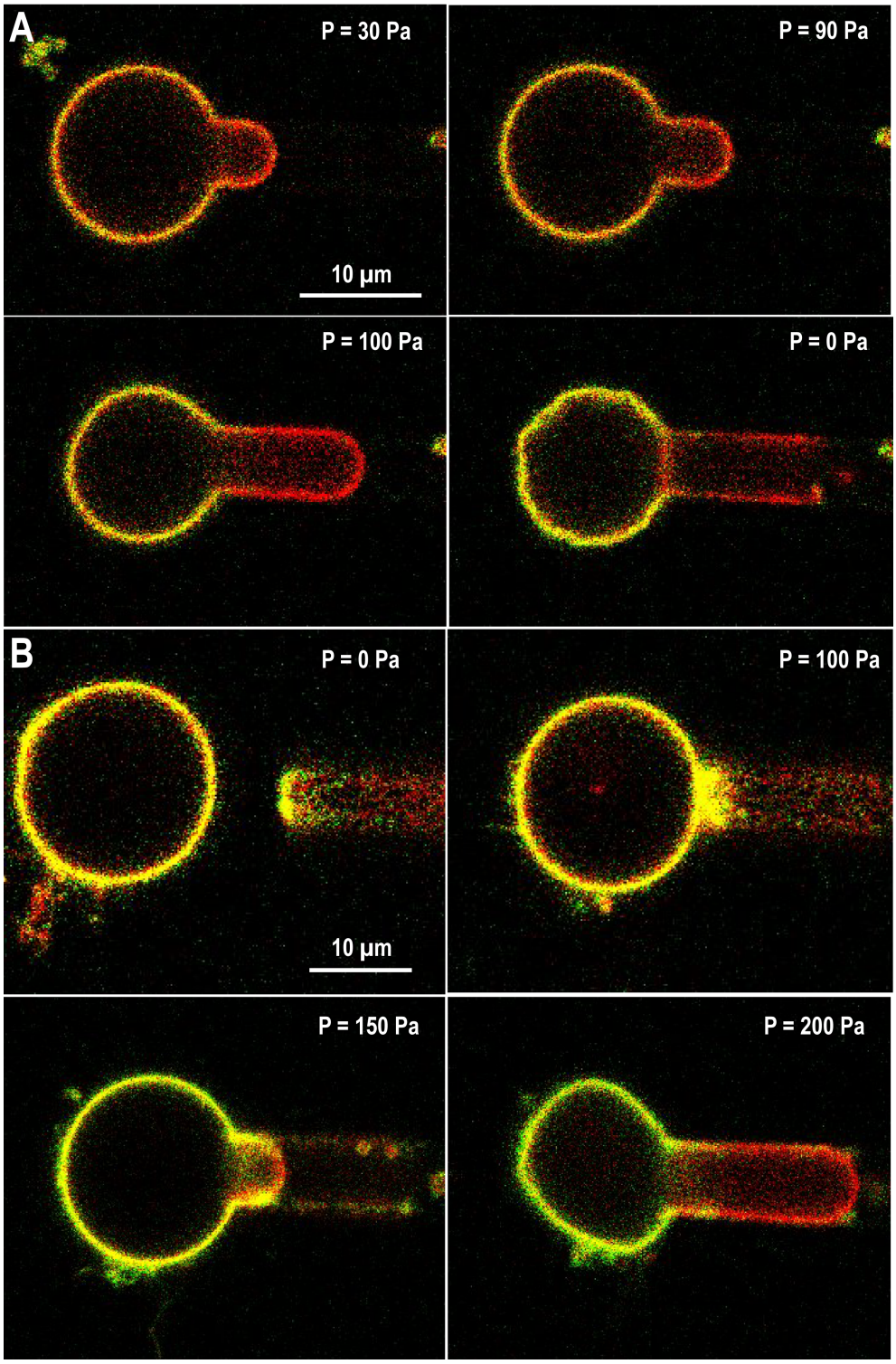

Figure 4.2 – Micropipette aspiration experiment. (A) GUV with a low septin signal, upon gentle aspiration a tongue would appear. It appeared that a threshold in aspiration was necessary to pull a longer tongue and once reached the tongue would be very elongated. Upon pressure release, the tongue goes back to the tip of the micropipette and the vesicle would appear wrinkled. (B) GUV with septin signal about 3x higher. To start pulling the tongue, a strong aspiration was need. Upon further increasing the aspiration, the tongue would again become very elongated after reaching a threshold.

populations. One population displayed apparent Young's modulus similar to vesicles from the control experiment, and the second one showed Young's modulus 3 to 5 times higher than the control experiment. This second population corresponded exclusively to vesicles with radii smaller than 2 µm.

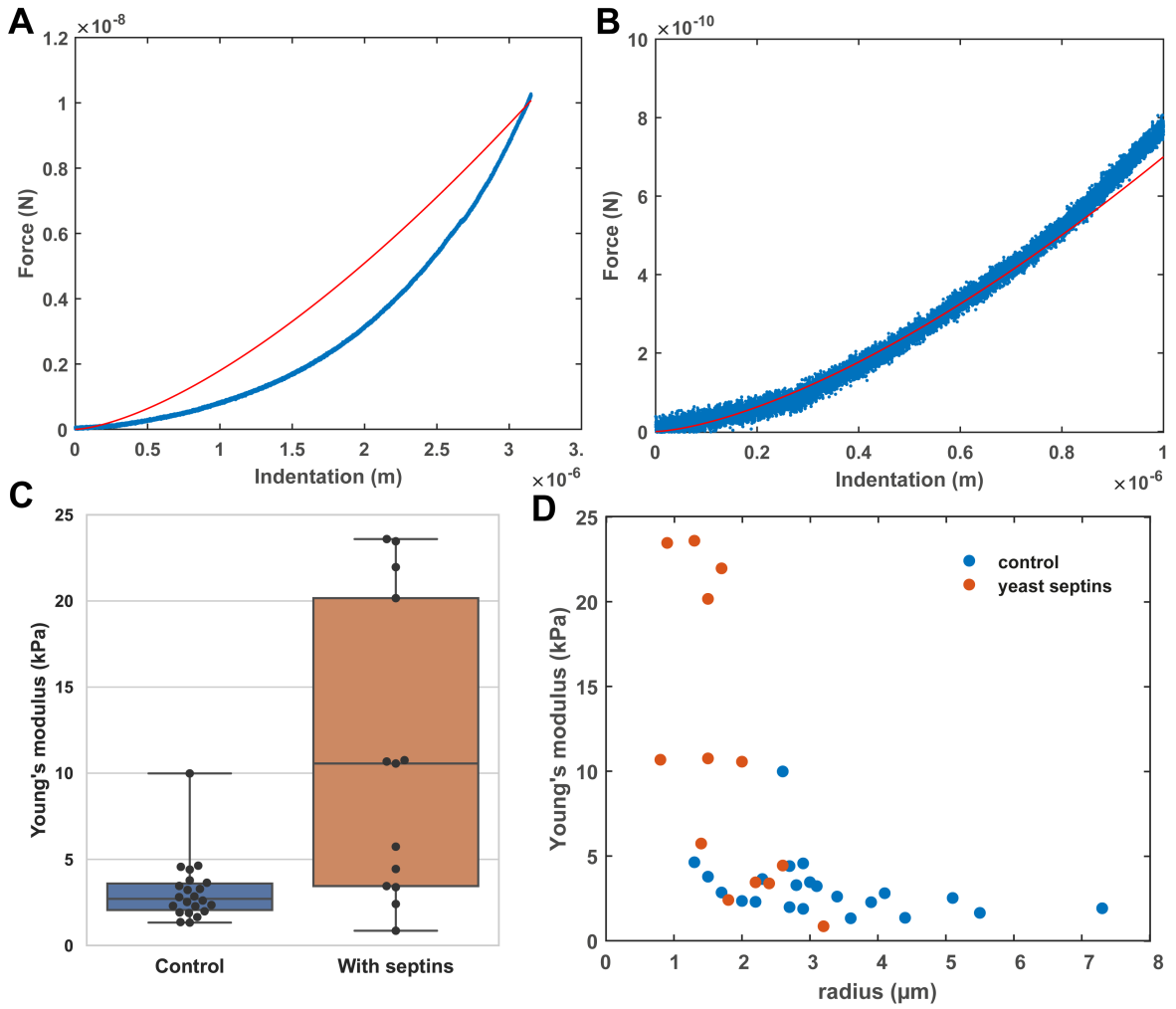

Figure 4.3 – Experiments from AFM indentation with analysis performed using Hertz contact law. (A) The force applied on the GUV as a function of the indentation depth. Plotted is the fit using Hertz contact going as $x^{3/2}$. (B) Zoom on the first micrometre of indentation and fitted using the Hertz contact law. (C) Young's modulus obtained from the fit on the first 200 nm of indentation in the control experiment and when septins are bound to the membrane. (D) Young's modulus as a function of the radius for both the control experiment and when septins are bound to the membrane.

These results suggest that upon septins binding, the membrane is more rigid, as expected. Howeve,r a high variability is observed with the radius of the vesicle. To quantify whether this observation was an artefact of the model or a feature of the septin mesh, I had to improve the model. I plotted in Figure 4.4 A the force indentation curve in a log log scale and fitted with a linear fit. It generated a slope of approximately 1.6, but the fitting was poor. I removed the initial points that are very noise sensitive and fitted only the curve with forces higher than 0.2 nN in Figure 4.4 B. The resulting slope is then found equal to 1.95. This indicated that the chosen model was definitely

not adapted to the quantitative study of GUVs. It could still be used to estimate the apparent rigidity of a vesicle.

To better quantify the rigidity of the lipid membrane with bound septins filaments, a more realistic model based on the geometry of a GUV (a sphere filled with an incompressible fluid) would have to be used. Such a model would provide the elastic modulus of the membrane which should be independent of the size of the vesicle. A model has been proposed by Schäfer et al. (2015) where the exact shape of the vesicle is computed from the Laplace equation. The geometries of both the Hertz contact and the Schäfer et al. (2015) model are shown in 4.4 C and D respectively. Importantly, in the Hertz model the object is a volume, while in the model from Schäfer et al. (2015), only the surface of the sphere is considered.

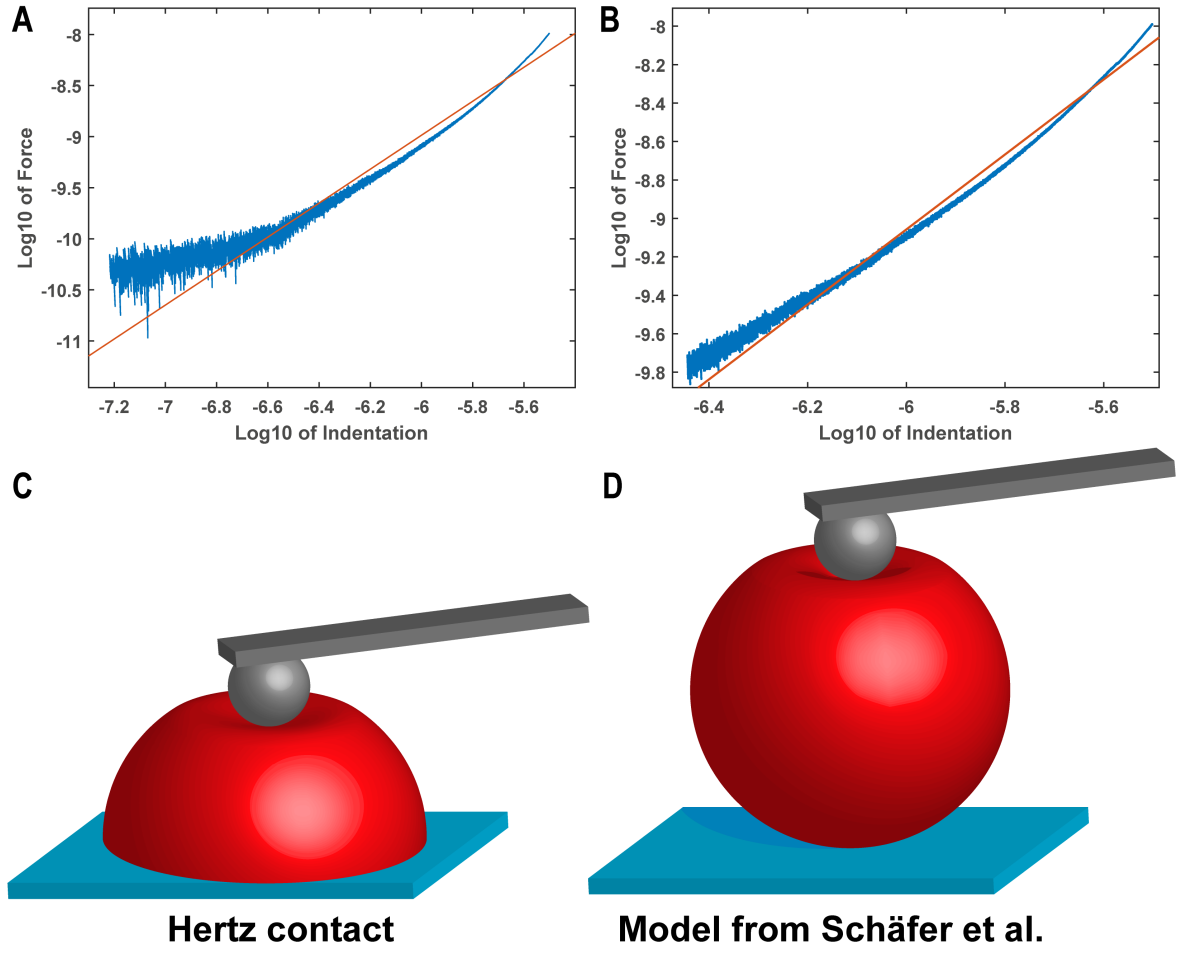

Figure 4.4 – (A) and (B) Log-log plot of the force as a function of the indentation depth recorded on a GUV and fitted with a linear function to obtain the power law. The Hertz model predicts a slop of 1.5, while on the left one the slope obtained was 1.67, and 1.95 on the right plot after removing the initial points. (C) Scheme of the geometry of the Hertz contact, considering a half ball with elastic properties. (D) Scheme of the model developed in Schäfer et al. (2015) considering a sphere with elastic properties, some initial tension, and no dissipation by viscosity.

4.4 AFM analysis using a spherical model

The model described by Schäfer et al. (2015) relies on numerically solving a system of equation – see section 2.8.3 – to find the equilibrium shape of the vesicle when a given force is applied by a tip with a known geometry. From the shape of the vesicle, it is possible to obtain the indentation depth, and thus plot the force indentation curves. This leaves two parameters to be fitted, the initial tension and the compressibility – equivalent to the elastic modulus. By fitting the experimental data with this model, both can be recovered. However, this fit relies on numerically solving a system of non linear equations. The numerical stability of the system is poor when the tip is bigger than the vesicle. I therefore worked with a new batch of vesicles, and tried to limit the washing steps to preserve the biggest vesicles. I also changed the activation of the coverslip to have a weaker interaction because polylysine would induce bursting of the biggest GUVs on the coverslip.

The vesicles were produced by gel assisted swelling, and were incubated with septins prior to the deposition on the glass coverslips. They were then diluted 10 times and left to sediment on the coverslips. Further dilution of the septins was performed by washing and replacing half of the solution, for a final dilution by 20. In the presence of septins no extra treatment was necessary to ensure strong interaction of the vesicles with the coverslip. For the control experiment, I pre incubated the coverslip with 20 µL of 10 mM of $MgCl_2$ before adding 1 mL of sample to provide enough interaction of the vesicles with the glass coverslips.

I used the same spherical tips with a radius of 1.7 µm and studied the mechanical properties of vesicles with either no septins or pre incubated septins at either 200 nM or 400 nM. The vesicles had radii ranging from 10 to 20 µm. Each vesicle was indented several times with a full cycle of the tip coming in contact, lowered until a set maximum force was reached and then retracted. The maximum force in the cycle was increased after each cycle starting at 1 nN, and up to 15 nN. A force indentation curve is displayed in Figure 4.5 A. The grey circles correspond to the numerically solved model for the vesicle. The indentation depth would often reach more than 3 µm, while the tip was only 1.7 µm in radius. I thereby discarded the portion of the curves corresponding to indentation higher than 3 µm, because the cantilever might also touch the vesicles.

After fitting the experimental data, I was able to recover the elastic area compressibility of the vesicles in the different conditions. This constant characterises the resistance to area expansion under mechanical load. A high area compressibility means that a high force is required to extend the membrane. The compressibility for individual vesicles are displayed in Figure 4.5 B for all three conditions. The vesicles in the control experiment (in the absence of septins) had compressibility of 32 $\pm$ 6 mN/m, 11 $\pm$ 2 mN/m for the low septin concentration (200 nM of septins) and 7 $\pm$ 2 mN/m for the high septin concentration (400 nM of septins). The compressibility obtained for the control experiment is quite low as compared to the values in the literature which are around 200 mN/m (Kwok and Evans, 1981; Rawicz et al., 2000). It was surprising to observe that increasing the septin concentration and therefore the average septin density on the vesicles led to a reduction in the compressibility, meaning that the vesicles were more easily deformed.

To confirm this observation, and fit the data at even higher force to validate the model, I used a bigger tip with a radius of 5.1 µm. This ensures that the cantilever should not enter in contact with the vesicles, and thus only the tip will press on the

vesicles. I used septins at concentrations of 200 nM to compare with the control experiment, in the absence of septins. The compressibility for individual vesicles are displayed in Figure 4.5 C for both the control experiment and after the addition of septins. The vesicles in the control experiment had a compressibility of 74 ± 20 mN/m and 11 ± 2 mN/m in the presence septins. The reduction of compressibility after the addition of septins was confirmed.

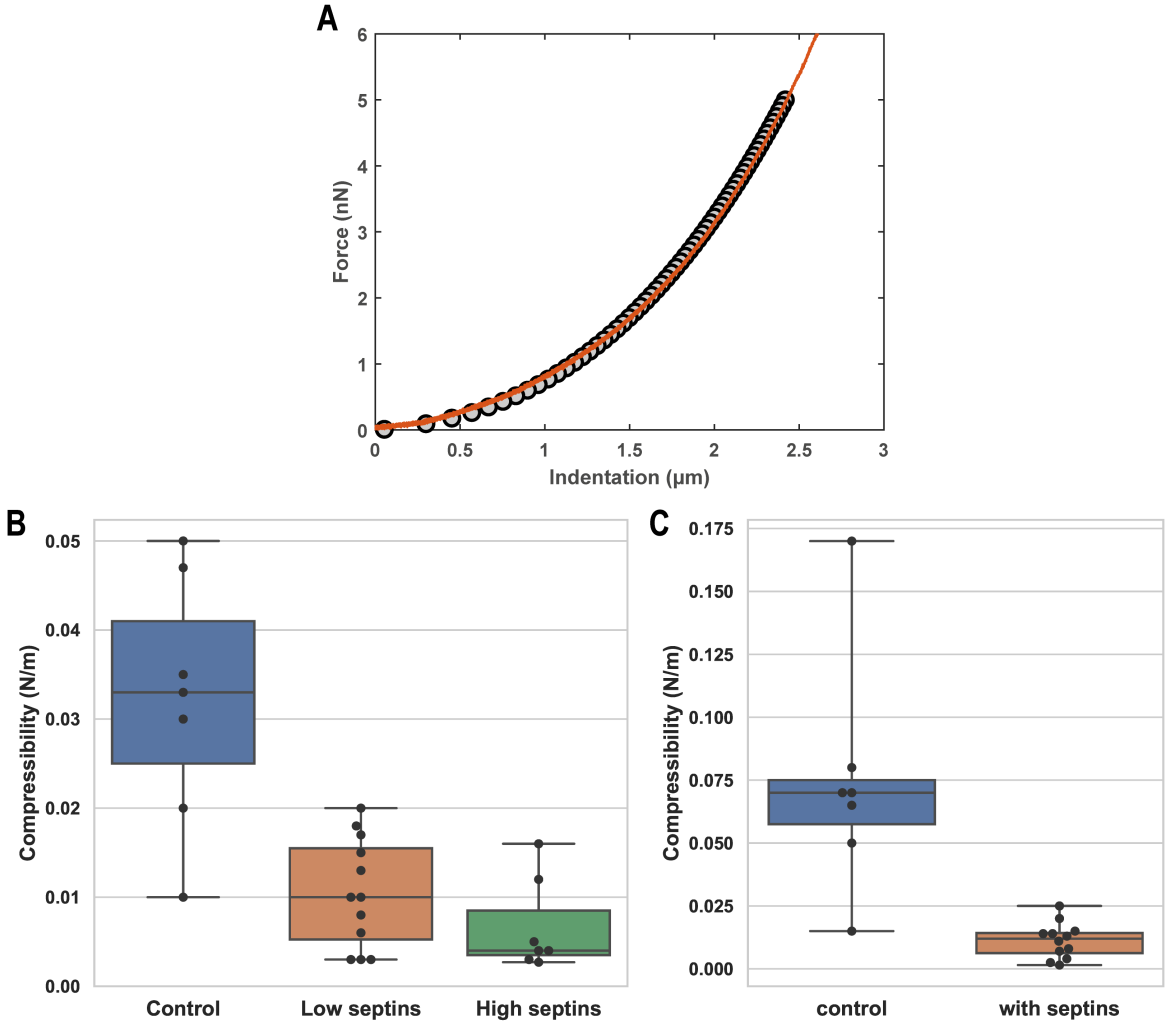

Figure 4.5 – AFM experiments analysed using the model developed in Schäfer et al. (2015). (A) Force applied on the GUV as a function of the indentation. Grey dots are the values obtaiend when modelling the experiment with a compressibility of 65 mN/m and a tension of 0.3 mN/m. (B) Compressibility modulus using a small AFM tip (radius = 1.7 μm) for the control experiment, in the presence of 200 nM of septins (low septins) and 400 nM of septins (high septins). (C) Compressibility modulus using a bigger AFM tip (radius = 5.1 μm) for the control experiment and in the presence of 200 nM of septins.

To understand how the addition of filaments on a membrane can lead to a reduction in its apparent rigidity and reconcile these results with the earlier results showing an increase in membrane rigidity, I analysed the movies obtained during the indentation experiments. I could observe the swelling of the vesicle in the equatorial plane when the tip is lowered and how it retracts when the tip returns to its initial position. In the

presence of septins the vesicles were often pre-deformed. The deformation was highly vesicle dependent. Snapshots from an indentation experiment on a pre deformed GUV are displayed in Figure 4.6. The vesicle was incubated with 400 nM of septins before indentation. It displayed a recognisable short inward tubulation prior to indentation (see arrow in Figure 4.6). When the force increased, the tubulation gets smaller while the rest of the vesicle surface gets flattened and the overall diameter in the equatorial plane increases. At a given applied force, the tubulation was completely flattened. The vesicle displayed no defect. Upon release of the force, the vesicle recovered its initial shape, with the small tubulation at the same place and similar ruffles on the surface. Similar reversible unfolding of initial defects was observed in all the experiments with septins. I hypothesised that the reduction of the compressibility could be directly related to these initial defects acting as membrane reservoir.

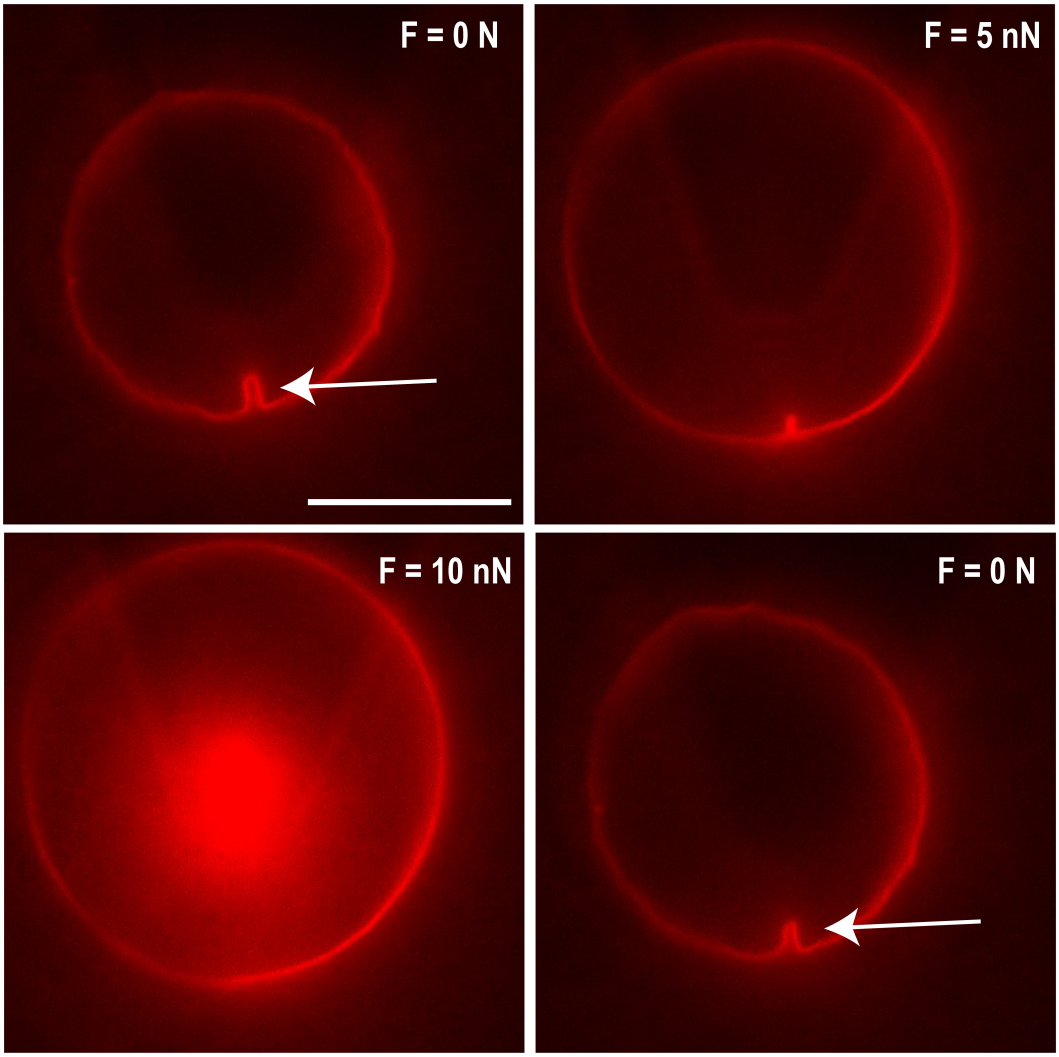

Figure 4.6 – Snapshots from an AFM indentation experiment on a GUV coated with yeast septins. Before indentation, the vesicle has ruffles and some tubulation going inwards (see arrow). Upon indentation, the ruffles and the tube unfold, and the GUV swells. After release of the force from the tip, the ruffles as well as the tube reappear. Scale bar is 10 μm.

4.5 Explanation for softening

The apparent softening of the membrane might be a consequence of the ruffles appearing after the addition of septins. Indeed, when the membrane is ruffled, an excess area can be recovered by flattening these ruffles. To estimate the effect of the deformations, I considered a model accounting for membrane deformations.

I first compared the shape of the vesicle before indentation as a function of the septin density. Images of different vesicles prior to indentation are displayed in Figure 4.7 A. The top row corresponds to vesicles incubated with 400 nM of septins while the bottom row corresponds to vesicles incubated with 200 nM of septins. The vesicles incubated with higher septin density showed, on average, more important initial deformations. The deformations were not periodic, and trying to extract the exact shape of the vesicles seemed too complicated. After discussing with a theoretician, Martin Lenz, I propose a model to explain the apparent softening of the vesicles after the addition of septins. This model can also recover some of the mechanical features of septin meshes.

This model proposes that the addition of septins induces an intrinsic curvature to the membrane. This intrinsic curvature leads to the formation of ruffles which store an excess area of membrane. The ruffles can accommodate the deformation by unfolding, preventing the membrane expansion. Importantly, the bending modulus of membranes is much lower than their area compressibility. Therefore the force required to flatten the membrane is lower than the one needed to expand it. In my experiments, I will need to also consider the bending modulus of septin filaments, which can be estimated from their persistence length as detailed below – see equation 4.12.

To estimate the importance of the ruffles on the mechanical properties of the septin-membrane system in my experiment, I considered the Helfrich Hamiltonian:

$$H = \iint \frac{\kappa}{2}(C(\overrightarrow{r}) - C_0(\overrightarrow{r}))^2 + \frac{\sigma}{2}(\overrightarrow{\nabla} h)^2 \; d^2\overrightarrow{r} \tag{4.1}$$

Where κ is the bending modulus of the membrane, C_0 its intrinsic curvature, σ the tension in the membrane and h is the height of the membrane. To take into account the initial deformations, I impose a non null intrinsic curvature to the membrane. The exact shape of the intrinsic curvature for each GUV is too complicated to model. Therefore, I needed to chose a shape that could mimic the bumps observed in fluorescence microscopy. I arbitrarily chose C_0 as a random coloured gaussian noise. It is described by the two following equations:

$$< C_0(\overrightarrow{r}) > = \; A \tag{4.2}$$

$$< (C_0(\overrightarrow{r_1}) - A)(C_0(\overrightarrow{r_2}) - A) > = \; B \exp\left(-\frac{|\overrightarrow{r_1} - \overrightarrow{r_2}|}{a}\right) \tag{4.3}$$

Where A is the average curvature, corresponding to the curvature of the spherical GUV in our experiment. B is related to the amplitude of the local variations of the intrinsic curvature. It is therefore related to the amplitude of the deformations. a is the distance for which curvatures are strongly correlated, it is related to the typical size of the bumps in the membrane plan. In my study typical values for a and B are 1 μm[1] and 10^{13} m^{-2}. A membrane with curvature following this distribution is displayed in Figure 4.7 B. Note that the vertical axis is not to scale. The exact shape of the membrane is not crucial as I only performed the first order calculation.

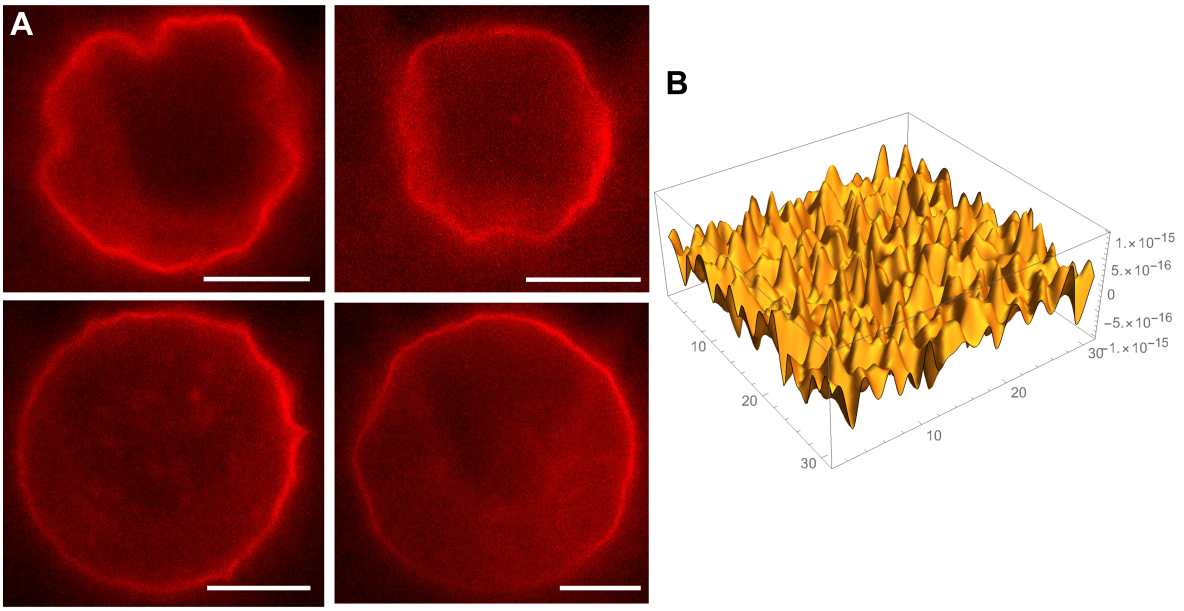

Figure 4.7 – (A) Snapshots of vesicles interacting with yeast septins. Top row, the concentration of septins is 400 nM, bottom row, septin concentration is 200 nM. Some big ruffles could be observed, mainly for the higher septin concentration. Scale bars are 10 μm. (B) Surface following the curvature law that we propose to estimate the consequence of ruffling on the vesicle effective compressibility modulus.

Analytical calculations can only be performed on the linear equations (first order). In our conditions, the second order correction could lead to errors close to 30%. However, I considered that performing the non linear calculation would be unreasonably complicated considering that we do not match the real geometry of the membrane. I detail the equations in Appendix A.

From the Helfrich Hamiltonian expressed in equation 4.1 and considering force balance one can obtain:

$$\Delta\left[\left(\Delta - \frac{\sigma}{\kappa}\right)h - C_0\right] = 0 \tag{4.4}$$

Which becomes in Fourier space:

$$\tilde{h} = -\frac{\widetilde{C_0}}{q^2 + \lambda^2} \;;\; \lambda = \sqrt{\frac{\sigma}{\kappa}} \tag{4.5}$$

It is possible to recover the fraction area contained within the ruffles – difference between the projected area and the total area – of the membrane:

$$< \delta A > = \iint (\overrightarrow{\nabla} h)^2 \; d^2\overrightarrow{r} \tag{4.6}$$

This equation can be solved considering:

$$\widetilde{C_0}(\overrightarrow{q}) = 4A\pi^2\delta(\overrightarrow{q}) + d(\overrightarrow{q}) \tag{4.7}$$

and using Fourier transform. Finally the fraction of area within the ruffles is:

$$< \delta A > = \frac{a^2 B}{2(1-(\lambda a)^2)^2}\left[\frac{(2+(\lambda a)^2)Arsec(\lambda a)}{\sqrt{(\lambda a)^2 - 1}} - 3\right] \tag{4.8}$$

For values typical of the membranes that I studied, $\lambda a >> 1$. The previous equation then simplifies as:

$$< \delta A > = \frac{\pi B a}{4} \sqrt{\frac{\kappa}{\sigma}} \tag{4.9}$$

The area in the ruffles depends on the tension of the membrane which can vary by more than one order of magnitude. Introducing this equation in the model from Schäfer et al. (2015) – see section 4.4 – is possible. An additional term should be added to describe the apparent extension of the membrane due to the unfolding of ruffles. However, the number of parameters that have to be set becomes too high to be practically and reasonably usable. I therefore decided to only focus on the apparent initial area compressibility by comparing the value of the initial slope to stretch the membrane for a ruffled membrane to an flat membrane. I would then compare the compressibility of the membrane to the derivate of (3.11):

$$\left(\frac{d < \delta A >}{d\sigma} \right)^{-1} = \frac{8\sigma^{3/2}}{\pi a B \kappa^{1/2}} \tag{4.10}$$

The initial apparent rigidity strongly depends on the tension, which cannot be obtained directly. I took the opposite approach of estimating the other parameters including the fraction of area contained in the ruffles and replace the tension. The relation then becomes:

$$\left(\frac{d < \delta A >}{d\sigma} \right)^{-1} = \frac{2\pi^2 a^2 B^2 \kappa}{< \delta A >^3} \tag{4.11}$$

The fraction of area contained within the ruffles strongly depends on the septin concentration and strongly varies from one GUV to another. I wanted to obtain an order of magnitude of the initial apparent area compressibility. The values chosen for each parameters are based on observations but could strongly vary.

The estimation of the fraction of area was performed considering a 2D sinusoidal function displaying the curvatures septins have been shown to induce on membranes (Beber et al., 2019b). I chose a wavelength of 2 µm with an amplitude of 250 nm corresponding to typical deformations of vesicles by septins as reported in Beber et al. (2019b). I obtained $< \delta A >= 0.3$. Then the bending modulus was estimated from the persistence length of the septin filaments. For filaments with persistence length L_p and with typical spacing of l, the bending modulus is:

$$\kappa = \frac{k_B T L_p}{l} \tag{4.12}$$

I took $L_p = 10$ µm, typical value for the persistence length of septin filaments from the literature (Bridges et al., 2014; Beber et al., 2019b) and $l = 25$ nm, typical distance between septin filaments from SEM experiments. I based the value of a on the typical wavelength of the deformation, typically of the order of the micrometre. The value of B is chosen as the square of the typical curvature preferred by septins which is $-3\ \mu m^{-1}$.

$$\begin{aligned} a &= 10^{-6}\ \text{m} \\ B &= 10^{13}\ \text{m}^{-2} \end{aligned}$$

From those values, I obtained an apparent area compressibility of 10 mN.m^{-1}. This estimated value is close to the area compressibility obtained from the experiments.

I concluded that the unfolding of ruffles can accurately explain the softening of the membrane upon addition of septins. Interestingly, while the apparent area compressibility is reduced, the bending modulus is increased by a factor of 20 from a naked lipid membrane.

This model can also explain the reason for the increased Young's modulus in the case of the small vesicles. When the size of the vesicle becomes smaller than the typical size of the deformation and typical length of a septin filament, the vesicles are initially spherical. The absence of initial deformations prevents the softening of the vesicle and only the increase in bending rigidity matters.

The vesicles did not display a very high area compressibility modulus after the unfolding of ruffles. It is expected that septin filaments would possess a high elastic modulus. However, in the AFM indentation experiment I tested the expansion of the membrane exclusively. During membrane extension, I suspect that septin filaments are not stressed along their main axis. As I observed previously, the bilayer is fluid under the septin network. Therefore, even though the membrane expands, no stress is transmitted to the septin filaments. Once the ruffles are unfolded, the membrane will start expanding similarly to the control experiment.

4.6 Conclusion

Using AFM indentation, I was able to probe some of the mechanical properties of septin networks bound to membranes. It appeared that the addition of septins seemed to reduce the compressibility modulus of the membrane. This result was counter-intuitive as micropipette aspiration experiments showed that septins played a role in the mechanical stabilisation of the membrane. Both results were conciliated considering the pre-deformations of membranes before indentation when septins were added. By deforming the membrane prior to the AFM indentation experiment, septins can reduce the apparent area compressibility modulus. Indeed, the ruffles act as a reservoir of membrane, and during early indentation, the unfolding of the ruffles can accommodate for the imposed deformation with no expansion of the membrane – Figure 4.8. In the case of the lower septin concentration, the deformations were less important and thus the reduction of apparent area compressibility was lower. The energy necessary to bend septins is smaller than the one required to expand the membrane, the area compressibility modulus of the vesicle will therefore appear smaller than its real value.

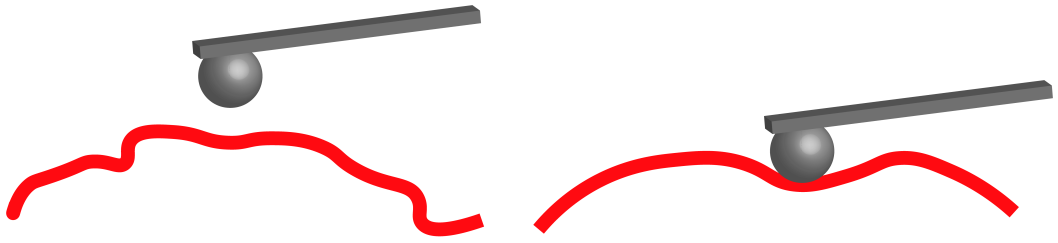

Figure 4.8 – Schematic representation of a pre-deformed membrane indented with an AFM tip. Due to the initial deformations, There is an excess in the area (here the length) that can accommodate early indentation with no area expansion.

Summary

- **Septins can strongly deform supported lipid bilayers deposited on mica**
- **Micropipette aspiration experiments showed that septins change the mechanical properties of membranes**
- **Using AFM indentation and a simple contact model, I showed that septins increase the overall rigidity of small vesicles**
- **Using a model made for studying vesicle indentation, septins seemed to reduce the apparent area compressibility of the vesicle**
- **Finally, I explained this reduction of the apparent area compressibility of the vesicle using a simple model accounting for initial deformations of the vesicles**

Chapter 5

Discussion

5.1 Diffusion barrier

Studies performed in vivo have shown that septins play a role in the establishment of diffusion barriers. These barriers, essential to many cellular processes, are still poorly understood and the mechanisms behind their functions are unknown. A handful of in vivo studies have analysed the behaviour of proteins in the absence of septins. In all of those studies, the artefactual effects (unspecific interactions, steric hindrance etc.) that might come from the fluorescent probe used to track these proteins is not discussed.

I aimed at determining the mechanism through which septins generate these diffusion barriers. I proposed a systematic *in vitro* approach to study the properties of possible diffusion barriers established by septins using reconstituted assays. I studied the diffusion of different models of membrane components (membrane bound proteins and lipids) to understand the mechanism of the diffusion barriers established by septins. During my PhD I chose the fluorescent probes according to the geometry and model I was studying.

5.1.1 Diffusion of lipids

I used FRAP to study the overall fluidity of the bilayer in the context of septin binding. I was able to show that septins do not affect the fluidity of the bilayer nor immobilise PI(4,5)P_2, lipid necessary for the septin-membrane interaction. It had indeed been observed *in vivo* that septins do not alter the fluidity of the external layer of lipids (Ewers et al., 2014). It had been proposed that septins could immobilise some lipids which could then prevent the diffusion of transmembrane proteins and membrane bound proteins. This proposition was supported by observation made in Pacheco et al. (2022) where they observed that septins could act as a diffusion barrier for PIP_2. However, in this study published on bioRxiv, they did not discuss the effect of the probe used to assess the diffusion of PIP_2. The total size of their probe ranges around 6 to 10 nm. I believe that the steric effect of the probe should be considered. Since I used reconstituted biomimetic membranes, I could probe the diffusion of PI(4,5)P_2 by using a chemically synthesised Texas Red-PI(4,5)P_2, with the fluorescent molecule placed on one the lipids' tail. This should ensure that septins can interact freely with the labelled PI(4,5)P_2. In my study, septins did not immobilise PI(4,5)P_2. In vivo this strategy cannot be used, and the probes available will likely alter the properties of PI(4,5)P_2.

5.1.2 Diffusion of models of proteins

I looked at the diffusion of model membrane bound proteins. I tested different models reflecting different geometries for membrane associated proteins from transmembrane with no cytosolic domain (SD4, Sstr3), proteins with small cytosolic domain (basigin, Smo) and proteins part of big complexes (sec5p spa2)(Barral et al., 2000; Kwitny et al., 2010; Hu et al., 2010; Ewers et al., 2014). I observed that the models for both transmembrane proteins and even for proteins with a cytosolic domain were able to diffuse, while the one accounting for bigger protein complexes could not.

In vivo, septins interact with many binding partners, which might change the properties of the diffusion barrier. Most notably, they might create a crowding effect, which could further reduce or even prevent the diffusion of many molecules *in vivo*. I tested two known interactors of septins, playing a key role during cell division, the Bud3 and Bud4 proteins. The addition of the Bud proteins reshaped the organisation of the septin filaments but did not change the ability of the streptavidin to diffuse through septin networks.

It is possible that other binding partners of the septins influence the barrier effect *in vivo*. A large number of proteins are involved in cell division. The best candidates would be proteins also interacting with the membrane or transmembrane proteins. Interestingly, at the bud neck, the ER is in close proximity with the plasma membrane, and some contact sites are present. The contact sites are stabilised by proteins connecting the two membranes. These proteins would not be able to diffuse due to the presence of septin filaments, notably. Their accumulation, as well as the accumulation of many other proteins could also result in the formation of a specific lipidic domain at the bud neck as suggested in Clay et al. (2014). The formation of such a domain could result in the establishment of a diffusion barrier preventing the diffusion of lipids.

I propose that on their own, septins do not block the majority of membrane bound proteins, except for larger protein complexes (more than 10 nm from the membrane). The compartmentalisation of protein complexes can still account for the polarisation of the membrane and the ability to differentiate compartments. Depending on the proteins recruited by septins, it would be possible for cells to regulate the properties of the diffusion barrier in cells.

Similarly, human septin filaments displayed the same propensity to generate diffusion barriers. Because septins are involved in diffusion barriers in various cell types and organisms, I would expect that the septin dependent diffusion barriers properties are conserved. However, the proteins they recruit may differ, which could alter the *in vivo* features of diffusion barriers established by septins.

In all experiments assaying the diffusion of streptavidin, an important immobile fraction was detected. The size of the DSPE-PEG-streptavidin molecule might reach the threshold for the maximal size of particles able to diffuse in the presence of septin networks. This suggestion is supported by the significantly reduced diffusion rate of the molecule in the presence of septins. Some particles might therefore be trapped. Streptavidin being a tetramer, it is possible for one streptavidin to interact with more than one biotinylated lipid. In the control experiment, this would result in a smaller diffusion coefficient, but after the addition of septins, it is possible that it could result in fully entrapping the streptavidin.

Concerning Quantum Dots, an immobile fraction was also detected, but as Quantum Dots were never able to diffuse across septin filaments, this could be the consequence of a local high density of septins.

Spacing between septins and the membrane

Proteins possessing a large cytosolic domain (about 6 nm) can diffuse across septin networks. I hypothesise that there is a gap between the membrane and the septins. Interestingly, a spacing between septin filaments and the membrane has been observed *in situ* in dividing yeast cells (Bertin et al., 2012). Because septins interact directly with the membrane, I propose that septins can interact with the membrane via the coiled coils domains (which are about 10 nm long) localised at their C-terminus. From sequence analysis, it has been proposed that the coiled coils of cdc12 and SEPT6 possess an amphipathic helix that can interact with lipid membranes (Cannon et al., 2019).

The spacing between septins and the membrane might also experience dynamic variations. Indeed, I observed that increasing the tension and therefore reducing the entropic fluctuations of the membrane led to a reduction of the diffusion rate of streptavidin.

Structural studies of septin filaments bound to the membrane could confirm which domain of septins is involved in the septin-membrane binding. Identifying the domain of interaction would help confirm the hypothesis that septin filaments are distant from the membrane and therefore that transmembrane proteins and proteins with small cytosolic domains could possibly diffuse.

Perspectives

From my results, I expect that, *in vivo*, septins would only block the diffusion of protein complexes or proteins connecting the plasma membrane to the ER (Ist2). *In vivo* experiments assaying the diffusion of lipids and proteins at the bud neck would allow a more comprehensive study of the mechanisms. Analysing the lipid diffusion in the PM during cell division at the bud neck would confirm that an accumulation of lipids is not effective. It would also be interesting to study the diffusion of particles bound to the membrane with a small cytosolic domain. Ideally, these particles should not interact with other particles in cells to prevent effects from binding partners.

Finally, experiments assaying the diffusion of various model proteins at various stages during cell division would give some insight on the time evolution of the properties of the diffusion barrier. Binding partners of septins or other proteins recruited at the bud neck might alter the properties of the diffusion barrier. It would therefore be possible for cells to dynamically control the features of diffusion barriers established by septin filaments.

5.2 Mechanical properties

Septins have been identified *in vivo* to play some mechanical roles in stabilising the membrane. The persistence length of single septin filaments has been studied as well as their ability to deform membranes *in vitro*. Both observations suggest that septins have intrinsic mechanical properties that likely have a functional role *in vivo*. In the continuity of previous studies performed in the lab, I analysed the mechanical properties of septin networks bound on a lipid biomimetic membrane.

Performing micropipette aspiration, I observed that vesicles with septins bound would require a much higher aspiration pressure than without septins. After an initial aspiration, the vesicle would not deform. This demonstrated that septins would

strongly rigidify the membrane which is not able to deform until the septin filaments are disrupted. At a pressure required to disrupt the septin filaments, the vesicles are fully aspirated showing how stiff the septin network is. This clearly indicates that septins could play an important role in the stabilisation of the membrane by modifying its mechanical properties.

I used AFM indentation to probe the mechanical properties of vesicles with bound septin filaments. I observed that on GUVs, septins could surprisingly reduce the apparent area compressibility of the membrane. Vesicles were therefore easier to deform after the addition of septins. I proposed with the help of Martin Lenz an explanation relying on the unfolding of the initial deformations caused by septins to accommodate the indentation by the AFM tip. The energy necessary to unfold the membrane being lower than the one required to expand it, the force necessary to indent the GUVs was lower.

The AFM indentation experiments allowed the estimation of the bending modulus of septins. However, the elastic modulus was not probed. To probe the elastic modulus of septins, it would be necessary to force the filaments to elongate. Such elongation could happen when the membrane is forced to expand, however because lipids seem to be able to flow underneath septin filaments, I think that during indentation, filaments are never stressed along their main axis. They only bend with the unfolding of the membrane deformations.

It is possible that septins can act as a membrane reservoir. By deforming locally the membrane, they could create ruffles that can unfold under mechanical stress. Some protein machineries have already been identified as playing a similar role such as the caveolae (Del Pozo et al., 2021).

Perspectives

To force septin filaments to deform along their main axis, it could be interesting to use cross linked septin networks. If the septin filaments are cross linked, the expansion of the membrane will impose some stress on the septin network. To accommodate the expansion, filaments would have to either elongate or cross-linker and/or filaments would have to disassemble. The difference between these two mechanisms would be sorted out by consecutive AFM experiments. From the micropipette experiments where septins prevented the deformation of the membrane under loads important enough to fully aspirate the vesicles, I would assume that indeed, septins could strongly increase the area compressibility modulus of the membrane when forced to expand.

5.3 Conclusion

Finally, I would argue that it is possible that septins carry an important role of membrane stabilisation and organisation. My results suggest that septin filaments are not in direct contact with the membrane but are connected with long coiled coils domains creating a gap. This spacing could allow the diffusion of membrane proteins except for large protein complexes. I argue that the consideration that septins would be in close contact with the membrane would lead to fully blocking the diffusion of all proteins possessing any cytosolic domain. I believe that creating such barrier at all places where septins interact with the membrane would result in very important compartmentalisation of the plasma membrane, even in regions where it is not necessary. I believe that my results suggest a much more flexible barrier which properties could be tuned dynamically by recruiting other proteins.

Appendix A

Deriving the area contained in the ruffles

I used the Helfrich Hamiltonian which describes the state of a membrane:

$$H = \iint \frac{\kappa}{2}(C(\overrightarrow{r}) - C_0(\overrightarrow{r}))^2 + \frac{\sigma}{2}(\overrightarrow{\nabla} h)^2 \; d^2\overrightarrow{r} \tag{A.1}$$

The first consideration is the the curvature C is related to the height h by the following equation:

$$C = \Delta h \tag{A.2}$$

I then consider force equilibrium, which translates to the hamiltonian $\delta H = 0$ as: :

$$\delta H = \iint \kappa(\Delta h(\overrightarrow{r}) - C_0(\overrightarrow{r}))^2 \Delta\delta h + \sigma \overrightarrow{\nabla} h \overrightarrow{\nabla} \delta h \; d^2\overrightarrow{r} \tag{A.3}$$

when considering a small deflection of δh.

$$\kappa\Delta(\Delta h - C_0) - \sigma\Delta h = 0 \tag{A.4}$$

$$\Delta\left[\left(\Delta - \frac{\sigma}{\kappa}\right) h - C_0\right] = 0 \tag{A.5}$$

In Fourier space the previous equation transforms as:

$$\tilde{h} = -\frac{\widetilde{C_0}}{q^2 + \lambda^2} \; ; \; \lambda = \sqrt{\frac{\sigma}{\kappa}} \tag{A.6}$$

I had to define a geometry for the initial state of the membrane. I chose a coloured gaussian noise, which gives a typical amplitude of the curvature and a spatial correlation. The intrinsic curvature is therefore defined by the following two equations:

$$< C_0(\overrightarrow{r}) > = \; A \tag{A.7}$$

$$< (C_0(\overrightarrow{r_1}) - A)(C_0(\overrightarrow{r_2}) - A) > = \; B \exp\left(-\frac{|\overrightarrow{r_1} - \overrightarrow{r_2}|}{a}\right) \tag{A.8}$$

The area contained in the ruffles is:

$$\delta A \ = \iint (\overrightarrow{\nabla} h)^2 \ d^2\overrightarrow{r} \tag{A.9}$$

Using Fourier transform, the equation becomes:

$$\delta A \ = \iint d^2\overrightarrow{r} \iint \frac{d^2\overrightarrow{q_1}}{(2\pi)^2} \iint \frac{d^2\overrightarrow{q_2}}{(2\pi)^2} i\overrightarrow{q_1}.i\overrightarrow{q_2} e^{i\overrightarrow{q1}.\overrightarrow{r_1}} e^{i\overrightarrow{q_2}.\overrightarrow{r_2}} < \tilde{h}(\overrightarrow{q_1})\tilde{h}(\overrightarrow{q_2}) > \tag{A.10}$$

To compute $< \tilde{h}(\overrightarrow{q_1})\tilde{h}(\overrightarrow{q_2}) >$ I defined $\widetilde{d}(\overrightarrow{q})$ as:

$$\widetilde{C_0}(\overrightarrow{q}) = 4A\pi^2\delta(\overrightarrow{q}) + \widetilde{d}(\overrightarrow{q}) \tag{A.11}$$

And therefore:

$$< \widetilde{d}(\overrightarrow{q}) > = 0 \tag{A.12}$$

Next I calculated $< \widetilde{d}(\overrightarrow{q_1})\widetilde{d}(\overrightarrow{q_2}) >$:

$$< \widetilde{d}(\overrightarrow{q_1})\widetilde{d}(\overrightarrow{q_2}) > = \iint d^2\overrightarrow{r_1} \iint d^2\overrightarrow{r_2} \ e^{-i\overrightarrow{q1}.\overrightarrow{r1}} e^{-i\overrightarrow{q2}.\overrightarrow{r2}} B \exp\left(-\frac{|\overrightarrow{r_1} - \overrightarrow{r_2}|}{a}\right) \tag{A.13}$$

By applying a change of variable $\overrightarrow{\rho} = \overrightarrow{r_1} - \overrightarrow{r_2}$ the equation becomes:

$$< \widetilde{d}(\overrightarrow{q_1})\widetilde{d}(\overrightarrow{q_2}) > = B \iint d^2\overrightarrow{r_1} \iint d^2\overrightarrow{\rho} \ e^{-i(\overrightarrow{q_1}+\overrightarrow{q_2}).\overrightarrow{r_1}} e^{-i\overrightarrow{q_2}.\overrightarrow{\rho}} \exp\left(-\frac{|\overrightarrow{\rho}|}{a}\right) \tag{A.14}$$

$$< \widetilde{d}(\overrightarrow{q_1})\widetilde{d}(\overrightarrow{q_2}) > = 4B\pi^2\delta(\overrightarrow{q_1} + \overrightarrow{q_2}) \iint d^2\overrightarrow{\rho} \ e^{-i\overrightarrow{q_2}.\overrightarrow{\rho}} \exp\left(-\frac{|\overrightarrow{\rho}|}{a}\right) \tag{A.15}$$

The second integral is invariant by rotation, so I assume $\overrightarrow{q_2} = q\overrightarrow{e_x}$ and define ϕ as the angle of $\overrightarrow{\rho}$:

$$\overrightarrow{\rho} = \rho(cos(\phi)\overrightarrow{e_x} + sin(\phi)\overrightarrow{e_y}) \tag{A.16}$$

Then equation A.15 bcomes:

$$< \widetilde{d}(\overrightarrow{q_1})\widetilde{d}(\overrightarrow{q_2}) > = 4B\pi^2\delta(\overrightarrow{q_1} + \overrightarrow{q_2}) \int_{-\pi}^{\pi} d\phi \ \int_0^{\infty} d\rho \ e^{(iqcos(\phi) - \frac{1}{a})\rho} \tag{A.17}$$

By performing in integration by part and considering that $cos(\pi - \phi) = -cos(\phi)$ the equations becomes:

$$< \widetilde{d}(\overrightarrow{q_1})\widetilde{d}(\overrightarrow{q_2}) > = 8a^2B\pi^2\delta(\overrightarrow{q_1} + \overrightarrow{q_2}) \int_{-\frac{\pi}{2}}^{\frac{\pi}{2}} d\phi \ Re\left[\frac{1}{(1 - iqacos(\phi))^2}\right] \tag{A.18}$$

The last can be computed using Mathematica, and finally:

$$< \widetilde{d}(\overrightarrow{q_1})\widetilde{d}(\overrightarrow{q_2}) > = \frac{8a^2B\pi^3\delta(\overrightarrow{q_1} + \overrightarrow{q_2})}{(1 + (qa)^2)^{3/2}} \tag{A.19}$$

Injecting this result in $< \tilde{h}(\overrightarrow{q_1})\tilde{h}(\overrightarrow{q_2}) >$ I obtained:

$$< \tilde{h}(\overrightarrow{q_1})\tilde{h}(\overrightarrow{q_2}) > = (2\pi)^4 \frac{A^2}{\lambda^2}\delta(\overrightarrow{q_1})\delta(\overrightarrow{q_2}) + \frac{8a^2B\pi^3\delta(\overrightarrow{q_1} + \overrightarrow{q_2})}{(1+(qa)^2)^{3/2}(q^2+\lambda^2)} \tag{A.20}$$

Injecting this result in equation A.10, I obtained:

$$\delta A = \iint \frac{d^2\overrightarrow{q}}{(2\pi)^2}\overrightarrow{q}^2 \iint d^2\overrightarrow{r}e^{i\overrightarrow{0}.\overrightarrow{r}}\frac{2a^2B\pi}{(1+(qa)^2)^{3/2}(q^2+\lambda^2)} \tag{A.21}$$

$$\iint d^2\overrightarrow{r} = A_{tot} \tag{A.22}$$

Where A_{tot} is the total area of the membrane. Therefore, $< \delta A >$ the portion of area contained in the ruffles is:

$$< \delta A > = a^2B \int \frac{q^3dq}{(1+(qa)^2)^{3/2}(q^2+\lambda^2)} \tag{A.23}$$

By using the change of variable $Q = (qa)^2$, the equations becomes:

$$< \delta A > = \frac{a^2B}{2} \int \frac{QdQ}{(1+Q^2)^{3/2}(Q+(a\lambda)^2)} \tag{A.24}$$

The integral can be computed using Mathematica, finally:

$$< \delta A > = \frac{a^2B}{2(1-(\lambda a)^2)^2}\left[\frac{(2+(\lambda a)^2)Arsec(\lambda a)}{\sqrt{(\lambda a)^2-1}} - 3\right] \tag{A.25}$$

Bibliography

M. Abbey, M. Gaestel, and M. B. Menon. Septins: Active GTPases or just GTP-binding proteins? *Cytoskeleton*, 76(1):55–62, Jan. 2019. ISSN 1949-3584, 1949-3592. doi: 10.1002/cm.21451.

N. Ageta-Ishihara, T. Miyata, C. Ohshima, M. Watanabe, Y. Sato, Y. Hamamura, T. Higashiyama, R. Mazitschek, H. Bito, and M. Kinoshita. Septins promote dendrite and axon development by negatively regulating microtubule stability via HDAC6-mediated deacetylation. *Nature Communications*, 4(1):2532, Dec. 2013. ISSN 2041-1723. doi: 10.1038/ncomms3532.

M. C. Ashby, S. R. Maier, A. Nishimune, and J. M. Henley. Lateral Diffusion Drives Constitutive Exchange of AMPA Receptors at Dendritic Spines and Is Regulated by Spine Morphology. *Journal of Neuroscience*, 26(26):7046–7055, June 2006. ISSN 0270-6474, 1529-2401. doi: 10.1523/JNEUROSCI.1235-06.2006.

J. Atherton, A. Houdusse, and C. Moores. MAPping out distribution routes for kinesin couriers: MAPping out distribution routes for kinesin couriers. *Biology of the Cell*, 105:465–487, July 2013. ISSN 02484900. doi: 10.1111/boc.201300012.

D. Axelrod, D. Koppel, J. Schlessinger, E. Elson, and W. Webb. Mobility measurement by analysis of fluorescence photobleaching recovery kinetics. *Biophysical Journal*, 16 (9):1055–1069, Sept. 1976. ISSN 00063495. doi: 10.1016/S0006-3495(76)85755-4.

X. Bai, J. R. Bowen, T. K. Knox, K. Zhou, M. Pendziwiat, G. Kuhlenbäumer, C. V. Sindelar, and E. T. Spiliotis. Novel septin 9 repeat motifs altered in neuralgic amyotrophy bind and bundle microtubules. *Journal of Cell Biology*, 203(6):895–905, Dec. 2013. ISSN 1540-8140, 0021-9525. doi: 10.1083/jcb.201308068.

Y. Barral, V. Mermall, M. S. Mooseker, and M. Snyder. Compartmentalization of the Cell Cortex by Septins Is Required for Maintenance of Cell Polarity in Yeast. *Molecular Cell*, 5(5):841–851, May 2000. ISSN 10972765. doi: 10.1016/S1097-2765(00)80324-X.

P. M. Beard, S. J. Griffiths, O. Gonzalez, I. R. Haga, T. Pechenick Jowers, D. K. Reynolds, J. Wildenhain, H. Tekotte, M. Auer, M. Tyers, P. Ghazal, R. Zimmer, and J. Haas. A Loss of Function Analysis of Host Factors Influencing Vaccinia virus Replication by RNA Interference. *PLoS ONE*, 9(6):e98431, June 2014. ISSN 1932-6203. doi: 10.1371/journal.pone.0098431.

A. Beber, M. Alqabandi, C. Prévost, F. Viars, D. Lévy, P. Bassereau, A. Bertin, and S. Mangenot. Septin-based readout of PI(4,5)P2 incorporation into membranes of

giant unilamellar vesicles. *Cytoskeleton*, 76(1):92–103, Jan. 2019a. ISSN 1949-3584, 1949-3592. doi: 10.1002/cm.21480.

A. Beber, C. Taveneau, M. Nania, F.-C. Tsai, A. Di Cicco, P. Bassereau, D. Lévy, J. T. Cabral, H. Isambert, S. Mangenot, and A. Bertin. Membrane reshaping by micrometric curvature sensitive septin filaments. *Nature Communications*, 10(1): 420, Dec. 2019b. ISSN 2041-1723. doi: 10.1038/s41467-019-08344-5.

C. Beites, K. Campbell, and W. Trimble. The septin Sept5/CDCrel-1 competes with α-SNAP for binding to the SNARE complex. *Biochemical Journal*, 385(2):347–353, Jan. 2005. ISSN 0264-6021, 1470-8728. doi: 10.1042/BJ20041090.

C. L. Beites, H. Xie, R. Bowser, and W. S. Trimble. The septin CDCrel-1 binds syntaxin and inhibits exocytosis. *Nature Neuroscience*, 2(5):434–439, May 1999. ISSN 1097-6256, 1546-1726. doi: 10.1038/8100.

A. Bertin, M. A. McMurray, P. Grob, S.-S. Park, G. Garcia, I. Patanwala, H.-l. Ng, T. Alber, J. Thorner, and E. Nogales. *Saccharomyces cerevisiae* septins: Supramolecular organization of heterooligomers and the mechanism of filament assembly. *Proceedings of the National Academy of Sciences*, 105(24):8274–8279, June 2008. ISSN 0027-8424, 1091-6490. doi: 10.1073/pnas.0803330105.

A. Bertin, M. A. McMurray, L. Thai, G. Garcia, V. Votin, P. Grob, T. Allyn, J. Thorner, and E. Nogales. Phosphatidylinositol-4,5-bisphosphate Promotes Budding Yeast Septin Filament Assembly and Organization. *Journal of Molecular Biology*, 404(4): 711–731, Dec. 2010. ISSN 00222836. doi: 10.1016/j.jmb.2010.10.002.

A. Bertin, M. A. McMurray, J. Pierson, L. Thai, K. L. McDonald, E. A. Zehr, G. García, P. Peters, J. Thorner, and E. Nogales. Three-dimensional ultrastructure of the septin filament network in *Saccharomyces cerevisiae*. *Molecular Biology of the Cell*, 23(3): 423–432, Feb. 2012. ISSN 1059-1524, 1939-4586. doi: 10.1091/mbc.e11-10-0850.

E. Bi and H.-O. Park. Cell Polarization and Cytokinesis in Budding Yeast. *Genetics*, 191(2):347–387, June 2012. ISSN 1943-2631. doi: 10.1534/genetics.111.132886.

E. Bi, P. Maddox, D. J. Lew, E. Salmon, J. N. McMillan, E. Yeh, and J. R. Pringle. Involvement of an Actomyosin Contractile Ring in Saccharomyces cerevisiae Cytokinesis. *Journal of Cell Biology*, 142(5):1301–1312, Sept. 1998. ISSN 0021-9525, 1540-8140. doi: 10.1083/jcb.142.5.1301.

J. Bigay and B. Antonny. Curvature, Lipid Packing, and Electrostatics of Membrane Organelles: Defining Cellular Territories in Determining Specificity. *Developmental Cell*, 23(5):886–895, Nov. 2012. ISSN 15345807. doi: 10.1016/j.devcel.2012.10.009.

A. J. Borgdorff and D. Choquet. Regulation of AMPA receptor lateral movements. *Nature*, 417(6889):649–653, June 2002. ISSN 0028-0836, 1476-4687. doi: 10.1038/nature00780.

J. R. Bowen, D. Hwang, X. Bai, D. Roy, and E. T. Spiliotis. Septin GTPases spatially guide microtubule organization and plus end dynamics in polarizing epithelia. *Journal of Cell Biology*, 194(2):187–197, July 2011. ISSN 1540-8140, 0021-9525. doi: 10.1083/jcb.201102076.

J. A. Braunger, C. Kramer, D. Morick, and C. Steinem. Solid Supported Membranes Doped with PIP $_2$: Influence of Ionic Strength and pH on Bilayer Formation and Membrane Organization. *Langmuir*, 29(46):14204–14213, Nov. 2013. ISSN 0743-7463, 1520-5827. doi: 10.1021/la402646k.

A. A. Bridges, H. Zhang, S. B. Mehta, P. Occhipinti, T. Tani, and A. S. Gladfelter. Septin assemblies form by diffusion-driven annealing on membranes. *Proceedings of the National Academy of Sciences*, 111(6):2146–2151, Feb. 2014. ISSN 0027-8424, 1091-6490. doi: 10.1073/pnas.1314138111.

A. A. Bridges, M. S. Jentzsch, P. W. Oakes, P. Occhipinti, and A. S. Gladfelter. Micron-scale plasma membrane curvature is recognized by the septin cytoskeleton. *Journal of Cell Biology*, 213(1):23–32, Apr. 2016. ISSN 0021-9525, 1540-8140. doi: 10.1083/jcb.201512029.

B. Byers and L. Goetsch. A highly ordered ring of membrane associated filaments in budding yeast. *The Journal of Cell Biology*, 69:717–721, 1976. doi: doi:10.1083/jcb.69.3.717.

K. S. Cannon, B. L. Woods, J. M. Crutchley, and A. S. Gladfelter. An amphipathic helix enables septins to sense micrometer-scale membrane curvature. *Journal of Cell Biology*, 218(4):1128–1137, Apr. 2019. ISSN 0021-9525, 1540-8140. doi: 10.1083/jcb.201807211.

L. Cao, X. Ding, W. Yu, X. Yang, S. Shen, and L. Yu. Phylogenetic and evolutionary analysis of the septin protein family in metazoan. *FEBS Letters*, 581(28):5526–5532, Nov. 2007. ISSN 00145793. doi: 10.1016/j.febslet.2007.10.032.

A. Casamayor and M. Snyder. Molecular Dissection of a Yeast Septin: Distinct Domains Are Required for Septin Interaction, Localization, and Function. *Molecular and Cellular Biology*, 23(8):2762–2777, Apr. 2003. ISSN 0270-7306, 1098-5549. doi: 10.1128/MCB.23.8.2762-2777.2003.

F. Caudron and Y. Barral. Septins and the Lateral Compartmentalization of Eukaryotic Membranes. *Developmental Cell*, 16(4):493–506, Apr. 2009. ISSN 15345807. doi: 10.1016/j.devcel.2009.04.003.

M. M. Cesario and J. R. Bartles. Compartmentalization, processing and redistribution of the plasma membrane protein CE9 on rodent spermatozoa. *Journal of Cell Science*, 107:561–570, 1994. doi: 10.1242/jcs.107.2.561.

A. D. Chacko, P. L. Hyland, S. S. McDade, P. W. Hamilton, S. H. Russell, and P. A. Hall. SEPT9_v4 expression induces morphological change, increased motility and disturbed polarity. *The Journal of Pathology*, 206(4):458–465, Aug. 2005. ISSN 00223417, 10969896. doi: 10.1002/path.1794.

J. Chant and J. R. Pringle. Patterns of bud-site selection in the yeast Saccharomyces cerevisiae. *Journal of Cell Biology*, 129(3):751–765, May 1995. ISSN 0021-9525, 1540-8140. doi: 10.1083/jcb.129.3.751.

X. Chen, K. Wang, T. Svitkina, and E. Bi. Critical Roles of a RhoGEF-Anillin Module in Septin Architectural Remodeling during Cytokinesis. *Current Biology*, 30(8):1477–1490.e3, Apr. 2020. ISSN 09609822. doi: 10.1016/j.cub.2020.02.023.

A. Chiche, C. M. Stafford, and J. T. Cabral. Complex micropatterning of periodic structures on elastomeric surfaces. *Soft Matter*, 4(12):2360, 2008. ISSN 1744-683X, 1744-6848. doi: 10.1039/b811817e.

S.-J. Cho, H. Lee, S. Dutta, J. Song, R. Walikonis, and I. S. Moon. Septin 6 regulates the cytoarchitecture of neurons through localization at dendritic branch points and bases of protrusions. *Molecules and Cells*, 32(1):89–98, July 2011. ISSN 1016-8478, 0219-1032. doi: 10.1007/s10059-011-1048-9.

L. Clay, F. Caudron, A. Denoth-Lippuner, B. Boettcher, S. Buvelot Frei, E. L. Snapp, and Y. Barral. A sphingolipid-dependent diffusion barrier confines ER stress to the yeast mother cell. *eLife*, 3:e01883, May 2014. ISSN 2050-084X. doi: 10.7554/eLife.01883.

S. Collier, H. Lee, R. Burgess, and P. Adler. The WD40 Repeat Protein Fritz Links Cytoskeletal Planar Polarity to Frizzled Subcellular Localization in the Drosophila Epidermis. *Genetics*, 169(4):2035–2045, Apr. 2005. ISSN 1943-2631. doi: 10.1534/genetics.104.033381.

D. Connolly, Z. Yang, M. Castaldi, N. Simmons, M. H. Oktay, S. Coniglio, M. J. Fazzari, P. Verdier-Pinard, and C. Montagna. Septin 9 isoform expression, localization and epigenetic changes during human and mouse breast cancer progression. *Breast Cancer Research*, 13(4):R76, Aug. 2011. ISSN 1465-542X. doi: 10.1186/bcr2924.

Y. Cui, M. Yu, X. Yao, J. Xing, J. Lin, and X. Li. Single-Particle Tracking for the Quantification of Membrane Protein Dynamics in Living Plant Cells. *Molecular Plant*, 11(11):1315–1327, Nov. 2018. ISSN 16742052. doi: 10.1016/j.molp.2018.09.008.

S. N. Dash, E. Lehtonen, A. A. Wasik, A. Schepis, J. Paavola, P. Panula, W. J. Nelson, and S. Lehtonen. *Sept7b* is essential for pronephric function and development of left-right asymmetry in zebrafish embryogenesis. *Journal of Cell Science*, 127:1476–1486, Jan. 2014. ISSN 1477-9137, 0021-9533. doi: 10.1242/jcs.138495.

M. A. Del Pozo, F.-N. Lolo, and A. Echarri. Caveolae: Mechanosensing and mechanotransduction devices linking membrane trafficking to mechanoadaptation. *Current Opinion in Cell Biology*, 68:113–123, Feb. 2021. ISSN 09550674. doi: 10.1016/j.ceb.2020.10.008.

J. Dobbelaere and Y. Barral. Spatial Coordination of Cytokinetic Events by Compartmentalization of the Cell Cortex. *Science, New Series*, 305(5682):393–396, 2004.

L. Dolat, J. L. Hunyara, J. R. Bowen, E. P. Karasmanis, M. Elgawly, V. E. Galkin, and E. T. Spiliotis. Septins promote stress fiber–mediated maturation of focal adhesions and renal epithelial motility. *Journal of Cell Biology*, 207(2):225–235, Oct. 2014. ISSN 1540-8140, 0021-9525. doi: 10.1083/jcb.201405050.

C. G. Dotti, R. G. Parton, and K. Simons. Polarized sorting of glypiated proteins in hippocampal neurons. *Nature*, 349(6305):158–161, Jan. 1991. ISSN 0028-0836, 1476-4687. doi: 10.1038/349158a0.

P. R. Dragsten, R. Blumenthal, and J. S. Handler. Membrane asymmetry in epithelia: is the tight junction a barrier to diffusion in the plasma membrane? *Nature*, 294: 718–722, 1981.

M. P. Estey, C. Di Ciano-Oliveira, C. D. Froese, M. T. Bejide, and W. S. Trimble. Distinct roles of septins in cytokinesis: SEPT9 mediates midbody abscission. *Journal of Cell Biology*, 191(4):741–749, Nov. 2010. ISSN 1540-8140, 0021-9525. doi: 10.1083/jcb.201006031.

H. Ewers, T. Tada, J. D. Petersen, B. Racz, M. Sheng, and D. Choquet. A Septin-Dependent Diffusion Barrier at Dendritic Spine Necks. *PLoS ONE*, 9(12):e113916, Dec. 2014. ISSN 1932-6203. doi: 10.1371/journal.pone.0113916.

H. A. Faizi, A. Tsui, R. Dimova, and P. M. Vlahovska. Bending Rigidity, Capacitance, and Shear Viscosity of Giant Vesicle Membranes Prepared by Spontaneous Swelling, Electroformation, Gel-Assisted, and Phase Transfer Methods: A Comparative Study. *Langmuir*, 38(34):10548–10557, Aug. 2022. ISSN 0743-7463, 1520-5827. doi: 10.1021/acs.langmuir.2c01402.

H. Fares, M. Peifer, and J. R. Pringle. Localization and possible functions of Drosophila septins. *Molecular Biology of the Cell*, 6(12):1843–1859, Dec. 1995. ISSN 1059-1524, 1939-4586. doi: 10.1091/mbc.6.12.1843.

C. M. Field, O. al Awar, J. Rosenblatt, M. L. Wong, B. Alberts, and T. J. Mitchison. A purified Drosophila septin complex forms filaments and exhibits GTPase activity. *Journal of Cell Biology*, 133(3):605–616, May 1996. ISSN 0021-9525, 1540-8140. doi: 10.1083/jcb.133.3.605.

C. M. Field, M. Coughlin, S. Doberstein, T. Marty, and W. Sullivan. Characterization of *anillin* mutants reveals essential roles in septin localization and plasma membrane integrity. *Development*, 132(12):2849–2860, June 2005. ISSN 1477-9129, 0950-1991. doi: 10.1242/dev.01843.

F. P. Finger, K. R. Kopish, and J. G. White. A role for septins in cellular and axonal migration in C. elegans. *Developmental Biology*, 261(1):220–234, Sept. 2003. ISSN 00121606. doi: 10.1016/S0012-1606(03)00296-3.

G. C. Finnigan, E. A. Booth, A. Duvalyan, E. N. Liao, and J. Thorner. The Carboxy-Terminal Tails of Septins Cdc11 and Shs1 Recruit Myosin-II Binding Factor Bni5 to the Bud Neck in *Saccharomyces cerevisiae*. *Genetics*, 200(3):843–862, July 2015. ISSN 1943-2631. doi: 10.1534/genetics.115.176503.

G. C. Finnigan, A. Duvalyan, E. N. Liao, A. Sargsyan, and J. Thorner. Detection of protein–protein interactions at the septin collar in *Saccharomyces cerevisiae* using a tripartite split-GFP system. *Molecular Biology of the Cell*, 27(17):2708–2725, Sept. 2016. ISSN 1059-1524, 1939-4586. doi: 10.1091/mbc.e16-05-0337.

M. Fliegauf, A. Kahle, K. Häffner, and B. Zieger. Distinct localization of septin proteins to ciliary sub-compartments in airway epithelial cells. *Biological Chemistry*, 395(2):151–156, Feb. 2014. ISSN 1437-4315, 1431-6730. doi: 10.1515/hsz-2013-0252.

S. K. Ford and J. R. Pringle. Cellular Morphogenesis in the Saccharomyces cereuisiae Cell Cycle: Localization of the CDCII Gene Product and the Timing of Events at the Budding Site. *Developmental Genetics*, 12:281–292, 1991. doi: 10.1083/jcb.112.4.535.

T. K. Fujiwara, K. Iwasawa, Z. Kalay, T. A. Tsunoyama, Y. Watanabe, Y. M. Umemura, H. Murakoshi, K. G. N. Suzuki, Y. L. Nemoto, N. Morone, and A. Kusumi. Confined diffusion of transmembrane proteins and lipids induced by the same actin meshwork lining the plasma membrane. *Molecular Biology of the Cell*, 27(7):1101–1119, Apr. 2016. ISSN 1059-1524, 1939-4586. doi: 10.1091/mbc.E15-04-0186.

H. Fölsch. Regulation of membrane trafficking in polarized epithelial cells. *Current Opinion in Cell Biology*, 20(2):208–213, 2008. doi: 10.1016/j.ceb.2008.01.003.

A. Füchtbauer, L. B. Lassen, A. B. Jensen, J. Howard, A. d. S. Quiroga, S. Warming, A. B. Sørensen, F. S. Pedersen, and E.-M. Füchtbauer. Septin9 is involved in septin filament formation and cellular stability. *bchm*, 392(8-9):769–777, Aug. 2011. ISSN 1437-4315, 1431-6730. doi: 10.1515/BC.2011.088.

Y. Gambin, R. Lopez-Esparza, M. Reffay, E. Sierecki, N. S. Gov, M. Genest, R. S. Hodges, and W. Urbach. Lateral mobility of proteins in liquid membranes revisited. *Proceedings of the National Academy of Sciences*, 103(7):2098–2102, Feb. 2006. ISSN 0027-8424, 1091-6490. doi: 10.1073/pnas.0511026103.

M. V. Garabedian, A. Wirshing, A. Vakhrusheva, B. Turegun, O. S. Sokolova, and B. L. Goode. A septin-Hof1 scaffold at the yeast bud neck binds and organizes actin cables. *Molecular Biology of the Cell*, 31(18):1988–2001, Aug. 2020. ISSN 1059-1524, 1939-4586. doi: 10.1091/mbc.E19-12-0693.

G. Garcia, A. Bertin, Z. Li, Y. Song, M. A. McMurray, J. Thorner, and E. Nogales. Subunit-dependent modulation of septin assembly: Budding yeast septin Shs1 promotes ring and gauze formation. *Journal of Cell Biology*, 195(6):993–1004, Dec. 2011. ISSN 1540-8140, 0021-9525. doi: 10.1083/jcb.201107123.

W. Garcia, A. P. U. de Araújo, M. de Oliveira Neto, M. R. M. Ballestero, I. Polikarpov, M. Tanaka, T. Tanaka, and R. C. Garratt. Dissection of a Human Septin: Definition and Characterization of Distinct Domains within Human SEPT4. *Biochemistry*, 45 (46):13918–13931, Nov. 2006. ISSN 0006-2960, 1520-4995. doi: 10.1021/bi061549z.

W. Garcia, A. P. U. de Araújo, F. Lara, D. Foguel, M. Tanaka, T. Tanaka, and R. C. Garratt. An Intermediate Structure in the Thermal Unfolding of the GTPase Domain of Human Septin 4 (SEPT4/Bradeion-β) Forms Amyloid-like Filaments in Vitro. *Biochemistry*, 46(39):11101–11109, Oct. 2007. ISSN 0006-2960, 1520-4995. doi: 10.1021/bi700702w.

R. Ghossoub, Q. Hu, M. Failler, M.-C. Rouyez, B. Spitzbarth, S. Mostowy, U. Wolfrum, S. Saunier, P. Cossart, W. J. Nelson, and A. Benmerah. Septins 2, 7, and 9 and MAP4 co-localize along the axoneme in the primary cilium and control ciliary length. *Journal of Cell Science*, 126:2583–2594, Jan. 2013. ISSN 1477-9137, 0021-9533. doi: 10.1242/jcs.111377.

J. K. Gilden, S. Peck, Y.-C. M. Chen, and M. F. Krummel. The septin cytoskeleton facilitates membrane retraction during motility and blebbing. *Journal of Cell Biology*, 196(1):103–114, Jan. 2012. ISSN 1540-8140, 0021-9525. doi: 10.1083/jcb.201105127.

R. Grützmann, B. Molnar, C. Pilarsky, J. K. Habermann, P. M. Schlag, H. D. Saeger, S. Miehlke, T. Stolz, F. Model, U. J. Roblick, H.-P. Bruch, R. Koch, V. Liebenberg, T. deVos, X. Song, R. H. Day, A. Z. Sledziewski, and C. Lofton-Day. Sensitive Detection of Colorectal Cancer in Peripheral Blood by Septin 9 DNA Methylation Assay. *PLoS ONE*, 3(11):e3759, Nov. 2008. ISSN 1932-6203. doi: 10.1371/journal.pone.0003759.

G. Hammond. Does PtdIns(4,5) P 2 concentrate so it can multi-task? *Biochemical Society Transactions*, 44(1):228–233, Feb. 2016. ISSN 0300-5127, 1470-8752. doi: 10.1042/BST20150211.

L. H. Hartwell. Macromolecule Synthesis in Temperature-sensitive Mutants of Yeast. *Journal of Bacteriology*, 93(5):1662–1670, 1967. doi: 10.1128/jb.93.5.1662-1670.1967.

L. H. Hartwell. Genetic control of the cell division cycle in yeast II. Genes controlling DNA replication and its initiation. *Journal of Molecular Biology*, 59:183–194, 1971. ISSN 00222836. doi: 10.1016/0022-2836(72)90246-X.

C. D. Harvey and K. Svoboda. Locally dynamic synaptic learning rules in pyramidal neuron dendrites. *Nature*, 450(7173):1195–1200, Dec. 2007. ISSN 0028-0836, 1476-4687. doi: 10.1038/nature06416.

C. D. Harvey, R. Yasuda, H. Zhong, and K. Svoboda. The Spread of Ras Activity Triggered by Activation of a Single Dendritic Spine. *Science*, 321(5885):136–140, July 2008. ISSN 0036-8075, 1095-9203. doi: 10.1126/science.1159675.

F. A. Heberle and G. W. Feigenson. Phase Separation in Lipid Membranes. *Cold Spring Harbor Perspectives in Biology*, 3(4):a004630–a004630, Apr. 2011. ISSN 1943-0264. doi: 10.1101/cshperspect.a004630.

J. Hu, X. Bai, J. Bowen, L. Dolat, F. Korobova, W. Yu, P. Baas, T. Svitkina, G. Gallo, and E. Spiliotis. Septin-Driven Coordination of Actin and Microtubule Remodeling Regulates the Collateral Branching of Axons. *Current Biology*, 22(12):1109–1115, June 2012. ISSN 09609822. doi: 10.1016/j.cub.2012.04.019.

Q. Hu, L. Milenkovic, H. Jin, M. P. Scott, M. V. Nachury, E. T. Spiliotis, and W. J. Nelson. A Septin Diffusion Barrier at the Base of the Primary Cilium Maintains Ciliary Membrane Protein Distribution. *Science*, 329(5990):436–439, July 2010. ISSN 0036-8075, 1095-9203. doi: 10.1126/science.1191054.

M. Ihara, H. Tomimoto, H. Kitayama, Y. Morioka, I. Akiguchi, H. Shibasaki, M. Noda, and M. Kinoshita. Association of the Cytoskeletal GTP-binding Protein Sept4/H5 with Cytoplasmic Inclusions Found in Parkinson's Disease and Other Synucleinopathies. *Journal of Biological Chemistry*, 278(26):24095–24102, June 2003. ISSN 00219258. doi: 10.1074/jbc.M301352200.

M. Ihara, A. Kinoshita, S. Yamada, H. Tanaka, A. Tanigaki, A. Kitano, M. Goto, K. Okubo, H. Nishiyama, O. Ogawa, C. Takahashi, S. Itohara, Y. Nishimune, M. Noda, and M. Kinoshita. Cortical Organization by the Septin Cytoskeleton Is Essential for Structural and Mechanical Integrity of Mammalian Spermatozoa. *Developmental Cell*, 8(3):343–352, Mar. 2005. ISSN 15345807. doi: 10.1016/j.devcel.2004.12.005.

R. Iino, I. Koyama, and A. Kusumi. Single Molecule Imaging of Green Fluorescent Proteins in Living Cells: E-Cadherin Forms Oligomers on the Free Cell Surface. *Biophysical Journal*, 80(6):2667–2677, June 2001. ISSN 00063495. doi: 10.1016/S0006-3495(01)76236-4.

W. Jahr, P. Velicky, and J. G. Danzl. Strategies to maximize performance in STimulated Emission Depletion (STED) nanoscopy of biological specimens. *Methods*, 174:27–41, Mar. 2020. ISSN 10462023. doi: 10.1016/j.ymeth.2019.07.019.

C. Janke and M. M. Magiera. The tubulin code and its role in controlling microtubule properties and functions. *Nature Reviews Molecular Cell Biology*, 21(6):307–326, June 2020. ISSN 1471-0072, 1471-0080. doi: 10.1038/s41580-020-0214-3.

E. Joo, M. C. Surka, and W. S. Trimble. Mammalian SEPT2 Is Required for Scaffolding Nonmuscle Myosin II and Its Kinases. *Developmental Cell*, 13(5):677–690, Nov. 2007. ISSN 15345807. doi: 10.1016/j.devcel.2007.09.001.

L. M. Kalikin, H. L. Sims, and E. M. Petty. Genomic and Expression Analyses of Alternatively Spliced Transcripts of the MLL Septin-like Fusion Gene (MSF) That Map to a 17q25 Region of Loss in Breast and Ovarian Tumors. *Genomics*, 63(2):165–172, Jan. 2000. ISSN 08887543. doi: 10.1006/geno.1999.6077.

E. P. Karasmanis, C.-T. Phan, D. Angelis, I. A. Kesisova, C. C. Hoogenraad, R. J. McKenney, and E. T. Spiliotis. Polarity of Neuronal Membrane Traffic Requires Sorting of Kinesin Motor Cargo during Entry into Dendrites by a Microtubule-Associated Septin. *Developmental Cell*, 46(2):204–218.e7, July 2018. ISSN 15345807. doi: 10.1016/j.devcel.2018.06.013.

E. P. Karasmanis, D. Hwang, K. Nakos, J. R. Bowen, D. Angelis, and E. T. Spiliotis. A Septin Double Ring Controls the Spatiotemporal Organization of the ESCRT Machinery in Cytokinetic Abscission. *Current Biology*, 29(13):2174–2182.e7, July 2019. ISSN 09609822. doi: 10.1016/j.cub.2019.05.050.

I. A. Kesisova, B. P. Robinson, and E. T. Spiliotis. A septin GTPase scaffold of dynein–dynactin motors triggers retrograde lysosome transport. *Journal of Cell Biology*, 220(2):e202005219, Feb. 2021. ISSN 0021-9525, 1540-8140. doi: 10.1083/jcb.202005219.

A. Khan, J. Newby, and A. S. Gladfelter. Control of septin filament flexibility and bundling by subunit composition and nucleotide interactions. *Molecular Biology of the Cell*, 29(6):702–712, Mar. 2018. ISSN 1059-1524, 1939-4586. doi: 10.1091/mbc.E17-10-0608.

M. Kinoshita. Assembly of Mammalian Septins. *Journal of Biochemistry*, 134(4):491–496, Oct. 2003a. ISSN 0021-924X. doi: 10.1093/jb/mvg182.

M. Kinoshita. The septins. *Genome Biol*, 4(11):236, 2003b.

M. Kinoshita, S. Kumar, A. Mizoguchi, C. Ide, A. Kinoshita, T. Haraguchi, Y. Hiraoka, and M. Noda. Nedd5, a mammalian septin, is a novel cytoskeletal component interacting with actin-based structures. *Genes & Development*, 11(12):1535–1547, June 1997. ISSN 0890-9369, 1549-5477. doi: 10.1101/gad.11.12.1535.

M. Kinoshita, C. M. Field, M. L. Coughlin, A. F. Straight, and T. J. Mitchison. Self- and Actin-Templated Assembly of Mammalian Septins. *Developmental Cell*, 3(6): 791–802, Dec. 2002. ISSN 15345807. doi: 10.1016/S1534-5807(02)00366-0.

H. Kissel, M.-M. Georgescu, S. Larisch, K. Manova, G. R. Hunnicutt, and H. Steller. The Sept4 Septin Locus Is Required for Sperm Terminal Differentiation in Mice. *Developmental Cell*, 8(3):353–364, Mar. 2005. ISSN 15345807. doi: 10.1016/j.devcel.2005.01.021.

T. Kobayashi and K. Simons. A functional barrier to movement of lipids in polarized neurons. *Nature*, 359:647–650, 1992.

S. Krokowski, D. Lobato-Márquez, A. Chastanet, P. M. Pereira, D. Angelis, D. Galea, G. Larrouy-Maumus, R. Henriques, E. T. Spiliotis, R. Carballido-López, and S. Mostowy. Septins Recognize and Entrap Dividing Bacterial Cells for Delivery to Lysosomes. *Cell Host & Microbe*, 24(6):866–874.e4, Dec. 2018. ISSN 19313128. doi: 10.1016/j.chom.2018.11.005.

Y.-C. Kuo, Y.-R. Shen, H.-I. Chen, Y.-H. Lin, Y.-Y. Wang, Y.-R. Chen, C.-Y. Wang, and P.-L. Kuo. SEPT12 orchestrates the formation of mammalian sperm annulus by organizing SEPT12-7-6-2/-4 core complexes. *Journal of Cell Science*, 128:923–934, Jan. 2015. ISSN 1477-9137, 0021-9533. doi: 10.1242/jcs.158998.

M. Kuzmić, G. Castro Linares, J. Leischner Fialová, F. Iv, D. Salaün, A. Llewellyn, M. Gomes, M. Belhabib, Y. Liu, K. Asano, M. Rodrigues, D. Isnardon, T. Tachibana, G. H. Koenderink, A. Badache, M. Mavrakis, and P. Verdier-Pinard. Septin-microtubule association via a motif unique to isoform 1 of septin 9 tunes stress fibers. *Journal of Cell Science*, 135(1):jcs258850, Jan. 2022. ISSN 0021-9533, 1477-9137. doi: 10.1242/jcs.258850.

S. Kwitny, A. V. Klaus, and G. R. Hunnicutt. The Annulus of the Mouse Sperm Tail Is Required to Establish a Membrane Diffusion Barrier That Is Engaged During the Late Steps of Spermiogenesis1. *Biology of Reproduction*, 82(4):669–678, Apr. 2010. ISSN 0006-3363, 1529-7268. doi: 10.1095/biolreprod.109.079566.

R. Kwok and E. Evans. Thermoelasticity of large lecithin bilayer vesicles. *Biophysical Journal*, 35(3):637–652, Sept. 1981. ISSN 00063495. doi: 10.1016/S0006-3495(81)84817-5.

J. Lasiene, A. Matsui, Y. Sawa, F. Wong, and P. J. Horner. Age-related myelin dynamics revealed by increased oligodendrogenesis and short internodes. *Aging Cell*, 8:201–213, 2009.

F. Leite and M. Way. The role of signalling and the cytoskeleton during Vaccinia Virus egress. *Virus Research*, 209:87–99, Nov. 2015. ISSN 01681702. doi: 10.1016/j.virusres.2015.01.024.

X. Li, D. R. Serwanski, C. P. Miralles, K.-i. Nagata, and A. L. De Blas. Septin 11 Is Present in GABAergic Synapses and Plays a Functional Role in the Cytoarchitecture of Neurons and GABAergic Synaptic Connectivity. *Journal of Biological Chemistry*, 284(25):17253–17265, June 2009. ISSN 00219258. doi: 10.1074/jbc.M109.008870.

W.-C. Lin, C.-H. Yu, S. Triffo, and J. T. Groves. Supported Membrane Formation, Characterization, Functionalization, and Patterning for Application in Biological Science and Technology. *Current Protocols in Chemical Biology*, 2(4):235–269, Oct. 2010. ISSN 21604762. doi: 10.1002/9780470559277.ch100131.

Y.-H. Lin, C.-K. Chou, Y.-C. Hung, I.-S. Yu, H.-A. Pan, S.-W. Lin, and P.-L. Kuo. SEPT12 deficiency causes sperm nucleus damage and developmental arrest of preimplantation embryos. *Fertility and Sterility*, 95(1):363–365, Jan. 2011. ISSN 00150282. doi: 10.1016/j.fertnstert.2010.07.1064.

D. Lingwood and K. Simons. Lipid Rafts As a Membrane-Organizing Principle. *Science*, 327(5961):46–50, Jan. 2010. ISSN 0036-8075, 1095-9203. doi: 10.1126/science.1174621.

J. Lippincott and R. Li. Sequential Assembly of Myosin II, an IQGAP-like Protein, and Filamentous Actin to a Ring Structure Involved in Budding Yeast Cytokinesis. *Journal of Cell Biology*, 140(2):355–366, Jan. 1998. ISSN 0021-9525, 1540-8140. doi: 10.1083/jcb.140.2.355.

M. S. Longtime, D. J. DeMarini, M. L. Valencik, O. S. Al-Awar, H. Fares, C. De Virgilo, and J. R. Pringle. The septins: Roles in cytokinesis and other processes. *Current Opinion in Cell Biology*, 8:106–119, 1996.

C. Luedeke, S. B. Frei, I. Sbalzarini, H. Schwarz, A. Spang, and Y. Barral. Septin-dependent compartmentalization of the endoplasmic reticulum during yeast polarized growth. *Journal of Cell Biology*, 169(6):897–908, June 2005. ISSN 1540-8140, 0021-9525. doi: 10.1083/jcb.200412143.

A. S. Maddox, L. Lewellyn, A. Desai, and K. Oegema. Anillin and the Septins Promote Asymmetric Ingression of the Cytokinetic Furrow. *Developmental Cell*, 12(5):827–835, May 2007. ISSN 15345807. doi: 10.1016/j.devcel.2007.02.018.

E. Marcus, E. Tokhtaeva, S. Turdikulova, J. Capri, J. Whitelegge, D. Scott, G. Sachs, F. Berditchevski, and O. Vagin. Septin oligomerization regulates persistent expression of ErbB2/HER2 in gastric cancer cells. *Biochemical Journal*, 473(12):1703–1718, June 2016. ISSN 0264-6021, 1470-8728. doi: 10.1042/BCJ20160203.

S. J. Marrink, V. Corradi, P. C. Souza, H. I. Ingólfsson, D. P. Tieleman, and M. S. Sansom. Computational Modeling of Realistic Cell Membranes. *Chemical Reviews*, 119(9):6184–6226, May 2019. ISSN 0009-2665, 1520-6890. doi: 10.1021/acs.chemrev.8b00460.

C. Martinez, J. Corral, J. A. Dent, L. Sesma, V. Vicente, and J. Ware. Platelet septin complexes form rings and associate with the microtubular network. *Journal of Thrombosis and Haemostasis*, 4(6):1388–1395, June 2006. ISSN 1538-7933, 1538-7836. doi: 10.1111/j.1538-7836.2006.01952.x.

C. S. Martins, C. Taveneau, G. Castro-Linares, M. Baibakov, N. Buzhinsky, M. Eroles, V. Milanović, F. Iv, L. Bouillard, A. Llewellyn, M. Gomes, M. Belhabib, M. Kuzmić, P. Verdier-Pinard, S. Lee, A. Badache, S. Kumar, C. Chandre, S. Brasselet, F. Rico,

O. Rossier, G. H. Koenderink, J. Wenger, S. Cabantous, and M. Mavrakis. Human septins in cells organize as octamer-based filaments mediating actin-membrane anchoring. preprint, bioRxiv, Feb. 2022.

A. Masuda, K. Ushida, and T. Okamoto. New Fluorescence Correlation Spectroscopy Enabling Direct Observation of Spatiotemporal Dependence of Diffusion Constants as an Evidence of Anomalous Transport in Extracellular Matrices. *Biophysical Journal*, 88(5):3584–3591, May 2005. ISSN 00063495. doi: 10.1529/biophysj.104.048009.

M. Mavrakis, Y. Azou-Gros, F.-C. Tsai, J. Alvarado, A. Bertin, F. Iv, A. Kress, S. Brasselet, G. H. Koenderink, and T. Lecuit. Septins promote F-actin ring formation by crosslinking actin filaments into curved bundles. *Nature Cell Biology*, 16(4):322–334, Apr. 2014. ISSN 1465-7392, 1476-4679. doi: 10.1038/ncb2921.

M. A. McMurray and J. Thorner. Turning it inside out: The organization of human septin heterooligomers. *Cytoskeleton*, 76(9-10):449–456, Sept. 2019. ISSN 1949-3584, 1949-3592. doi: 10.1002/cm.21571.

D. C. Mendonça, J. N. Macedo, S. L. Guimarães, F. L. Barroso da Silva, A. Cassago, R. C. Garratt, R. V. Portugal, and A. P. U. Araujo. A revised order of subunits in mammalian septin complexes. *Cytoskeleton*, 76(9-10):457–466, Sept. 2019. ISSN 1949-3584, 1949-3592. doi: 10.1002/cm.21569.

D. C. Mendonça, S. L. Guimarães, H. D. Pereira, A. A. Pinto, M. A. de Farias, A. S. de Godoy, A. P. Araujo, M. van Heel, R. V. Portugal, and R. C. Garratt. An atomic model for the human septin hexamer by cryo-EM. *Journal of Molecular Biology*, 433 (15):167096, July 2021. ISSN 00222836. doi: 10.1016/j.jmb.2021.167096.

M. Mendoza, A. A. Hyman, and M. Glotzer. GTP Binding Induces Filament Assembly of a Recombinant Septin. *Current Biology*, 12(21):1858–1863, Oct. 2002. ISSN 09609822. doi: 10.1016/S0960-9822(02)01258-7.

M. B. Menon, A. Sawada, A. Chaturvedi, P. Mishra, K. Schuster-Gossler, M. Galla, A. Schambach, A. Gossler, A. Kotlyarov, M. Kinoshita, and M. Gaestel. Genetic Deletion of SEPT7 Reveals a Cell Type-Specific Role of Septins in Microtubule Destabilization for the Completion of Cytokinesis. *PLOS Genetics*, 10(8):e1004558, 2014.

M. Momany, J. Zhao, R. Lindsey, and P. J. Westfall. Characterization of the *Aspergillus nidulans* Septin (*asp*) Gene Family. *Genetics*, 157(3):969–977, Mar. 2001. ISSN 1943-2631. doi: 10.1093/genetics/157.3.969.

C. Montagna, M.-S. Lyu, K. Hunter, L. Lukes, W. Lowther, T. Reppert, B. Hissong, Z. Weaver, and T. Ried. The Septin 9 (MSF) gene is amplified and overexpressed in mouse mammary gland adenocarcinomas and human breast cancer cell lines. *Cancer Research*, 63(9):2179–2187, 2003.

C. Montagna, M. Sagie, and J. Zechmeister. Mammalian septins in health and disease. *Research and Reports in Biochemistry*, 5:59–72, Feb. 2015. ISSN 2230-3154. doi: 10.2147/RRBC.S59060.

S. Mostowy and P. Cossart. Septins: the fourth component of the cytoskeleton. *Nature Reviews Molecular Cell Biology*, 13(3):183–194, Mar. 2012. ISSN 1471-0072, 1471-0080. doi: 10.1038/nrm3284.

S. Mostowy, M. Bonazzi, M. A. Hamon, T. N. Tham, A. Mallet, M. Lelek, E. Gouin, C. Demangel, R. Brosch, C. Zimmer, A. Sartori, M. Kinoshita, M. Lecuit, and P. Cossart. Entrapment of Intracytosolic Bacteria by Septin Cage-like Structures. *Cell Host & Microbe*, 8(5):433–444, Nov. 2010. ISSN 19313128. doi: 10.1016/j.chom.2010.10.009.

A. Musgrave, P. de Wildt, I. van Etten, H. Pijst, C. Scholma, R. Kooyman, W. Homan, and H. van den Ende. Evidence for a functional membrane barrier in the transition zone between the flagellum and cell body of Chlamydomonas eugametos gametes. *Planta*, 167(4):544–553, Apr. 1986. ISSN 0032-0935, 1432-2048. doi: 10.1007/BF00391231.

S. Musunuri, M. Wetterhall, M. Ingelsson, L. Lannfelt, K. Artemenko, J. Bergquist, K. Kultima, and G. Shevchenko. Quantification of the Brain Proteome in Alzheimer's Disease Using Multiplexed Mass Spectrometry. *Journal of Proteome Research*, 13: 2056–2068, 2014. doi: 10.1021/pr401202d.

D. G. Myles, P. Primakoff, and A. R. Bellvé. Surface Domains of the Guinea Pig Sperm Defined with Monoclonal Antibodies. *Cell*, 23:433–439, 1981.

C. Nakada, K. Ritchie, Y. Oba, M. Nakamura, Y. Hotta, R. Iino, R. S. Kasai, K. Yamaguchi, T. Fujiwara, and A. Kusumi. Accumulation of anchored proteins forms membrane diffusion barriers during neuronal polarization. *Nature Cell Biology*, 5(7): 626–632, July 2003. ISSN 1465-7392, 1476-4679. doi: 10.1038/ncb1009.

K. Nakos, M. R. Radler, and E. T. Spiliotis. Septin 2/6/7 complexes tune microtubule plus-end growth and EB1 binding in a concentration- and filament-dependent manner. *Molecular Biology of the Cell*, 30:2913–2928, 2019a.

K. Nakos, M. Rosenberg, and E. T. Spiliotis. Regulation of microtubule plus end dynamics by septin 9. *Cytoskeleton*, 76:83–91, 2019b.

T. Neufeld. The Drosophila peanut gene is required for cytokinesis and encodes a protein similar to yeast putative bud neck filament proteins. *Cell*, 77(3):371–379, May 1994. ISSN 00928674. doi: 10.1016/0092-8674(94)90152-X.

T. Q. Nguyen, H. Sawa, H. Okano, and J. G. White. The septin genes of C. elegans. *Journal of Cell Science*, 113:3825–3837, 2000.

J. Nian, X. Sun, S. Ming, C. Yan, Y. Ma, Y. Feng, L. Yang, M. Yu, G. Zhang, and X. Wang. Diagnostic Accuracy of Methylated SEPT9 for Blood-based Colorectal Cancer Detection: A Systematic Review and Meta-Analysis. *Clinical and Translational Gastroenterology*, 8(1):e216, Jan. 2017. ISSN 2155-384X. doi: 10.1038/ctg.2016.66.

R. Nishihama, M. Onishi, and J. R. Pringle. New insights into the phylogenetic distribution and evolutionary origins of the septins. *Journal of Biological Chemistry*, 392 (8-9):681–687, Aug. 2011. ISSN 1437-4315, 1431-6730. doi: 10.1515/BC.2011.086.

Y. Oh and E. Bi. Septin structure and function in yeast and beyond. *Trends in Cell Biology*, 21(3):141–148, Mar. 2011. ISSN 09628924. doi: 10.1016/j.tcb.2010.11.006.

Y. Oh, J. Schreiter, R. Nishihama, C. Wloka, and E. Bi. Targeting and functional mechanisms of the cytokinesis-related F-BAR protein Hof1 during the cell cycle. *Molecular Biology of the Cell*, 24(9):1305–1320, May 2013. ISSN 1059-1524, 1939-4586. doi: 10.1091/mbc.e12-11-0804.

K. Ong, C. Wloka, S. Okada, T. Svitkina, and E. Bi. Architecture and dynamic remodelling of the septin cytoskeleton during the cell cycle. *Nature Communications*, 5(1):5698, Dec. 2014. ISSN 2041-1723. doi: 10.1038/ncomms6698.

M. Osaka, J. D. Rowley, and N. J. Zeleznik-Le. *MSF* (MLL septin-like fusion), a fusion partner gene of *MLL,* in a therapy-related acute myeloid leukemia with a t(11;17)(q23;q25). *Proceedings of the National Academy of Sciences*, 96(11):6428–6433, May 1999. ISSN 0027-8424, 1091-6490. doi: 10.1073/pnas.96.11.6428.

J. Pacheco, A. C. Cassidy, J. P. Zewe, R. C. Wills, and G. R. V. Hammond. Free diffusion of PI(4,5)P $_2$ in the plasma membrane in the presence of high density effector protein complexes. preprint, bioRxiv, Jan. 2022.

F. Pan, R. L. Malmberg, and M. Momany. Analysis of septins across kingdoms reveals orthology and new motifs. *BMC Evolutionary Biology*, 7(1):103, Dec. 2007. ISSN 1471-2148. doi: 10.1186/1471-2148-7-103.

J. Patzig, M. S. Erwig, S. Tenzer, K. Kusch, P. Dibaj, W. Möbius, S. Goebbels, N. Schaeren-Wiemers, K.-A. Nave, and H. B. Werner. Septin/anillin filaments scaffold central nervous system myelin to accelerate nerve conduction. *eLife*, 5:e17119, Aug. 2016. ISSN 2050-084X. doi: 10.7554/eLife.17119.

B. J. Peter, H. M. Kent, I. G. Mills, Y. Vallis, P. J. G. Butler, P. R. Evans, and H. T. McMahon. BAR Domains as Sensors of Membrane Curvature: The Amphiphysin BAR Structure. *Science*, 303(5657):495–499, Jan. 2004. ISSN 0036-8075, 1095-9203. doi: 10.1126/science.1092586.

R. Peters and R. J. Cherry. Lateral and rotational diffusion of bacteriorhodopsin in lipid bilayers: Experimental test of the Saffman-Delbriick equations. *Proceedings of the National Academy of Sciences*, 79:4317–4321, 1982.

E. A. Peterson, L. M. Kalikin, J. D. Steels, M. P. Estey, W. S. Trimble, and E. M. Petty. Characterization of a SEPT9 interacting protein, SEPT14, a novel testis-specific septin. *Mammalian Genome*, 18(11):796–807, Nov. 2007. ISSN 0938-8990, 1432-1777. doi: 10.1007/s00335-007-9065-x.

J. A. M. Petruszak, C. L. Nehme, and J. R. Bartles. Endoproteolytic Cleavage in the Extracellular Domain of the Integral Plasma Membrane Protein CE9 Precedes Its Redistribution from the Pbsterior to the Anterior Tail of the Rat Spermatozoon during Epididymal Maturation. *The Journal of Cell Biology*, 114:917–927, 1991. doi: 10.1083/jcb.114.5.917.

J. Pfanzelter, S. Mostowy, and M. Way. Septins suppress the release of vaccinia virus from infected cells. *Journal of Cell Biology*, 217(8):2911–2929, Aug. 2018. ISSN 0021-9525, 1540-8140. doi: 10.1083/jcb.201708091.

J. C. Pissuti Damalio, W. Garcia, J. N. Alves Macêdo, I. de Almeida Marques, J. M. Andreu, R. Giraldo, R. C. Garratt, and A. P. Ulian Araújo. Self assembly of human septin 2 into amyloid filaments. *Biochimie*, 94(3):628–636, Mar. 2012. ISSN 03009084. doi: 10.1016/j.biochi.2011.09.014.

D. Pruyne, A. Legesse-Miller, L. Gao, Y. Dong, and A. Bretscher. Mechnisms of polarized growth and organelle segregation in yeast. *Annual Review of Cell and Developmental Biology*, 20(1):559–591, Nov. 2004. ISSN 1081-0706, 1530-8995. doi: 10.1146/annurev.cellbio.20.010403.103108.

C. Prévost, H. Zhao, J. Manzi, E. Lemichez, P. Lappalainen, A. Callan-Jones, and P. Bassereau. IRSp53 senses negative membrane curvature and phase separates along membrane tubules. *Nature Communications*, 6(1):8529, Dec. 2015. ISSN 2041-1723. doi: 10.1038/ncomms9529.

M. R. Radler. Spatial control of membrane traffic in neuronal dendrites. *Molecular and Cellular Neuroscience*, 105:103492, 2020. doi: 10.1016/j.mcn.2020.103492.

S. Ramadurai, A. Holt, V. Krasnikov, G. van den Bogaart, J. A. Killian, and B. Poolman. Lateral Diffusion of Membrane Proteins. *Journal of the American Chemical Society*, 131(35):12650–12656, Sept. 2009. ISSN 0002-7863, 1520-5126. doi: 10.1021/ja902853g.

W. Rawicz, K. C. Olbrich, T. McIntosh, D. Needham, and E. Evans. Effect of Chain Length and Unsaturation on Elasticity of Lipid Bilayers. *Biophysical Journal*, 79: 328–339, 2000. doi: 10.1016/S0006-3495(00)76295-3.

J. P. Reeves and R. M. Dowben. Formation and properties of thin-walled phospholipid vesicles. *Journal of Cellular Physiology*, 73(1):49–60, Feb. 1969. ISSN 0021-9541, 1097-4652. doi: 10.1002/jcp.1040730108.

M. J. Renshaw, J. Liu, B. D. Lavoie, and A. Wilde. Anillin-dependent organization of septin filaments promotes intercellular bridge elongation and Chmp4B targeting to the abscission site. *Open Biology*, 4(1):130190, Jan. 2014. ISSN 2046-2441. doi: 10.1098/rsob.130190.

R. P. Richter, R. Bérat, and A. R. Brisson. Formation of Solid-Supported Lipid Bilayers: An Integrated View. *Langmuir*, 22(8):3497–3505, Apr. 2006. ISSN 0743-7463, 1520-5827. doi: 10.1021/la052687c.

J.-L. Rigaud, D. Levy, G. Mosser, and O. Lambert. Detergent removal by non-polar polystyrene beads. *European Biophysics Journal*, 27(4):305–319, June 1998. ISSN 0175-7571, 1432-1017. doi: 10.1007/s002490050138.

P. G. Saffman and M. Delbrück. Brownian motion in biological membranes. *Proceedings of the National Academy of Sciences*, 72(8):3111–3113, Aug. 1975. ISSN 0027-8424, 1091-6490. doi: 10.1073/pnas.72.8.3111.

F. A. Sala, N. F. Valadares, J. N. Macedo, J. C. Borges, and R. C. Garratt. Heterotypic Coiled-Coil Formation is Essential for the Correct Assembly of the Septin Heterofilament. *Biophysical Journal*, 111(12):2608–2619, Dec. 2016. ISSN 00063495. doi: 10.1016/j.bpj.2016.10.032.

S. L. Sanders and I. Herskowitz. The BUD4 protein of yeast, required for axial budding, is localized to the mother/BUD neck in a cell cycle-dependent manner. *Journal of Cell Biology*, 134(2):413–427, July 1996. ISSN 0021-9525, 1540-8140. doi: 10.1083/jcb.134.2.413.

F. Schneider, D. Waithe, M. P. Clausen, S. Galiani, T. Koller, G. Ozhan, C. Eggeling, and E. Sezgin. Diffusion of lipids and GPI-anchored proteins in actin-free plasma membrane vesicles measured by STED-FCS. *Molecular Biology of the Cell*, 28(11): 1507–1518, June 2017. ISSN 1059-1524, 1939-4586. doi: 10.1091/mbc.e16-07-0536.

E. Schäfer, M. Vache, T.-T. Kliesch, and A. Janshoff. Mechanical response of adherent giant liposomes to indentation with a conical AFM-tip. *Soft Matter*, 11(22):4487–4495, 2015. ISSN 1744-683X, 1744-6848. doi: 10.1039/C5SM00191A.

M. Scott, W. G. McCluggage, K. J. Hillan, P. A. Hall, and S. H. Russell. Altered patterns of transcription of the septin gene, SEPT9, in ovarian tumorigenesis. *International Journal of Cancer*, 118(5):1325–1329, Mar. 2006. ISSN 00207136. doi: 10.1002/ijc.21486.

M. E. Sellin, S. Stenmark, and M. Gullberg. Cell type–specific expression of SEPT3-homology subgroup members controls the subunit number of heteromeric septin complexes. *Molecular Biology of the Cell*, 25(10):1594–1607, May 2014. ISSN 1059-1524, 1939-4586. doi: 10.1091/mbc.e13-09-0553.

Z. Shcheprova, S. Baldi, S. B. Frei, G. Gonnet, and Y. Barral. A mechanism for asymmetric segregation of age during yeast budding. *Nature*, 454(7205):728–734, Aug. 2008. ISSN 0028-0836, 1476-4687. doi: 10.1038/nature07212.

E. J. Shimshick and H. M. McConnell. Lateral phase separation in phospholipid membranes. *Biochemistry*, 12(12):2351–2360, June 1973. ISSN 0006-2960, 1520-4995. doi: 10.1021/bi00736a026.

T. Shinoda, H. Ito, K. Sudo, I. Iwamoto, R. Morishita, and K.-i. Nagata. Septin 14 Is Involved in Cortical Neuronal Migration via Interaction with Septin 4. *Molecular Biology of the Cell*, 21:1324–1334, 2010. doi: 10.1091/mbc.E09100869.

V. Singla and J. F. Reiter. The Primary Cilium as the Cell's Antenna: Signaling at a Sensory Organelle. *Science*, 313:629–633, 2006. doi: 10.1126/science.1124534.

M. Sirajuddin, M. Farkasovsky, F. Hauer, D. Kühlmann, I. G. Macara, M. Weyand, H. Stark, and A. Wittinghofer. Structural insight into filament formation by mammalian septins. *Nature*, 449(7160):311–315, Sept. 2007. ISSN 0028-0836, 1476-4687. doi: 10.1038/nature06052.

A. Sirianni, S. Krokowski, D. Lobato-Márquez, S. Buranyi, J. Pfanzelter, D. Galea, A. Willis, S. Culley, R. Henriques, G. Larrouy-Maumus, M. Hollinshead, V. Sancho-Shimizu, M. Way, and S. Mostowy. Mitochondria mediate septin cage assembly to promote autophagy of *Shigella*. *EMBO reports*, 17(7):1029–1043, July 2016. ISSN 1469-221X, 1469-3178. doi: 10.15252/embr.201541832.

C. Smith, L. Dolat, D. Angelis, E. Forgacs, E. T. Spiliotis, and V. E. Galkin. Septin 9 Exhibits Polymorphic Binding to F-Actin and Inhibits Myosin and Cofilin Activity. *Journal of Molecular Biology*, 427(20):3273–3284, Oct. 2015. ISSN 00222836. doi: 10.1016/j.jmb.2015.07.026.

J. H. Son, H. Kawamata, M. S. Yoo, D. J. Kim, Y. K. Lee, S. Kim, T. M. Dawson, H. Zhang, D. Sulzer, L. Yang, M. F. Beal, L. A. DeGiorgio, H. S. Chun, H. Baker, and C. Peng. Neurotoxicity and behavioral deficits associated with Septin 5 accumulation in dopaminergic neurons: Septin 5 accumulation in dopaminergic neurons. *Journal of Neurochemistry*, 94(4):1040–1053, June 2005. ISSN 00223042, 14714159. doi: 10.1111/j.1471-4159.2005.03257.x.

D. Soumpasis. Theoretical analysis of fluorescence photobleaching recovery experiments. *Biophysical Journal*, 41(1):95–97, Jan. 1983. ISSN 00063495. doi: 10.1016/S0006-3495(83)84410-5.

S. Spiegel, R. Blumenthal, P. H. Fishman, and J. S. Handler. Gangliosides do not move from apical to basolateral plasma membrane in cultured epithelial cells. *Biochimica et Biophysica Acta*, 821:310–318, 1985. doi: 10.1016/0005-2736(85)90101-4.

E. T. Spiliotis, S. J. Hunt, Q. Hu, M. Kinoshita, and W. J. Nelson. Epithelial polarity requires septin coupling of vesicle transport to polyglutamylated microtubules. *Journal of Cell Biology*, 180(2):295–303, Jan. 2008. ISSN 1540-8140, 0021-9525. doi: 10.1083/jcb.200710039.

J. D. Steels, M. P. Estey, C. D. Froese, D. Reynaud, C. Pace-Asciak, and W. S. Trimble. Sept12 is a component of the mammalian sperm tail annulus. *Cell Motility and the Cytoskeleton*, 64(10):794–807, Oct. 2007. ISSN 08861544, 10970169. doi: 10.1002/cm.20224.

M. C. Surka, C. W. Tsang, and W. S. Trimble. The Mammalian Septin MSF Localizes with Microtubules and Is Required for Completion of Cytokinesis. *Molecular Biology of the Cell*, 13:3532–3545, 2002. doi: 10.1091/mbc.E02010042.

T. Tada, A. Simonetta, M. Batterton, M. Kinoshita, D. Edbauer, and M. Sheng. Role of Septin Cytoskeleton in Spine Morphogenesis and Dendrite Development in Neurons. *Current Biology*, 17(20):1752–1758, Oct. 2007. ISSN 09609822. doi: 10.1016/j.cub.2007.09.039.

P. A. Takizawa, J. L. DeRisi, J. E. Wilhelm, and R. D. Vale. Plasma Membrane Compartmentalization in Yeast by Messenger RNA Transport and a Septin Diffusion Barrier. *Science*, 290(5490):341–344, Oct. 2000. ISSN 0036-8075, 1095-9203. doi: 10.1126/science.290.5490.341.

L. Tamm and H. McConnell. Supported phospholipid bilayers. *Biophysical Journal*, 47 (1):105–113, Jan. 1985. ISSN 00063495. doi: 10.1016/S0006-3495(85)83882-0.

K. Tarassov, V. Messier, C. R. Landry, S. Radinovic, M. M. S. Molina, I. Shames, Y. Malitskaya, J. Vogel, H. Bussey, and S. W. Michnick. An in vivo Map of the Yeast Protein Interactome. *Science, New Series*, 320(5882):1465–1470, 2008.

A. J. Tooley, J. Gilden, J. Jacobelli, P. Beemiller, W. S. Trimble, M. Kinoshita, and M. F. Krummel. Amoeboid T lymphocytes require the septin cytoskeleton for cortical integrity and persistent motility. *Nature Cell Biology*, 11(1):17–26, Jan. 2009. ISSN 1465-7392, 1476-4679. doi: 10.1038/ncb1808.

K. Tóth, O. Galamb, S. Spisák, B. Wichmann, F. Sipos, G. Valcz, K. Leiszter, B. Molnár, and Z. Tulassay. The Influence of Methylated Septin 9 Gene on RNA and Protein Level in Colorectal Cancer. *Pathology & Oncology Research*, 17(3):503–509, Sept. 2011. ISSN 1219-4956, 1532-2807. doi: 10.1007/s12253-010-9338-7.

M. T. Valentine, P. D. Kaplan, D. Thota, J. C. Crocker, T. Gisler, R. K. Prud'homme, M. Beck, and D. A. Weitz. Investigating the microenvironments of inhomogeneous soft materials with multiple particle tracking. *Physical Review E*, 64(6):061506, Nov. 2001. ISSN 1063-651X, 1095-3787. doi: 10.1103/PhysRevE.64.061506.

F. Valverde. Apical dendritic spines of the visual cortex and light deprivation in the mouse. *Experimental Brain Research*, 3(4):337–352, May 1967. ISSN 0014-4819, 1432-1106. doi: 10.1007/BF00237559.

F. Valverde. Rate and extent of recovery from dark rearing in the visual cortex of the mouse. *Brain Research*, 33(1):1–11, Oct. 1971. ISSN 00068993. doi: 10.1016/0006-8993(71)90302-7.

G. van Meer and K. Simons. The function of tight junctions in maintaining differences in lipid composition between the apical and the basolateral cell surface domains of MDCK cells. *The EMBO Journal*, 5(7):1455–1464, 1986. doi: 10.1002/j.1460-2075.1986.tb04382.x.

P. Verdier-Pinard, D. Salaun, H. Bouguenina, S. Shimada, M. Pophillat, S. Audebert, E. Agavnian, S. Coslet, E. Charafe-Jauffret, T. Tachibana, and A. Badache. Septin 9_i2 is downregulated in tumors, impairs cancer cell migration and alters subnuclear actin filaments. *Scientific Reports*, 7(1):44976, July 2017. ISSN 2045-2322. doi: 10.1038/srep44976.

C. L. Vestergaard, P. C. Blainey, and H. Flyvbjerg. Optimal estimation of diffusion coefficients from single-particle trajectories. *Physical Review E*, 89(2):022726, Feb. 2014. ISSN 1539-3755, 1550-2376. doi: 10.1103/PhysRevE.89.022726.

A. Vial, C. Taveneau, L. Costa, B. Chauvin, H. Nasrallah, C. Godefroy, P. Dosset, H. Isambert, K. X. Ngo, S. Mangenot, D. Levy, A. Bertin, and P.-E. Milhiet. Correlative AFM and fluorescence imaging demonstrate nanoscale membrane remodeling and ring-like and tubular structure formation by septins. *Nanoscale*, 13(29):12484–12493, 2021. ISSN 2040-3364, 2040-3372. doi: 10.1039/D1NR01978C.

O. V. Vieira, K. Gaus, P. Verkade, J. Fullekrug, W. L. C. Vaz, and K. Simons. FAPP2, cilium formation, and compartmentalization of the apical membrane in polarized Madin–Darby canine kidney (MDCK) cells. *Proceedings of the National Academy of Sciences*, 103(49):18556 –18561, 2006. doi: 10.1073/pnas.0608291103.

A. M. Vrabioiu and T. J. Mitchison. Structural insights into yeast septin organization from polarized fluorescence microscopy. *Nature*, 443(7110):466–469, Sept. 2006. ISSN 0028-0836, 1476-4687. doi: 10.1038/nature05109.

S. R. Walsh and R. Dolin. Vaccinia viruses: vaccines against smallpox and vectors against infectious diseases and tumors. *Expert Review of Vaccines*, 10(8):1221–1240, Aug. 2011. ISSN 1476-0584, 1744-8395. doi: 10.1586/erv.11.79.

J. D. Warren, W. Xiong, A. M. Bunker, C. P. Vaughn, L. V. Furtado, W. L. Roberts, J. C. Fang, W. S. Samowitz, and K. A. Heichman. Septin 9 methylated DNA is a sensitive and specific blood test for colorectal cancer. *BMC Medicine*, 9(1):133, Dec. 2011. ISSN 1741-7015. doi: 10.1186/1741-7015-9-133.

L. Wawrezinieck, H. Rigneault, D. Marguet, and P.-F. Lenne. Fluorescence Correlation Spectroscopy Diffusion Laws to Probe the Submicron Cell Membrane Organization. *Biophysical Journal*, 89(6):4029–4042, Dec. 2005. ISSN 00063495. doi: 10.1529/biophysj.105.067959.

W. A. Webber and J. Lee. Fine structure of mammalian renal cilia. *The Anatomical Record*, 182(3):339–343, July 1975. ISSN 0003-276X, 1097-0185. doi: 10.1002/ar.1091820307.

R. L. Weiss, D. A. Goodenough, and U. W. Goodenough. Membrane particle arrays associated with the basal body and with contractile vacuole secretion in Chlamydomonas. *The Journal of Cell Biology*, 72:133–143, 1977. doi: 10.1083/jcb.72.1.133.

M. Welch and M. Way. Arp2/3-Mediated Actin-Based Motility: A Tail of Pathogen Abuse. *Cell Host & Microbe*, 14(3):242–255, Sept. 2013. ISSN 19313128. doi: 10.1016/j.chom.2013.08.011.

B. L. Woods, I. Seim, J. Liu, G. McLaughlin, K. S. Cannon, and A. S. Gladfelter. Biophysical properties governing septin assembly. preprint, bioRxiv, Mar. 2021.

H. Xie, M. Surka, J. Howard, and W. S. Trimble. Characterization of the mammalian septin H5: Distinct patterns of cytoskeletal and membrane association from other septin proteins. *Cell Motility and the Cytoskeleton*, 43(1):52–62, 1999. ISSN 0886-1544, 1097-0169. doi: 10.1002/(SICI)1097-0169(1999)43:1⟨52::AID-CM6⟩3.0.CO;2-5.

Y. Xie, J. P. Vessey, A. Konecna, R. Dahm, P. Macchi, and M. A. Kiebler. The GTP-Binding Protein Septin 7 Is Critical for Dendrite Branching and Dendritic-Spine Morphology. *Current Biology*, 17(20):1746–1751, Oct. 2007. ISSN 09609822. doi: 10.1016/j.cub.2007.08.042.

E. Zent and A. Wittinghofer. Human septin isoforms and the GDP-GTP cycle. *Biological Chemistry*, 395(2):169–180, Feb. 2014. ISSN 1437-4315, 1431-6730. doi: 10.1515/hsz-2013-0268.

J. Zhang, C. Kong, H. Xie, P. S. McPherson, S. Grinstein, and W. S. Trimble. Phosphatidylinositol polyphosphate binding to the mammalian septin H5 is modulated by GTP. *Current Biology*, 9(24):1458–1467, Dec. 1999. ISSN 09609822. doi: 10.1016/S0960-9822(00)80115-3.

Y. Zhang, J. Gao, K. K. K. Chung, H. Huang, V. L. Dawson, and T. M. Dawson. Parkin functions as an E2-dependent ubiquitin– protein ligase and promotes the degradation of the synaptic vesicle-associated protein, CDCrel-1. *Proceedings of the National Academy of Sciences*, 97(24):13354–13359, Nov. 2000. ISSN 0027-8424, 1091-6490. doi: 10.1073/pnas.240347797.

M. Zhu, F. Wang, F. Yan, P. Y. Yao, J. Du, X. Gao, X. Wang, Q. Wu, T. Ward, J. Li, S. Kioko, R. Hu, W. Xie, X. Ding, and X. Yao. Septin 7 Interacts with Centromere-associated Protein E and Is Required for Its Kinetochore Localization. *Journal of Biological Chemistry*, 283(27):18916–18925, July 2008. ISSN 00219258. doi: 10.1074/jbc.M710591200.

K. Østevold, A. V. Meléndez, F. Lehmann, G. Schmidt, K. Aktories, and C. Schwan. Septin remodeling is essential for the formation of cell membrane protrusions (microtentacles) in detached tumor cells. *Oncotarget*, 8(44):76686–76698, Sept. 2017. ISSN 1949-2553. doi: 10.18632/oncotarget.20805.